UNIVERSITY OF SOUTHAMPTON
FACULTY OF ENGINEERING, SCIENCE AND MATHEMATICS
SCHOOL OF ELECTRONICS AND COMPUTER SCIENCE

Smart Antenna-Aided Multicarrier Transceivers for Mobile Communications

by

Jos Akhtman

A thesis submitted in partial fulfilment of the
requirements for the award of Doctor of Philosophy
at the University of Southampton

January 2007

SUPERVISOR:
Professor Lajos Hanzo

University of Southampton
Southampton SO17 1BJ
United Kingdom

UNIVERSITY OF SOUTHAMPTON

ABSTRACT

Faculty of Engineering, Science and Mathematics
School of Electronics and Computer Science
A thesis submitted in partial fulfilment of the
requirements for the award of Doctor of Philosophy

Smart Antenna-Aided Multicarrier Transceivers for Mobile Communications

by Jos Akhtman

In spite of an immense interest from both the academic and the industrial communities, a practical multiple-input multiple-output (MIMO) transceiver architecture, capable of approaching channel capacity boundaries in realistic channel conditions remains largely an open problem. Consequently, in this treatise I derive an advanced iterative, so called *turbo* multi-antenna-multi-carrier (MAMC) receiver architecture. Following the philosophy of turbo processing [26], our turbo spacial division multiplexed (SDM)-orthogonal frequency division multiplexed (OFDM) receiver comprises a succession of soft-input-soft-output detection modules, which iteratively exchange soft bit-related information and thus facilitate a substantial improvement of the overall system performance. In this treatise, I explore two major aspects of the turbo wireless mobile receiver design. Firstly, I consider the problem of soft-decision-feedback aided acquisition of the propagation conditions experienced by the transmitted signal and secondly, I explore the issue of the soft-input-soft-output detection of the spatially-multiplexed information-carrying signals.

More specifically, in Chapter 2 I derive an advanced decision-directed channel estimation (DDCE) scheme, which is suitable for employment in a wide range of multi-antenna multi-carrier systems as well as over the entire range of practical channel conditions. In particular, I consider mobile wireless multipath channels, which exhibit fast Rayleigh frequency-selective fading and are typically characterized by time-variant power delay profile (PDP). Furthermore, I develop a method of parametric tracking of the channel impulse response (CIR) taps, which facilitates low-complexity channel estimation in realistic channel conditions characterized by time-variant fractionally-spaced power delay profile. More specifically I employ the Projection Approximation Subspace Tracking (PAST) method for the sake of recursive tracking of the channel transfer function's (CTF) covariance matrix and subsequent tracking of the corresponding CIR taps. I demonstrate that the PAST-aided decision directed channel estimation scheme proposed exhibits good performance over the entire range of practical conditions. Our discourse evolves further with a discussion of an adaptive CIR tap prediction method, which is based on recursive least squares (RLS) filtering. I analyse the achievable performance of the prediction method proposed and demonstrate that the RLS prediction technique outperforms the so-called robust prediction approach discussed in the literature. Additionally, I explore a family of recursive MIMO-CTF tracking methods, which in conjunction with the aforementioned PAST-aided CIR-tracking method as well as the RLS CIR tap prediction method, facilitate an effective channel estimation scheme in the context of a MIMO-OFDM system. More specifically, I consider both hard- and soft-feedback assisted least mean squares (LMS) and recursive least squares (RLS) tracking algorithms as well as the modified RLS algorithm, which is capable of improved utilization of the soft information associated with the decision-based estimates. Subsequently, I document the achievable performance of resultant MIMO-DDCE scheme employing the recursive CTF tracking followed by the parametric CIR tap tracking and CIR tap prediction. I demonstrate that the SDM-OFDM system employing the MIMO-DDCE scheme proposed exhibits a BER performance, which is within 2 dB from the corresponding performance exhibited by the system assuming a perfect channel knowledge.

In Chapter 3 I investigate the attainable performance benefits of employing multiple-antenna architectures in wireless communication systems. I explore the merits of a family of space-time processing methods reminiscent of multi-user detection employed in *multi-user* systems and apply them in the context of a BLAST-type MIMO architecture with the aim of maximising the overall capacity of the system. I demonstrate that the linear capacity increase, predicted by the information-theoretic analysis can indeed be achieved by employing a relatively low-complexity linear detection technique, such as the Minimum Mean Square Error (MMSE) detector.

In Chapter 4 I propose a novel SDM detection method, which I refer to as the Soft-output OPtimized HIErarchy (SOPHIE) Spatial Division Multiplexing (SDM) detector. The proposed method may be regarded as an advanced extension of the Sphere Decoder method. More specifically, our method can be employed in the rank-deficient scenario, where the number of transmit antenna elements exceeds that of the receive antenna elements. Furthermore our scheme is suitable for high-throughput modulation schemes such as 16- and 64-QAM. I introduce a list of optimization rules, which facilitate the achievement of the near optimum BER performance of a Log-MAP detector at a relatively low computational complexity. The trade-off between the achievable BER performance and the associated computational complexity is controlled using two parameters. The proposed detection method exhibits two major advantages over all previously proposed techniques. Firstly, the bit-related soft information, which facilitates the achievement of near-optimum Log-MAP performance, is attained at the expense of a modest complexity increase over that of hard-decision ML detection. Secondly, our method exhibits a particularly low polynomial complexity in both the low- and high-SNR regions. In the critical range of SNR values, which corresponds to the “waterfall” region of the BER versus SNR curve, the detection complexity versus the number of transmit antennas remains exponential. Nevertheless, I demonstrate that the complexity can be dramatically reduced at the cost of a minor BER degradation. Namely, in 8x8 SDM-OFDM system a BER performance within 1 dB from that exhibited by the exhaustive Log-MAP search may be achieved with a complexity which is *four* orders of magnitude lower than the complexity imposed by the exhaustive Log-MAP search.

Finally, in Chapter 5 I explore the performance trends exhibited by the resultant turbo SDM-OFDM receiver, which comprises three major components, namely, the soft-feedback decision-directed channel estimator derived in Chapter 2, followed by the soft-input-soft-output OHRSA Log-MAP SDM detector of Chapter 4 as well as a soft-input-soft-output serially concatenated turbo code [27]. I analyze the achievable performance of each individual constituent of our turbo receiver, as well as the achievable performance of the entire iterative system. Our aim is to identify the optimum system configuration, while considering various design trade-offs, such as achievable error-rate performance, achievable data-rate as well as associated computational complexity.

We demonstrate that the turbo SDM-OFDM system employing the MIMO-DDCE scheme of Chapter 2 as well as the OHRSA Log-MAP SDM detector of Chapter 4 remains effective in channel conditions associated with high terminal speeds of up to 130 km/h, which corresponds to the OFDM-symbol normalized Doppler frequency of 0.006. Additionally, I report a virtually error-free performance of a rate $1/2$ turbo-coded 8x8-QPSK-OFDM system, exhibiting a total bit rate of 8 bits/s/Hz and having a pilot overhead of only 10%, at SNR of 7.5dB and normalized Doppler frequency of 0.003, which corresponds to the mobile terminal speed of roughly 65 km/h[1].

---

[1] Additional system parameters are characterized in Table 1.4.

Acknowledgement

I would like to take this opportunity to express my deep gratitude to Professor Lajos Hanzo, who's exceptional supervision and support enabled this work. His generous investment of time and energy as well as perpetual enthusiasm deserve my uttermost acknowledgement.

I would like also to thank staff members and colleagues in the Communications Research group, namely Prof. Sheng Chen, Dr. Stephan Weiss, Dr. Bee Leong Yeap, Dr. Lie Liang Yang, Dr. Soon X Ng, Dr. Mohamad Yusoff Alias, Dr. Hubert Dietl, Dr. Hua Wei, Dr. Ming Jiang, Andreas Wolfgang, the group secretary Denise Harvey and many others, too numerous to mention here.

My grateful thanks go to Dr. Walter Tuttlebee and the Virtual Centre of Excellence in Mobile and Personal Communications Ltd. (Mobile VCE) for their generous financial support.

My sincere personal thanks are due to many precious friends both here and in Israel, who made my stay in UK such a memorable experience. I would like to thank my family, my father and mother as well as my brother for everything they have done for me throughout my life. Finally, I want to thank my adorable fiancée Sophie for her love, patience and support. This thesis is dedicated to her and our lovable baby daughter Noa Julie, who has lightened my world with her sudden arrival and bright smiles.

List of Publications

[1] J. Akhtman and L. Hanzo. Maximum-Likelihood Advanced Sphere Decoding for MIMO-OFDM. In *OFDM and MC-CDMA: A Primer by L. Hanzo and T. Keller*, pages 253–302. John Wiley, New York, USA, 2006.

[2] M. Jiang, J. Akhtman, and L. Hanzo. Genetic Algorithm Aided Channel Estimation and MUD for SDMA OFDM. In *OFDM and MC-CDMA: A Primer by L. Hanzo and T. Keller*, pages 303–329. John Wiley, New York, USA, 2006.

[3] J. Akhtman. Method and apparatus of peak-to-average power ratio reduction. EU Patent Number EP1469649, granted June 2006. Available from: `http://v3.espacenet.com/textdoc?DB=EPODOC&IDX=EP1469649`.

[4] J. Akhtman and L. Hanzo. Decision directed channel estimation employing sample-spaced and fractionally-spaced CIR estimators. *IEEE Trans. on Wireless Comm.*, 2007, to be published.

[5] M. Jiang, J. Akhtman, and L. Hanzo. Soft-information assisted near-optimum nonlinear detection for BLAST-type space division multiplexing OFDM systems. *IEEE Trans. on Wireless Comm.*, vol. 6, no. 3, March 2007, to be published.

[6] J. Akhtman and L. Hanzo. Channel impulse response tap prediction for time-varying wireless channels. *IEEE Transaction on Vehicular Technology*, November 2007, to be published.

[7] J. Akhtman and L. Hanzo. An optimized-hierarchy-aided near-LogMAP detector for MIMO systems. *IEEE Trans. on Wireless Communications*, 2007, to be published.

[8] A. Wolfgang, J. Akhtman, S. Chen, and L. Hanzo. Iterative MIMO detection for rank-deficient systems. *IEEE Signal Processing Letters*, vol. 13, no. 11, pp. 699–702, November 2006.

[9] A. Wolfgang, J. Akhtman, S. Chen, and L. Hanzo. Reduced complexity near maximum-likelihood uplink detection for decision feedback assisted space-time equalization. *IEEE Transactions on Wireless Communications*, 2007, to be published.

[10] J. Akhtman and L. Hanzo. PAST aided channel estimation for MIMO-OFDM. *IEEE Transactions on Signal Processing*, submitted January 2007.

[11] J. Akhtman, A. Wolfgang, S. Chen, and L. Hanzo. Advanced iterative receiver architecture for MIMO-OFDM systems in realistic channel condition. *IEEE Transactions on Wireless Communications*, submitted January 2007.

[12] J. Akhtman, B-Z. Bobrovsky, and L. Hanzo. Peak to average power reduction for OFDM modems. In *Proceedings of the Spring'03 IEEE Vehicular Technology Conference*, pp. 1188–1192, vol. 2, Jeju, South Korea, April 22–25 2003.

[13] J. Akhtman and L. Hanzo. Low complexity channel estimation for OFDM and MC-CDMA. In *Proceedings of the Spring'04 IEEE Vehicular Technology Conference*, pp. 1134–1138, vol. 2, Milano, Italy, May 17–19 2004.

[14] J. Akhtman and L. Hanzo. Generic reduced-complexity MMSE channel estimation for OFDM and MC-CDMA. In *Proceedings of the Spring'05 IEEE Vehicular Technology Conference*, pp. 528–532, vol. 1, Stockholm, Sweden, May 30–June 1, 2005.

[15] J. Akhtman and L. Hanzo. Decision directed channel estimation employing sample-spaced and fractionally-spaced CIR estimators. In *Proceedings of the Fall'05 IEEE Vehicular Technology Conference*, pp. 1916–1920, vol. 3, Dallas, Texas, September 25-28, 2005.

[16] J. Akhtman and L. Hanzo. Reduced-complexity maximum-likelihood detection in multiple-antenna-aided multicarrier systems. In Kahled Fazer and Stefan Kaiser, editors, *Proceedings of the 5th Int'l Workshop on Multi-Carrier Spread-Spectrum*, pages 21–28, Oberpfaffenhofen, Germany, 14-16 September 2005. Springer, Dordrecht, Netherlands. Available from: `http://eprints.ecs.soton.ac.uk/11237/`.

[17] M. Jiang, J. Akhtman, and L. Hanzo. Near-optimum nonlinear soft detection for multiple-antenna assisted OFDM. In *Proceedings of the IEEE Wireless Communications and Networking Conference*, pages 1989–1993, Las Vegas, NV, USA, 3–6 April 2006.

[18] A. Wolfgang, J. Akhtman, S. Chen, and L. Hanzo. Reduced complexity near maximum-likelihood uplink detection for decision feedback assisted space-time equalization. In *Proceedings of the IEEE Wireless Communications and Networking Conference*, pages 1555–1560, Las Vegas, NV, USA, 3–6 April 2006.

[19] J. Akhtman and L. Hanzo. Low complexity approximate Log-MAP detection for MIMO systems. In *Proceedings of the IEEE Wireless Communications and Networking Conference*, pages 1759–1764, Las Vegas, NV, USA, 3–6 April 2006.

[20] J. Akhtman and L. Hanzo. OHRSA-ML space-time detector-aided MIMO-OFDM. In *Proceedings of the Spring'06 IEEE Vehicular Technology Conference*, pages 1526–1530, vol. 3, Melbourne, Australia, 7–10 May 2006.

[21] M. Jiang, J. Akhtman, F. Guo, and L. Hanzo. Iterative joint channel estimation and multi-user detection for high-throughput multiple-antenna OFDM systems. In *Proceedings of the Spring'06 IEEE Vehicular Technology Conference*, pages 221–225, vol. 1, Melbourne, Australia, 7–10 May 2006.

[22] J. Akhtman, C-Y. Wei, and L. Hanzo. Reduced-complexity maximum-likelihood detection in downlink SDMA systems. In *Proceedings of the Fall'06 IEEE Vehicular Technology Conference*, Montréal, Canada, 25-28 September 2006.

[23] J. Akhtman and L. Hanzo. Decision Directed Channel Estimation Employing Projection Approximation Subspace Tracking. In *Proceedings of the Spring'07 IEEE Vehicular Technology Conference*, Dublin, Ireland, 22–25 April 2007, to be published.

[24] J. Akhtman and L. Hanzo. Advanced channel estimation for MIMO-OFDM in realistic channel conditions. In *Proceedings of IEEE International Conference on Communications*, Glasgow, UK, 24–27 June 2007, to be published.

[25] J. Akhtman and L. Hanzo. Advanced iterative receiver architecture for MIMO-OFDM. In *Proceedings of the IEEE Wireless Communications and Networking Conference*, Hong Kong, China, 11–14 March 2007, to be published.

Contents

List of Symbols

$\mathcal{I}\{\cdot\}$	Imaginary part of a complex value
$\mathcal{I}$	Mutual information,sort
$\mathcal{R}\{\cdot\}$	Real part of a complex value

$\boldsymbol{A}^{\mathtt{T}}$	Matrix/vector transpose
$\boldsymbol{A}^{\mathtt{H}}$	Matrix/vector hermitian adjoint, *i.e.* complex conjugate transpose
$\boldsymbol{A}^{*}$	Matrix/vector/scalar complex conjugate
$\boldsymbol{A}^{-1}$	Matrix inverse
$\boldsymbol{A}^{+}$	Moore-Penrose pseudoinverse
$\mathtt{tr}\left(\boldsymbol{A}\right)$	Trace of matrix, *i.e.* the sum of its diagonal elements

$(i_{\text{ce}}, i_{\text{det}}, i_{\text{dec}})$	Number of (channel estimation,detection,decoding) iterations
E_b	Energy per transmitted bit
E_s	Energy per transmitted M-QAM symbol
L_f	Number of data-frames per transmission burst
N_d	Number of data SDM-OFDM symbols per data-frame
N_p	Number of pilot SDM-OFDM symbols in burst preamble
T	OFDM symbol duration
T_s	OFDM FFT frame duration
f_{D}	Maximum Doppler frequency
K	Number of OFDM subcarriers
B	Signal bandwidth
β	RLS CIR tap prediction filter forgetting factor
$\mathcal{C}$	Uncostrained capacity
f_{c}	Carrier frequency

η	PASTD aided CIR tap tracking filter forgetting factor
γ	OHRSA search resolution parameter
m_{t}	Number of receive antennas
n_{r}	Number of transmit antennas
ν_{τ}	OFDM-symbol-normalized PDP tap drift rate
ρ	OHRSA search radius factor parameter
σ_w^2	Gaussian noise variance
τ_{rms}	RMS delay spread
ε	Pilot overhead
ζ	MIMO-CTF RLS tracking filter forgetting factor
r	Size of the transmitted bit-wise signal vector $\mathbf{t}$

$\boldsymbol{I}$	Identity matrix
$\mathcal{H}$	Hadamard matrix
$\mathcal{L}$	Log Likelihood Ratio value
$\mathcal{M}$	Set of M-PSK/M-QAM constellation phasors

$\check{\mathbf{s}}$	*A priori* signal vector estimate
$\hat{\mathbf{s}}$	*A posteriori* signal vector estimate
$\hat{\mathbf{x}}$	Unconstrained *a posteriori* signal vector estimate
$\mathbf{H}$	Subcarrier-related MIMO CTF matrix
$\mathbf{d}$	Transmitted bit-wise signal
$\mathbf{s}$	Transmitted subcarrier-related SDM signal
$\mathbf{t}$	Transmitted subcarrier-related bit-wise SDM signal
$\mathbf{y}$	Received subcarrier-related SDM signal
$\mathbf{w}$	Gaussian noise sample vector
$\tilde{\mathbf{s}}$	Soft-information aided signal vector estimate

$\mathtt{Cov}\{\cdot,\cdot\}$	Covariance of two random variables
$\mathtt{Var}\{\cdot\}$	Variance of a random variable
$\mathtt{E}\{\cdot\}$	Expectation of a random variable
$\mathtt{Ei}\{\cdot\}$	Exponential integral
$\mathtt{JacLog}(\cdot)$	Jacobian logorithm
κ	Channel estimation efficiency criteria

$\|\cdot\|_2$	Second order norm
$\mathtt{P}\{\cdot\}$	Probability density function
$\mathrm{rms}\{\cdot\}$	Root mean square value

Chapter 1

Introduction

1.1 Outline

The ever-increasing demand for high data-rates in wireless networks requires the efficient utilisation of the limited bandwidth available, while supporting a high grade of mobility in diverse propagation environments. Correspondingly, the aim of this thesis is **the development of novel mobile wireless transceivers, which are capable of satisfying these requirements.** The specific objective of the research is **to address two major components of the transceiver architecture, namely the channel estimation module as well as the data detection scheme.** Consequently, in Chapter 2, we develop an advanced channel estimation scheme suitable for employment in a wide range of multi-antenna multi-carrier transceivers. In Chapters 3 and 4 we review several state-of-the-art data detection methods as well as propose a novel detector, which combines high performance with a relatively low computational complexity. Finally, in Chapter 5, we propose an advanced turbo-detected multi-antenna multi-carrier receiver architecture, which employs joint iterative channel estimation and data detection.

1.2 Channel Estimation for Multicarrier Systems

Orthogonal Frequency Division Multiplexing (OFDM) and Multi-Carrier Code Division Multiple Access (MC-CDMA) techniques [28] exhibit a high potential to satisfy the challenging requirements imposed by the rapidly evolving wireless communications technologies. This is a benefit of their ability to cope with highly time-variant wireless channel characteristics. However, as pointed out in [29], the capacity and the achievable integrity of communication systems is highly dependent on the system's knowledge concerning the channel conditions encountered. Thus, the provision of an accurate and robust channel estimation strategy is a crucial factor in achieving a high performance.

Table 1.1: Major contributions addressing channel estimation in multi-carrier systems.

[35, 36] Höher *et. al.*, 1997	Cascaded 1D-FIR Wiener filter based channel interpolation.
[37] Edfors *et al.*, 1998	Detailed analysis of SVD-aided CIR-related domain noise reduction for DDCE.
[38] Li, 1998	DDCE using DFT-based 2D interpolation and robust prediction.
[31] Li, 2000	2D pilot pattern aided channel estimation using 2D robust frequency domain Wiener filtering.
[33] Yang *et al.*, 2001	Detailed discussion of parametric, ESPRIT-assisted channel estimation.
[39] Münster and Hanzo, 2003	RLS-adaptive PIC assisted DDCE for OFDM.
[40] Otnes and Tüchler, 2004	Iterative channel estimation for turbo equalization.

Well-documented approaches to the problem of channel estimation are constituted by *pilot assisted*, *decision directed* and *blind* channel estimation methods [28, 30].

The family of *pilot assisted* channel estimation methods was investigated for example by Li [31], Morelli and Mengali [32], Yang *et al.* [33] as well as Chang and Su [34], where the channel parameters are typically estimated by exploiting the channel-sounding signal. For example, in OFDM and MC-CDMA often a set of frequency-domain pilots are transmitted for estimating the Frequency-Domain Channel Transfer Function (FD-CTF), which are known at the receiver [28]. The main drawback of this method is that the pilot symbols do not carry any useful information and thus they reduce the system's effective throughput.

By contrast, in Decision Directed Channel Estimation (DDCE) methods both the pilot symbols as well as all the information symbols are utilised for channel estimation [28]. The simple philosophy of this method is that in the absence of transmission errors we can benefit from the availability of 100% pilot information by using the detected subcarrier symbols as an *a posteriori* reference signal. The employment of this method allows us to reduce the number of pilot symbols required. This technique is particularly efficient under benign channel conditions, where the probability of a decision error is low, but naturally, this approach is also prone to error propagation effects. The family of DDCE techniques was investigated for example by van de Beek *et al.* [41], Mignone and Morello [42], Edfors *et al.* [37], Li *et al.* [38], Li and Sollenberg [43] as well as Münster and Hanzo [30, 39, 44, 45].

The class of iterative DDCE scemes, where the channel estimation is carried out through a series of iterations utilizing the increasingly-refined soft-decision-based feedback, was explored by Sandell *et. al.* [46], Valenti [47], Yeap *et. al.* [48], Song *et. al.* [49, 50], as well as by Otnes and Tüchler [40, 51].

The closely related class of joint receivers, where the channel parameters and the transmitted information-carrying symbols are estimated jointly was explored for example by Seshadri [52], Baccarelli and Cusani [53], developed further by Knickenberg *et. al.* [54] recently revisited by Cozzo and Hughes [55] as well as Cui and Tellambura [56, 57].

Finally, the class of *blind* estimation methods eliminates all redundant pilot symbols. Most of these methods rely on the employment of decision feedback and on the exploitation of the redundancy often found in the structure of the modulated signal, as exemplified by the techniques described for example by Antón-Haro *et. al.* [58], Boss *et. al.* [59], Endres *et. al.* [60], Giannakis and Halford [61], Zhou and Giannakis [62] as well as by Necker and Stüber [63].

Additional major subject, closely related to channel estimation, namely the prediction of fast fading channels was extensive studied by Haykin [64]. A so-called robust predictor was proposed by Li [38] and revised by Münster and Hanzo [45]. An adaptive RLS channel predictor was proposed by Schafhuber and Matz [65].

Subsequently, in this treatise we propose a DDCE scheme, which is suitable for employment in both OFDM and MC-CDMA systems. We analyse the achievable performance of the estimation scheme considered in conjunction with a realistic dispersive Rayleigh fading channel model having a Fractionally-Spaced (FS) rather than Symbol-Spaced (SS) Power Delay Profile (PDP).

A basic component of the DDCE schemes proposed in the literature is an *a posteriori* Least Squares (LS) temporal estimator of the OFDM-subcarrier-related Frequency-Domain Channel Transfer Function (FD-CTF) coefficients [28, 38]. The accuracy of the resultant temporal FD-CTF estimates is typically enhanced using one- or two-dimensional interpolation exploiting both the time- and the frequency-domain correlation between the desired FD-CTF coefficients. The LS-based temporal FD-CTF estimator was shown to be suitable for QPSK-modulated OFDM systems [28, 38], where the energy of the transmitted subcarrier-related information symbols is constant. However, as it will be pointed out in Section 2.4.1 of this treatise, the LS method cannot be readily employed in MC-CDMA systems, where – in contrast to OFDM systems – the energy of the transmitted subcarrier-related information symbols fluctuates as a function of both the modulated sequence and that of the choice of the potentially non-constant-modulus modulation scheme itself. Thus we propose a Minimum Mean Square Error (MMSE) estimation based DDCE method, which is an appropriate solution for employment in both OFDM and MC-CDMA systems.

The system model and the channel model considered are described in Section 1.7 of this treatise. The difficulty of employing the LS approach to the problem of estimating the OFDM-subcarrier-related FD-CTF coefficients is described in Section 2.4.1. The alternative MMSE FD-CTF estimator circumventing the problem outlined in Section 2.4.1 is analyzed in Section 2.4.2. Our discourse evolves further by proposing a MMSE CIR estimator exploiting the frequency-domain correlation of the FD-CTF coefficients in Section 2.5.1 and a reduced-complexity version of the CTF MMSE estimator considered is proposed in Section

2.5.2. The computational complexity of both methods is compared in Section 2.5.3.

In Section 2.5 we continue our discourse with the derivation of both sample-spaced as well as fractionally-spaced Channel Impulse Response (CIR) estimator. In Section 2.5.5 we then perform a comparison between the two methods considered and demonstrate the advantages of the later, *i. e.* fractionally-spaced scheme. Subsequently, in Section 2.6 we develope a method of parametric tracking of the fractionally-spaced channel impulse response (CIR) taps, which facilitates low-complexity channel etimation in realistic channel conditions characterized by time-variant fractionally-spaced power delay profile. More specifically we employ the Projection Approximation Subspace Tracking (PAST) method for the sake of recursive tracking of the channel transfer function's (CTF) covariance matrix and subsequent tracking of the corresponding CIR taps. We demonstrate that the PAST-aided decision directed channel estimation scheme proposed exhibits good performance over the entire range of practical conditions.

In Section 2.7 we discuss two major CIR tap prediction strategies. Specifically, In Section 2.7.2 the so-called *robust* implementation of the stationary Minimum Mean Square Error (MMSE) CIR predictor is considered. The *robust* CIR predictor [38] assumes a constant-valued, limited-support channel scattering function [28] during the design of the CIR tap prediction filter and hence relies on the assumption of encountering the worst possible channel conditions. On the other hand, in Section 2.7.4 we discuss the adaptive Recursive Least Squares (RLS) method of CIR prediction [65]. As opposed to the robust CIR predictor of [38], the RLS CIR predictor does not require any explicit information concerning the channel conditions encountered. Consequently, in Section 2.7.5 we characterize and compare the achievable performance of both methods considered and draw conclusions concerning their relative merits. Specifically, we demonstrate that the RLS prediction technique outperforms its robust counterpart over the entire range of the relevant channel conditions.

In Section 2.8 we characterize the achievable performance of the resultant PAST-aided DDCE scheme. We report an estimation efficiency of $\kappa = -18dB$ exhibited by a system employing 10% of pilots and communicating over a dispersive Rayleigh fading channel having a Doppler frequency of $f_D = 0.003$. Furthermore, we report a BER performance, which is only 3 dB from the corresponding BER performance exhibited by a similar system assuming perfect channel knowledge.

1.3 Channel Estimation for MIMO-OFDM

In spite of an immense interest from both the academic and the industrial communities, a practical multiple-input multiple-output (MIMO) transceiver architecture, capable of approaching channel capacity boundaries in realistic channel conditions remains largely an open problem. In particular, a robust and accurate channel estimation in MIMO systems constitutes a major issue, preventing us from achieving the high capacities

Table 1.2: Major contributions addressing the problem of channel estimation in MIMO systems.

[66] Li *et. al.*, 2002	MIMO-OFDM for wireless communications: signal detection with enhanced channel estimation.
[67] Stüber *et. al.*, 2004	An important overview encompassing most of the major aspects of the broadband MIMO-OFDM wireless communications including channel estimation, signal detection as well as time and frequency syncronization.
[68] Deng *et. al.*, 2003	Decision directed iterative channel estimation for MIMO systems.
[55] Cozzo and Hughes, 2003	Joint channel estimation and data detection in space-time communications.
[69] Münster and Hanzo,2005	Parallel-interference-cancellation-assisted decision-directed channel estimation for OFDM systems using multiple transmit antennas.
[70] Yatawatta and Petropulu, 2006	Blind channel estimation in MIMO-OFDM systems with multiuser interference.

predicted by the relevant theoretical analysis.

Some of the major contributions addressing the problem of channel estimation in MIMO systems are summarized in Table 1.2. More specifically, a combined OFDM/SDMA approach was discussed by Vandenameele *et. al.* [71]. A pilot-based approach to the problem of MIMO channel estimation has been explored by Jungnickel *et. al.* in [72], by Bolcskei *et. al.* [73] as well as by Zhu *et. al.* [74]. On the other hand, decision directed iterative channel estimation for MIMO systems was addressed by Li *et al* [66, 75, 76] as well as Deng *et al* [68]. Furthermore, parallel interference cancellation-assisted decision-directed channel estimation scheme for MIMO-OFDM systems was proposed by Münster and Hanzo [69,77]. Joint decoding and channel estimation for MIMO channels was considered by Grant [78] and further investigated by Cozzo and Hughes [55]. Iterative channel estimation for space-time block coded systems was addressed by Mai *et al* [79], while joint iterative DDCE for turbo coded MIMO-OFDM systems was investigated by Qiao [80]. Blind channel estimation in MIMO-OFDM systems with multiuser interference was explored by Yatawatta and Petropulu [70].

Other closely related issues, namely the iterative tracking of the channel-related parameters using soft decision feedback was studied by Sandell *et. al* [46], while the iterative channel estimation in the context of turbo equalization was considered by Song *et. al.* [50], Mai *et. al.* [81], as well as Otnes and Tüchler [40].

Finally, an important overview publication encompassing most major aspects of broadband MIMO-OFDM wireless communications including channel estimation and signal detection, as well as time and frequency syncronization was contributed by Stüber *et. al.* [67].

Agains this background, in this treatise we propose a decision-directed channel estimation (DDCE) scheme, which is suitable for employment in a wide range of multi-antenna multi-carrier systems as well as over the entire range of practical channel conditions. In particular, we consider mobile wireless multipath channels, which exhibit fast Rayleigh frequency-selective fading and are typically characterized by time-variant power delay profile (PDP).

We consider a generic MIMO-OFDM system employing K orthogonal frequency-domain subcarriers and having m_{t} and n_{r} transmit and receive antennas, respectively. Consequently, our MIMO channel estimation scheme comprises an array of K per-subcarrier MIMO-CTF estimators, followed by a $(n_{\mathrm{r}} \times m_{\mathrm{t}})$-dimensional array of parametric CIR estimators and a corresponding array of $(n_{\mathrm{r}} \times m_{\mathrm{t}} \times L)$ CIR tap predictors, where L is the number of tracked CIR taps per link for the MIMO channel.

In Section 2.9.1 we explore a family of recursive MIMO-CTF tracking methods, which in conjunction with the aforementioned PAST-aided CIR-tracking method of Section 2.6 as well as the RLS CIR tap prediction method of Section 2.7.4, facilitate an effective channel estimation scheme in the context of a MIMO-OFDM system. More specifically, in Section 2.9.1 we consider both hard- and soft-feedback assisted least mean squares (LMS) and recursive least squares (RLS) tracking algorithms as well as the modified RLS algorithm, which is capable of improved utilization of the soft information associated with the decision-based estimates.

Finally, in Section 2.9.1.5 we document the achievable performance of resultant MIMO-DDCE scheme employing the recursive CTF tracking followed by the parametric CIR tap tracking and CIR tap prediction. We demonstrate that the MIMO-DDCE scheme proposed exhibits good performance over the entire range of practical conditions.

Both the bit error rate (BER) as well as the corresponding mean square error (MSE) performance of the channel estimation scheme considered is characterized in the context of a turbo-coded MIMO-OFDM system. We demostrate that the MIMO-DDCE scheme proposed remains effective in channel conditions associated with high terminal speeds of up to 130 km/h, which corresponds to the OFDM-symbol normalized Doppler frequency of 0.006. Additionally, we report a virtually error-free performance of a rate $1/2$ turbo-coded 8x8-QPSK-OFDM system, exhibiting a total bit rate of 8 bits/s/Hz and having a pilot overhead of only 10%, at SNR of 10dB and normalized Doppler frequency of 0.003, which corresponds to the mobile terminal speed of roughly 65 km/h[1].

---

[1] Additional system parameters are characterized in Table 1.4.

1.4 Signal Detection in MIMO-OFDM Systems

The demand for both high data-rates, as well as for improved transmission integrity requires an efficient utilisation of the limited system resources, while supporting a high grade of mobility in diverse propagation environments. Consequently, the employment of an appropriate modulation format, as well as an efficient exploitation of the available bandwidth constitute crucial factors in achieving a high performance.

The OFDM modulation scheme employed in conjunction with a Multiple-Input Multiple-Output (MIMO) architecture [28], where multiple antennas are employed at both the transmitter and the receiver of the communication system, constitutes an attractive solution in terms of satisfying these requirements. Firstly, the OFDM modulation technique is capable of coping with the highly frequency selective, time-variant channel characteristics associated with mobile wireless communication channels, while possessing a high grade of structural flexibility for exploiting the beneficial properties of MIMO architectures.

It is highly beneficial that OFDM and MIMOs may be conveniently combined, since the information-theoretical analysis predicts [82] that substantial capacity gains are achievable in communication systems employing MIMO architectures. Specifically, if the fading processes corresponding to different transmit-receive antenna pairs may be assumed to be independently Rayleigh distributed[2], the attainable capacity was shown to increase linearly with the smaller of the numbers of the transmit and receive antennas [82]. Additionally, the employment of MIMO architectures allows for the efficient exploitation of the spatial diversity available in wireless MIMO environments, thus improving the system's BER, as well as further increasing the system's capacity.

The family of space-time signal processing methods, which allow for the efficient implementation of communication systems employing MIMO architectures are commonly referred to in parlance as *smart antennas*. In recent years, the concept of smart antennas has attracted intensive research interest in both the academic and the industrial communities. As a result, a multiplicity of smart antenna-related methods has been proposed. These include methods implemented at the transmitter, the receiver or both.

The classification of the smart-antenna techniques is illustrated in Figure 1.1. It should be noted, however, that the classification presented here is somewhat informal and its sole purpose is to appropriately position the content of this treatise in the context of the extensive material available on the subject.

Two distinctive system scenarios employing smart antennas can be identified. The first is the so-called Space Devision Multiplexing (SDM)-type scenario [83], where two *peer* terminals each employing multiple antennas, communicate with each other over a MIMO channel and the multiple antennas are primarily used for achieving a multiplexing gain, *i.e.* a higher throughput [84]. The second scenario corresponds to the

---

[2] This assumption is typically regarded as valid, if the appropriate antenna spacing is larger than of $\lambda/2$, where λ is the corresponding wavelength.

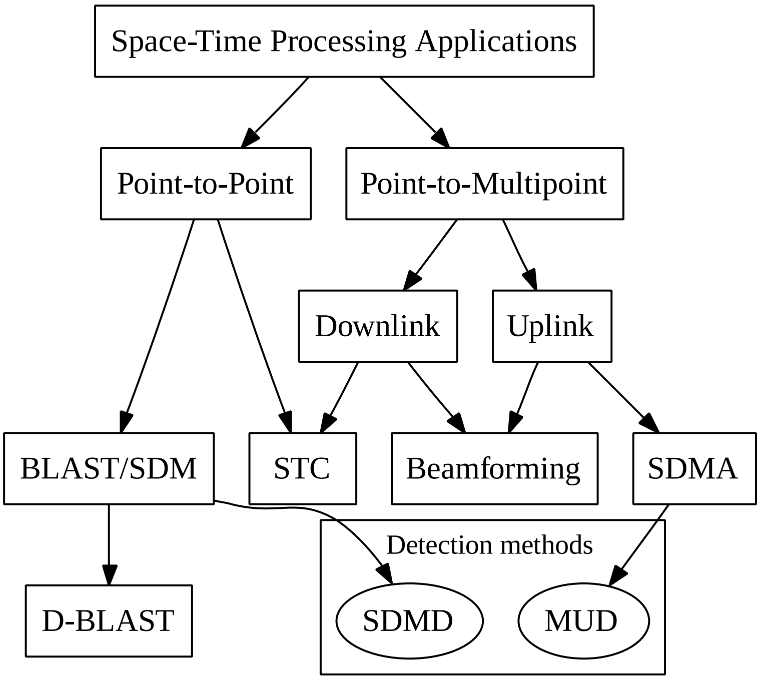

Figure 1.1: Classification of space-time processing techniques.

Space Devision Multiple Access (SDMA) configuration [28], where a single *base-station*, employing multiple antennas communicates simultaneously using a single carrier frequency with multiple *user* terminals, each employing one or several antennas.

The various *point-to-multipoint* smart antenna applications can be further subdivided into *uplink*- and *downlink*-related applications. The *uplink*-related methods constitute a set of techniques, which can be employed in the *base station* in order to detect the signals simultaneously transmitted by multiple *user* terminals. More specifically, provided that the Channel Impulse Response (CIR) of all users is accurately estimated, it may be used as their unique, user-specific spatial signature for differentiating them, despite communicating within the same frequency band [28]. Hence, the corresponding space-time signal processing problem is commonly referred to as Multi-User Detection (MUD) [28], while the multi-antenna multi-user systems employing *uplink* space-time MUD are commonly referred to as SDMA systems [28]. In contrast to the SDM-type systems designed for achieving the highest possible multiplexing gain, the design objective of the SDMA techniques is the maximization of the number of users supported. By contrast, the class of beamformers [85] creates angularly selective beams for both the up-link and down-link in the direction of the desired user, while forming nulls towards the interfering users. Finally, the family of Space-Time Codes (STC) [26] was optimized for achieving the highest possible transmit diversity gain, rather than for multiplexing gain or for increasing the number of users supported. At the time of writing new research is aiming for achieving both the maximum attainable diversity and multiplexing gain with the aid of eigen-value decomposition [86].

As stated above, two benefits of employing smart antennas are the system's improved integrity, as well as the increased aggregate throughput. Hence an adequate performance criterion of the particular smart antenna implementation is a combination of the system's attainable aggregate data-throughput, as well as the corresponding data integrity, which can be quantified in terms of the average Bit Error Rate (BER). Consequently, in the context of point-to-multipoint-related smart antenna applications the achievable capacity associated with the particular space-time processing method considered may be assessed as a product of the simultaneously supported number of individual users and the attainable data-rate associated with each supported user. The measure of data-integrity may be the average BER of all the users supported. Thus, the typical objective of the multi-user-related smart antenna implementations, such as that of an SDMA scheme is that of increasing the number of the simultaneously supported users, while sustaining the highest possible integrity of all the data communicated.

In this treatise, however, we would like to focus our attention on the family of space-time processing methods associated with the *point-to-point* system scenario. The main objective of point-to-point space-time processing is to increase the overall throughput of the system considered, as opposed to increasing the number of individual users simultaneously supported by the system, which was the case in the multi-user SDMA scenario described above. As illustrated in Figure 1.1, the family of time-space processing methods associated with the *point-to-point*-related smart antenna applications entail two different approaches, namely that of Space-Time Codes (STC) [26] as well as various layered space-time architectures, best known from Bell Labs Layered Space-Time (BLAST) scheme [84].

The STC methods may be classified in two major categories, namely the Space-Time Block Codes (STBC) and the Space-Time Trellis Codes (STTC). A simple method of STBC was first presented by Alamouti in [87]. Various STBC techniques were then extensively studied in a series of major publications by Tarokh *et al.* in [88–94] as well as by Ariyavistakul *et al.* in [95, 96]. On the other hand, the original variant of BLAST, known as the Diagonal BLAST (D-BLAST) scheme, was first introduced by Foschini in [84]. A more generic version of the BLAST architecture, the so-called Vertical BLAST (V-BLAST) arrangement was proposed by Golden *et al.* in [97]. Furthermore, the comparative study of the D-BLAST, as well as the V-BLAST systems employing various detection techniques such as Least Squares (LS) and Minimum Mean Square Error (MMSE)-aided Parallel Interference Cancellation (PIC), as well as the LS- and MMSE-aided Successive Interference Cancellation (SIC) was carried out by Sweatman *et al.* in [98]. Typically, however, the term BLAST refers to the point-to-point single-carrier MIMO architecture employing the SIC detection method, as it was originally proposed in [84].

For the sake of accuracy, in this work we employ the alternative terminology of Space Division Multiplexing (SDM) in order to refer to a generic MIMO architecture. The corresponding detection methods are referred to as SDM Detection (SDMD) techniques, as opposed to the MUD techniques employed in the context of SDMA systems [28]. Naturally, however, the SDMD and MUD schemes share the same signal detection methods, regardless, whether the signal arrived from multiple antennas of the same or different users. The classification of the most popular SDMD/MUD schemes is depicted in Figure 1.2. The methods considered include the linear LS and MMSE techniques, as well as non-linear techniques, such as Maximum Likelihood (ML), Successive Interference Cancellation (SIC), Genetic Algorithm-aided MMSE (GA-MMSE) [99, 100] as well as the novel Optimized Hierarchy Reduced Search Algorithm (OHRSA)-aided methods proposed in this treatise.

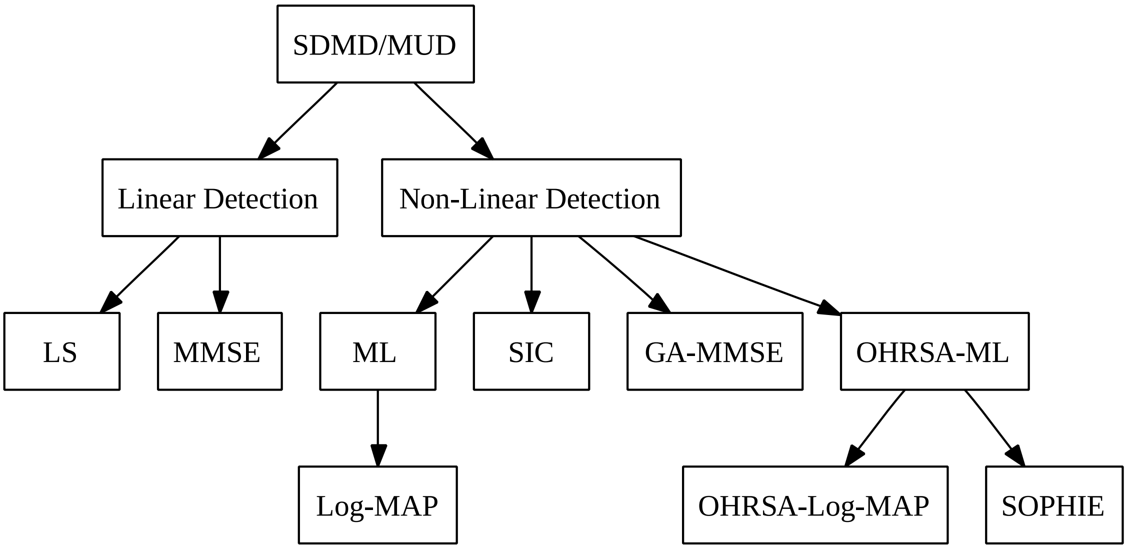

Figure 1.2: SDM detection methods classification.

In the course of this treatise both the MIMO channel model considered as well as the SDM-OFDM system model are described in Section 1.8. The various SDM detection methods considered are outlined in Chapter 3. Specifically, in Section 3.3.1 we demonstrate that the linear increase in capacity, predicted by the information-theoretic analysis [29], may indeed be achieved by employing a relatively low-complexity linear SDM detection method, such as the MMSE SDM detection technique [101]. Secondly, in Section 3.4.1 we show that a substantially better performance can be achieved by employing a non-linear Maximum Likelihood (ML) SDM detector [83, 102, 103], which constitutes the optimal detection method from a probabilistic sequence-estimation point of view. To elaborate a little further, the ML SDM detector is capable of attaining transmit diversity in *fully-loaded* systems, where the number of transmit and receive antennas is equal. Moreover, as opposed to the linear detection schemes considered, the ML SDM detector is capable of operating in the *rank-deficient* system configuration, when the number of transmit antennas exceeds that of the receive antennas. Unfortunately, however, the excessive computational complexity associated with the exhaustive search employed by the ML detection method renders it inapplicable to practical implementation in systems having a large number of transmit antennas. Subsequently, in Sections 3.4.2 and 3.4.3 we

Table 1.3: Major Contributions Addressing the Sphere Decoder-Aided Space-Time Processing.

[104] Fincke *et. al.*, 1985	Sphere decoder technique introduced.
[105] Damen *et. al.*, 2000	Sphere decoder was first proposed for employment in the context of space-time processing, where it is utilized for computing the ML estimates of the modulated symbols transmitted simultaneously from multiple transmit antennas.
[106] Hochwald and Brink, 2003	The *complex* version of the sphere decoder.
[107] Damen *et. al.*, 2003	Further results on SD.
[108] Pham *et al.*, 2004	Improved version of the complex sphere decoder.
[109] Tellambura *et al.*, 2005	Multistage sphere decoding was introduced.

explore a range of advanced non-linear SDM detection methods, namely the SIC and Genetic Algorithm-aided MMSE detection, respectively, where the latter may potentially constitute an attractive compromise between the low complexity of the linear SDM detection and the high performance of the ML SDM detection schemes. Indeed, we will demonstrate in Section 3.4.3 that the SDM detection method based on the SIC as well as on the GA-MMSE detector [100] are both capable of satisfying these requirements.

In Section 3.5 our discourse evolves further by proposing an enhancement of the SDMD schemes considered by employing both Space-Frequency Interleaving (SFI) and Space-Frequency Walsh-Hadamard Transform (SFWHT)-aided spreading. The performance benefits of employing SFI and SFWHT are quantified in Section 3.5. Finally, our conclusions are summarized in Section 3.7.

Recently, a family of potent Reduced Search Algorithm (RSA) aided Space-Time processing methods has been explored. These new methods utilize the Sphere Decoder (SD) technique introduced by Fincke *et al.* [104]. The SD was first proposed for employment in the context of space-time processing by Damen *et. al.* in [105], where it is utilized for computing the ML estimates of the modulated symbols transmitted simultaneously from multiple transmit antennas. The *complex* version of the sphere decoder was proposed by Hochwald and Brink in [106]. The subject was further investigated by Damen *et al.* in [107]. Subsequently, an improved version of the Complex Sphere Decoder (CSD) was advocated by Pham *et al.* in [108]. Furthermore, CSD-aided detection was considered by Cui and Tellambura in a joint channel estimation and data detection scheme explored in [56], while a revised version of the CSD method, namely the so-called Multistage Sphere Decoding (MSD) was introduced in [109]. The generalized version of the sphere decoder, which is suitable for employment in rank-deficient MIMO systems supporting more transmitters than the number of receive antennas was introduced by Damen *et al.* in [110] and further refined by Cui and Tellambura in [111]. The so-called *fast* generalized sphere decoding was introduced by Yang *et al.* [112]. Yet another variant of sphere decoder algorithms with improved radius search was introduced by Zhao and

Giannakis [113]. The subject of approaching MIMO channel capacity using soft detection on hard sphere decoding was explored by Wang and Giannakis [114]. Iterative detection and decoding in MIMO systems using sphere decoding was considered by Vikalo *et al.* [115].

Consequently, a set of novel Optimized Hierarchy Reduced Search Algorithm (OHRSA)-aided SDM detection methods are outlined in Section 4.2. Specifically, in Section 4.2.1 we derive the OHRSA-aided ML SDM detector, which benefits from the optimal performance of the ML SDM detector [28], while exhibiting a relatively low computational complexity, which is only slightly higher than that required by the low-complexity MMSE SDM detector [28]. To elaborate a little further, in Section 4.2.2 we derive a bit-wise OHRSA-aided ML SDM detector, which allows us to apply the OHRSA method of Section 4.2 in high-throughput systems, which employ multi-level modulation schemes, such as M-QAM [28].

In Section 4.2.3 our discourse evolves further by deducing the OHRSA-aided Max-Log-MAP SDM detector, which allows for an efficient evaluation of the soft-bit information and therefore results in highly efficient turbo decoding. Unfortunately however, in comparison to the OHRSA-aided ML SDM detector of Section 4.2.2 the OHRSA-aided Max-Log-MAP SDM detector of Section 4.2.3 exhibits a substantially higher complexity. Consequently, in Section 4.2.5 we derive an approximate Max-Log-MAP method, which we refer to as Soft-output OPtimized HIErarchy (SOPHIE) SDM detector. The SOPHIE SDM detector combines the advantages of both the OHRSA-aided ML and OHRSA-aided Max-Log-MAP SDM detectors of Sections 4.2.2 and 4.2.3, respectively. Specifically, it exhibits a similar performance to that of the optimal Max-Log-MAP detector, while imposing a modest complexity, which is only slightly higher than that required by the low-complexity MMSE SDM detector [28]. The computational complexity as well as the achievable performance of the SOPHIE SDM detector of Section 4.2.5 are analysed and quantified in Sections 4.2.5.1 and 4.2.5.2, respectively.

Our conclusions are summarized in Section 4.3. Specifically, we report achieving a BER of 10^{-4} at SNRs of $\gamma = 4.2, 9.2$ and 14.5 in high-throughput 8x8 rate-$\frac{1}{2}$ turbo-coded $M = 4, 16$ and 64-QAM systems communicating over dispersive Rayleigh fading channel. Additionally, we report achieving a BER of 10^{-4} at SNRs of $\gamma = 9.5, 16.3$ and 22.8 in high-throughput rank-deficient 4x4, 6x4 and 8x4 rate-$\frac{1}{2}$ turbo-coded 16-QAM systems, respectively.

1.5 Iterative Signal Processing for SDM-OFDM

In spite of an immense interest from both the academic and the industrial communities, a practical multiple-input multiple-output (MIMO) transceiver architecture, capable of approaching channel capacity boundaries in realistic channel conditions remains largely an open problem. An important overview publication encompassing most major aspects of broadband MIMO-OFDM wireless communications including channel

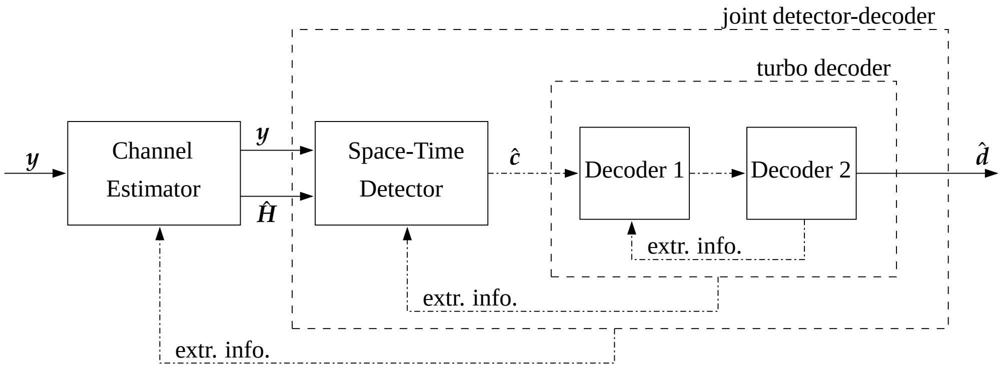

Figure 1.3: Schematic of a joint iterative receiver comprising channel estimator, SDM detector, as well as turbo decoder employing two RCS serially-concatenated component codes.

estimation and signal detection, as well as time and frequency syncronization was contributed by Stüber *et al.* [67]. Other important publications considering MIMO systems in realistic conditions include those by Münster and Hanzo [69], Li *et. al.* [66], Mai *et. al.* [81], Ronen *et. al.* [116] as well as Qiao *et. al.* [80]. Nevertheless, substantial contributions addressing all the major issues inherent to MIMO transceivers, namely error correction, space-time detection as well as channel estimation in realistic channel conditions remain scarce.

Against this background, in Chapter 5.1 we derive an iterative, so called *turbo* multi-antenna-multi-carrier (MAMC) receiver architecture. Our turbo receiver is illustrated in Figure 1.3. Following the philosophy of turbo processing [26], our turbo SDM-OFDM receiver comprises a succession of detection modules, which iteratively exchange soft bit-related information and thus facilitate a substantial improvement of the overall system performance.

More specifically, our turbo SDM-OFDM receiver comprises three major components, namely, the soft-feedback decision-directed channel estimator, discussed in detail in Section 2.9, followed by the soft-input-soft-output OHRSA Log-MAP SDM detector derived in Section 4.2.3 as well as a soft-input-soft-output serially concatenated turbo code [27]. Consequently, in this chapter we would like to analyze the achievable performance of each individual constituent of our turbo receiver, as well as the achievable performance of the entire iterative system. Our aim is to identify the optimum system configuration, while considering various design trade-offs, such as achievable error-rate performance, achievable data-rate as well as associated computational complexity.

In Section 5.4.2.4 we demonstrate that our turbo SDM-OFDM system employing the MIMO-DDCE scheme of Section 2.9 as well as the OHRSA Log-MAP SDM detector of Section 4.2.3 remains effective in channel conditions associated with high terminal speeds of up to 130 km/h, which corresponds to the OFDM-symbol normalized Doppler frequency of 0.006. Additionally, we report a virtually error-free performance for a rate $1/2$ turbo-coded 8x8-QPSK-OFDM system, exhibiting an effective throughput of

8 MHz · 8 bits/s/Hz=64 Mbps and having a pilot overhead of only 10% at SNR of 7.5dB and a normalized Doppler frequency of 0.003, which corresponds to a mobile terminal speed of about 65 km/h.

1.6 Novel Contributions of the Thesis

In order to build on top of the state-of-the-art results available in the literature, this treatise presents a rigorous derivation of an iterative turbo receiver architecture suitable for employment in a wide range of multi-antenna multi-carrier systems operating in realistic rapidly-fluctuating channel conditions. In this thesis we address the following open problems:

1. Channel estimation for multi-antenna multi-carrier systems in dispersive fast-fading channels.
2. Computationaly efficient signal detection in multi-antenna systems.
3. Error propagation in decision directed channel estimation-aided systems.

More specifically, we would like to highlight the following major findings:

- In Chapter 2 we derive an advanced decision directed channel estimation (DDCE) scheme, which is capable of recursive tracking and prediction of the rapidly-fluctuating channel parameters, characterized by time-variant statistics. More specifically, we employ a Projection Approximation Subspace Tracking (PAST) [117] technique for the sake of tracking the channel transfer function's low-rank signal subspace and thus fascilitating a high accuracy tracking of the channel's transfer function, while imposing a relatively low computational complexity. The corresponding results are summarized in [4, 15] as well as [23].

- Additionally, in Chapter 2 we introduce an advanced MIMO channel estimation scheme for multi-antenna multi-carrier systems. Our method comprises the aforementioned PAST aided subspace technique in conjunction with an enhanced soft-decision aided RLS MIMO-CTF estimator, which utilizes a modified RLS tracking technique outlined in [40]. We demonstrate that our soft-decision aided MIMO-DDCE scheme is suitable for multi-carrier systems employing any practical number of transmit and receive antennas. The results discussed in Chapter 2 are reported in [24] and [10].

- In Chapter 4 we explore a family of novel Optimized Hierarchy Reduced Search Algorithm (OHRSA)-aided space-time processing methods, which may be regarded as an advanced extension of the Complex Sphere Decoder (CSD) method, portrayed in [108]. The algorithm proposed extends the potential application range of the CSD methods of [106] and [108], as well as reduces the associated computational complexity. Moreover, the OHRSA-aided SDM detector proposed exhibits the near-optimum performance of the Log-MAP SDM detector, while imposing a substantially lower computational complexity, which renders it an attractive design alternative for practical systems. Our findings are extensively documented in [1, 16, 19, 20] as well as [7].

- Finally, in Chapter 5 we discuss an iterative turbo receiver architecture, which utilises both the soft decision feedback aided MIMO channel estimation scheme of Chapter 2 as well as the Log-MAP SDM detection method derived in Chapter 4. Additionally, we carry out an analysis of the associated design trade-offs. The results outlined in Chapter 5 are reported in [11, 25].

1.7 System Model

1.7.1 Channel Statistics

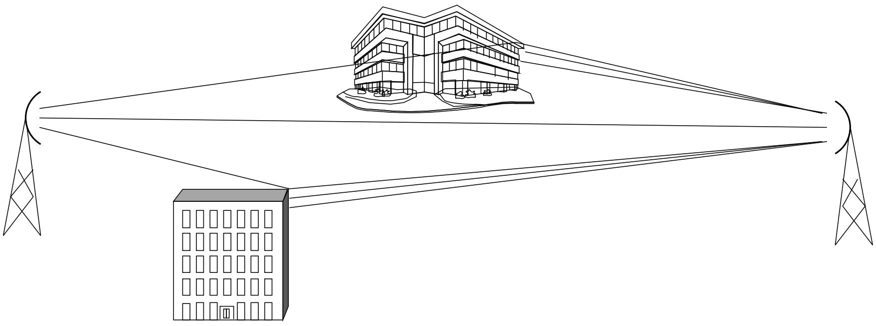

Figure 1.4: Illustration of a wireless multi-path communication link. Note that the non-line of sight paths are randomly faded as a result of the diffraction induced by scattering surfaces.

A Single Input Single Output (SISO) wireless communication link is constituted by a multiplicity of statistically independent components, termed as *paths*. Thus, such a channel is referred to as a *multipath* channel. A *multipath* channel is typically characterized by its Power Delay Profile (PDP), which is a set of parameters constituted by the paths' average powers σ_l^2 and the corresponding relative delays τ_l. Some examples of the commonly used PDPs are illustrated in Figure 1.6. The physical interpretation of each individual path is a single distortionless ray between the transmitter and the receiver antennas. While the term PDP corresponds to the average power values associated with the different multi-path channel components, the term CIR refers to the instantaneous state of the dispersive channel encountered and corresponds to the vector of the instantaneous amplitudes $\alpha_l[n]$ associated with different multi-path components. Thus, the statistical distribution of the CIR is determined by the channel's PDP. In the case of independently Rayleigh fading multiple paths we have $\alpha_l[n] \in \mathcal{CN}(0, \sigma_l^2),\ l = 1, 2, \cdots, L$, where $\mathcal{CN}(0, \sigma^2)$ is a complex-Gaussian distribution having the mean 0 and the variance of σ^2.

The individual scattered and delayed signal components usually arise as a result of refraction or diffrac-

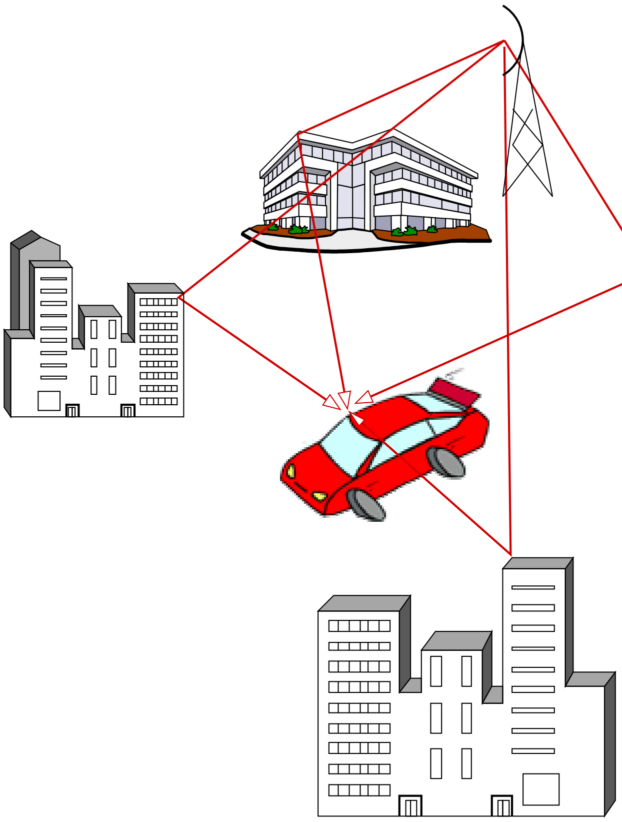

Figure 1.5: Illustration of a wireless multi-path communication link. Note that the non-line of sight paths are randomly faded as a result of the diffraction induced by scattering surfaces.

tion from scattering surfaces, as illustrated in Figure 1.4, and are termed as Non-Line-Of-Sight (NLOS) paths. In most recently proposed wireless mobile channel models each such CIR component α_l associated with an individual channel path is modelled by a Wide Sense Stationary (WSS) narrow-band complex Gaussian process [120] having correlation properties characterised by the cross-correlation function

$$r_\alpha[m,j] = E\{\alpha_i[n]\alpha_j^*[n-m]\} = r_{t;i}[m]\delta[i-j] \ , \tag{1.1}$$

where n is a discrete OFDM-block-related time-domain index and $\delta[\cdot]$ is the Kronecker delta function. The above equation suggests that the different CIR components are assumed to be mutually uncorrelated and each exhibits time-domain autocorrelation properties defined by the time-domain correlation function $r_{t;i}[m]$. The Fourier transform pair of the correlation function $r_t[n]$ associated with each CIR tap corresponds to a band-limited Power Spectral Density (PSD) $p_t(f)$, such that we have $p_t(f) = 0$, if $|f| > f_D$, where Fd is termed as the *maximum Doppler frequency*. The time period $1/f_\text{D}$ is the so-called *coherence time* of the channel [120] and usually we have: $1/f_\text{D} \gg T$, where T is the duration of the OFDM block.

A particularly popular model of the time-domain correlation function $r_t[n]$ was proposed by Jakes in [121] and is described by

$$r_t[n] = r_J[n] = J_0(nw_d), \tag{1.2}$$

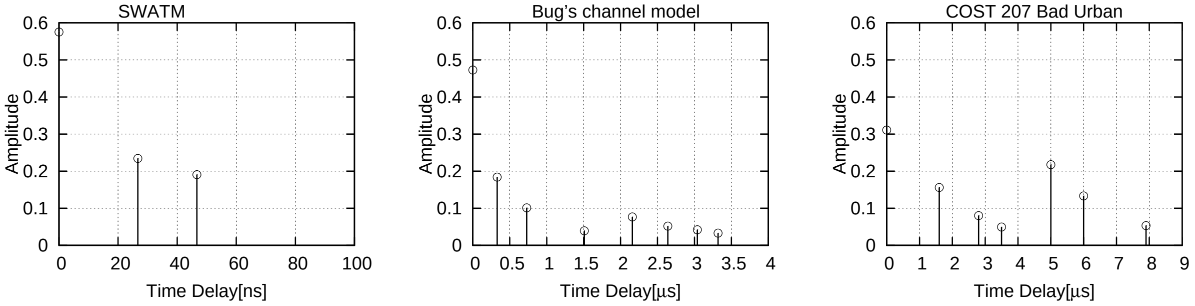

(a) (b) (c)

Figure 1.6: Power Delay Profiles (PDP) corresponding to three different channel models, namely (a) the Short Wireless Asynchronous Transfer Mode (SWATM) channel model of [28], (b) Bug's channel model [118] and (c) the COST-207 Bad Urban (BU) channel model defined for UMTS-type system, as characterized in [119].

where $J_0(x)$ is a zero-order Bessel function of the first kind and $w_d = 2\pi T f_D$ is the normalised Doppler frequency. The corresponding U-shaped PSD function, termed as the Jakes-spectrum is given by [121]

$$p_J(w) = \begin{cases} \frac{2}{w_d}\frac{1}{\sqrt{1-(w/w_d)^2}}, & \text{if } |w| < w_d \\ 0, & \text{otherwise.} \end{cases}$$

Generally speaking the Doppler frequencies f_D can assume different values for different signal paths. However, as it was advocated in [38], for the sake of exploiting the time-domain correlation in the context of channel parameters estimation and prediction, it is sufficient to make a worst-case assumption about the nature of time-domain correlation of the channel parameters encountered. The associated worst-case channel time-domain correlation properties can be characterized by an ideally band-limited Doppler PSD function given by [28, 38]

$$p_t(f) = p_{B,unif}(f) = \begin{cases} \frac{1}{2f_D}, & \text{if } |f| < f_D \\ 0, & \text{otherwise ,} \end{cases} \tag{1.3}$$

where f_D is the assumed value of the maximum Doppler frequency over all channel paths. The corresponding time-domain correlation function can be described as

$$r_t[m] = r_B[m] = \frac{\sin 2\pi f_D m}{2\pi f_D m}. \tag{1.4}$$

We adopt the complex baseband representation of the continuous-time Channel Impulse Response (CIR), as given by [120]

$$h(t,\tau) = \sum_l \alpha_l(t) c(\tau - \tau_l), \tag{1.5}$$

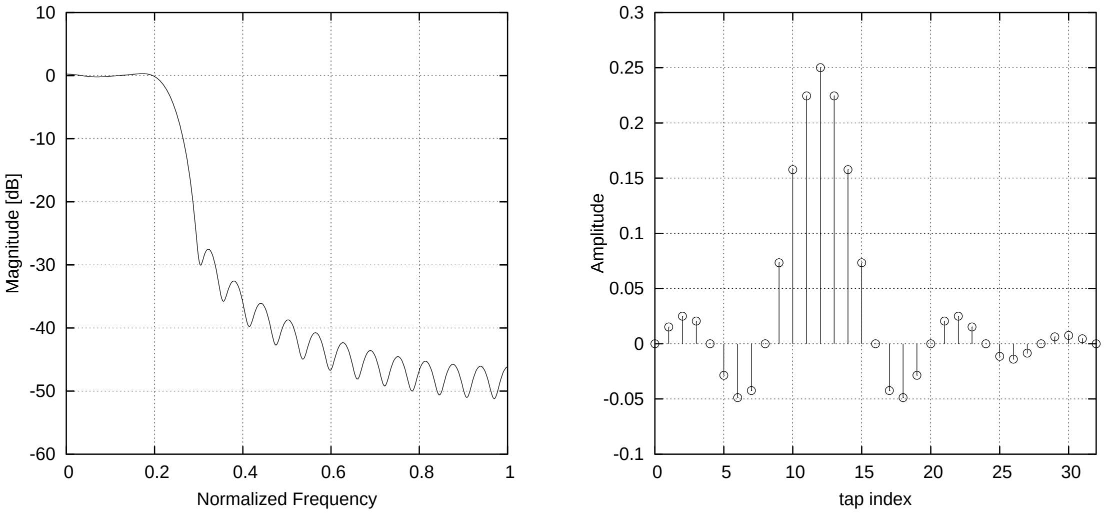

(a) (b)

Figure 1.7: (a) Frequency response and (b) impulse response of an order 8 raised cosine shaping filter with the oversampling rate of 4, the roll-off factor of 0.2 and the delay of 3 samples.

where $\alpha_l(t)$ is the time-variant complex amplitude of the lth path and the τ_l is the corresponding path delay, while $c(\tau)$ is the aggregate impulse response of the transmitter-receiver pair, which usually corresponds to the raised-cosine Nyquist filter. From (1.5) the continuous Channel Transfer Function (CTF) can be described as in [76]

$$\begin{aligned} H(t,f) &= \int_{-\infty}^{\infty} h(t,\tau)\, e^{-\jmath 2\pi f \tau} d\tau \\ &= C(f) \sum_l \alpha_l(t) e^{-\jmath 2\pi f \tau_l}, \end{aligned} \tag{1.6}$$

where $C(f)$ is the Fourier transform pair of the transceiver impulse response $c(\tau)$ characterized in Figure 1.7.

As it was pointed out in [38], in OFDM/MC-CDMA systems using a sufficiently long cyclic prefix and adequate synchronisation, the discrete subcarrier-related CTF can be expressed as

$$H[n,k] = H(nT, k\Delta f) = C(k\Delta f) \sum_{l=1}^{L} \alpha_l[n] W_K^{k\tau_l/T_s} \tag{1.7}$$

$$= \sum_{m=0}^{K_0-1} h[n,m] W_K^{km}, \tag{1.8}$$

where $T_s = T/K$ is the baseband sample duration, while K_0 is the length of the cyclic prefix, which normally corresponds to the maximum delay spread encountered, such that we have $K_0 > \tau_{\max}/T_s$. Subsequently

$$h[n,m] = h(nT, mT_s) = \sum_{l=1}^{L} \alpha_l[n] c(mT_s - \tau_l) \tag{1.9}$$

is the Sample-Spaced CIR (SS-CIR) and $W_K = \exp(-\jmath 2\pi/K)$. Note, that in realistic channel conditions associated with non-sample-spaced time-variant path-delays $\tau_l(n)$ the receiver will encounter dispersed received signal components in several neighbouring samples owing to the convolution of the transmitted signal with the system's impulse response, which we refer to as leakage. This phenomenon is usually unavoidable and therefore the resultant SS-CIR $h[n,m]$ will be constituted of numerous correlated non-zero taps described by Equation (1.5) and illustrated in Figure 1.8. By contrast, the Fractionally-Spaced CIR (FS-CIR) $\alpha_l[n] = \alpha_l(nT)$ will be constituted by a lower number of $L \ll K_0 \ll K$ non-zero statistically independent taps associated with distinctive propagation paths, as depicted in Figure 1.8.

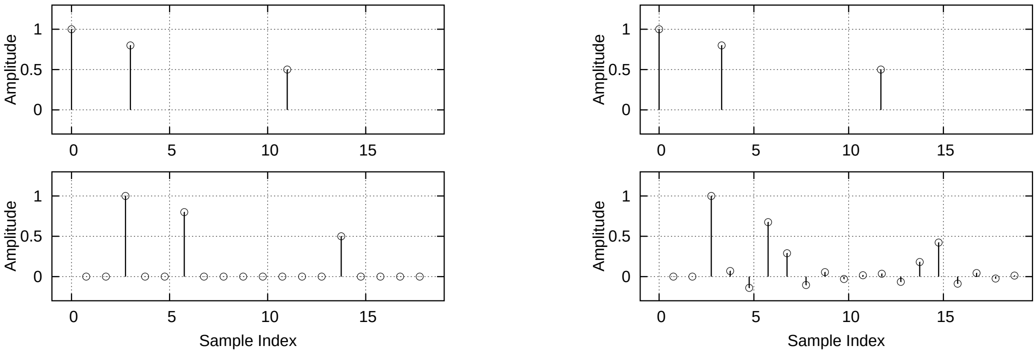

(a)

(b)

Figure 1.8: The **FS-CIR** (top) and the effective **SS-CIR** (bottom) resulting from the convolution of the original FS-CIR with the raised cosine filter impulse response of Figure 1.7 for the cases of (a) sample-spaced and (b) fractionally-spaced power delay profiles.

As it was shown in [38], the crosscorrelation function $r_H[m,l]$, which characterized both time- and frequency-domain correlation properties of the discrete CTF coefficients $H[n,k]$ associated with different OFDM blocks and subcarriers can be described as

$$\begin{aligned} r_H[m,l] &= \mathtt{E}\{H[n+m,k+l]H^*[n,k]\} \\ &= \sigma_H^2 r_t[m] r_f[l], \end{aligned} \tag{1.10}$$

where $r_t[m]$ is the time-domain correlation function described by Equation (1.4), while $r_f[i]$ is the frequency-domain correlation functions, which can be expressed as follows [31]

$$r_f[l] = |C(l\Delta f)|^2 \sum_{i=1}^{L} \frac{\sigma_i^2}{\sigma_H^2} e^{-\jmath 2\pi l \Delta f \tau_i}, \tag{1.11}$$

where $\sigma_H^2 = \sum_{i=1}^{L} \sigma_i^2$.

1.7.2 Realistic Channel Properties

The majority of existing advanced channel estimation methods rely on the *a priori* knowledge of the channel statistics commonly characterized by the channel's Power Delay Profile (PDP) for the sake of estimating the instantaneous Channel Impulse Response (CIR) and the corresponding Channel Transfer Function (CTF). It is evident however, that in realistic wireless mobile channels, where at least one of the communicating terminals is in motion, the channel's PDP will also become time-variant and thus may not be *a priori* known at the receiver.

For the sake of designing as we as characterizing the performance of an efficient and robust channel estimation scheme, which will be suitable for realistic channel conditions, we propose a channel model, which sustains the important characteristics of the realistic wireless mobile channels. More specifically, as opposed to the conventional constant PDP, our channel model is characterized by a time-variant PDP, where both the relative delays τ_l as well as the corresponding average powers σ_l^2 of different PDP taps vary with time.

Our channel model is dynamically generated using a geometric scattering model illustrated in Figure 1.9. More specifically, the individual scatterers associated with different propagation paths are randomly generated using a Marcov statistical model. The corresponding relative delays τ_l and powers σ_l^2 associated with each propagation path are calculated based on the geometrical location of each of the scatterers. Correspondingly, the rate of change in the values of the PDP tap delays τ_l is determined by the speed of the mobile wireless terminal and is characterized by the PDP *tap drift rate* parameter ν_τ. The specific assumptions regarding the practical range of values of the parameter ν_τ is discussed in the next chapter. Furthermore, each propagation path experiences independent fast Rayleigh fading. Finally, the set of parameters characterizing the Marcov model employed is chosen such that the average channel statistics corresponds to the desired static-PDP channel model.

1.7.3 Baseline Scenario Characteristics

As a baseline scenario we consider a mobile wireless communication system utilizing a frequency bandwidth of $B = 10$ MHz at a carrier frequency of $f_c = 2.5$ GHz. Furthermore, we assume an OFDM system having $K = 128$ orthogonal subcarriers. The corresponding FFT-frame duration is $T_s = K/B = 16\ \mu$s. We assume having a cyclic prefix of $1/4T_s = 4\ \mu$s and thus the total OFDM symbol duration of $T = 20\ \mu$s.

Some other important system-related assumptions include the relative speed of the communicating terminals, which we assume not to exceed $v = 130\ \mathrm{km/h} = 36\ \mathrm{m/s}$. Furthermore, the OFDM-symbol-

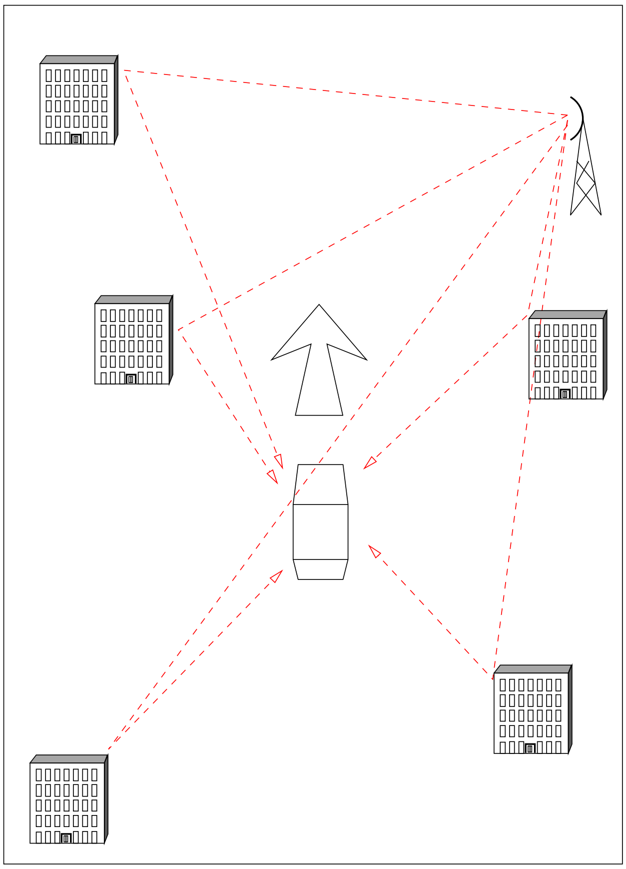

Figure 1.9: PDP examples corresponding.

normalized Doppler frequency f_D relates to the relative speed of the communicating terminals as follows

$$f_D = T\frac{vf_c}{c}, \tag{1.12}$$

where $c = 3 \cdot 10^8$ m/s denotes the speed of light. The actual Doppler frequency f_D/T encountered in the mobile wireless environment is assumed to be in the range of 3 to 300 Hz, where the maximum value of 300 Hz correponds to the relative terminal speed of $v = 130$ km/h and the carrier frequency of $f_c = 2.5$ GHz. Finally, the OFDM-symbol-normalized PDP tap drift speed ν_τ may be calculated as follows

$$\nu_\tau = T\frac{v}{c}, \tag{1.13}$$

which suggests the that value of the PDP tap drift speed parameter does not exceed the maximum value of $\nu_\tau = 2.4 \cdot 10^{-6}\ \mu\text{s} = T \cdot 0.12\ \mu\text{s/s}$.

The resultant baseline scenario system characteristics are summarized in Table 1.4

1.7.4 MC Transceiver

The transmitter part of the system is typically constituted of an OFDM / MC-CDMA Encoder and Modulator, the output of which is a complex-valued base-band time-domain signal. The resultant base-band signal

Table 1.4: Baseline scenario system characteristics.

Parameter	Value
Carrier frequency f_c	2.5 GHz
Channel bandwidth B	8 MHz
Number of carriers K	128
FFT frame duration T_s	16 μs
OFDM symbol duration T	20 μs (4 μs of cyclic prefix)
Max. delay spread τ_{max}	4 μs
Max. terminal speed v	130 km/h
Norm. Max. Doppler spread f_D	0.006 = $T \cdot 300$ Hz
Norm. Max. PDP tap drift ν_τ	$2.4 \cdot 10^{-6}\ \mu\text{s} = T \cdot 0.12\ \mu\text{s/s}$

is oversampled and pulse-shaped using a Nyquist filter, such as, for example, a root-raised-cosine filter characterized in Figure 1.7. The resultant oversampled signal is then converted into an analog pass-band signal using a D/A converter and upconverted to the Radio Frequency (RF) band. At the receiver side a reciprocal process is taking place, where the received RF signal is amplified by the RF frontend and downconverted to an intermediate frequency pass-band, then sampled by the A/D converter, downconverted to the base-band, filtered by a matched Nyquist filter and finally decimated. The resultant complex-valued base-band signal is processed by the corresponding OFDM / MC-CDMA Demodulator and Decoder block, where the transmitted information symbols are detected.

In this treatise we consider the link between the output of the MC Modulator and the input of the MC Demodulator of Figure 1.10 as an *Effective Base-Band Channel*. The proof of feasibility for this assumption is beyond the scope this contribution, however it can be found for example in [120, 122].

The discrete frequency-domain model of the OFDM/MC-CDMA system illustrated in Figure 1.10 can be described as in [76]

$$y[n,k] = H[n,k]x[n,k] + w[n,k], \tag{1.14}$$

for $k = 0, \ldots, K-1$ and all n, where $y[n,k], x[n,k]$ and $w[n,k]$ are the received symbol, the transmitted symbol and the Gaussian noise sample respectively, corresponding to the kth subcarrier of the nth OFDM block. Furthermore, $H[n,k]$ represents the complex-valued CTF coefficient associated with the kth subcarrier and time instance n. Note that in the case of an M-QAM modulated OFDM system, $x[n,k]$ corresponds to the M-QAM symbol accommodated by the kth subcarrier, while in a MC-CDMA system, such as a Walsh-Hadamard Transform (WHT) assisted OFDM scheme using G-chip WH spreading code and hence

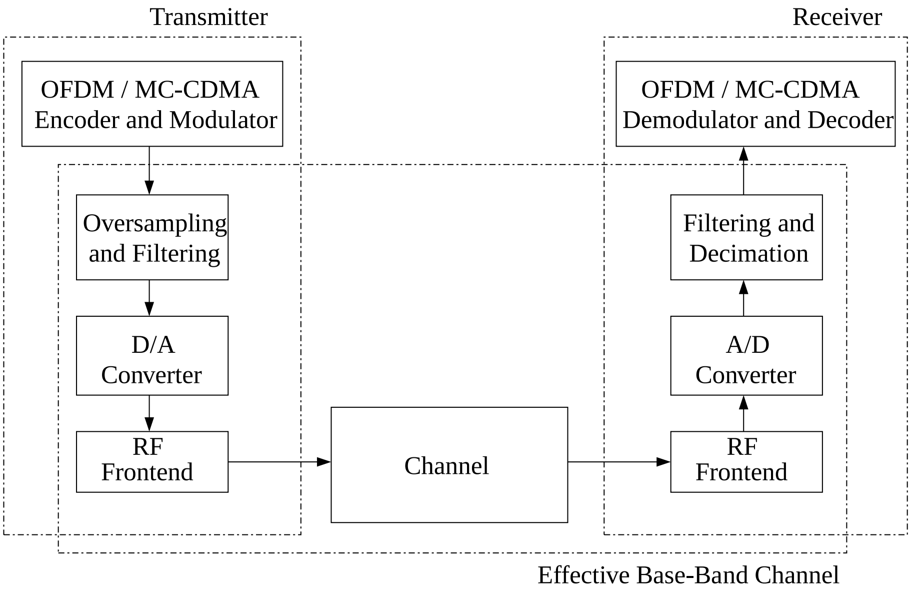

Figure 1.10: Schematic illustration of a typical OFDM/MC-CDMA system's PHY layer.

capable of supporting G users [28] we have

$$x[n,k] = \sum_{p=0}^{G-1} c[k,p]s[n,p], \tag{1.15}$$

where $c[k,p]$ is the kth chip of the pth spreading code, while $s[n,p]$ is the M-QAM symbol spread by the pth code. Each of the G spreading codes is constituted by G chips.

1.8 SDM-OFDM System Model

1.8.1 MIMO Channel Model

We consider a MIMO wireless communication system employing m_{t} transmit and n_{r} receive antennas, hence, the corresponding MIMO wireless communication channel is constituted by $(n_{\mathrm{r}} \times m_{\mathrm{t}})$ propagation links, as illustrated in Figure 1.11. Furthermore, each of the corresponding $(n_{\mathrm{r}} \times m_{\mathrm{t}})$ Single Input Single Output (SISO) propagation links comprises a multiplicity of statistically independent components, termed as *paths*. Thus, each of these SISO propagation links can be characterised as a *multipath* SISO channel discussed in detail in Section 1.7.1. Similarly to the SISO case, the multi-carrier structure of our SDM-OFDM transceiver allows us to characterise the broadband frequency-selective channel considered as an OFDM subcarrier-related vector of flat-fading Channel Transfer Function (CTF) coefficients. However, as opposed to the SISO case, for each OFDM symbol n and subcarrier k the MIMO channel is characterized by a $(n_{\mathrm{r}} \times m_{\mathrm{t}})$-dimensional matrix $\mathbf{H}[n,k]$ of the CTF coefficients associated with the different propagation links, such that the element $H_{ij}[n,k]$ of the CTF matrix $\mathbf{H}[n,k]$ corresponds to the propagation link connecting the jth transmit and ith receive antennas.

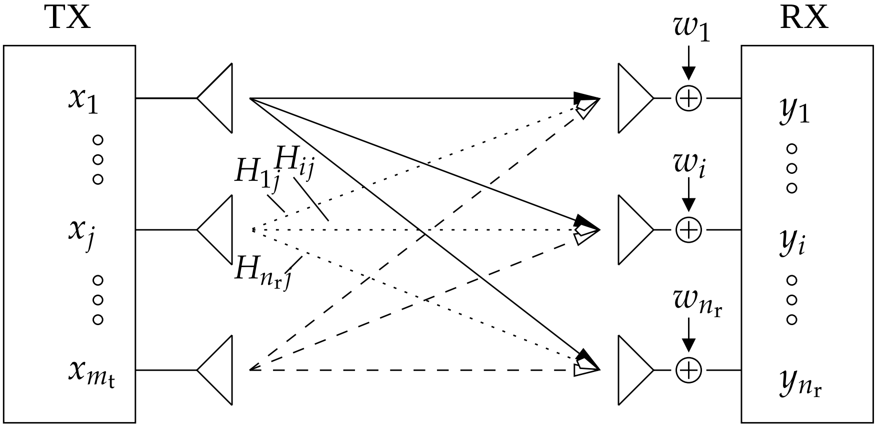

Figure 1.11: Illustration of a MIMO channel constituted by m_t transmit and n_r receive antennas. The corresponding MIMO channel is characterized by the $(n_r \times m_t)$-dimensional matrix $\mathbf{H}$ of CTF coefficients.

Furthermore, the correlation properties of the MIMO-OFDM channel can be readily derived as a generalisation of the SISO-OFDM channel scenario discussed in detail in Section 1.7.1. As it was shown in [38], the crosscorrelation function $r_H[m,l]$, which characterizes both the time- and frequency-domain correlation properties of the discrete CTF coefficients $H_{ij}[n,k]$ associated with the particular (i,j)th propagation link of the MIMO channel, as well as with the different OFDM symbol and subcarrier indices n and k can be described as

$$\begin{aligned} r_{H;ij}[m,l] &= \mathrm{E}\left\{H_{ij}^*[n+m,k+l], H_{ij}[n,k]\right\} \\ &= \sigma_H^2 r_t[m] r_f[l], \end{aligned} \tag{1.16}$$

where $r_t[m]$ is the time-domain correlation function, which may be characterized by a time-domain correlation model proposed by Jakes in [121], where we have

$$r_t[m] = r_J[m] = J_0(nw_d), \tag{1.17}$$

and $J_0(x)$ is a zero-order Bessel function of the first kind, while $w_d = 2\pi T f_D$ is the normalised Doppler frequency. On the other hand, the frequency-domain correlation function $r_f[l]$ can be expressed as follows [31]

$$r_f[l] = |C(l\Delta f)|^2 \sum_{i=1}^{L} \frac{\sigma_i^2}{\sigma_H^2} e^{-\jmath 2\pi l \Delta f \tau_i}, \tag{1.18}$$

where $C(f)$ is the frequency response of the pulse-shaping filter employed by the particular system, σ_i^2 and τ_i, $i = 1, \cdots, L$ are the average power and the corresponding delay of the L-tap Power Delay Profile (PDP) encountered, while σ_H^2 is the average power per MIMO channel link, such that we have $\sigma_H^2 = \sum_{i=1}^{L} \sigma_i^2$.

In this report we assume the different MIMO channel links to be mutually uncorrelated. This common assumption is usually valid, if the spacing between the adjacent antenna elements exceeds $\lambda/2$, where λ is the wavelength corresponding to the RF signal employed. Thus, the overall crosscorrelation function between the (i,j)th and (i',j')th propagation links may be described as

$$\begin{aligned} r_{H;ij;i'j'}[m,l] &= \mathtt{E}\left\{H^*_{i'j'}[n+m,k+l], H_{ij}[n,k]\right\} \\ &= \sigma_H^2 r_t[m] r_f[l]\delta[i-i']\delta[j-j'], \end{aligned} \tag{1.19}$$

where $\delta[i]$ is the discrete Kronecker Delta function.

1.8.2 Channel Capacity

Whilst most of the multi-path NLOS channel models can be collectively categorized as Rayleigh fading, different channel models characterized by different PDPs exhibit substantial differences in terms of their *information-carrying capacity* and *potential diversity gain*. The channel's capacity determines the upper-bound for the overall system's throughput. On the other hand, the available diversity gain allows the communication system to increase its transmission integrity. Various modulation and coding schemes can be employed by the communication system in order to increase its spectral efficiency and also to take advantage of diversity. Some of these methods are widely discussed in the literature, *e.g.* in [123], and include the employment of antenna arrays, space-time coding, time- and frequency-domain spreading, channel coding, time- and frequency-domain repetition *etc*. The theoretical performance boundaries of such methods are discussed in [29, 124]. Furthermore, the trade-offs between the attainable system capacity gain and the corresponding diversity gain are addressed in [125].

Consequently, the unrestricted capacity of a generic single-carrier ergodic-flat-fading MIMO channel can be expressed as in [106], where we have

$$\mathcal{C} = \mathtt{E}\left\{\log\det\left[\sigma_w^2\mathbf{I} + \frac{1}{m_\mathrm{t}}\mathbf{H}\mathbf{H}^\mathrm{H}\right]\right\}, \tag{1.20}$$

where $\mathbf{H}$ is a $(n_\mathrm{r} \times m_\mathrm{t})$-dimensional matrix with independent complex Gaussian distributed entries.

In realistic communication system, however, the achievable throughput is limited by the modulation scheme employed. Some examples of such modulation schemes are Mary PSK or Mary QAM constellation schemes, where M is the number of complex symbols constituting the constellation map corresponding to the particular modulation scheme employed. The upper bound defining the maximum throughput achievable by a particular discrete modulation scheme was first discussed by Shannon in [126] and was shown to be determined by the mutual information $I(\mathbf{s};\mathbf{y})$ exhibited by the modulation scheme employed. The mutual information can be calculated using the following expression

$$I(\mathbf{s};\mathbf{y}) = H(\mathbf{y}) - H(\mathbf{y}|\mathbf{s}), \tag{1.21}$$

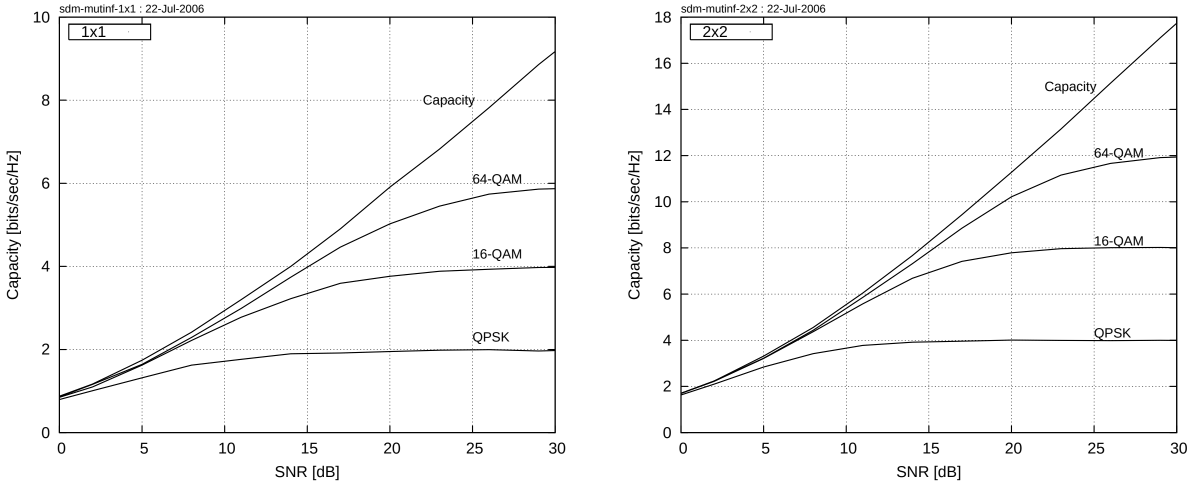

(a) (b)

Figure 1.12: Capacity $\mathcal{C}$ of Equation (1.20) as well as mutual information $I(\mathbf{s};\mathbf{y})$ of Equation (1.21) versus SNR for (a) 1x1 and (2) 2x2 systems in Rayleigh uncorrelated flat fading.

where $H(\cdot) = -\mathrm{E}\log p(\cdot)$ denotes the entropy function [126]. In the case of having a Gaussian i.i.d. noise sample vector $\mathbf{w}$ with the corresponding covariance matrix given by $C_w = \sigma_w^2\mathbf{I}$, the constrained entropy constituent $H(\mathbf{y}|\mathbf{s})$ of Equation (1.21) is may be expressed as follows [106]

$$H(\mathbf{y}|\mathbf{x}) = n_{\mathrm{r}} \log 2\pi\sigma_w^2 e, \tag{1.22}$$

whereas the unconstrained entropy constituent $H(\mathbf{y})$ can be approximated numerically using a Monte-Carlo simulation as in [106], where we have

$$H(\mathbf{y}) = -\mathrm{E}\log\left(\frac{1}{M^{m_{\mathrm{t}}}(2\pi\sigma_w^2)^{n_{\mathrm{r}}}}\sum_{\mathbf{s}}\exp\left[-\frac{1}{2\sigma_w^2}\|\mathbf{y}-\mathbf{Hs}\|^2\right]\right), \tag{1.23}$$

where the expectation is taken over the three sources of randomness in the choice of $\mathbf{s}, \mathbf{H}$ and $\mathbf{w}$. Moreover, the summation in Equation (1.23) is carried out over all $M^{m_{\mathrm{t}}}$ possible values of $\mathbf{s}$.

Figures 1.12(a) and 1.12(b) characterize both the capacity $\mathcal{C}$ of Equation (1.20) as well as the mutual information $I(\mathbf{s};\mathbf{y})$ of Equation (1.21) for SISO and 2x2-MIMO systems, respectively. The mutual information plots depicted in both figures correspond to systems employing QPSK as well as 16- and 64-QAM modulations.

1.8.3 SDM-OFDM Transceiver Structure

The schematic of a typical SDM-OFDM system's physical layer is depicted in Figure 1.13. The transmitter of the SDM-OFDM system considered is typically constituted by the Encoder and Modulator seen in Figure 1.13, generating a set of m_{t} complex-valued base-band time-domain signals [28]. The modulated base-band

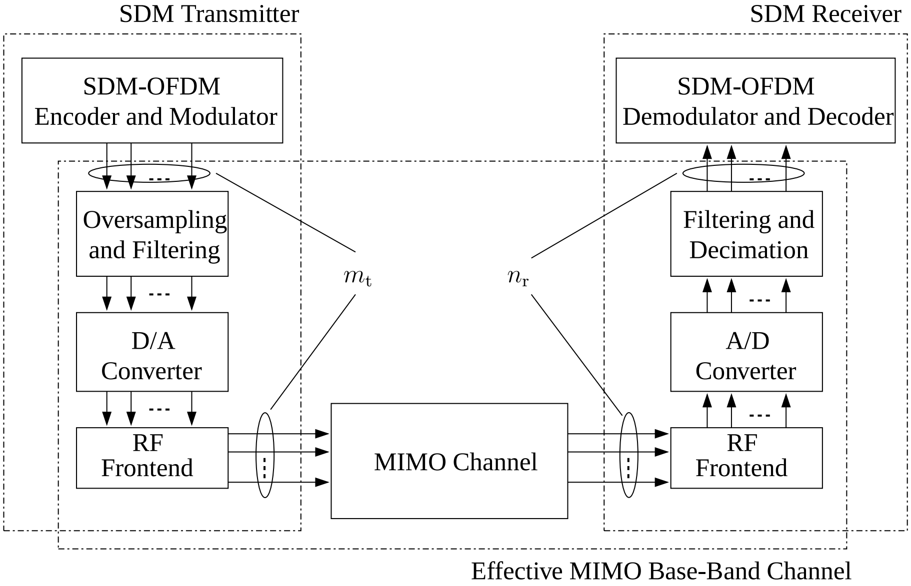

Figure 1.13: Schematic of a typical SDM-OFDM system's physical layer.

signals are then processed in parallel. Specifically, they are oversampled and shaped using a Nyquist filter, such as for example a root-raised-cosine filter. The resultant oversampled signals are then converted into an analog pass-band signal using a bank of D/A converters and upconverted to the Radio Frequency (RF) band. At the receiver side of the SDM-OFDM transceiver the inverse process takes place, where the set of received RF signals associated with the n_r receive antenna elements are amplified by the RF amplifier and down-converted to an intermediate frequency pass-band. The resultant pass-band signals are then sampled by a bank of A/D converters, down-converted to the base-band, filtered by a matched Nyquist filter and finally decimated, in order to produce a set of discrete complex-valued base-band signals. The resultant set of discrete signals is processed by the corresponding Demodulator and Decoder module seen in Figure 1.13, where the transmitted information-carrying symbols are detected.

In this treatise we consider the link between the output of the SDM-OFDM Modulator and the input of the corresponding SDM-OFDM Demodulator of Figure 1.13 as an *Effective Base-Band MIMO Channel*. The proof of feasibility for this assumption is beyond the scope this contribution, however it can be found for example in [120, 122]. The structure of the resultant base-band SDM-OFDM system is depicted in Figure 1.14, where the bold grey arrows illustrate subcarrier-related signals represented by the vectors $\mathbf{x}_i$ and $\mathbf{y}_i$, while the black thin arrows accommodate scalar time-domain signals.

The discrete frequency-domain model of the SDM-OFDM system, illustrated in Figure 1.14, may be characterised as a generalisation of the SISO case described in of Section 1.7.1. Namely, we have

$$y_i[n,k] = \sum_{j=1}^{m_\mathrm{t}} H_{ij}[n,k]x_j[n,k] + w_i[n,k], \tag{1.24}$$

where $n = 0, 1, \cdots$ and $k = 0, \ldots, K-1$ are the OFDM symbol and subcarrier indices, respectively, while

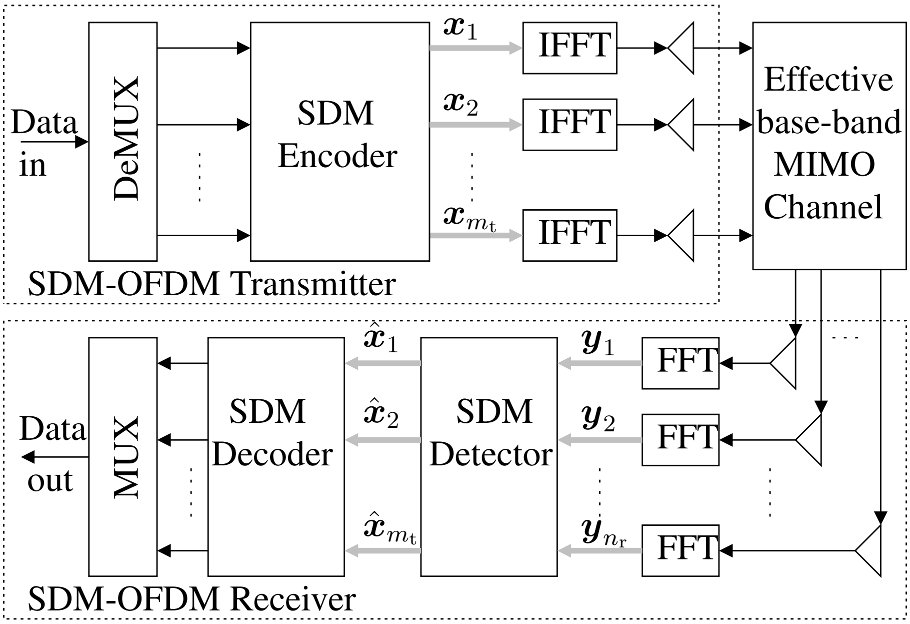

Figure 1.14: Schematic of a generic SDM-OFDM BLAST-type transceiver.

$y_i[n,k], x_j[n,k]$ and $w_i[n,k]$ denote the symbol received at the ith receive antenna, the symbol transmitted from the jth transmit antenna and the Gaussian noise sample encountered at the ith receive antenna, respectively. Furthermore, $H_{ij}[n,k]$ represents the complex-valued CTF coefficient associated with the propagation link connecting the jth transmit and ith receive antennas at the kth OFDM subcarrier and time instance n. Note that in the case of an M-QAM modulated OFDM system, $x_j[n,k]$ corresponds to the M-QAM symbol accommodated by the kth subcarrier of the nth OFDM symbol transmitted from the jth transmit antenna element.

The SDM-OFDM system model described by Equation (1.24) can be interpreted as the per OFDM-subcarrier vector expression of

$$\mathbf{y}[n,k] = \mathbf{H}[n,k]\mathbf{x}[n,k] + \mathbf{w}[n,k], \tag{1.25}$$

where we introduce the space-devision-related vectors $\mathbf{y}[n,k]$, $\mathbf{x}[n,k]$ and $\mathbf{w}[n,k]$, as well as a space-devision-related $(n_\mathrm{r} \times m_\mathrm{t})$-dimensional matrix of CTF coefficients $\mathbf{H}[n,k]$. Note that similarly to the SISO case, the multi-carrier structure of the SDM-OFDM transceiver allows us to represent the broadband frequency-selective MIMO channel as a subcarrier-related vector of flat-fading MIMO-CTF matrices $\mathbf{H}[n,k]$.

1.9 Motivation of This Thesis

Historically speaking, OFDM research was inspired by the celebrated paper conceived by Chang in 1966 [127]. Initially the developments were relatively slow owing to implementational difficulties. More substantial developments were stimulated by Cimini [128] in 1985. In the late 1990s OFDM was adopted by numerous standartization bodies, such as Digital Video Broadcasting (DVB), Digital Audio Broadcasting (DAB), as well as by the IEEE 802.11 Wireless Local Area Network (LAN) - aka WiFi - standard. During the most recent decade further interest was stimulated by the introduction of multiple antennas in the context of both SDM and SDMA. The culmination of this process was that OFDM is now considered to be the strongest candidate for the 3GPP LTE initiative and this motivated the research reported in this thesis. The development of an entire MIMO-OFDM system requires the investigation of numerous system components, most importantly sophisticated channel estimation, multi-antenna signal detection as well as their interactions with the channel decoder.

Chapter 2

Channel Estimation for OFDM and MC-CDMA

2.1 Outline

In this chapter we develop an advanced decision directed channel estimation scheme suitable for employment in a wide range of multi-antenna multi-carrier systems. Firstly, both pilot-aided as well as decision directed channel estimation are briefly discussed and compared in Section 2.2. We conclude that decision directed approach exhibits substantial benefits over its pilot-based counterpart. Correspondingly, in this chapter we focus our attention on the family of decision directed methods. Specifically, the difficulty of employing the LS approach to the problem of estimating the OFDM-subcarrier-related FD-CTF coefficients is described in Section 2.4.1. The alternative MMSE FD-CTF estimator circumventing the problem outlined in Section 2.4.1 is analyzed in Section 2.4.2. Our discourse evolves further by proposing an MMSE CIR estimator exploiting the frequency-domain correlation of the FD-CTF coefficients in Section 2.5.1 and a reduced-complexity version of the CTF MMSE estimator is proposed in Section 2.5.2. The computational complexity of both methods is compared in Section 2.5.3.

In Section 2.5 we continue our discourse with the derivation of both sample-spaced as well as fractionally-spaced Channel Impulse Response (CIR) estimators. In Section 2.5.5 we then perform a comparison between the two methods considered and demonstrate the advantages of the latter, *i.e.* of the fractionally-spaced scheme. Subsequently, in Section 2.6 we develop a method of parametric tracking of the fractionally-spaced CIR taps, which facilitates low-complexity channel estimation in realistic channel conditions characterized by time-variant fractionally-spaced power delay profile. More specifically, we employ the Projection Approximation Subspace Tracking (PAST) method for the sake of recursive tracking of the channel transfer function's (CTF) covariance matrix and for the subsequent tracking of the corresponding CIR taps. We demonstrate that the PAST-aided decision directed channel estimation scheme proposed exhibits a good performance over the entire range of practical conditions.

In Section 2.7 we discuss two major CIR tap prediction strategies. Specifically, in Section 2.7.2 the so-called *robust* implementation of the stationary Minimum Mean Square Error (MMSE) CIR predictor is considered. The *robust* CIR predictor [38] assumes a constant-valued, limited-support channel scattering function [28] during the design of the CIR tap prediction filter and hence relies on the assumption of encountering the worst possible channel conditions. On the other hand, in Section 2.7.4 we discuss the adaptive Recursive Least Squares (RLS) method of CIR prediction [65]. As opposed to the robust CIR predictor of [38], the RLS CIR predictor does not require any explicit information concerning the channel conditions encountered. Consequently, in Section 2.7.5 we characterize and compare the achievable performance of both methods considered and draw conclusions concerning their relative merits. Specifically, we demonstrate that the RLS prediction technique outperforms its robust counterpart over the entire range of the relevant channel conditions.

In Section 2.9.1 of this chapter we explore a family of recursive MIMO-CTF tracking methods, which in conjunction with the aforementioned PAST-aided CIR-tracking method of Section 2.6 as well as the RLS CIR tap prediction method of Section 2.7.4, facilitate the design of an effective channel estimation scheme in the context of a MIMO-OFDM system. More specifically, in Section 2.9.1 we consider both hard- and soft-feedback assisted least mean squares (LMS) and recursive least squares (RLS) tracking algorithms as well as the modified RLS algorithm, which is capable of improved utilization of the soft information associated with the decision-based estimates.

Finally, in Section 2.9.1.5 we document the achievable performance of the resultant MIMO-DDCE scheme employing the recursive CTF tracking of Section 2.4.2 followed by the parametric CIR tap tracking and CIR tap prediction. We demonstrate that the MIMO-DDCE scheme proposed exhibits good performance over the entire range of practical conditions.

2.2 Pilot-Assisted Channel Estimation

In this treatise we concentrate our attention on both the derivation and on the performance analysis of decision-directed channel estimation methods, additionally providing a brief performance comparison between Decision-Directed and Pilot-Aided channel estimation methods. Our motivation is that any technique applicable to DDCE can be equally employed in the context of pilot-aided schemes and the difference between their attainable performance can be predicted as outlined below.

The attainable performance of both the Decision-Directed (DD) and Pilot-Assisted (PA) channel estimation methods can be compared in the following simple way.

The performance of any pilot-assisted channel estimation method expressed in terms of the achievable Mean Square Error (MSE) is upper-bounded by the expression

$$MSE_{\text{PA}} > \frac{N_0 L}{E_p}, \tag{2.1}$$

where E_p is the total power associated with the transmitted pilots, N_0 is the Gaussian noise variance and L is the number of non-zero CIR components.

On the other hand, in the case of DD channel estimation the corresponding performance bound, using the assumption of error-free decisions, can be described by

$$MSE_{\text{DD}} > \frac{N_0}{E_s}\frac{L}{K}, \tag{2.2}$$

where E_s is the average signal energy per transmitted complex base-band sample and K is the number of OFDM subcarriers, while N_0 and L are as defined previously.

Thus the resultant performance gain may be quantified as

$$\frac{MSE_{\text{DD}}}{MSE_{\text{PA}}} = \frac{E_p}{E_s K}. \tag{2.3}$$

We would also like to emphasize the trade-off between the PA channel estimator's performance and the system's spectral-efficiency loss associated with the allocation of valuable signal power to pilot symbols. The corresponding data-rate loss can be quantified by a simple expression similar to that of Equation (2.3):

$$r_{\text{loss}} = \frac{E_p}{E_s K}. \tag{2.4}$$

2.3 Decision Directed Channel Estimation

The schematic of the channel estimation method considered is depicted in Figure 2.1. The symbols $\boldsymbol{y}[n]$ and $\hat{\boldsymbol{s}}[n]$ in the figure represent the received vector of the subcarrier-related samples and the *a posteriori* decision-based estimated vector of the transmitted information-carrying symbols $\boldsymbol{s}[n]$, respectively. Furthermore, symbols $\boldsymbol{H}[n+1], \alpha[n]$ and $\alpha[n+1]$ represent the CTF and the CIR vectors corresponding to time instants n and $n+1$, respectively. Finally, the accents $\check{x}$ and $\hat{x}$ represent the *a priori* predicted and *a posteriori* estimated values of the variable x, respectively. Figure 2.1 corresponds to the general case of the CIR estimation and both sample-spaced as well as fractionally-spaced cases may be considered.

For the sake of clarity, we would like to emphasis the notational difference between the Sample Spaced CIR vector $\boldsymbol{h}[n]$ and the Fractionally Spaced CIR vector $\boldsymbol{\alpha}[n]$. Specifically, we would like to commence by considering the simpler case of the SS-CIR. Thus, the CIR vector $\boldsymbol{\alpha}[n]$ in Figure 2.1 may be substituted by its sample-spaced projection $\boldsymbol{h}[n]$ described by Equation (1.8).

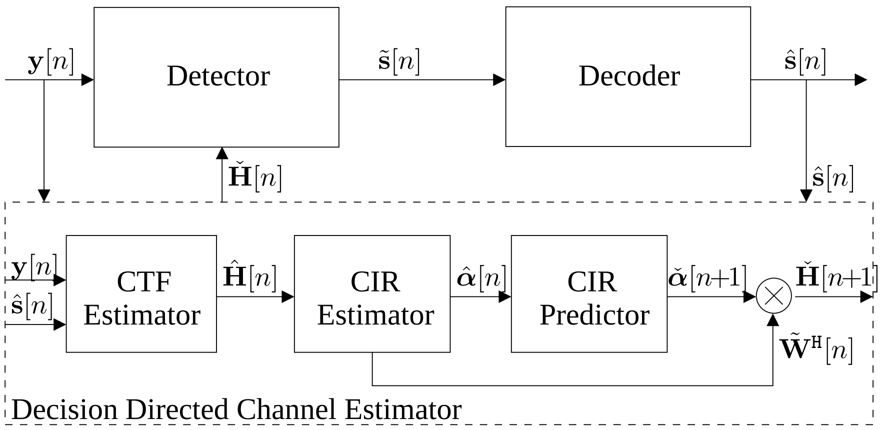

Figure 2.1: Schematics of a generic receiver employing Decision Directed Channel Estimator constituted by an *a posteriori* decision-directed CTF Estimator, followed by a CIR Estimator and an *a priori* CIR predictor.

Our channel estimator is constituted by what we refer to as an *a posteriori* decision-directed CTF estimator followed by a CIR estimator and an *a priori* CIR predictor [28]. As seen in Figure 2.1, the task of the CTF estimator is to evaluate the tentative values of the subcarrier-related CTF coefficiets of Equation (1.14). Correspondingly, the task of the CIR estimator is to estimate the SS-CIR taps of Equation (1.8). In the case of the sample-spaced CIR aided channel estimation, discussed in this section, the Inverse Fast Fourier Transform (IFFT) based transformation from the subcarrier-related frequency domain to the sample-spaced CIR-related time domain is invoked in order to exploit the frequency-domain correlation of the subcarrier-related CTF coefficients as well as to reduce the computational complexity associated with the CTF prediction process, because the SS-CIR typically has a lower number of $K_0 \ll K$ taps, which have to be predicted, than the K number of FD-CTF coefficients. Hence the overall channel estimation complexity is reduced, even when the complexity of the FD-CTF to CIR transformation and its inverse are taken into account[1].

As can be seen in Figure 2.1, the *a posteriori* CTF estimator inputs are the subcarrier-related signal $\boldsymbol{y}[n]$ and the decision-based estimate $\hat{\mathbf{s}}[n]$. The transformation from the frequency to time domain is performed within the CIR estimator of Figure 2.1 and its output is an *a posteriori* estimate $\hat{s}[n,k]$ of the CIR taps of Equation (1.8), which is fed into the low-rank time-domain CIR tap predictor of Figure 2.1 for the sake of producing an *a priori* estimate $\check{h}[n+1,l],\ l=0,1,\cdots,K_0-1$ of the next SS-CIR on a SS-CIR tap-by-tap basis [28]. Finally, the predicted SS-CIR is converted to the subcarrier-related CTF estimates with the aid of the FFT. The resultant FD-CTF is employed by the receiver for the sake of detecting and decoding of the next OFDM symbol. Note, that this principle requires the transmission of a pilot-based channel sounding sequence, such as for example pilot-assisted OFDM block, during the initialisation stage.

---

[1] The computational complexity associated with the prediction of the K CTF coefficients is of order $O(K^2 N_{\mathrm{prd}})$, where N_{prd} is the order of the prediction filter. On the other hand, the CIR prediction combined with the FFT and IFFT operations can be associated with the computational complexity of order $O(K_0^2 N_{\mathrm{prd}} + 2K\log_2 K)$. It is evident, that in the typical case of $N_{\mathrm{prd}} < K_0 \ll K$ the overall estimation complexity is reduced if the aforementioned method of the CIR prediction is employed.

2.4 *A Posteriori* FD-CTF Estimation

In order to emphasize the major difference between the OFDM and MC-CDMA systems in the context of the associated channel estimation scheme, first we would like to analyze the performance of the temporal estimator of the subcarrier-related FD-CTF coefficients $H[n,k]$ based on the *a posteriori* decision-aided estimates of the transmitted subcarrier-related samples $s[n,k]$ of Equation (1.14). In Section 2.4.1 we will show that the LS approach typically employed in DDCE-aided OFDM systems [28, 38] is not applicable in the case of MC-CDMA systems. In Section 2.5.1 we propose an MMSE estimator, which renders the DDCE philosophy discussed in [28,38] suitable for MC-CDMA systems. However, the estimator introduced in Section 2.5.1 exhibits a computational complexity, which is significantly higher than the computational complexity of the conventional LS-based estimator of [28, 38]. Thus a reduced-complexity approximation of the MMSE estimator of Section 2.5.1 is proposed in Section 2.5.2.

2.4.1 Least Squares CTF Estimator

Following Equation (1.14), the Least Squares (LS) approach [101] to the problem of estimating the discrete-abscissa FD-CTF coefficients $H[n,k]$, based on the knowledge of the decision-aided estimates $\hat{s}[n,k]$ of the transmitted frequency-domain samples $s[n,k]$ of Equation (1.14) can be expressed as

$$\tilde{H}[n,k] = \frac{y[n,k]}{\hat{s}[n,k]} = H[n,k] \cdot \frac{s[n,k]}{\hat{s}[n,k]} + \frac{w[n,k]}{\hat{s}[n,k]}, \tag{2.5}$$

where $H[n,k]$ represents the Rayleigh-distributed FD-CTF coefficients having a variance of σ_H^2, while $s[n,k]$ denotes the transmitted subcarrier-related samples having zero mean and a variance of σ_s^2. The distribution of the samples $s[n,k]$ is dependent on the particular modulation scheme employed by the system. For instance, in a MC-CDMA system using an arbitrary modulation scheme, the samples $s[n,k]$ are complex-Gaussian distributed, having a Rayleigh-distributed amplitude $|x[n,k]|$ and uniformly-distributed phase $\theta[n,k]$. By contrast, in a M-PSK-modulated OFDM system the samples $s[n,k]$ are uniformly distributed within the set of M-PSK symbols having a constant amplitude $|s[n,k]| = \sigma_s$ and a discrete-uniform distributed phase $\theta[n,k] = 2\pi\frac{m}{M}, m = 0, 1, \cdots, M-1$. Finally, the noise samples $w[n,k]$ are independent identically distributed (i.i.d.) complex-Gaussian variables having a zero mean and a variance of σ_w^2.

Under the assumption of carrying out error-free decisions we have $\hat{s}[n,k] = s[n,k]$ and Equation (2.5) may be simplified to

$$\tilde{H}[n,k] = \frac{y[n,k]}{\hat{s}[n,k]} = H[n,k] + \frac{w[n,k]}{\hat{s}[n,k]}. \tag{2.6}$$

The Mean Square Error (MSE) associated with the LS FD-CTF estimator of (2.6) is given by

$$MSE_{\text{LS}} = \mathtt{E}\left\{\left|H[n,k] - \tilde{H}[n,k]\right|^2\right\} = \mathtt{E}\left\{\left|\frac{w[n,k]}{s[n,k]}\right|^2\right\}. \tag{2.7}$$

The less ambiguous measure of the estimator's performance is the Normalized MSE (NMSE), which is defined as the MSE normalized by the variance of the parameter being estimated. The NMSE corresponding to the estimator of Equation (2.6) is given by

$$NMSE_{\text{LS}} = \frac{1}{\sigma_H^2}\mathrm{E}\left\{\left|\frac{w[n,k]}{s[n,k]}\right|^2\right\}. \tag{2.8}$$

The AWGN samples $w[n,k]$ are known to be i.i.d. complex-Gaussian and hence the MSE of Equation (2.7) is determined by the statistical distribution of the transmitted subcarrier-related samples $s[n,k]$. The NMSE encountered assumes its minimum value, when $|s[n,k]|^2 = \sigma_s^2$ is constant, as in the case of an M-PSK-modulated OFDM system. Thus, we have

$$NMSE_{\text{LS,min}} = \frac{1}{\sigma_H^2\sigma_s^2}\mathrm{E}\left\{|w[n,k]|^2\right\} = \frac{\sigma_w^2}{\sigma_H^2\sigma_s^2} = \frac{1}{\gamma} \quad , \tag{2.9}$$

where

$$\gamma = \frac{1}{\sigma_w^2}\mathrm{E}\left\{|H[n,k]s[n,k]|^2\right\} = \frac{\sigma_H^2\sigma_s^2}{\sigma_w^2} \tag{2.10}$$

is the average SNR level. On the other hand, the NMSE value will increase substantially, if the energy of the transmitted samples $s[n,k]$ varies as in the case of M-ary Quadrature Amplitude Modulation (M-QAM)-based OFDM or MC-CDMA. In fact, in the case of strictly Gaussian-distributed samples $s[n,k]$, which corresponds to encountering a MC-CDMA system having a sufficiently long spreading code, the NMSE value of Equation (2.8) does not exist, since the variance of the resultant Cauchy distributed variable associated with the ratio of two Gaussian-distributed variables $s[n,k]$ and $w[n,k]$ of Equation (2.8) cannot be defined [129]. The NMSE of the LS estimator of Equation (2.6) derived for QPSK, 16-, 64- and 256-QAM-modulated OFDM, as well as QPSK-modulated MC-CDMA is depicted in Figure 2.2(a). The solid line in Figure 2.2(a) corresponds to the lower NMSE bound described by Equation (2.9).

The performance degradation of the LS estimator of Equation (2.6) was imposed by the energy-fluctuation of the near-Gaussian distributed subcarrier-related samples $s[n,k]$, which renders the LS estimator inapplicable for employment in MC-CDMA systems. Therefore, for the sake of mitigating this performance degradation we would like to turn our attention to the MMSE estimation approach.

2.4.2 MMSE CTF Estimator

In order to derive a FD-CTF estimator, which is suitable for employment in a MC-CDMA system, where the energy-fluctuation of the subcarrier-related samples $s[n,k]$ is near-Gaussian, we turn to the MMSE approach. Following the Bayesian linear model theory of [101], the MMSE estimator of the FD-CTF coefficients $H[n,k]$ of the scalar linear model described by Equation (1.14), where the parameters $H[n,k]$ are assumed

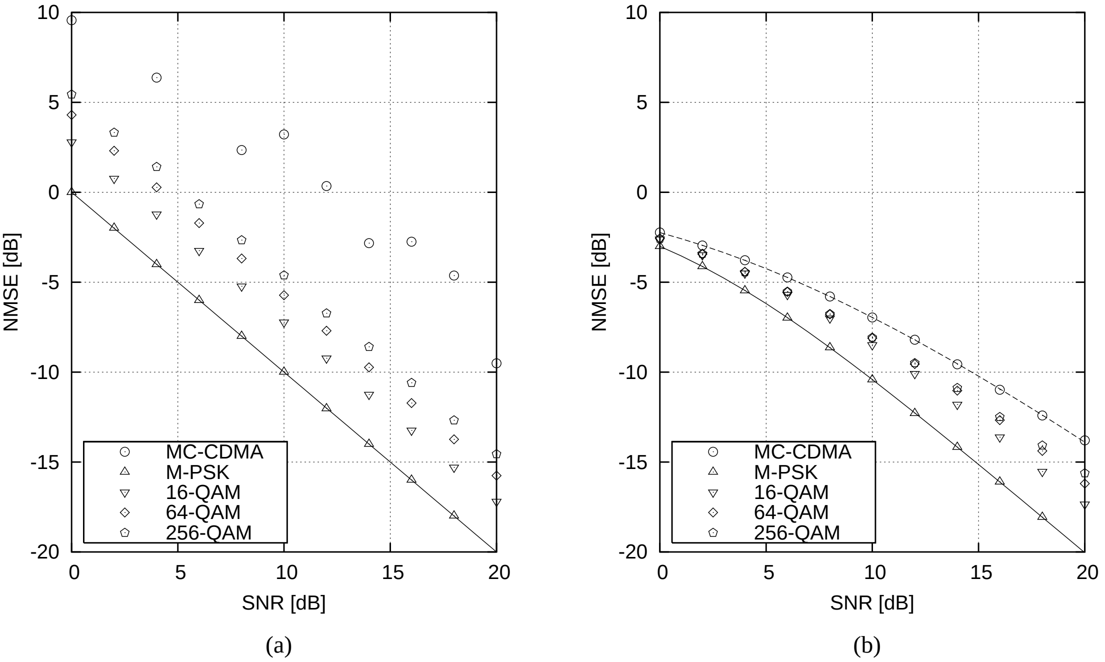

(a)

(b)

Figure 2.2: NMSE associated with (a) **Least Squares (LS)** and (b) **Minimum Mean Square Error (MMSE)** estimators of the uncorrelated Rayleigh-distributed subcarrier-related CTF coefficients $H[n,k]$ of Equation (1.14) corresponding to the various statistical distributions of the transmitted subcarrier-related samples $x[n,k]$. The markers on the plot correspond to the simulated cases of M-PSK, 16-, 64- and 256-QAM modulated OFDM as well as M-QAM modulated MC-CDMA, while the lines correspond to the analytically calculated performance recorded for the cases of M-PSK OFDM (solid) and MC-CDMA (dashed), which represent the lower and the upper NMSE bounds, respectively. Note that the upper bound for the LS estimator in conjunction with MC-CDMA does not exist.

to be complex-Gaussian distributed with a zero mean and a variance of σ_H^2, is given by [101]:

$$\begin{aligned}\tilde{H}_{\text{MMSE}}[n,k] &= \left(\frac{x^*[n,k]s[n,k]}{\sigma_w^2} + \frac{1}{\sigma_H^2}\right)^{-1} \\ &\cdot \frac{x^*[n,k]y[n,k]}{\sigma_w^2} = \frac{s^*[n,k]y[n,k]}{|s[n,k]|^2 + \frac{\sigma_w^2}{\sigma_H^2}}.\end{aligned} \tag{2.11}$$

The corresponding NMSE can be expressed as [101]

$$\begin{aligned}NMSE_{\text{MMSE}} &= \frac{1}{\sigma_H^2}\left(\frac{1}{\sigma_H^2} + \frac{|s[n,k]|^2}{\sigma_w^2}\right)^{-1} \\ &= \frac{\sigma_w^2}{\sigma_H^2|s[n,k]|^2 + \sigma_w^2} = \frac{1}{\gamma\left|\frac{s[n,k]}{\sigma_x}\right|^2 + 1},\end{aligned} \tag{2.12}$$

where γ is the average SNR level defined by Equation (2.10). As we have seen previously in the context of Equation (2.12), the NMSE is determined by the statistical distribution of the transmitted subcarrier-related samples $s[n,k]$ and assumes its minimum value, when the energy of these samples $|s[n,k]|^2 = \sigma_s^2$ is constant. On the other hand, in contrast to the NMSE of the LS estimator of Equation (2.5), the NMSE of the MMSE estimator of Equation (2.11) is upper-bounded, which is evidenced by Figure 2.2(b). The NMSE assumes its maximum value, when the samples $s[n,k]$ are complex-Gaussian distributed, as in the case of a MC-CDMA system having a sufficiently high spreading factor. Explicitly, the maximum NMSE may be derived as follows:

$$\begin{aligned} NMSE_{H,\max}(\gamma) &= \underset{x\in N(0,\sigma_x^2)}{E}\{NMSE(\gamma,x)\} \\ &= \underset{r=|\frac{x}{\sigma_x}|^2\in\chi^2}{E}\{NMSE(\gamma,r)\} \\ &= \int_0^\infty \frac{1}{\gamma r+1}\, e^{-r}\mathrm{d}r = \frac{1}{\gamma}\, e^{\frac{1}{\gamma}}\mathtt{Ei}\left(\frac{1}{\gamma}\right), \end{aligned} \tag{2.13}$$

where we integrate *i.e.* average the first multiplicative term upon weighting it by the χ^2-distributed Probability Density Function (PDF) of the NMSE described by $P_{\chi^2}(r) = e^{-r}$ over its entire range spanning from 0 to ∞ and define the *exponential integral* function as:

$$\mathtt{Ei}(x) = \int_x^\infty \frac{e^{-t}}{t}\,\mathrm{d}t. \tag{2.14}$$

2.4.3 *A Priori* Predicted Value Aided CTF Estimator

In MC-CDMA systems employing spreading codes having a relatively low spreading factor G, there is a finite probability of encountering zero-energy subcarrier-related samples $s[n,k] = 0$ when superimposing the chips of various users corresponding to the subcarrier considered. This probability decreases with increasing spreading factor G as the corresponding power distribution function approaches Gaussian distribution. As can be seen from Equation (2.11), this will result in a corresponding the CTF coefficient MMSE estimate $\tilde{H}[n,k] = 0$, which is unrelated to the actual value of $H[n,k]$ encountered. This problem can be circumvented in the context of the DDCE scheme of Figure 2.1, where the *a priori* predicted estimate of the subcarrier-related coefficient $H[n,k]$ is readily available, by performing a Maximum Ratio Combining (MRC) of the *a posteriori* MMSE estimate $\tilde{H}[n,k]$ of Equation (2.11) and the corresponding *a priori* estimate $\check{H}[n,k]$. It can be shown that the resultant MRC-aided CTF estimator can be expressed as

$$\tilde{H}[n,k] = \frac{\check{H}[n,k] + \hat{s}^*[n,k]y[n,k]}{1+|\hat{s}[n,k]|^2 + \frac{K_0}{K}\frac{\sigma_w^2}{\sigma_H^2}}. \tag{2.15}$$

In the following section we employ the following vectorial notation $\boldsymbol{v}[n] = (v[n,1],\cdots,v[n,K])^{\mathrm{T}}$.

2.5 *A Posteriori* CIR Estimation

2.5.1 MMSE SS-CIR Estimator

We would like to commence our portrayal of the proposed channel estimation philosophy rendering the DDCE OFDM scheme of [28, 38] also applicable to employment in MC-CDMA with the derivation of the *a posteriori* MMSE SS-CIR estimator of Figure 2.1.

By substituting the FD-CTF of Equation (1.7) into (1.14) we arrive at

$$y[n,k] = \sum_{l=0}^{K_0-1} W_K^{kl} h[n,l] x[n,k] + w[n,k], \tag{2.16}$$

which can be expressed in a matrix form as

$$\boldsymbol{y}[n] \;=\; \mathrm{diag}\left(x[n,k]\right) \boldsymbol{W}\boldsymbol{h}[n] + \boldsymbol{w}[n], \tag{2.17}$$

where we define the $(K \times K)$-dimensional matrix $\mathrm{diag}\left(v[k]\right)$ as a diagonal matrix having the corresponding elements of the vector $v[k]$ on the main diagonal, as well as the $(K \times K_0)$-dimensional Fourier Transform matrix $\boldsymbol{W}$, which corresponds to the Fourier transform of the zero-padded SS-CIR vector $\boldsymbol{h}[n]$ and is defined by $W_{kl} = W_K^{kl}$ for $k = 0, 1, \cdots, K-1$ and $l = 0, 1, \cdots, K_0 - 1$.

As before, the SS-CIR taps $h[l]$ are assumed to be uncorrelated complex-Gaussian distributed variables having a zero mean and a covariance matrix given by

$$\boldsymbol{C}_h = \mathrm{diag}\left(\sigma_l^2\right). \tag{2.18}$$

The MMSE estimator of the SS-CIR taps $h[n,l]$ of the linear vector model described by Equation (2.17) is given by [101]

$$\begin{aligned}\hat{\boldsymbol{h}} \;&=\; \left(\mathrm{diag}\left(\frac{1}{\sigma_l^2}\right) + \frac{1}{\sigma_w^2}\boldsymbol{W}^{\mathrm{H}}\mathrm{diag}\left(|\hat{x}[k]|^2\right)\boldsymbol{W}\right)^{-1} \\ &\times\; \frac{1}{\sigma_w^2}\boldsymbol{W}^{\mathrm{H}}\mathrm{diag}\left(\hat{x}^*[k]\right)\boldsymbol{y},\end{aligned} \tag{2.19}$$

where we omit the time-domain OFDM-block-spaced index n for the sake of notational simplicity. Following the assumptions made in Section 1.7.1 about the nature of the channel model considered, some of the parameters σ_l^2 may assume a zero value. Hence for the sake of avoiding devision by zero, we would like to rewrite the Equation (2.19) in a more practical form as follows:

$$\begin{aligned}\hat{\boldsymbol{h}} \;&=\; \left(\sigma_w^2\boldsymbol{I} + \mathrm{diag}\left(\sigma_l^2\right)\boldsymbol{W}^{\mathrm{H}}\mathrm{diag}\left(|\hat{x}[k]|^2\right)\boldsymbol{W}\right)^{-1} \\ &\times\; \mathrm{diag}\left(\sigma_l^2\right)\boldsymbol{W}^{\mathrm{H}}\mathrm{diag}\left(\hat{x}^*[k]\right)\boldsymbol{y}.\end{aligned} \tag{2.20}$$

The covariance matrix of the vector $\hat{\boldsymbol{h}}$ of the MMSE SS-CIR estimates can be expressed as [101]

$$\begin{aligned} \boldsymbol{C}_{\hat{h}|\hat{x}} = & \left(\boldsymbol{I} + \mathrm{diag}\left(\frac{\sigma_l^2}{\sigma_w^2} \right) \boldsymbol{W}^{\mathrm{H}} \mathrm{diag}\left(|\hat{x}[k]|^2 \right) \boldsymbol{W} \right)^{-1} \\ \times & \ \ \mathrm{diag}\left(\sigma_l^2 \right). \end{aligned} \tag{2.21}$$

The corresponding NMSE associated with the lth MMSE SS-CIR tap estimate $\hat{h}[l]$ can be found be approximating the lth diagonal element of the covariance matrix $\boldsymbol{C}_{\hat{h}|\hat{x}}$ of Equation (2.21) and normalising it by the average channel output power σ_H^2. The above-mentioned approximation is performed by replacing the matrix $\mathrm{diag}\left(|\hat{x}[k]|^2 \right)$ in Equation (2.21) by its average value $\sigma_x^2 \boldsymbol{I}$. Thus, we arrive at

$$\begin{aligned} NMSE_{\mathrm{MMSE},l} &= \frac{\sigma_l^2}{\sigma_H^2} \frac{\sigma_w^2}{\sigma_w^2 + K\sigma_l^2\sigma_x^2} \\ &= \frac{\sigma_w^2}{\sigma_H^2\sigma_x^2} \frac{\sigma_l^2}{\frac{\sigma_w^2}{\sigma_x^2} + K\sigma_l^2} = \frac{1}{\gamma} \frac{1}{\frac{\sigma_w^2}{\sigma_x^2\sigma_l^2} + K}. \end{aligned} \tag{2.22}$$

The overall NMSE corresponding to the MMSE SS-CIR estimator of Equation (2.20) may be found by summing all the lth NMSE contributions in Equation (2.22) over the K_0 taps of the CIR encountered, which can be expressed as

$$NMSE_{\mathrm{MMSE}} = \frac{1}{\gamma} \sum_{l=0}^{K_0-1} \frac{1}{\frac{\sigma_w^2}{\sigma_x^2\sigma_l^2} + K} \approx \frac{1}{\gamma} \frac{L}{K}, \tag{2.23}$$

where, as before, K is the number of OFDM subcarriers and γ is the average SNR value, while L is the number of non-zero SS-CIR taps encountered. The resultant NMSE described by Equation (2.23) is depicted in Figure 2.3.

2.5.2 Reduced Complexity SS-CIR Estimator

As it is seen from Equation (2.19), the direct MMSE approach to the problem of estimating the SS-CIR taps $h[n,l]$ involves a time-variant matrix inversion, which introduces a relatively high computational complexity [28]. In order to reduce the associated computation complexity, we introduce a two-step low-complexity SS-CIR estimator invoking an approach, which bypasses the computationally intensive matrix inversion operation encountered in Equation (2.19). We will show that the method proposed first employs a scalar MMSE estimator of the subcarrier-related FD-CTF coefficients $H[n,k]$ of Equation (2.11), followed by employing a simplified MMSE SS-CIR estimator, which exploits the average MSE expression of Equation (2.13) associated with the scalar MMSE FD-CTF estimator of the first processing step.

Following the Bayesian estimation theory of [101] the MMSE CTF estimates $\tilde{H}_{\mathrm{MMSE}}[n,k]$ of Equation (2.11) may be modelled as complex Gaussian-distributed variables having a mean identical to that of $H[n,k]$, which represents the actual FD-CTF coefficients encountered and a variance of $\sigma_v^2 = \sigma_H^2 NMSE_{\max}$, where

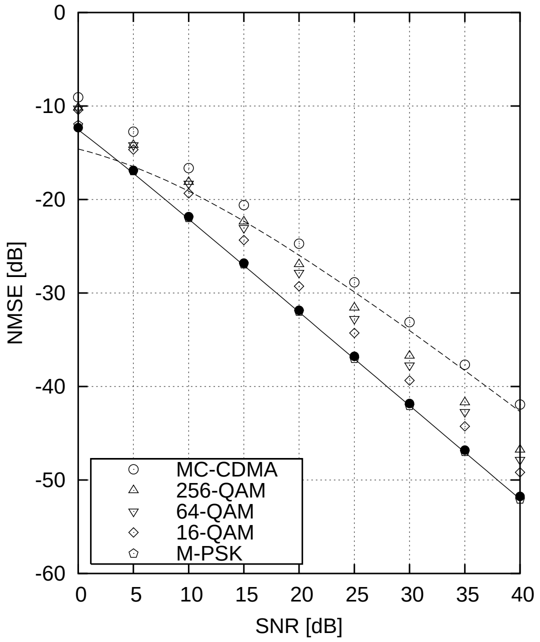

Figure 2.3: NMSE associated with both the **Minimum Mean Square Error (MMSE)** and the **Reduced-Complexity (RC) MMSE** SS-CIR estimators described be Equations (2.20) and (2.30), respectively. The markers on the plot correspond to the simulated cases of M-PSK, 16-, 64- and 256-QAM modulated OFDM, as well as M-QAM modulated MC-CDMA in conjunction with MMSE (bold) and RC-MMSE (hollow) SS-CIR estimators, while the lines correspond to the analytically calculated NMSE lower-bounds for the cases of MC-CDMA in conjunction with both the MMSE (solid) and the RC-MMSE (dashed) estimators evaluated using Equations (2.23) and (2.32), respectively. Note, that the markers associated with different modulation schemes and RC-MMSE estimator coincide.

σ_H^2 is the average channel output power and $NMSE_{\max}$ is the average NMSE quantified in Equation (2.13). Thus we can write

$$\tilde{H}_{\text{MMSE}}[n,k] = H[n,k] + v[n,k], \tag{2.24}$$

where $v[n,k]$ represents the i.i.d. complex-Gaussian noise samples having a zero mean and a variance of σ_v^2.

By substituting (1.8) into (2.24) we arrive at

$$\tilde{H}_{\text{MMSE}}[n,k] = \sum_{l=0}^{K_0-1} W_K^{kl} h[n,k] + v[n,k], \tag{2.25}$$

where $W_K = e^{-\jmath 2\pi \frac{1}{K}}$, which can be rewritten in matrix form as

$$\tilde{\boldsymbol{H}}_{\text{MMSE}}[n] = \boldsymbol{W}\boldsymbol{h}[n] + \boldsymbol{v}[n], \tag{2.26}$$

where the $(K \times K_0)$-dimensional matrix $\boldsymbol{W}$ corresponds to the Fourier transform of the zero-padded SS-CIR vector $\boldsymbol{h}[n]$ and is defined by $W_{kl} = W_K^{kl}$ for $k = 0, 1, \cdots, K-1$ and $l = 0, 1, \cdots, K_0 - 1$.

The MMSE estimator of the SS-CIR taps $h[n,k]$ of the linear vector model described by Equation (2.26) is given by [101]

$$\hat{\boldsymbol{h}} = (\boldsymbol{C}_h^{-1} + \boldsymbol{W}^{\mathrm{H}}\boldsymbol{C}_v^{-1}\boldsymbol{W})^{-1}\boldsymbol{W}^{\mathrm{H}}\boldsymbol{C}_v^{-1}\tilde{\boldsymbol{H}}_{\mathrm{MMSE}}, \tag{2.27}$$

where we omit the time-domain OFDM-block-spaced index n for the sake of notational simplicity and define $\boldsymbol{C}_h$ and $\boldsymbol{C}_v$ as the covariance matrices of the SS-CIR vector $\boldsymbol{h}$ and the scalar MMSE FD-CTF estimator's noise vector $\boldsymbol{v}$, respectively. The elements of the noise vector $\boldsymbol{v}$ are assumed to be complex-Gaussian i.i.d. samples and therefore we have $\boldsymbol{C}_v = \sigma_v^2\boldsymbol{I}$. On the other hand, as follows from the assumption of having uncorrelated SS-CIR taps, the SS-CIR taps' covariance matrix is a diagonal matrix $\boldsymbol{C}_h = \mathrm{diag}\left(\sigma_l^2\right)$, where $\sigma_l^2 = \mathrm{E}\left\{|h[n,l]|^2\right\}$. Substituting $\boldsymbol{C}_h$ and $\boldsymbol{C}_v$ into Equation (2.27) yields [101]

$$\begin{aligned}
\hat{\boldsymbol{h}} &= \left(\mathrm{diag}\left(\frac{1}{\sigma_l^2}\right) + \frac{1}{\sigma_v^2}\boldsymbol{W}^{\mathrm{H}}\boldsymbol{W}\right)^{-1} W^{\mathrm{H}}\frac{1}{\sigma_v^2}\tilde{\boldsymbol{H}}_{\mathrm{MMSE}} \\
&= \left(\mathrm{diag}\left(\frac{\sigma_v^2}{\sigma_l^2}\right) + K\boldsymbol{I}\right)^{-1} \boldsymbol{W}^{\mathrm{H}}\tilde{\boldsymbol{H}}_{\mathrm{MMSE}} \\
&= \mathrm{diag}\left(\frac{\sigma_l^2}{\sigma_v^2 + K\sigma_l^2}\right)\boldsymbol{W}^{\mathrm{H}}\tilde{\boldsymbol{H}}_{\mathrm{MMSE}},
\end{aligned} \tag{2.28}$$

where we have exploited the fact that

$$[\boldsymbol{W}^{\mathrm{H}}\boldsymbol{W}]_{l,l'} = \sum_{k=0}^{K-1} e^{-\jmath 2\pi \frac{k(l-l')}{K}} = K\delta[l-l'] \tag{2.29}$$

and therefore $\boldsymbol{W}^{\mathrm{H}}\boldsymbol{W} = K\boldsymbol{I}$, where $\boldsymbol{I}$ is a $(K_0 \times K_0)$-dimensional identity matrix.

Finally, upon substituting Equation (2.11) into Equation (2.28) we arrive at a scalar expression for the Reduced-Complexity (RC) *a posteriori* MMSE SS-CIR estimator in the form of:

$$\hat{h}[n,l] = \frac{\sigma_l^2}{\sigma_v^2 + K\sigma_l^2}\sum_{k=0}^{K-1} W_K^{kl}\frac{\hat{x}^*[n,k]y[n,k]}{|\hat{x}[n,k]|^2 + \frac{\sigma_w^2}{\sigma_H^2}}. \tag{2.30}$$

The corresponding NMSE associated with the lth RC-MMSE SS-CIR tap estimate $\hat{h}[l]$ is given by [101]

$$\begin{aligned}
NMSE_{\mathrm{RCMMSE},l} &= \frac{\sigma_v^2}{\sigma_H^2}\frac{\sigma_l^2}{\sigma_v^2 + K\sigma_l^2} \\
&= \frac{\sigma_v^2}{\sigma_H^2}\frac{1}{\frac{\sigma_v^2}{\sigma_l^2} + K},
\end{aligned} \tag{2.31}$$

where $\sigma_v^2 = \sigma_H^2 NMSE_{H,\max}$ is the variance of the noise samples $v[k]$ in Equation (2.24), while $NMSE_{H,\max}$ is the maximum NMSE of the scalar MMSE FD-CTF estimator of Equation (2.11). The overall NMSE corresponding to the MMSE SS-CIR estimator of Equation (2.30) can be found similarly to Equation (2.23) by summing all of the lth contributions quantified by Equation (2.31) over the K_0 taps of the CIR encountered, which can be expressed using Equation (2.13) as

$$\begin{aligned} NMSE_{\text{RCMMSE}} &= \frac{1}{\gamma}\exp\left(\frac{1}{\gamma}\right)\mathtt{Ei}\frac{1}{\gamma}\sum_{l=0}^{K_0-1}\frac{1}{\frac{\sigma_v^2}{\sigma_l^2}+K} \\ &\approx \frac{1}{\gamma}\exp\frac{1}{\gamma}\mathtt{Ei}\left(\frac{1}{\gamma}\right)\frac{L}{K}, \end{aligned} \tag{2.32}$$

where, as before, K is the number of OFDM subcarriers and γ is the average SNR value, while L is the number of non-zero SS-CIR taps encountered. The resultant NMSE described by Equation (2.32) represents the lower-bound of the NMSE exhibited by the RC-MMSE SS-CIR estimator in conjunction with complex-Gaussian distributed transmitted samples $x[n, k]$ typically encountered in a MC-CDMA system having a high spreading factor. The resultant NMSE performance is depicted in Figure 2.3 using a dashed line.

2.5.3 Complexity Study

As it was shown in Section 2.4, the LS approach to the problem of DDCE-aided OFDM schemes [28] is not suitable in the case of MC-CDMA systems. The MMSE approach of Section 2.5.1 constitutes an appropriate solution, however it exhibits a relatively high computational complexity imposed by the evaluation and inversion of the $(K_0 \times K_0)$-dimensional matrix $\left(\boldsymbol{A} + \boldsymbol{W}^{\mathtt{H}}\text{diag}\left(|x[k]|^2\right)\boldsymbol{W}\right)$ in Equation (2.20). More explicitly, the MMSE SS-CIR estimator of Equation (2.20) has a computational complexity, which is of the order of $O(K^2K_0 + KK_0^2 + K_0^3)$, where K is the number of OFDM subcarriers and K_0 is the number of SS-CIR taps encountered. By contrast, the reduced-complexity SS-CIR estimator of Equation (2.30), which avoids the matrix inversion operation, has a complexity of the order of $O(K + K\log_2 K + K_0)$, which is similar to the complexity associated with the conventional LS estimator employed in [28]. It can be seen that the difference between the proposed estimation methods expressed in terms of the associated computational complexity is substantial. In the next section we would like to derive an alternative Reduced Complexity (RC) MMSE estimator, which is capable of estimating the Fractionally-Spaced (FS) CIR taps of Equation (1.7) using an approach similar to that described above.

2.5.4 MMSE FS-CIR Estimator

As was advocated in Section 1.7.1, realistic mobile wireless channel may be characterized by a fractionally spaced PDP, constituded by a relatively small number of statistically independent multipath components. Correspondingly, the FS-CIR based channel estimation method exhibits the potential to improve the achievable system's performance as well as to reduce the associated computational complexity. In this section we derive a MMSE FS-CIR estimator. The achievable performance of decision-directed channel estimation (DDCE) methods employing both the SS- and the FS-CIR estimators is analyzed in the context of an OFDM system. The performance of the two estimation methods is compared and it is shown that the DDCE scheme employing the FS-CIR estimator outperforms its SS-CIR estimator-based counterpart.

The first constituent component of our estimator, namely the scalar MMSE CTF estimator is identical to that derived in Section 2.5.2 and described by Equation (2.11). Furthermore, our approach used for deriving the MMSE FS-CIR estimator is similar to that utilized in Section 2.5.2, however it exhibits several substantial differences, as detailed bellow.

By substituting the FD-CTF of Equation (1.7) into (2.24) we arrive at

$$\tilde{H}[n,k] = C(k\Delta f)\sum_{l=1}^{L}\alpha_l[n]W_K^{k\tau_l/T_s} + v[n,k], \tag{2.33}$$

where, as previously, $C(f)$ is the frequency response of the transceiver's pulse-shaping filter, $W_K \triangleq e^{-\jmath 2\pi\frac{1}{K}}$, while $\alpha_l[n]$ and τ_l are the amplitudes and the relative delays of the FS-CIR taps, respectively. Equation (2.33) can be expressed in a matrix form as

$$\begin{aligned}\tilde{\boldsymbol{H}}[n] &= \operatorname{diag}\left(C[k]\right)\boldsymbol{W}\boldsymbol{\alpha}[n] + \boldsymbol{v}[n] \\ &= \boldsymbol{T}\boldsymbol{\alpha}[n] + \boldsymbol{v}[n],\end{aligned} \tag{2.34}$$

where we define the $(K \times L)$-dimensional matrix $\boldsymbol{T} \triangleq \operatorname{diag}\left(C[k]\right)\boldsymbol{W}$, in which $\operatorname{diag}\left(C[k]\right)$ is a $(K \times K)$-dimensional diagonal matrix with the corresponding elements of the vector $C[k]$ on the main diagonal, while $\boldsymbol{W}$ is the Fourier Transform matrix defined by $W_{kl} \triangleq W_K^{k\frac{\tau_l}{T_s}}$ for $k = -\frac{K}{2}, \cdots, \frac{K}{2} - 1$ and $l = 1, \cdots, L$.

The MMSE estimator of the FS-CIR taps $\alpha_l[n]$ of the linear vector model described by (2.34) is given by [101]

$$\hat{\boldsymbol{\alpha}} = (\boldsymbol{C}_{\alpha}^{-1} + \boldsymbol{T}^{\mathrm{H}}\boldsymbol{C}_v^{-1}\boldsymbol{T})^{-1}\boldsymbol{T}^{\mathrm{H}}\boldsymbol{C}_v^{-1}\tilde{\boldsymbol{H}}, \tag{2.35}$$

where we omit the time-domain OFDM-block-spaced index n for the sake of notational simplicity and define $\boldsymbol{C}_{\alpha}$ and $\boldsymbol{C}_v$ as the covariance matrices of the FS-CIR vector $\boldsymbol{\alpha}$ and CTF-estimator noise vector $\boldsymbol{v}$, respectively. The elements of the noise vector $\boldsymbol{v}$ are assumed to be independent identically distributed (i.i.d.) complex-Gaussian-distributed samples and therefore we have $\boldsymbol{C}_v = \sigma_v^2\boldsymbol{I}$. On the other hand, as follows from Equation (1.1), the FS-CIR taps' covariance matrix is a diagonal matrix $\boldsymbol{C}_h = \operatorname{diag}\left(\sigma_l^2\right)$, where $\sigma_l^2 \triangleq \mathtt{E}\left\{|\alpha_l[n]|^2\right\}$. Substituting $\boldsymbol{C}_{\alpha}$ and $\boldsymbol{C}_v$ into (2.35) yields

$$\begin{aligned}\hat{\boldsymbol{\alpha}} &= \left(\operatorname{diag}\left(\frac{1}{\sigma_l^2}\right) + \frac{1}{\sigma_v^2}\boldsymbol{T}^{\mathrm{H}}\boldsymbol{T}\right)^{-1}\boldsymbol{T}^{\mathrm{H}}\frac{1}{\sigma_v^2}\tilde{\boldsymbol{H}} \\ &= \left(\sigma_v^2\boldsymbol{I} + \operatorname{diag}\left(\sigma_l^2\right)\boldsymbol{T}^{\mathrm{H}}\boldsymbol{T}\right)^{-1}\operatorname{diag}\left(\sigma_l^2\right)\boldsymbol{T}^{\mathrm{H}}\tilde{\boldsymbol{H}} = \boldsymbol{A}\tilde{\boldsymbol{H}}.\end{aligned} \tag{2.36}$$

The matrix inversion operation associated with the process of evaluating the estimator matrix $\boldsymbol{A}$ in Equation (2.36) cannot be avoided as opposed to the case of the SS-CIR estimation scheme of Section 2.5.2.

However, the estimator matrix $\boldsymbol{A}$ is data-independent and may be calculated only once for the case of encountering Wide Sense Stationary (WSS) channel statistics. In the case of non-WSS channels, where the average FS-CIR taps' magnitudes σ_l^2 and the corresponding relative delays τ_l are time variant, the estimator matrix $\boldsymbol{A}$ can be tracked using the low complexity Projection Approximation Subspace Tracking (PAST) techniques discussed for example in [117] and [130].

The corresponding covariance matrix associated with the FS-CIR estimate vector $\hat{\boldsymbol{\alpha}}$ can be expressed as in [101]

$$\boldsymbol{C}_\alpha = \sigma_v^2 \left(\sigma_v^2 \boldsymbol{I} + \mathrm{diag}\left(\sigma_l^2\right) \boldsymbol{T}^{\mathtt{H}} \boldsymbol{T}\right)^{-1} \mathrm{diag}\left(\sigma_l^2\right) \tag{2.37}$$

and the resultant Normalized Mean Square Error (NMSE) of the RC-MMSE FS-CIR estimator proposed is given by

$$NMSE_\alpha = \frac{\sigma_v^2}{\sigma_H^2}\, \mathtt{tr}\left(\left(\sigma_v^2 \boldsymbol{I} + \mathrm{diag}\left(\sigma_l^2\right) \boldsymbol{T}^{\mathtt{H}} \boldsymbol{T}\right)^{-1} \mathrm{diag}\left(\sigma_l^2\right)\right), \tag{2.38}$$

where $tr(\boldsymbol{A})$ is the *trace* of the matrix $\boldsymbol{A}$.

The performance criteria $NMSE_h$ and $NMSE_\alpha$ of Equations (2.32) and (2.38) respectively cannot be compared directly, since they refer to the estimation processes of different sets of parameters, namely the SS-CIR taps $h[n,k],\ k = 0,\ldots,K_0 - 1$ and the FS-CIR taps $\alpha_l[n],\ l = 1,\ldots L$. In order to perform a meaningful comparison of the methods considered we used the NMSE between the two CTFs corresponding to the encountered CIR and the estimated CIR, thus we have

$$NMSE_H \triangleq \mathtt{E}\left\{|H[n,k] - \hat{H}[n,k]|^2\right\}. \tag{2.39}$$

In the case of the SS-CIR estimator we have

$$\begin{aligned} NMSE_{H;SS} &= \frac{1}{\sigma_H^2}\mathtt{E}\left\{\mathtt{tr}\left((\boldsymbol{H} - \hat{\boldsymbol{H}})(\boldsymbol{H} - \hat{\boldsymbol{H}})^{\mathtt{H}}\right)\right\} \\ &= \frac{1}{K\sigma_H^2}\mathtt{tr}\left(\boldsymbol{W}\mathtt{E}\left\{(\boldsymbol{h} - \hat{\boldsymbol{h}})(\boldsymbol{h} - \hat{\boldsymbol{h}})^{\mathtt{H}}\right\}\boldsymbol{W}^{\mathtt{H}}\right) \\ &= NMSE_h, \end{aligned} \tag{2.40}$$

where the Discrete Fourier Transform (DFT) $\boldsymbol{W}$ of Equation (2.25) is a unitary matrix. On the other hand, for the case of the FS-CIR estimator we have

$$\begin{aligned} NMSE_{H;FS} &= \frac{1}{\sigma_H^2}\mathtt{E}\left\{\mathtt{tr}\left((\boldsymbol{H} - \hat{\boldsymbol{H}})(\boldsymbol{H} - \hat{\boldsymbol{H}})^{\mathtt{H}}\right)\right\} \\ &= \frac{1}{K\sigma_H^2}\mathtt{tr}\left(\boldsymbol{T}\mathtt{E}\left\{(\boldsymbol{\alpha} - \hat{\boldsymbol{\alpha}})(\boldsymbol{\alpha} - \hat{\boldsymbol{\alpha}})^{\mathtt{H}}\right\}\boldsymbol{T}^{\mathtt{H}}\right) \\ &= \frac{\sigma_v^2}{K\sigma_H^2}\,\mathtt{tr}\left(\boldsymbol{T}\boldsymbol{C}_\alpha\boldsymbol{T}^{\mathtt{H}}\right), \end{aligned} \tag{2.41}$$

where $\boldsymbol{C}_\alpha$ is the covariance matrix of the FS-CIR taps' estimates described by Equation (2.37).

The $NMSE_H$ performances of both the SS-CIR and the FS-CIR RC-MMSE estimators discussed in Sections 2.5.2 and 2.5.4 and described by Equations (2.40) and (2.41) respectively are depicted in Figure

2.4. As is suggested by Figure 2.4, the NMSE performance exhibited by the SS-CIR estimator of Section 2.5.2 is highly sensitive to the particular delay profile $\boldsymbol{\tau}$ as well as to the RMS delay spread τ_{rms}. More specifically, the NMSE becomes better when the channel estimator encounters near sample-spaced delays τ_l, which results in a minimum leakage of the FS-CIR taps' power into the neighbouring SS-CIR taps. On the other hand, the NMSE exhibited by the SS-CIR estimator deteriorates when the delays τ_l depart from sample-spaced values and thus the leakage of the FS-CIR taps' power is maximised. As expected, the FS-CIR estimator exhibits a lower NMSE over the whole range of the delay spread RMS values τ_{rms}, which demonstrates its robustness in severe channel conditions exhibiting time-variant delay spread.

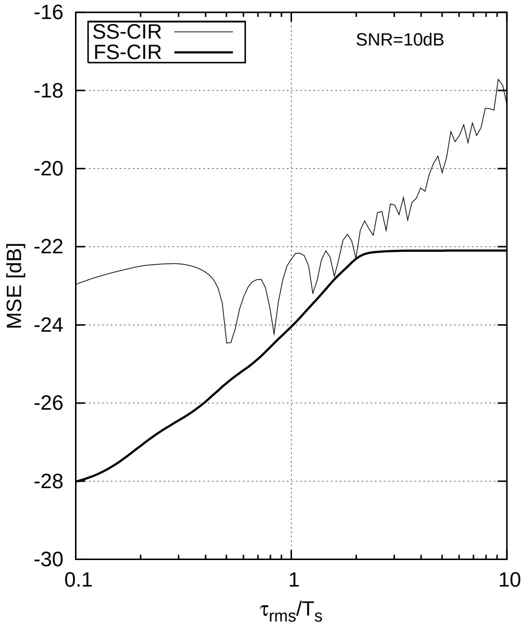

Figure 2.4: Mean Square Error exhibited by an *a posteriori* SS- and FS-CIR-based CTF estimators as a function of the channel's sample-rate-normalized RMS delay value τ_{rms}/T_s. The channel encountered corresponds to the eight-path Rayleigh-fading Bug's channel model characterized in [118] having a Gaussian noise variance of 10 dB. The results were avaluated from Equations (2.40) and (2.41).

2.5.5 Performance Analysis

In this section, we present our simulation results for both the OFDM and the MC-CDMA systems employing the channel estimation schemes considered.

Our simulations were performed in the base-band frequency domain and the system configuration characterised in Table 2.1 is to a large extent similar to that used in [38]. We assume having a total bandwidth of 800kHz. In the OFDM mode, the system utilises 128 QPSK-modulated orthogonal subcarriers. In the MC-CDMA mode we employ eight concatenated of 16-chip Walsh-Hadamard (WH) codes for frequency-domain interleaved spreading of the QPSK-modulated bits over the $8 \cdot 16 = 128$ orthogonal subcarriers. All the 128 WH spreading codes, each constituted by 8 interleaved groups of 16 codes, are assigned to a

Table 2.1: System parameters.

Parameter	OFDM	MC-CDMA
Channel bandwidth	800 kHz	
Number of carriers K	128	
Symbol duration T	160 μs	
Max. delay spread τ_{max}	40 μs	
Channel interleaver	WCDMA [131] 248 bit	–
Modulation	QPSK	
Spreading scheme	–	WH
FEC	Turbo code [26] , rate 1/2	
component codes	RSC, K=3(7,5)	
code interleaver	WCDMA (124 bit)	

single user and hence the effective data-rate is similar in both the OFDM and the MC-CDMA modes. For forward error correction (FEC) we use $\frac{1}{2}$-rate turbo coding [26] employing two constraint-length $K = 3$ Recursive Systematic Convolutional (RSC) component codes and the standard 124-bit WCDMA UMTS code interleaver of [131]. The octally represented RCS generator polynomials of (7,5) were used.

Firstly, we would like to demonstrate the achievable performance of the system considered under the assumption of perfect channel knowledge, where the knowledge of the frequency-domain subcarrier-related coefficients $H[n,k]$ is available in the receiver. Figure 2.5 characterizes both (a) the uncoded and (b) the Turbo-coded Bit Error Rate (BER) exhibited by the QPSK-modulated OFDM and MC-CDMA systems in conjunction with the three different channel models discussed in Section 1.7.1, namely, the SWATM channel [28], the COST-207 BU channel [119] and Bug's channel characterized in [118]. As expected, in the uncoded OFDM scenario the achievable BER is similar to the BER associated with a flat Rayleigh-fading channel, regardless of the actual channel model encountered. This can be explained by the fact that the uncoded OFDM system effectively experiences flat Rayleigh fading on each frequency-domain subcarrier. In an uncoded OFDM system the adjacent information-carrying symbols are demodulated independently and thus the associated system's BER performance is dominated by the error rates associated with the severely faded subcarriers. In other words, such a system is incapable of exploiting the potential frequency-domain diversity gains available in the dispersive channel, as discussed in Section 1.8.2. By contrast, the uncoded MC-CDMA system avoids this phenomenon with the aid of frequency-domain spreading of the information-carrying symbols. Furthermore, different channel models characterized by different PDPs result

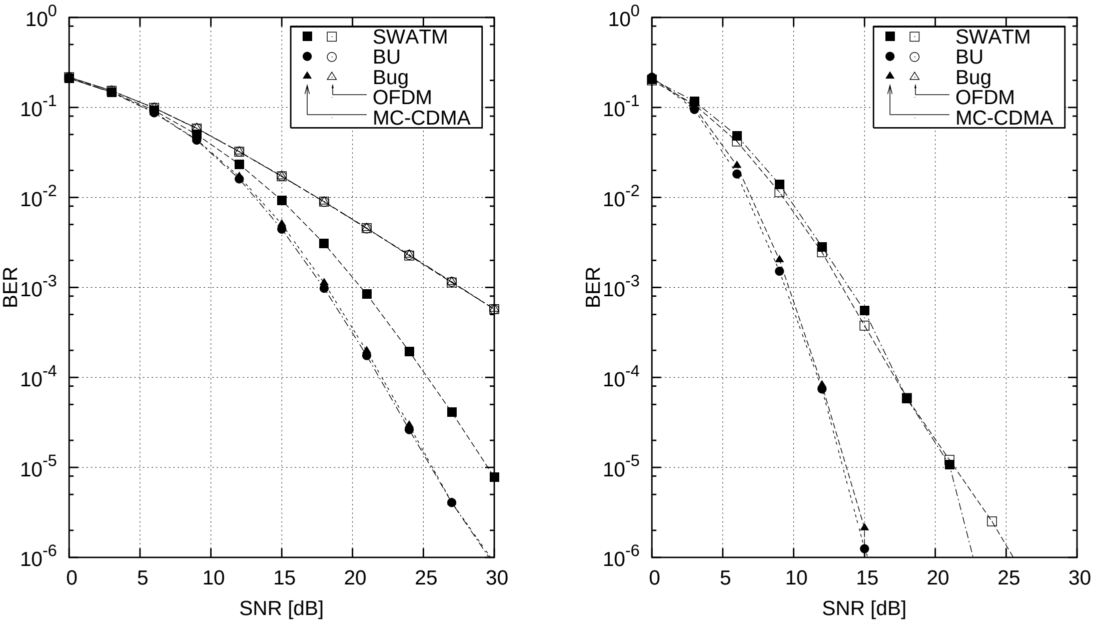

(a) (b)

Figure 2.5: Bit Error Rate (BER) exhibited by the (a) **uncoded** and (b) **Turbo-coded** QPSK-modulated OFDM and MC-CDMA systems under channel conditions described by SWATM, COST-207 Bad-Urban (BU) and Bug channel models.

in different potential frequency-domain diversity gains. As illustrated in Figure 1.6, the SWATM channel model is characterized by a CIR having three taps, where most of the signal power is accommodated by the first tap, hence it behaves similar to a non-dispersive channel and results in a relatively low potential frequency diversity gain, as confirmed by the results depicted in Figure 2.5. By contrast, both the COST-207 BU and Bug's channel models, have 7- and 8-tap CIRs respectively and hence allow for the MC-CDMA system to benefit from a relatively high frequency diversity gain. Similar conclusions can be inferred from Figure 2.5(b), where both the OFDM and MC-CDMA systems benefit from the available frequency diversity gain with the aid of turbo-coding. It can be seen in Figure 2.5(b) that the MC-CDMA system slightly outperforms its OFDM counterpart as a result of averaging the error effects with the aid frequency-domain spreading of the information-carrying symbols.

2.5.5.1 Reduced Complexity MMSE SS-CIR Estimator Performance

Here we employed the eight-path Rayleigh-fading Bug channel model characterised in [118], using the delay spread of $\tau_{rms} = 1\mu$s and the OFDM-symbol-normalized Doppler frequency of $f_D = 0.01$.

Figure 2.6(a) characterizes the Normalized Mean Square Error (NMSE) exhibited by the DDCE scheme of Figure 2.1 using both the full-complexity MMSE SS-CIR estimator and the Reduced Complexity MMSE SS-CIR estimator of Sections 2.5.1 and 2.5.2, respectively. Furthermore, the achievable turbo-coded BER of the corresponding QPSK-modulated OFDM and MC-CDMA systems is depicted in Figure 2.6(b). The

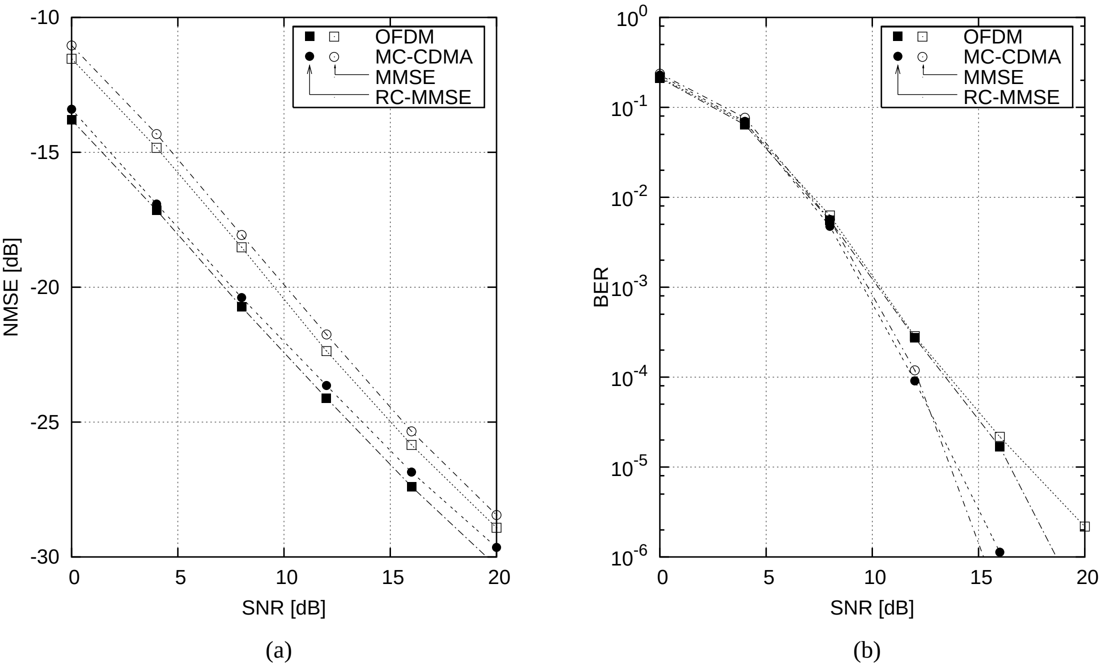

(a) (b)

Figure 2.6: (a) **Normalised Mean Square Error (NMSE)** and (b) **Bit Error Rate (BER)** exhibited by the channel estimator which follows the philosophy of Figure 2.1 and employs the Minimum Mean Square Error (MMSE) and the Reduced-Complexity MMSE *a posteriori* SS-CIR estimators of Equations (2.19) and (2.27), respectively. The *a priori* prediction is performed using the robust SS-CIR predictor [28] assuming matching propagation conditions described by the COST-207 BU channel model having a normalised Doppler frequency of $f_D = 0.01$. The turbo-coded QPSK-modulated OFDM and MC-CDMA modes are identified using the □ and ○ markers, respectively.

simulations were carried out over the period of 100,000 QPSK-modulated $K = 128$-subcarrier OFDM/MC-CDMA symbols. It can be seen in Figure 2.6(a), that the RC-MMSE method outperforms its MMSE counterpart in the context of both the OFDM and MC-CDMA systems considered. This result can be explained by the fact that in our RC-MMSE CIR estimator we employ the MRC-aided MMSE CTF estimator of Equation (2.15), which takes advantage of the available *a priori* predicted CTF estimates $\check{H}[n,k]$ and enhances the performance of the RC-MMSE CIR estimator in comparison to the pure *a posteriori* full-complexity MMSE CIR estimator of Section 2.5.1. Moreover, as it becomes evident from Figure 2.6(b), the MMSE/RC-MMSE SS-CIR operating in the context of the MC-CDMA system outperforms its OFDM counterpart.

2.5.5.2 Fractionally-Spaced CIR Estimator Performance

In this section we consider the achievable performance of our DDCE scheme employing both the Sample-Spaced CIR RC-MMSE estimator of Section 2.5.2 and the Fractionally-Spaced RC-MMSE CIR estimator advocated in Section 2.5.4 in the context of both OFDM and MC-CDMA systems communicating over Bug's eight-path dispersive Rayleigh fading channel characterized in [118]. Here we employ a fractionally-

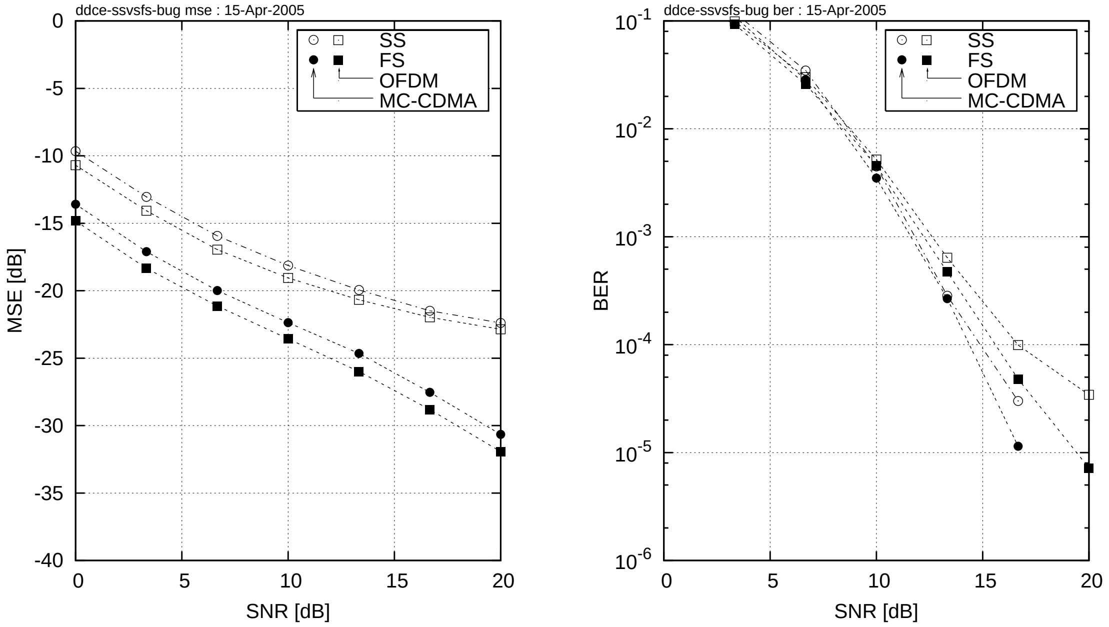

(a)

(b)

Figure 2.7: (a) **MSE** exhibited by the decision-directed channel estimator of Section 2.3 in the context of QPSK-modulated OFDM and MC-CDMA systems and (b) the corresponding achievable **BER** performance. Both performance curves are shown as a function of the average SNR at the receiver antenna. The *frame-variant* fading channel characterized by Bug's channel model [118] was associated with the OFDM symbol-normalized Doppler frequency of $f_D = 0.01$.

spaced CIR as opposed to the sample-spaced CIR considered in Section 2.5.5.1.

Figure 2.7(a) portrays the NMSE exhibited by the DDCE scheme of Figure 2.1 employing both the SS-CIR estimator described in Section 2.5.2 and that of the FS-CIR estimator derived in Section 2.5.4 in the context of both the OFDM and the MC-CDMA systems considered. The corresponding achievable BER performance is depicted in Figure 2.7(b). The simulations were carried out over the period of 100,000 QPSK-modulated $K = 128$-subcarrier OFDM/MC-CDMA symbols. Comparing the results of Figures 2.6 and 2.7 we may conclude that the DDCE employing the *a posteriori* SS-CIR RC-MMSE method suffers from a substantial performance degradation when assessed in conjunction with the channel characterized by a FS-CIR. Furthermore, the DDCE scheme utilising the SS-CIR estimator for communicating over a channel characterized by a FS-CIR exhibits an irreducible noise-floor at high SNR values. In order to explain this result we would like to refer to the *leakage* effect discussed in Section 1.7.1 and illustrated in Figure 1.8. Let us recall that a channel characterized by a FS-PDP results in numerous correlated non-zero SS-CIR taps. As a result, the *a priori* CIR predictor of Section 2.7 designed to track and predict a relatively low number of non-zero uncorrelated CIR taps fails to exploit the leakage-intuced correlation observed between the adjucent SS-CIR taps. Furthermore, the correlation of the SS-CIR taps becomes different from the time-domain correlation model assumed during the predictor design and described in Section 1.7.1,

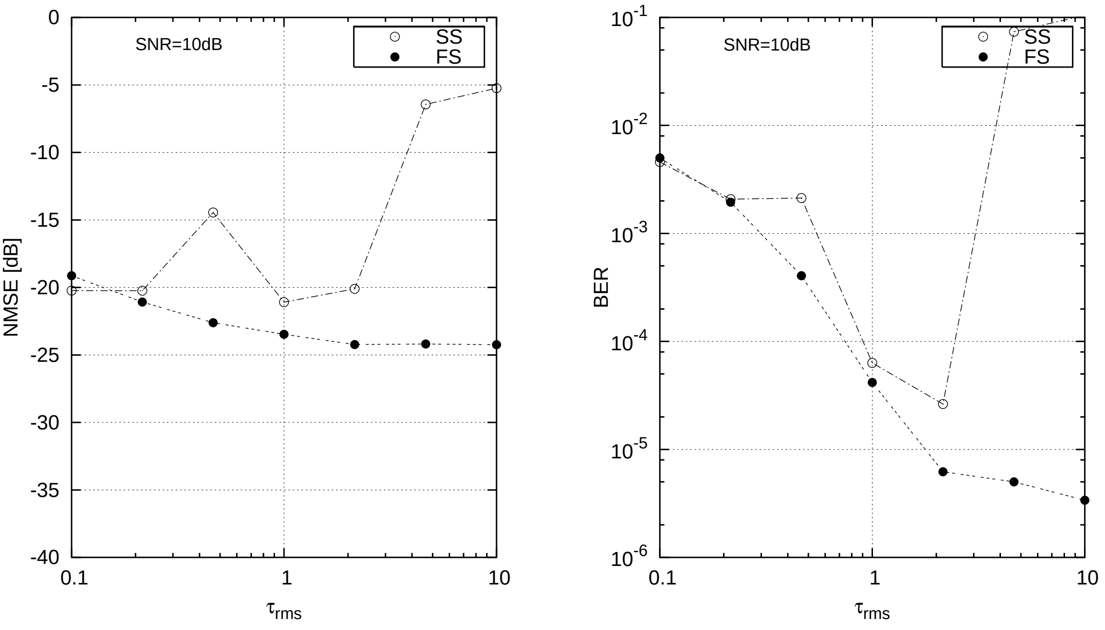

(a) (b)

Figure 2.8: (a) **NMSE** exhibited by the decision-directed channel estimator of Section 2.3 as a function of the sample-period-normalized RMS delay spread $\tau_{\rm rms}$ and (b) the corresponding achievable **BER** performance of the MC-CDMA system employing the aforementioned channel estimation scheme. Both curves correspond to Bug's channel model associated with the OFDM-symbol-normalized Doppler frequency of 0.01 and the average SNR of 10 dB recorded at the receive antenna.

which results in a biased channel estimation process. On the other hand, as can be seen in Figure 2.7, the DDCE employing the *a posteriori* FS-CIR RC-MMSE method of Section 2.5.2 does not experience any performance degradation and outperforms its SS-CIR estimator-based counterpart over the entire range of the SNR values considered. In addition, the achievable NMSE of the DDCE employed in an OFDM system is slightly lower than that exhibited by its MC-CDMA counterpart. This effect is caused by the energy distribution of the subcarrier-related samples $x[n,k]$ used in the channel estimation process. This effect was discussed in Section 2.5 and is illustrated in Figure 2.3.

This conclusion is further substantiated by Figure 2.8, where both the NMSE performance of the channel estimator schemes considered and the corresponding achievable BER performance of the MC-CDMA system are plotted as a function of the channel's Root Mean Square (RMS) delay spread value $\tau_{\rm rms}$. It can be seen in Figure 2.8(a) that the NMSE performance of the SS-CIR estimator-based DDCE scheme exhibits substantial sensitivity to the channel's delay spread, which is also confirmed by the theoretical results depicted in Figure 2.4. This effect can be explained by the fact that the SS-CIR estimator estimates the projections of the actual FS-CIR taps encountered onto the adjacent SS-CIR taps. As can be seen in Figure 2.4, the accuracy of this process is highly sensitive to the delays and the amplitudes of the actual FS-CIR taps encountered. Furthermore, as the channel's RMS delay spread increases the number of effective non-zero

SS-CIR taps increases and hence the associated estimation accuracy degrades. On the other hand, the *a posteriori* FS-CIR estimator exhibits a higher robustness against the channel's delay spread variations, since the channel estimator tends to estimate only the actual FS-CIR taps encountered regardless of the specific values of the RMS delay spread. Additionally, as expected, the corresponding BER of the MC-CDMA system increases upon increasing the RMS delay spread τ_{rms}, because the frequency-diversity rank tends to increase, when τ_{rms} increases.

2.6 Parametric FS-CIR Estimation

2.6.1 Projection Approximation Subspace Tracking

Let $\boldsymbol{H}[n] \in \mathbb{C}^K$ be the vector of the subcarrier-related CTF coefficients associated with the channel model of Equation (1.14). As described in Section 1.7.1, the CIR associated with the CTF coefficient vector $\boldsymbol{H}[n]$ is constituted by a relatively low number of $L \ll K$ statistically-independent Rayleigh fading paths. The corresponding CIR components are related to the CTF coefficients $H[n,k]$ by means of Equation (1.7). The motivation for employing the so-called subspace technique [132] here is that usually we have $L \ll K$ and thus it is more efficient to estimate a low number of CIR-related taps in the low-dimensional signal subspace than estimating all the K FD-CTF coefficients.

Let λ_l and $\boldsymbol{u}_l$ be the eigenvalues and the corresponding eigenvectors of the CTF's covariance matrix $\boldsymbol{C}_H$, which is defined as follows

$$\boldsymbol{C}_H = \underset{n}{E}\left\{\boldsymbol{H}[n]\boldsymbol{H}^{\mathrm{H}}[n]\right\}. \tag{2.42}$$

Then, we have $\boldsymbol{C}_H = \boldsymbol{U}\boldsymbol{\Sigma}\boldsymbol{U}^{\mathrm{H}}$, where $\boldsymbol{\Sigma} = \operatorname{diag}(\lambda_l)$ and $\boldsymbol{U} = [\boldsymbol{u}_1 \cdots \boldsymbol{u}_K]$.

The eigenvalues aligned in a descending order may be expressed as

$$\lambda_1 \geq \cdots \geq \lambda_L > \lambda_{L+1} = \cdots = \lambda_K = \sigma_w^2, \tag{2.43}$$

where the first L dominant eigenvalues $\lambda_1, \cdots, \lambda_L$ in conjunction with the L corresponding eigenvectors $\boldsymbol{u}_1, \cdots, \boldsymbol{u}_L$ may be termed as the *signal* eigenvalues and eigenvectors, respectively [117]. The remaining eigenvalues $\lambda_{L+1}, \cdots, \lambda_K$ and eigenvectors $\boldsymbol{u}_{L+1}, \cdots, \boldsymbol{u}_K$ are termed the *noise* eigenvalues and eigenvectors. The resultant sets of *signal* and *noise* eigenvectors, which are column vectors, span the mutually orthogonal *signal* and *noise* subspaces U_S and U_N, such that we have

$$\boldsymbol{U}_S = [\boldsymbol{u}_1, \cdots, \boldsymbol{u}_L] \quad \text{and} \quad \boldsymbol{U}_N = [\boldsymbol{u}_{L+1}, \cdots, \boldsymbol{u}_K]. \tag{2.44}$$

The corresponding time-domain-related L-tap estimate of the FS-CIR vector $\boldsymbol{\alpha}[n]$ may be obtained as follows

$$\hat{\boldsymbol{\alpha}} = \boldsymbol{U}_S^{\mathtt{H}}[n]\tilde{\boldsymbol{H}}[n]. \tag{2.45}$$

Furthermore, the reduced-noise estimate of the CTF vector $\boldsymbol{H}[n]$ may reconstructed using

$$\hat{\boldsymbol{H}}[n] = \boldsymbol{U}_S[n]\hat{\boldsymbol{\alpha}}[n]. \tag{2.46}$$

For the sake of evaluating and tracking the potentially time-variant signal subspace $\boldsymbol{U}_S[n]$ we employ subspace tracking method developed by Yang [117]. More specifically, we consider the following real-valued scalar objective function having the matrix argument of $\boldsymbol{W} \in \mathbb{C}^{K \times L}$

$$\begin{aligned} J(\boldsymbol{W}) &= \mathtt{E}\left\{\|\boldsymbol{H} - \boldsymbol{W}\boldsymbol{W}^{\mathtt{H}}\boldsymbol{H}\|^2\right\} \\ &= \mathtt{tr}\left(\boldsymbol{C}_H\right) - 2\,\mathtt{tr}\left(\boldsymbol{W}^{\mathtt{H}}\boldsymbol{C}_H\boldsymbol{W}\right) + \mathtt{tr}\left(\boldsymbol{W}^{\mathtt{H}}C_H\boldsymbol{W}\cdot\boldsymbol{W}^{\mathtt{H}}\boldsymbol{W}\right) \end{aligned} \tag{2.47}$$

As demonstrated by Yang in [117], the objective function $J(\boldsymbol{W})$ of Equation (2.47) exhibits the following important properties

1. $\boldsymbol{W}$ is a stationary point of $J(\boldsymbol{W})$ if and only if we have $\boldsymbol{W} = \boldsymbol{U}_L\boldsymbol{Q}$, where $\boldsymbol{U}_L \in \mathbb{C}^{K \times L}$ contains any L distinct eigenvectors of $\boldsymbol{C}_H$ and $\boldsymbol{Q} \in \mathbb{C}^{L \times L}$ is an arbitrary unitary matrix. Furthermore, at each stationary point, $J(\boldsymbol{W})$ equals the sum of these particular eigenvalues, whose eigenvectors are not involved in $\boldsymbol{U}_L$ [117, Theorem 1].

2. All stationary points of $J(\boldsymbol{W})$ are local saddle points except, when $\boldsymbol{U}_L$ contains the L dominant eigenvectors of $\boldsymbol{C}_H$. In this case, $J(\boldsymbol{W})$ attains the global minimum [117, Theorem 2].

3. The global convergence of $\boldsymbol{W}$ is guaranteed by using iterative minimization of $J(\boldsymbol{W})$ and the columns of the resultant value of $\boldsymbol{W}$ will span the signal subspace of $\boldsymbol{C}_H$.

4. The use of an iterative algorithm to minimize $J(\boldsymbol{W})$ will always converge to an orthonormal basis of the signal subspace of $\boldsymbol{C}_H$ without invoking any orthonormalization operations during the iterations.

5. The global minimum of $J(\boldsymbol{W})$, $\boldsymbol{W}$ does not necessarily contain the signal eigenvectors, but an arbitrary orthogonal basis of the signal subspace of $\boldsymbol{C}_H$ as indicated by the unitary matrix $\boldsymbol{Q}$ introduced in Property 1. In other words, we have $\boldsymbol{W} = \operatorname{argmin} J(\boldsymbol{W})$ if and only if $\boldsymbol{W} = \boldsymbol{U}_S\boldsymbol{Q}$, where $\boldsymbol{Q}$ is an arbitrary unitary matrix.

6. For the simple scalar case of $L = 1$, the solution minimizing $J(\boldsymbol{W})$ is given by the most dominant normalized eigenvector of $\boldsymbol{C}_H$.

Subsequently, Yang [117] proposes an iterative RLS algorithm for tracking of the signal subspace of the channel's covariance matrix $\boldsymbol{C}_H$. Specifically, upon replacing the expectation value in Equation (2.47) by the exponentially weighted sum of the RLS algorithm, we arrive at the following new objective function

$$\begin{aligned} J(\boldsymbol{W}[n]) &= \sum_{i=1}^{n} \eta^{n-i} \|\boldsymbol{H}[i] - \boldsymbol{W}[n]\boldsymbol{W}^{\mathrm{H}}[n]\boldsymbol{H}[i]\|^2 \\ &= \mathtt{tr}\left(\boldsymbol{C}_H\right) - 2\,\mathtt{tr}\left(\boldsymbol{W}^{\mathrm{H}}[n]\boldsymbol{C}_H[n]\boldsymbol{W}[n]\right) \\ &\quad + \mathtt{tr}\left(\boldsymbol{W}^{\mathrm{H}}[n]\boldsymbol{C}_H[n]\boldsymbol{W}[n] \cdot \boldsymbol{W}^{\mathrm{H}}[n]\boldsymbol{W}[n]\right), \end{aligned} \tag{2.48}$$

where $\eta \in (0, 1)$ is the so-called *forgetting factor*, which accounts for possible deviations of the actual channel statistics encountered from the WSS assumption. Observe that the sole difference between the objective functions of Equations (2.47) and (2.48) is the introduction of the time-variant exponentially weighted sample covariance matrix [117], which may be expressed as

$$\boldsymbol{C}_H[n] = \sum_{m=1}^{n} \eta^{n-m} \boldsymbol{H}[m]\boldsymbol{H}^{\mathrm{H}}[m] = \eta \boldsymbol{C}_H[n-1] + \boldsymbol{H}[n]\boldsymbol{H}^{\mathrm{H}}[n] \tag{2.49}$$

instead of the time-invariant matrix $\boldsymbol{C}_H = \mathtt{E}\left\{\boldsymbol{H}\boldsymbol{H}^{\mathrm{H}}\right\}$ of Equation (2.42).

The Projection Approximation Subspace Tracking (PAST) algorithm may be derived by approximating the expression $\boldsymbol{W}^{\mathrm{H}}[n]\boldsymbol{H}[m]$ in Equation (2.48), which may be interpreted as a projection of the vector $\boldsymbol{H}[m]$ onto the column space of the matrix $\boldsymbol{W}[n]$, by the readily available *a posteriori* vector $\boldsymbol{\alpha}[m] = \boldsymbol{W}^{\mathrm{H}}[m]\boldsymbol{H}[m]$. The resultant modified cost function may be formulated as

$$J'(\boldsymbol{W}[n]) = \sum_{m=1}^{n} \eta^{n-m} \|\boldsymbol{H}[m] - \boldsymbol{W}[n]\boldsymbol{\alpha}[m]\|^2. \tag{2.50}$$

As is argued in [117], for stationary or slowly varying signals, the aforementioned projection approximation, hence the name PAST, does not substantially change the error surface associated with the corresponding cost function of Equation (2.50) and therefore does not significantly affect the convergence properties of the derived algorithm.

Similarly to other RLS estimation schemes [64, 101], the cost function $J'(\boldsymbol{W}[n])$ is minimized if

$$\boldsymbol{W} = \boldsymbol{C}_{H\alpha}[n]\boldsymbol{C}_{\alpha\alpha}^{-1}[n], \tag{2.51}$$

where we have

$$\boldsymbol{C}_{H\alpha}[n] = \sum_{i=1}^{n} \eta^{n-i} \boldsymbol{H}[i]\boldsymbol{\alpha}^{\mathrm{H}}[i] = \eta \boldsymbol{C}_{H\alpha}[n-1] + \boldsymbol{H}[n]\boldsymbol{\alpha}^{\mathrm{H}}[n] \tag{2.52}$$

and

$$\boldsymbol{C}_{\alpha\alpha}[n] = \sum_{i=1}^{n} \eta^{n-i} \boldsymbol{\alpha}[i]\boldsymbol{\alpha}^{\mathrm{H}}[i] = \eta \boldsymbol{C}_{\alpha\alpha}[n-1] + \boldsymbol{\alpha}[n]\boldsymbol{\alpha}^{\mathrm{H}}[n]. \tag{2.53}$$

Algorithm 1 Projection Approximation Subspace Tracking

$$\hat{\boldsymbol{\alpha}}[n] = \boldsymbol{W}^{\mathtt{H}}[n-1]\hat{\boldsymbol{H}}[n] \tag{2.58a}$$

$$\boldsymbol{g}[n] = \boldsymbol{P}[n-1]\hat{\boldsymbol{\alpha}}[n] \tag{2.58b}$$

$$\boldsymbol{k}[n] = \frac{\boldsymbol{g}[n]}{\eta + \hat{\boldsymbol{\alpha}}^{\mathtt{H}}[n]\boldsymbol{g}[n]} \tag{2.58c}$$

$$\boldsymbol{P}[n] = \frac{1}{\eta}\texttt{Tri}\left\{\boldsymbol{P}[n-1] - \boldsymbol{k}[n]\boldsymbol{g}^{\mathtt{H}}[n]\right\} \tag{2.58d}$$

$$\boldsymbol{e}[n] = \hat{\boldsymbol{H}}[n] - \boldsymbol{W}[n-1]\hat{\boldsymbol{\alpha}}[n-1] \tag{2.58e}$$

$$\boldsymbol{W}[n] = \boldsymbol{W}[n-1] + \boldsymbol{e}[n]\boldsymbol{k}^{\mathtt{H}}[n] \tag{2.58f}$$

Following the RLS approach [117], a low-complexity solution of the computational problem associated with minimizing the cost function $J'(\boldsymbol{W}[n])$ of Equation (2.50) may be obtained using recursive updates of the matrix $\boldsymbol{W}[n]$. More specifically, we have

$$\boldsymbol{W}[n] = \boldsymbol{W}[n-1] + \boldsymbol{e}[n]\boldsymbol{k}^{\mathtt{H}}[n], \tag{2.54}$$

where $\boldsymbol{e}[n]$ is the estimation error vector, which may be recursively obtained as

$$\boldsymbol{e}[n] = \boldsymbol{H}[n] - \boldsymbol{W}[n-1]\boldsymbol{\alpha}[n-1], \tag{2.55}$$

while

$$\boldsymbol{k}[n] = \frac{\boldsymbol{P}[n-1]\boldsymbol{\alpha}[n]}{\eta + \boldsymbol{\alpha}^{\mathtt{H}}[n]\boldsymbol{P}[n-1]\boldsymbol{\alpha}[n]} \tag{2.56}$$

denotes the RLS gain vector. Furthermore, the matrix $\boldsymbol{P}[n]$ is the inverse of the CIR-related taps' $(L \times L)$-dimensional covariance matrix $\boldsymbol{C}_{\alpha\alpha}$, which can be recursively calculated as follows

$$\boldsymbol{P}[n] = \frac{1}{\eta}\texttt{Tri}\{(\boldsymbol{I} - \boldsymbol{k}[n]\boldsymbol{\alpha}^{\mathtt{H}}[n])\boldsymbol{P}[n-1]\}, \tag{2.57}$$

where the operator $\texttt{Tri}\{\cdot\}$ indicates that only the upper triangular part of $P[n]$ is calculated and its Hermitian conjugate version is copied to the lower triangular part [117]. The resultant PAST algorithm is summarized in Algorithm 1, where we introduced an additional quantity $\boldsymbol{g}[n] = \boldsymbol{P}[n-1]\boldsymbol{H}[n]$ for the sake of further reducing the associated complexity.

2.6.2 Deflation PAST

In this work, however, we aim for maintaining the lowest possible complexity hence we are particularly interested in the *deflation*-based version of the PAST algorithm derived in [117], which is referred to as the PASTD algorithm. The simple philosophy of the *deflation* method is the sequential estimation of the

Algorithm 2 Deflation PAST

```
$\boldsymbol{H}_1[n] = \boldsymbol{H}[n]$                                                  (2.60a)
for $l = 1, 2, \ldots, L$ do
    $\alpha_l[n] = \boldsymbol{w}_l^{\mathtt{H}}[n-1]\boldsymbol{H}_l[n]$                          (2.60b)
    $\lambda_l[n] = \beta\lambda_l[n-1] + |\alpha_l[n]|^2$                             (2.60c)
    $\boldsymbol{e}_l[n] = \boldsymbol{H}_l[n] - \boldsymbol{w}_l[n-1]\alpha_l[n]$                           (2.60d)
    $\boldsymbol{w}_l[n] = \boldsymbol{w}_l[n-1] + \boldsymbol{e}_l[n](\alpha_l^*[n]/\lambda_l[n])$                (2.60e)
    $\boldsymbol{H}_{l+1}[n] = \boldsymbol{H}_l[n] - \boldsymbol{w}_l[n]\alpha_l[n]$                         (2.60f)
end for
```

principal components of the CTF covariance matrix $\boldsymbol{C}_H$ [133]. Consequently, we first update the most dominant eigenvector $\boldsymbol{w}_1[n]$ by applying the PAST method of Algorithm 1 in conjunction with $L = 1$. Subsequently, the projection of the current sample vector $\boldsymbol{H}[n]$ onto the updated eigenvector $\boldsymbol{w}_1[n]$ is subtracted from itself, resulting in a modified (deflated) version of the CTF vector in the following form $\boldsymbol{H}_2[n] = \boldsymbol{H}[n] - \boldsymbol{w}_1[n]\boldsymbol{w}_1^{\mathtt{H}}[n]\boldsymbol{H}[n]$. The second most dominant eigenvector $\boldsymbol{w}_2[n]$ has now become the most dominant one and therefore may be updated similarly to $\boldsymbol{w}_1[n]$. By repeatedly applying this procedure, all the desired eigencomponents may be estimated.

The resultant PASTD method is summarized in Algorithm 2. Observe that Equations (2.60b-f) of Algorithm 2 constitute the PAST estimation procedure of Algorithm 1 in conjunction with $L = 1$. Note that the vector expressions of Equations (2.58b-d) in Algorithm 1 are substituted by the simple scalar expression of Equation (2.60c), where the new quantity $\lambda_l[n]$ constitutes an exponentially weighted estimate of the corresponding lth eigenvalue and can be identified as a scalar version of the $(L \times L)$-dimensional covariance matrix $\boldsymbol{C}_{\alpha\alpha}[n] = \boldsymbol{P}^{-1}[n]$ of Algorithm 1.

A particularly important property of the PASTD method of Algorithm 2 is that as opposed to the PAST method of Algorithm 1, it enables the explicit tracking of the time-variant eigencomponents of the channel covariance matrix $\boldsymbol{C}_H[n]$, namely the eigenvectors $\boldsymbol{w}_l[n]$ as well as of the corresponding eigenvalues $\lambda_l[n]$ according to

$$\boldsymbol{w}_l[n] = \boldsymbol{w}_l[n-1] + \frac{\alpha_l^*[n]}{\lambda_l[n]}(\boldsymbol{H}_l[n] - \boldsymbol{w}_l[n-1]\alpha_l[n]), \tag{2.59}$$

where we have $\boldsymbol{\alpha}_l[n] = \boldsymbol{w}_l^{\mathtt{H}}[n-1]\boldsymbol{H}[n]$ and $\lambda_l[n] = \beta\lambda_l[n-1] + |\alpha_l[n]|^2$.

2.6.3 PASTD -Aided FS-CIR Estimation

In this section we would like to utilize the PASTD method detailed in Section 2.6.2 in the context of the channel estimation scheme characterized by Figure 2.1. More specifically, we consider a PASTD -aided *a* *posteriori* FS-CIR estimator, which corresponds to the CIR Estimator module of Figure 2.1. In order to analyze the achievable performance of the CIR estimator derived, we conceive a channel estimation scheme comprising the MMSE CTF estimator of Section 2.4.2 followed by the PASTD aided CIR Estimator of Section 2.6.2.

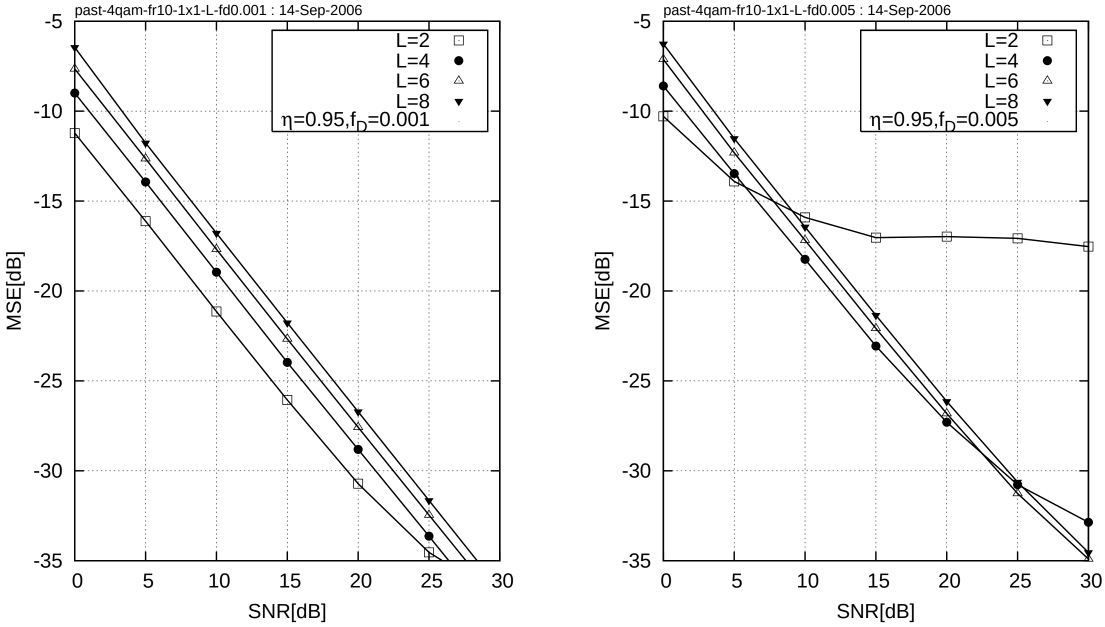

(a) (b)

Figure 2.9: The **Mean Square Error** exhibited by the **4QAM-OFDM** system employing the **PASTD** CIR estimator of Algorithm 2 and tracking $L = 2, 4, 6$ and 8 CIR taps. The value of the PASTD forgetting factor was $\eta = 0.95$. We considered the scenarios of encountering the Doppler frequencies of (a) $f_D = 0.001$ and (b) $f_D = 0.005$. The abscissa represents the average SNR recorded at the receive antenna elements. We employ COST-207 BU channel model [119]. Additional system parameters are summarized in Table 1.4.

The achievable performance of the subspace tracking method of Section 2.6.2 is characterized in Figures 2.9, 2.10 and 2.11, where we define the Mean Square Error (MSE) performance criterion as follows

$$MSE = \mathrm{E}\left\{\sum_{l} |e_l[n]|^2\right\}, \tag{2.61}$$

where e_l is the FD-CTF tracking error defined by Equation 2.55. In our simulations we consider an OFDM system having $K = 128$ orthogonal QPSK-modulated subcarriers. The system characteristics are outlined in Table 1.4. We employ an OFDM-frame-variant channel model having a time-variant 8-tap PDP characterized by the COST-207 BU channel model [119], as detailed in Section 1.7.2. Additionally, each individual propagation path undergoes fast Rayleigh fading with a corresponding OFDM-symbol-normalized Doppler frequency of either $f_D = 0.001$ or $f_D = 0.005$. The resultant channel can be characterised as a mutli-path Rayleigh-fading channel with slowly-varying PDP, where the relative delays τ_l associated with different PDP taps vary with time at a rate determined by the drift rate parameter ν_τ defined in Section 1.7.2.

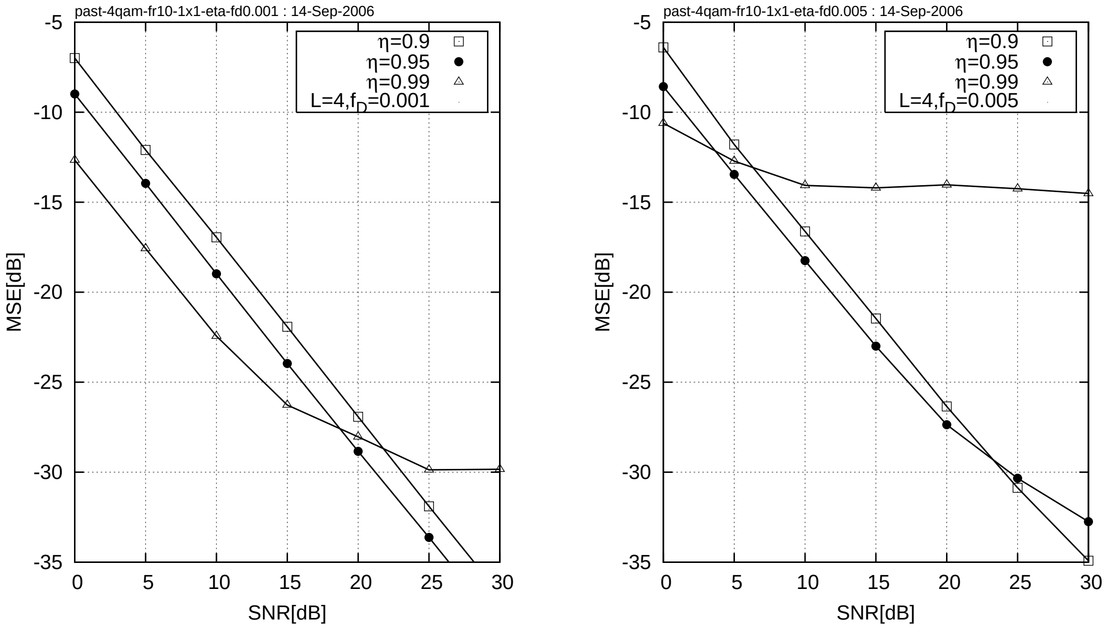

(a) (b)

Figure 2.10: The **Mean Square Error** exhibited by the **4QAM-OFDM** system employing the **PASTD** method of Algorithm 2. The values of the PASTD forgetting factor wwere $\eta = 0.9, 0.95$ and 0.9. We considered the scenarios of encountering the Doppler frequencies of (a) $f_D = 0.001$ and (b) $f_D = 0.005$. The abscissa represents the average SNR recorded at the receive antenna elements. We employ COST-207 BU channel model [119]. Additional system parameters are summarized in Table 1.4.

Firstly, Figure 2.9 characterizes the achievable FD-CTF MSE performance of the PASTD method of Algorithm 2 for different ranks L of the estimated subspace, while assuming a constant value of $\eta = 0.95$ for the forgetting factor. Figures 2.9(a) and 2.9(b) correspond to encountering the Doppler frequencies of $f_D = 0.001$ and 0.005, respectively. From Figure 2.9, we may conclude that a high CIR estimator performance may be achieved when assuming that the estimated CTF signal subspace has a rank of $L = 4$, regardless of the actual number of paths constituting the multi-path channel encountered.

Secondly, Figure 2.10 characterizes the achievable MSE performance of the PASTD method of Algorithm 2 for different values of the forgetting factor η, while assuming a constant rank of $L = 4$ for the estimated subspace. Figures 2.10(a) and 2.10(b) correspond to encountering the Doppler frequencies of $f_D = 0.001$ and 0.005, respectively. As may be concluded from Figure 2.10, the optimum value of the forgetting factor η is largely dependent on the SNR as well as on the Doppler frequency encountered. Nevertheless, the compromise value of $\eta = 0.95$ appears to constitute a relatively good choice in the practical ranges of both SNR values and Doppler frequencies.

Finally, Figure 2.11 characterizes the achievable MSE performance of the PASTD method of Algorithm 2 for different values of the OFDM-symbol-normalized PDP tap drift rate ν_τ. Figures 2.11(a) and 2.11(b) correspond to encountering the Doppler frequencies of $f_D = 0.001$ and 0.005, respectively. Observe that the specific values of the parameter ν_τ assumed in Figure 2.11 substantially exceed the maximum value considered in the base-line scenario outlined in Table 1.4. Consequently, we may conclude that the CIR tracking method of Algorithm 2 exhibits an adequate performance over the entire range of practical channel conditions.

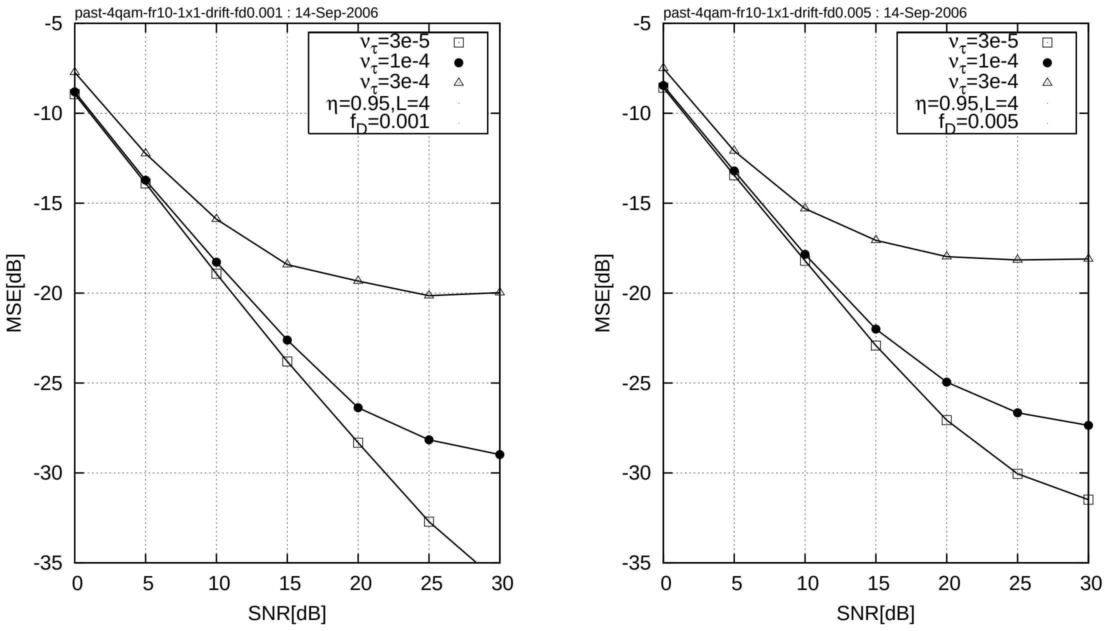

(a) (b)

Figure 2.11: The **Mean Square Error** exhibited by the **4QAM-OFDM** system employing the **PASTD** method of Algorithm 2, while encountering different values of the PDP tap drift rate $\nu_\tau = 3 \cdot 10^{-5}, 10^{-4}$ and $3 \cdot 10^{-4}$ as well as different values of the Doppler frequencies of (a) $f_D = 0.001$ and (b) $f_D = 0.005$. The abscissa represents the average SNR recorded at the receive antenna elements. We employ COST-207 BU channel model [119]. Additional system parameters are summarized in Table 1.4.

In conclusion of this section we would like to offer the following observations

- We have demonstrated that both PAST method of Algorithm 1 as well as PASTd method of Algorithm 2 facilitate recursive tracking of the CTF's signal subspace and thus allow for an efficient estimation of the channel's fractionally-spaced CIR.

- Furthermore, we have shown that the PASTd method exhibits higher stability as well as lower computational complexity and therefore is more suitable for employment in practical implementations.

- As suggested by Figure 2.9, an efficient estimation of the FS-CIR may be achieved by tracking as low as $L = 4$ number of significant FS-CIR taps at OFDM symbol normalized Doppler frequencies as high as $f_D = 0.005$.

- As suggested by Figure 2.10, the forgetting factor value $\eta = 0.95$ constitutes the optimum value in the context of a system characterized in Table 1.4.

- Finally, as is confirmed by the results depicted in Figure 2.11, the proposed channel estimation scheme employing the PASTd method of Algorithm 2 is capable of satisfying the requirements imposed by wireless systems involving mobile terminals moving at speeds as high as 200 km/h.

In order to complete the design of the DDCE scheme of Figure 2.1 we employ an *a priori* CIR predictor [28]. The CIR-related tap predictor considered can be employed in conjunction with both the SS-CIR and the FS-CIR estimators of Sections 2.5.2 and 2.5.4, as well as in combination with the parametric PASTD aided CIR estimator of Section 2.6.2. Observe, however, that the low-rank PASTD aided CIR estimator of Section 2.6.2 will require the prediction of a substantially lower number of $L \ll K_0$ CIR-related taps. More specifically, in the case of the system characterized by Table 1.4, the SS-CIR estimator of Section 2.5.2 will require the prediction of $K_0 = 32$ SS-CIR taps. This should be contrasted to the PASTD -aided CIR estimator of Section 2.6.2, which will require the prediction of only $L = 4$ FS-CIR-related taps, regardless of the actual number of paths encountered.

In the next section we present an overview of the major CIR tap prediction methods discussed in the literature [28, 38, 64, 65]. We analyse the achievable performance of each method with the aid of extensive simulations and conduct a comparative study aimed at identifying the most promising approaches.

2.7 Time-Domain *A Priori* CIR Tap Prediction

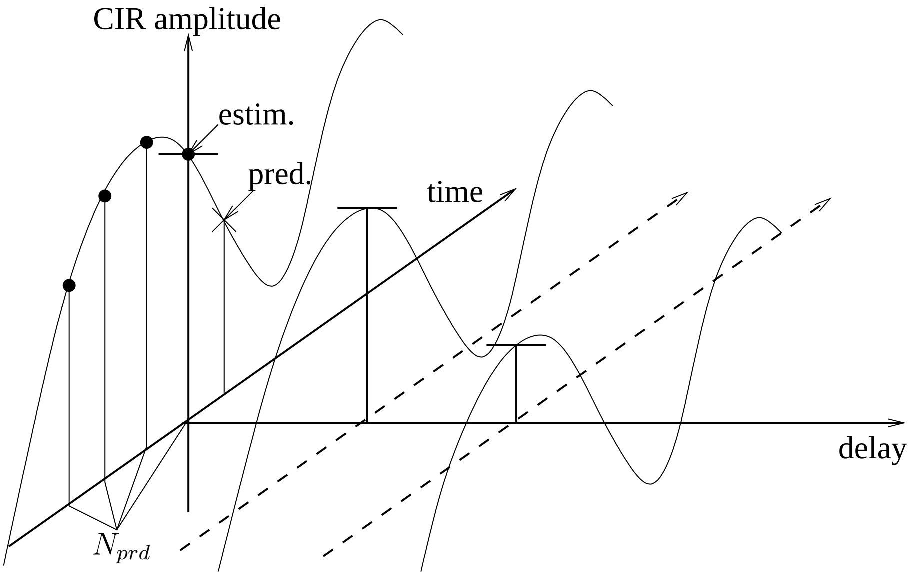

Figure 2.12: Stylized illustration of the estimation and prediction filter, both operating in the CIR-related domain using N_{prd} number of previous *a posteriori* CIR-related tap estimates © [28].

The philosophy of the *a priori* CIR predictor considered is illustrated in Figure 2.12. Our aim is to predict the SS/FS-CIR taps $\{\alpha_1[n+1], \cdots, \alpha_L[n+1]\}$ associated with the future channel conditions, given the history of the previous CIRs, namely the *a posteriori* estimates $\{\{\hat{\alpha}_l[n]\}, \{\hat{\alpha}_l[n-1]\}, \cdots\}$.

2.7.1 MMSE Predictor

As portrayed in Section 1.7.1, the lth CIR component $\alpha_l[n]$ undergoes a narrowband time-domain fading process characterised by the associated cross-correlation properties, which can be described by

$$\mathtt{E}\left\{\alpha_l^*[n]\alpha_{l'}[n-m]\right\} = r_t[m]\delta[l-l'] \,, \tag{2.62}$$

where $r_t[n]$ is the corresponding time-domain correlation function and $\delta[\cdot]$ is the Kronecker Delta function.

This WSS narrow-band process can be approximately modelled as a finite impulse response (FIR) auto-regressive process of the order N_{prd} [28], yielding

$$\alpha_l[n+1] = \sum_{m=0}^{N_{\text{prd}}-1} q[m]\alpha_l[n-m] + v_l[n+1], \tag{2.63}$$

where $q[m]$ represents the autoregressive coefficients and $v_l[n]$ is the model noise.

Let us define the following column vectors

$$\begin{aligned} \boldsymbol{\alpha}_l[n] &= (\alpha_l[n], \alpha_l[n-1], \cdots, \alpha_l[n-N_{\text{prd}}+1])^{\mathtt{T}} \\ \boldsymbol{q} &= (q[0], q[1], \cdots, q[N_{\text{prd}}-1])^{\mathtt{T}} \end{aligned} \tag{2.64}$$

and rewrite Equation (2.63) in a vectorial form as

$$\alpha_l[n+1] = \boldsymbol{\alpha}_l[n]^{\mathtt{T}}\boldsymbol{q} + v[n+1]. \tag{2.65}$$

Left-multiplying both sides of (2.65) with the complex conjugate of the column vector $\boldsymbol{\alpha}_l[n,l]$ and obtaining the expectation value over the time-domain index n yields

$$\mathtt{E}\left\{\boldsymbol{\alpha}_l^*[n]\alpha_l[n+1]\right\} = \mathtt{E}\left\{\boldsymbol{\alpha}_l^*[n](\boldsymbol{\alpha}_l^{\mathtt{T}}[n]\boldsymbol{q} + v[n+1])\right\}, \tag{2.66}$$

which can be represented as a set of Yule-Walker equations in the following form [134]

$$\boldsymbol{r}_{\text{apr}} = \boldsymbol{R}_{l;\text{apt}}\boldsymbol{q}_l, \tag{2.67}$$

where the vector $\boldsymbol{r}_{apr}$ is the autocorrelation vector of the predicted *a priori* CIR taps defined by

$$\boldsymbol{r}_{\text{apr}} = \frac{1}{\sigma_l^2}\mathtt{E}\left\{\boldsymbol{\alpha}_l^*[n]\alpha_l[n+1]\right\}, \tag{2.68}$$

and the matrix $\mathbf{R}_{apt}$ is the autocorrelation matrix of the *a posteriori* CIR taps described in [28]

$$\begin{aligned} \boldsymbol{R}_{l;\text{apt}} &= \frac{1}{\sigma_l^2}\mathtt{E}\left\{\hat{\boldsymbol{\alpha}}_l[n]\hat{\boldsymbol{\alpha}}_l^{\mathtt{H}}[n]\right\} \\ &= \boldsymbol{R}_{\text{apr}} + \rho_l\boldsymbol{I}, \end{aligned} \tag{2.69}$$

where

$$\boldsymbol{R}_{\text{apr}} = \frac{1}{\sigma_l^2}\mathtt{E}\left\{\boldsymbol{\alpha}_l[n]\boldsymbol{\alpha}_l^{\mathtt{H}}[n]\right\} \tag{2.70}$$

and ρ_l is the parameter determined by the variance of the effective estimation noise imposed by the *a posteriori* CIR estimator employed σ_{apt}^2, as well as the expectation magnitude of the CIR tap predicted σ_l^2, such that we have $\rho_l = \frac{\sigma_{\text{apt}}^2}{\sigma_l^2}$.

The optimal solution of Equation (2.67) evaluated in the MSE sense is given by

$$\boldsymbol{q}_{l;\text{prd}} = \boldsymbol{R}_{l;\text{apt}}^{-1}\boldsymbol{r}_{\text{apr}}. \tag{2.71}$$

In the specific scenario when the channel is described by Jakes' model [121], the *a priori* autocorrelation vector $\boldsymbol{r}_{\text{apr}}$ can be formulated as $r_{\text{apr}}[n] = r_J[n] = J_0(2\pi f_D n),\ n = 1, 2, \ldots, N_{\text{prd}}$, where $J_0(x)$ is a zero-order Bessel function of the first kind. The corresponding *a posteriori* autocorrelation matrix $\boldsymbol{R}_{\text{apr}}$ is given by $R_{\text{apr}}[n,m] = r_J[n-m] + \rho\delta[n-m],\ n,m = 0, 1, \ldots\ N_{\text{prd}} - 1$, while the CIR predictor's coefficient vector is described by (2.71) and the prediction is performed according to

$$\check{\alpha}_l[n+1] = \boldsymbol{q}_{l;\text{prd}}^{\mathtt{T}}\hat{\boldsymbol{\alpha}}_l[n],\ l = 1, 2, \ldots, L. \tag{2.72}$$

The corresponding performance can be characterised using the frequency-domain NMSE criterion as derived in [28]

$$NMSE_{H;\text{apr}} = \frac{1}{\sigma_H^2}\mathtt{E}\left\{|H[n,k] - \check{H}[n,k]|^2\right\}, \tag{2.73}$$

where $H[n,k]$ and $\check{H}[n,k]$ are the CTFs corresponding to the encountered CIR and the *a priori* predicted CIR $\check{\alpha}_l[n]$, respectively. From [28] we have

$$NMSE_{H;\text{apr}} = \frac{1}{K\sigma_H^2}\sum_{l=1}^{L} MSE_{l;\text{apr}}, \tag{2.74}$$

where

$$MSE_{l;\text{apr}} = \sigma_l^2 - \boldsymbol{q}_{l;\text{prd}}^{\mathtt{T}}\boldsymbol{r}_{l;\text{apt}}^{*} - \boldsymbol{q}_{l;\text{prd}}\boldsymbol{r}_{l;\text{apt}}^{\mathtt{H}} + \boldsymbol{q}_{l;\text{prd}}^{\mathtt{H}}\boldsymbol{R}_{l,\text{apt}}\boldsymbol{q}_{l;\text{prd}}. \tag{2.75}$$

The attainable NMSE performance of the *a priori* CIR predictor of Equation (2.72) evaluated for the scenario when the Doppler frequency assumed in the design of the receiver matches the actual Doppler frequency encountered, namely when we have $f_D = f_{D;\text{prd}}$, is depicted in Figures 2.13 and 2.14. More specifically in Figure 2.13 we demonstrate the NMSE of the CIR prediction method considered using the prediction filter of length $N_{\text{prd}} = 1, 2, 4, 8, 16, 32$ and 64 as a function of the average SNR recorded at the receive antenna. As expected, the performance of the estimator improves when the prediction filter length N_{prd} increases, although the corresponding additional NMSE reduction becomes more modest for high values of the prediction filter length and hence a trade-off between the desired NMSE performance and the associated computational complexity has to be found. A similar sytem behavior can be observed in Figure 2.14, where the NMSE is evaluated as a function of the OFDM-symbol-normalized Doppler frequency f_D.

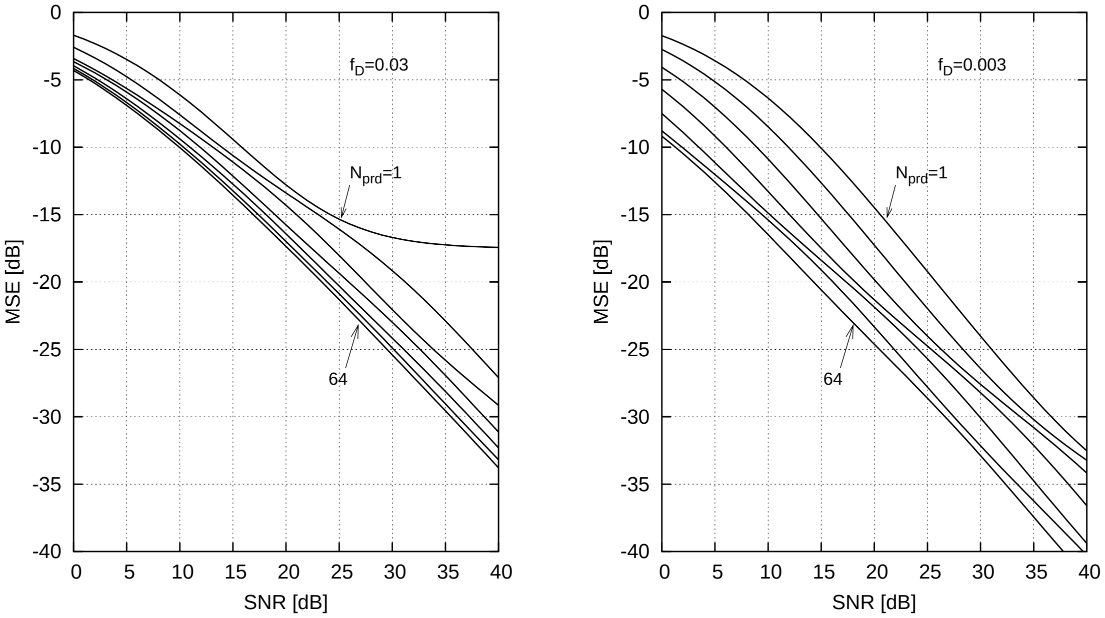

(a) (b)

Figure 2.13: Mean Square Error exhibited by the **robust *a priori* CIR predictor** as a function of the average SNR at the receive antenna. The curves on the plot correspond to the prediction filter lengths of $N_{\text{prd}} = 1, 2, 4, 8, 16, 32$ and 64 from top to bottom respectively. The Bug channel model with the OFDM-symbol-normalized Doppler frequency of (a) 0.003 and (b) 0.03 was considered. The results were evaluated from the Equation (2.74).

2.7.2 Robust Predictor

The CIR-tap prediction process described in the previous section exhibits a high CIR-tap estimation performance under the assumption of having perfect knowledge of the channel statistics. However, it suffers from a significant performance degradation, when the actual channel statistics deviate from the model assumed, such as for example Jakes' model. The issue of statistical mismatch becomes increasingly detrimental in diverse wireless environments, where the channel conditions and the corresponding statistics are time-dependent and cannot be assumed to be wide-sense stationary.

As it has been shown in [38] and [28], the MSE exhibited by the linear CIR predictor of (2.72) is upper-bounded by the MSE encountered, when communicating over an ideally band-limited channel having a perfect low-pass Doppler PSD function given by

$$p_{B;\text{unif}}(f) = \begin{cases} \frac{1}{2f_D}, & \text{if } |f| < f_D \\ 0, & \text{otherwise .} \end{cases} \tag{2.76}$$

Hence, we arrive at the concept of designing Li's [38] so-called *robust* linear predictor [28], which assumes encountering the worst possible channel statistics. As pointed out in [30], such a *robust* channel predictor, optimised for the worst-case PSD of Equation (2.76), can be designed by using the corresponding sinc-

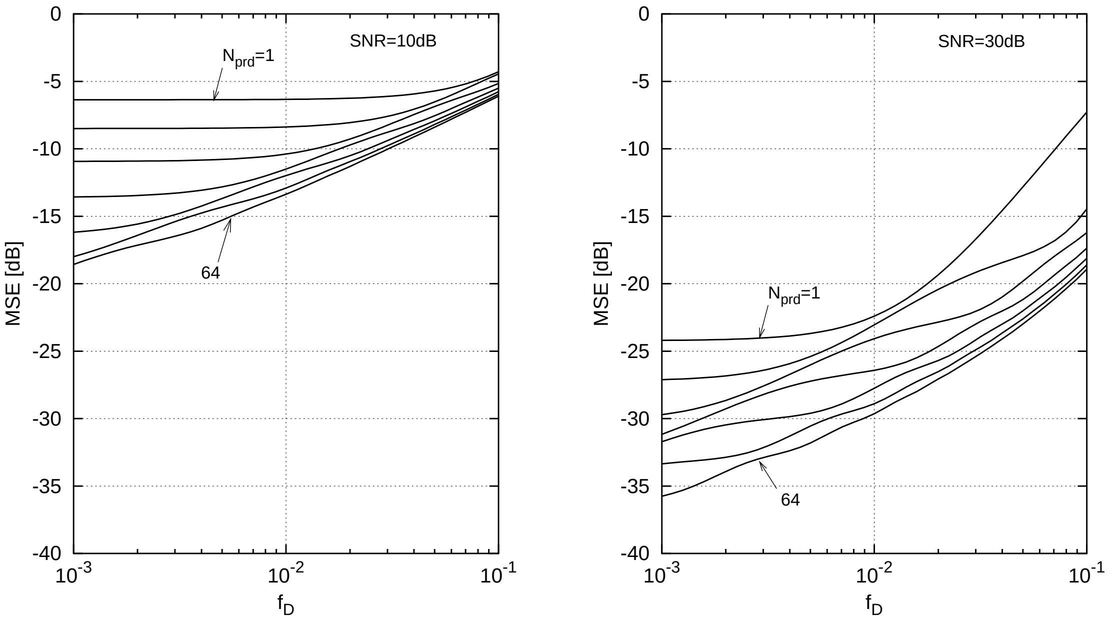

(a) (b)

Figure 2.14: Mean Square Error exhibited by the **robust *a priori* CIR predictor** as a function of the OFDM-symbol normalized Doppler frequency f_D. The curves on the plot correspond to the prediction filter lengths of $N_{\text{prd}} = 1, 2, 4, 8, 16, 32$ and 64 from top to bottom, respectively. Bug's channel model associated with the receive antenna SNRs of (a) 10 and (b) 30 dB was considered. The results were evaluated from the Equation (2.74).

shaped *a priori* autocorrelation vector $\boldsymbol{r}_{apr,rob}$, which is given by

$$r_{\text{apr;rob}}[n] = r_B[n] = \frac{\sin 2\pi f_D n}{2\pi f_D n},\ n = 1, 2, \ldots, N_{\text{prd}} \tag{2.77}$$

and by invoking the corresponding *a posteriori* autocorrelation matrix $\boldsymbol{R}_{\text{apt;rob}}$ defined by

$$R_{\text{apr;rob}}[n, m] = r_B[n - m] + \rho\delta[n - m], \tag{2.78}$$

where we have $n, m = 0, 1, \ldots\ N_{\text{prd}} - 1$.

In Figure 2.15 we characterize the attainable NMSE performance of the robust *a priori* CIR predictor of Equation (2.72) for the scenario when the Doppler frequency $f_{D;\text{prd}}$ assumed in the design of the receiver does not match the actual Doppler frequency f_D encountered. It can be seen that the estimation method considered is robust against a mismatches between the assumed and the encountered Doppler frequency, as long as the encountered Doppler frequency does not exceed the assumed value, namely as long as we have $f_D \leq f_{D;\text{prd}}$.

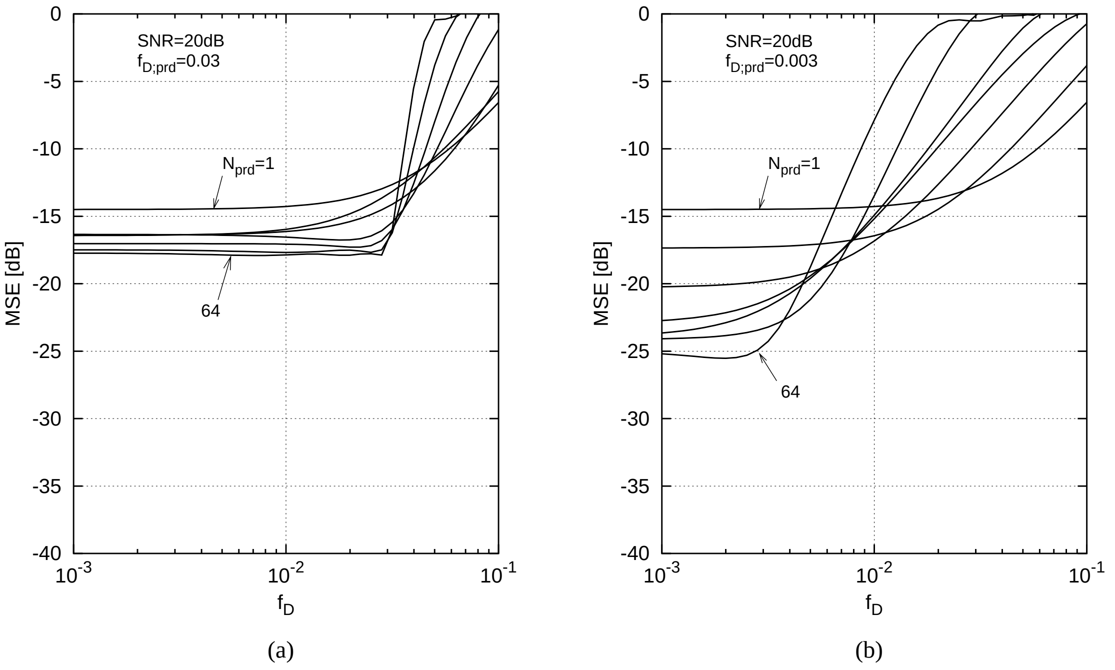

(a)

(b)

Figure 2.15: Mean Square Error exhibited by the **robust *a priori* CIR predictor** as a function of the encountered OFDM-symbol normalized Doppler frequency f_D. The results correspond to the case when the Doppler frequency assumed in the receiver does not match the actual value encountered. The assumed Doppler frequencies of (a) $f_D = 0.03$ and (b) 0.003 have been considered and different curves on each plot correspond to the prediction filter lengths of $N_{\text{prd}} = 1, 2, 4, 8, 16, 32$ and 64 from top to bottom, respectively. The Bug channel model with the average receive antenna SNR of 20dB is considered. The results were evaluated from the Equation (2.74).

2.7.3 MMSE Versus Robust Predictor Performance Comparison

The achievable performance of the DDCE scheme of Figure 2.1 employing the **robust** *a priori* CIR predictor of Section 2.7.2 under **matched** time-domain correlation conditions is quantified in Figure 2.16, when the assumed OFDM-symbol-normalized Doppler frequency $f_{D;\text{prd}}$ matches the actual value encountered. The **NMSE** exhibited by the channel estimation scheme considered is depicted in Figure 2.16(a), while the corresponding BER exhibited by the turbo-coded QPSK-modulated MC-CDMA system is shown in Figure 2.16(b). It can be seen that while the estimation accuracy decreases upon increasing the Doppler frequency, the corresponding BER performance remains relatively unaffected.

Finally, Figure 2.17 illustrates the achievable performance of QPSK-modulated MC-CDMA employing the DDCE scheme of Figure 2.1 under **unmatched** time-correlation conditions. Our simulations were performed at a constant value of the OFDM-symbol normalised Doppler frequency assumed at the receiver, namely at $f_{D;\text{prd}} = 0.03$. Furthermore, four different values of the actual normalised Doppler frequencies were used, namely $f_D = 0.03, 0.01, 0.003$ and 0.001. Figure 2.17(a) characterizes the NMSE performance of the DDCE scheme employed by the MC-CDMA system considered, while the corresponding turbo-coded

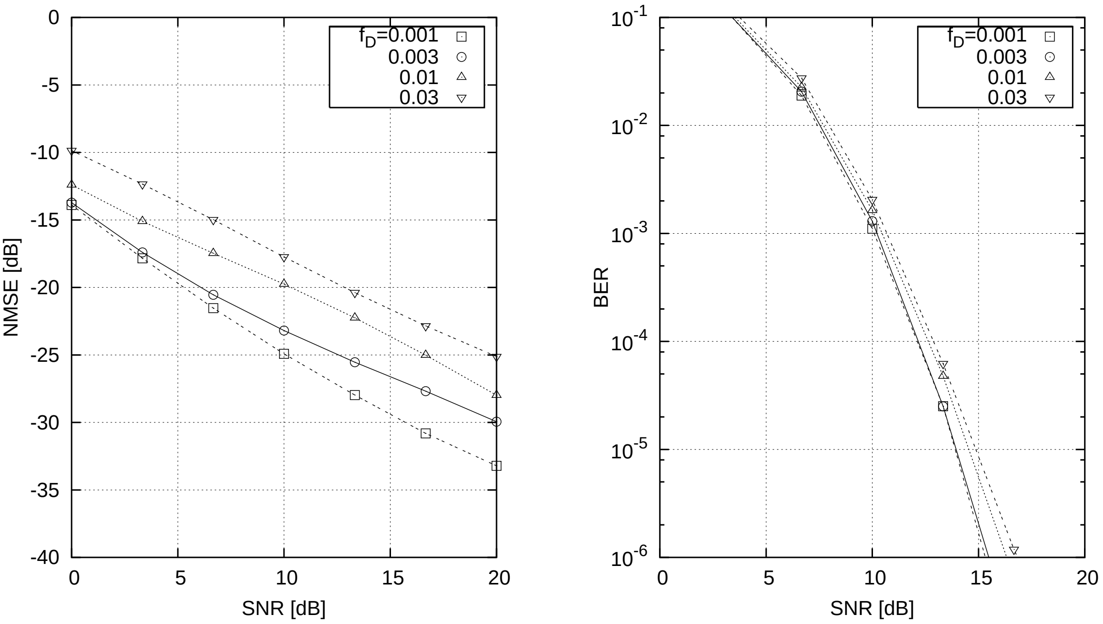

(a) (b)

Figure 2.16: (a) **NMSE** exhibited by the decision-directed channel estimator employing the **RC-MMSE FS-CIR** *a posteriori* estimator of Section 2.5.4 and the **robust** *a priori* CIR predictor of Section 2.7.2 as a function of the average SNR recorded at the receiver and (b) **BER** exhibited by the corresponding QPSK-modulated **turbo-coded** MC-CDMA system. The results correspond to **matched** Doppler conditions, when the Doppler frequency $f_{D;\mathrm{prd}}$ assumed in the receiver matches the actual value encountered. The *frame-variant* Bug channel model was assumed.

BER is depicted in Figure 2.17(b). The achievable BER performance in the case of perfect Channel State Information (CSI), namely when the CTF is perfectly known at the receiver, is also depicted in Figure 2.17(a). It can be seen that the performance of the CIR predictor advocated is indeed tolerant to the mismatch of the actual Doppler frequency and that assumed during the predictor design, as long as the actual Doppler frequency does not exceed the value assumed in the predictor's design. Furthermore, the results depicted in Figure 2.17(a) substantiate our conclusion that the performance of the MC-CDMA system employing channel estimation scheme of Figure 2.1 closely approaches the corresponding performance of the MC-CDMA system in the case of perfect CTF knowledge at the receiver. More explicitly, the BER performance corresponding to the different values of the Doppler frequency f_D fall within 1dB from the BER performance associated with the perfect CSI associated scenario.

2.7.4 Adaptive RLS Predictor

On the other hand, in the RLS-based adaptive CIR tap prediction approach of [64,65] no assumptions where made concerning the channel's stationarity. Consequently, the time-variant lth CIR tap's predictor filter

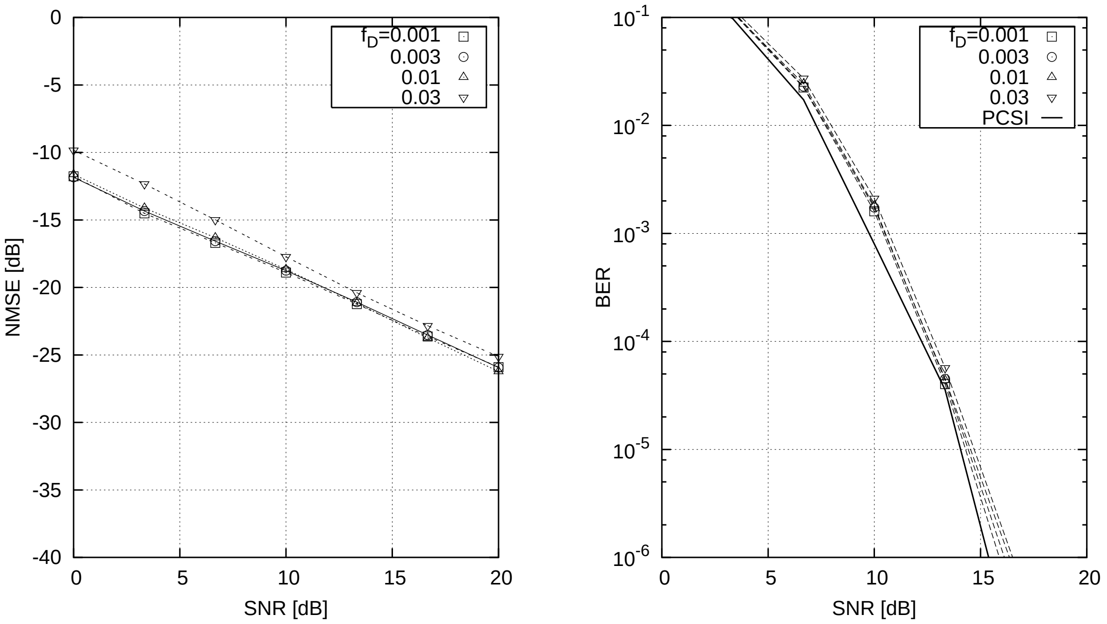

(a) (b)

Figure 2.17: (a) **NMSE** exhibited by the decision-directed channel estimator employing the **RC-MMSE FS-CIR** *a posteriori* estimator of Section 2.5.4 and the **robust** *a priori* CIR predictor of Section 2.7.2 as a function of the average SNR recorded at the receiver and (b) corresponding **BER** exhibited by the **turbo-coded** QPSK-modulated MC-CDMA system. The results correspond to **unmatched** Doppler conditions associated with the assumed Doppler frequency of $f_{D;\mathrm{prd}} = 0.03$ and the actual encountered values of $f_D = 0.001, 0.003, 0.01$ and 0.03. The bold line on the BER curve (b) portrays the BER performance of the MC-CDMA system considered in the case of perfect CSI.

coefficient vector $\boldsymbol{q}_l[n]$ is calculated by minimizing the following scalar cost function

$$J_{\mathrm{RLS};l}[n] = \sum_{i=1}^{n} \beta^{n-i} |\alpha_l[i+1] - \boldsymbol{q}_l^{\mathrm{H}}[n]\boldsymbol{\alpha}_l[i]|^2, \tag{2.80}$$

where $\beta \in (0,1)$ is the so-called *forgetting factor* [64], which accounts for possible deviations of the fading process encountered from the WSS assumption. The resultant recursive update for $\boldsymbol{q}_l[n]$ is given by

$$\boldsymbol{q}_l[n] = \boldsymbol{q}_l[n-1] + \boldsymbol{k}_l[n-1]e_l^*[n], \tag{2.81}$$

where

$$e_l[n] = \hat{\alpha}_l[n] - \boldsymbol{q}_l^{\mathrm{H}}[n-1]\hat{\boldsymbol{\alpha}}_l[n-1] \tag{2.82}$$

is the prediction error, while

$$\boldsymbol{k}_l[n] = \frac{\boldsymbol{P}_l[n-1]\hat{\boldsymbol{\alpha}}_l[n]}{\beta + \hat{\boldsymbol{\alpha}}_l^{\mathrm{H}}[n]\boldsymbol{P}_l[n-1]_l\hat{\boldsymbol{\alpha}}_l[n]} \tag{2.83}$$

denotes the RLS gain vector. Furthermore, the matrix $\boldsymbol{P}_l[n]$ is the inverse of the lth CIR tap's $(N_{\mathrm{prd}} \times N_{\mathrm{prd}})$-dimensional sample covariance matrix, which can be recursively calculated as follows

$$\boldsymbol{P}_l[n] = \frac{1}{\beta}(\boldsymbol{I} - \boldsymbol{k}_l[n]\hat{\boldsymbol{\alpha}}_l^{\mathrm{H}}[n])\boldsymbol{P}_l[n-1] \tag{2.84}$$

Algorithm 3 The RLS Prediction Algorithm.

$$e[n] = \hat{\alpha}[n] - \check{\alpha}[n] = \hat{\alpha}[n] - \boldsymbol{q}^{\mathrm{H}}[n-1]\hat{\boldsymbol{\alpha}}[n-1] \tag{2.79a}$$

$$\boldsymbol{q}[n] = \boldsymbol{q}[n-1] + \boldsymbol{k}[n-1]e^{*}[n] \tag{2.79b}$$

$$\check{\alpha}[n+1] = \boldsymbol{q}^{\mathrm{H}}[n]\hat{\boldsymbol{\alpha}}[n] \tag{2.79c}$$

$$\boldsymbol{g}[n] = \boldsymbol{P}[n-1]\hat{\boldsymbol{\alpha}}[n] \tag{2.79d}$$

$$\boldsymbol{k}[n] = \frac{\boldsymbol{g}[n]}{\beta + \hat{\boldsymbol{\alpha}}^{\mathrm{H}}[n]\boldsymbol{g}[n]} \tag{2.79e}$$

$$\boldsymbol{P}[n] = \frac{1}{\beta}(\boldsymbol{I} - \boldsymbol{k}[n]\hat{\boldsymbol{\alpha}}^{\mathrm{H}}[n])\boldsymbol{P}[n-1] \tag{2.79f}$$

As it was pointed out in [135] the choice of the forgetting factor's value β has only a moderate effect on the performance of the resultant predictor. Specifically, in our simulations we used the value suggested in [135], namely $\beta = 0.99$.

2.7.5 Robust Versus Adaptive Predictor Performance Comparison

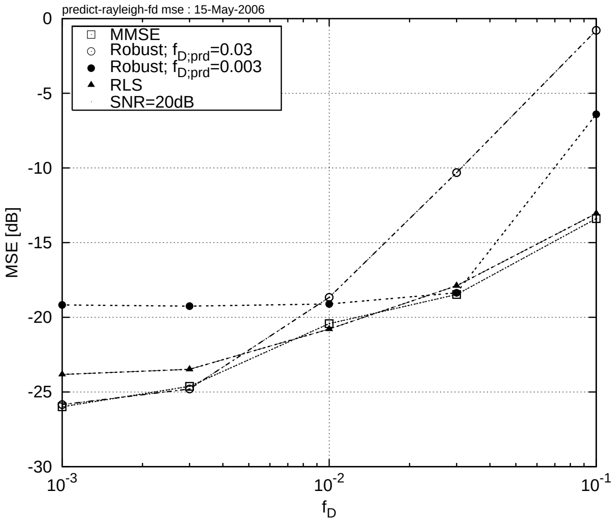

Figure 2.18: Mean Square Error exhibited by the **MMSE, Robust and RLS** *a priori* CIR predictors as a function of the symbol-normalized Doppler frequency encountered. Two cases of Robust prediction, namely when $f_{D;\mathrm{prd}} = 0.03$ and $f_{D;\mathrm{prd}} = 0.003$ are considered. The results correspond to the SNR level of 20 dB.

Figure 2.18 illustrates the achievable MSE performance of the CIR prediction methods considered as a function of the Doppler frequency f_{D} encountered. It can be seen that the MMSE CIR predictor, which relies on a perfect *a priori* knowledge of the underlying channel statistics represents the upper bound for the MSE performance achievable by a linear predictor. Furthermore, the robust CIR predictor exhibits a relatively high performance, as long as the actual Doppler frequency encountered does not exceed that assumed. Finally, the RLS CIR predictor, which does not require any explicit knowledge concerning the

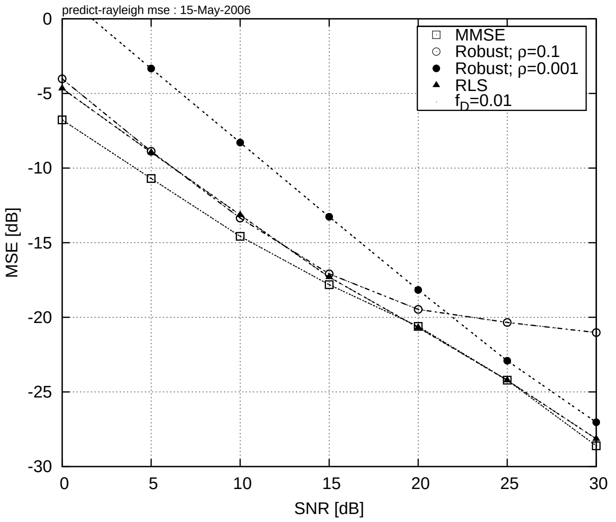

Figure 2.19: Mean Square Error exhibited by the **MMSE, Robust and RLS** *a priori* CIR predictors as a function of the **SNR** encountered. Two cases of Robust prediction, namely when $\rho = 0.1$ and $\rho = 0.001$ are considered. The results correspond to the symbol-rate-normalized Doppler frequencies of $f_D = 0.01$.

channel statistics exhibits a near-optimum performance over the entire range of the values of f_{D}. Furthermore, Figure 2.19 illustrates the achievable MSE performance of the CIR prediction methods considered as a function of the SNR encountered. Once again, the MMSE CIR predictor exhibits the highest achievable performance. The robust CIR predictor exhibits a relatively high performance, as long as the SNR encountered does not exceed the value $1/\rho$ assumed. On the other hand, the RLS predictor exhibits near optimum performance over the whole range of the SNR values. Additionally, the order of the computational complexity associated with both CIR predictors considered in the context of a DDCE-OFDM system and quantified in terms of the total number of complex multiplications and additions per OFDM symbol may be expressed as $O(K \log_2 K + LN_{\mathrm{prd}})$ and $O(K \log_2 K + LN_{\mathrm{prd}} + LN_{\mathrm{prd}}^2)$ for the robust [28] and RLS [65] CIR predictors, respectively[2]. Explicitly, the order of complexity imposed by the RLS CIR predictor is only slightly higher than that associated with the Robust CIR predictor.

2.8 PASTD Aided DDCE

The detailed schematic of the channel estimation scheme proposed is depicted in Figure 2.20. Our channel estimator is constituted by a bank of the per-subcarrier *a posteriori* MMSE CTF estimators outlined in Section 2.4, followed by the PASTD -aided CIR estimator of Section 2.6.2 and by the *a priori* RLS CIR predictor of Section 2.7.4. The task of the CTF estimator seen in Figure 2.20 is to estimate the subcarrier-related CTF coefficients $H[n,k]$ of Equation (1.7). The resultant estimated subcarrier-related samples $\tilde{H}[n,k]$, which serve as an observation vector of the FD-CTF coefficients $H[n,k]$ are fed to the PASTD subspace-based

---

[2] K denotes the number of subcarriers comprising the OFDM symbol, while L is the number of non-zero CIR taps encountered.

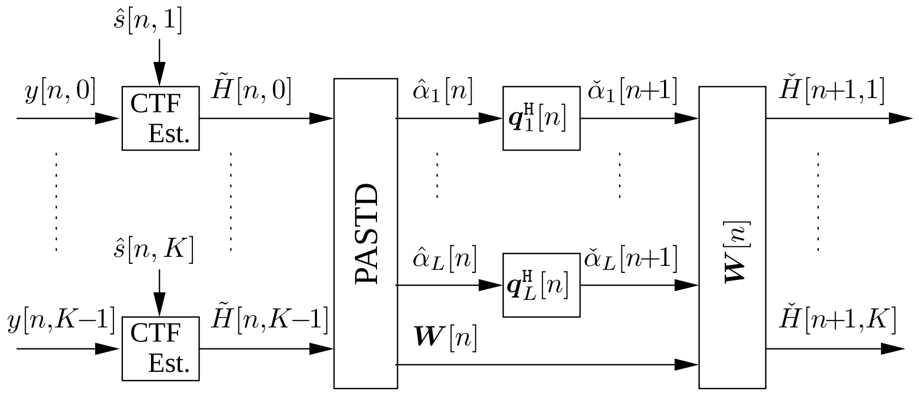

Figure 2.20: Detailed structure of the 2D channel estimator corresponding to the DDCE module of Figure 2.1. The channel estimator comprises a PAST module, which performs recursive tracking of the CIR. The resultant CIR related taps $\hat{\alpha}_l[n]$ are filtered by the adaptive RLS-based prediction filter resulting in the *a priori* estimates of the CIR-related taps $\check{\alpha}_l[n+1]$. Finally, the *a priori* estimates of the subcarrier-related coefficients $H[n+1,k]$ are obtained by applying the transform matrix $\boldsymbol{W}[n]$ provided by the PASTD module.

tracking module, which performs recursive tracking of the channel's covariance matrix $\boldsymbol{C}_H$ signal subspace and the associated CIR-related taps. The output of the PASTD module is constituted by the instantaneous CIR-related tap estimates $\hat{\alpha}_l[n]$ and the corresponding estimate of the transformation matrix $\boldsymbol{W}[n]$ of Equation (2.54). The CIR-related estimate vector $\hat{\alpha}_l[n]$ is then fed into the low-rank time-domain CIR-related tap predictor of Figure 2.20 for the sake of producing an *a priori* estimate $\check{\alpha}_l[n+1],\ l=1,\cdots,L$ of the next CIR-related tap-vector on a tap-by-tap basis [28]. Finally, the predicted CIR is converted to the subcarrier-related CTF with the aid of the transformation matrix $\boldsymbol{W}[n]$ provided by the PASTD module of Figure 2.20. The resultant FD-CTF is employed by the receiver for the sake of detecting and decoding of the next OFDM symbol. Note that this principle requires the transmission of a frequency-domain pilot-based channel sounding sequence, such as for example a pilot-assisted OFDM symbol, during the initialisation stage. The operation of the resultant DDCE scheme illustrated in Figure 2.20 is summarized in Algorithm 4.

In order to characterize the performance of the resultant channel estimation scheme, we would like to introduce an estimation efficiency criteria κ, which is defined as follows

$$\kappa = \frac{1}{\sigma_e^2\gamma}\frac{L}{K}, \tag{2.85}$$

where σ_e^2 and γ are the estimation MSE and SNR, respectively, while K and L are the number of OFDM subcarriers and the number of the estimated CIR taps.

The achievable performance of the PASTD aided DDCE scheme of Algorithm 4 is characterized in Figure 2.21. In our simulations we considered an OFDM system having $K=128$ QPSK-modulated or-

Algorithm 4 PASTD-aided DDCE

```
Signal Detection:
    $\hat{\boldsymbol{x}}[n] = \texttt{Detect}(\boldsymbol{y}[n], \check{\boldsymbol{H}}[n])$    (2.86a)
CTF Estimation:
    for $k = 1, 2, \ldots, K$ do
        $\tilde{H}[n,k] = \frac{y[n,k]\hat{x}^*[n,k]}{|\hat{x}[n,k]|^2 + \sigma_w^2}, \qquad k = 0, \cdots, K-1$    (2.86b)
    end for
Subspace Tracking-Aided CIR Estimation:
    $\boldsymbol{H}_1[n] = \tilde{\boldsymbol{H}}[n]$    (2.86c)
    for $l = 1, 2, \ldots, L$ do
        $\hat{\alpha}_l[n] = \boldsymbol{w}_l^{\mathtt{H}}[n-1]\boldsymbol{H}_l[n]$    (2.86d)
        $\lambda_l[n] = \eta\lambda_l[n-1] + |\hat{\alpha}_l[n]|^2$    (2.86e)
        $\boldsymbol{e}_l[n] = \boldsymbol{H}_l[n] - \boldsymbol{w}_l[n-1]\hat{\alpha}_l[n]$    (2.86f)
        $\boldsymbol{w}_l[n] = \boldsymbol{w}_l[n-1] + \boldsymbol{e}_l[n](\alpha_l^*[n]/\lambda_l[n])$    (2.86g)
        $\boldsymbol{H}_{l+1}[n] = \boldsymbol{H}_l[n] - \boldsymbol{w}_l[n]\hat{\alpha}_l[n]$    (2.86h)
    end for
CIR Tap Prediction:
    for $l = 1, 2, \ldots, L$ do
        $e[n] = \hat{\alpha}_l[n] - \check{\alpha}_l[n] = \hat{\alpha}_l[n] - \boldsymbol{q}_l^{\mathtt{H}}[n-1]\hat{\boldsymbol{\alpha}}_l[n-1]$    (2.86i)
        $\boldsymbol{q}_l[n] = \boldsymbol{q}_l[n-1] + \boldsymbol{k}_l[n-1]e^*[n]$    (2.86j)
        $\check{\alpha}_l[n+1] = \boldsymbol{q}_l^{\mathtt{H}}[n]\hat{\boldsymbol{\alpha}}_l[n]$    (2.86k)
        $\boldsymbol{g}[n] = \boldsymbol{P}_l[n-1]\hat{\boldsymbol{\alpha}}_l[n]$    (2.86l)
        $\boldsymbol{k}_l[n] = \frac{\boldsymbol{g}[n]}{\beta + \hat{\boldsymbol{\alpha}}_l^{\mathtt{H}}[n]\boldsymbol{g}[n]}$    (2.86m)
        $\boldsymbol{P}_l[n] = \frac{1}{\beta}(\boldsymbol{I} - \boldsymbol{k}_l[n]\hat{\boldsymbol{\alpha}}_l^{\mathtt{H}}[n])\boldsymbol{P}_l[n-1]$    (2.86n)
    end for
CTF Reconstraction:
    $\check{\boldsymbol{H}}[n+1] = \boldsymbol{W}[n]\check{\boldsymbol{\alpha}}[n+1]$    (2.86o)
```

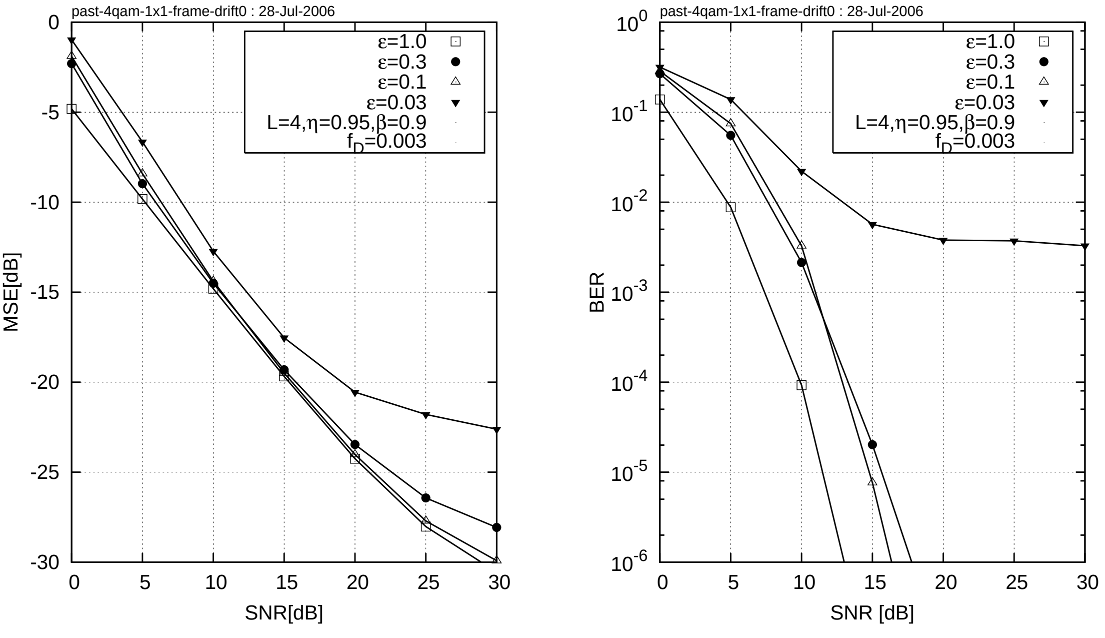

(a) (b)

Figure 2.21: The (a) **Mean Square Error** and (b) **Bit Error Rate** exhibited by the **4QAM-OFDM** system employing the **PASTD** -aided DDCE scheme of Algorithm 4. The value of the parameters $L = 4, \eta = 0.95$ and $\beta = 0.9$ has been assumed. We considered the scenarios of encountering the Doppler frequency $f_D = 0.003$. The abscissa represents the average SNR recorded at the receive antenna elements.

thogonal subcarriers. The system characteristics are outlined in Table 1.4. We employ an OFDM-frame-variant channel model associated with a time-variant 7-tap PDP characterized by the COST-207 BU channel model [119], as detailed in Section 1.7.2. Additionally, each individual propagation path undergoes fast Rayleigh fading having an OFDM-symbol-normalized Doppler frequency of $f_D = 0.003$. We assumed the values $L = 4$ and $\eta = 0.95$ for the PASTD module-related subspace rank and forgetting factor parameters respectively, as well as the value of $\beta = 0.9$ for the RLS CIR-tap predictor-related forgetting factor.

Figure 2.21(a) portrays the achievable MSE performance of the PASTD aided DDCE scheme of Algorihtm 4 for the pilot overhead ratios $\varepsilon = 0.03, 0.1, 0.3$ and 1.0, where $\varepsilon = 0.03$ and $\varepsilon = 1.0$ correspond to having 3% and 100% pilots, respectively. Specifically, we may identify an estimation efficiency of $\kappa = 5 - 10 = -5dB$.

Furthermore, Figure 2.21(b) portrays the corresponding BER performance of the rate $\frac{1}{2}$ turbo-coded QPSK-modulated OFDM system.

2.9 Channel Estimation for MIMO-OFDM

The main challenge associated with the estimation of the MIMO-CTF coefficients in the context of multi-antenna multi-carrier systems rests in the fact that, as opposed to the SISO scenario outlined in Section 2.4.2, the estimation of the MIMO-CTFs constitutes a highly rank-deficient problem. More specifically, let us consider the SDM-OFDM system model associated with the k-th subcarrier of the n-th SDM-OFDM symbol, which may be characterized as follows

$$\mathbf{y}[n,k] = \mathbf{H}[n,k]\mathbf{s}[n,k] + \mathbf{w}[n,k], \tag{2.87}$$

where $\mathbf{s}[n,k], \mathbf{y}[n,k], \mathbf{w}[n,k]$ and $\mathbf{H}[n,k]$ are the signals associated with the k-th subcarrier of the n-th SDM-OFDM symbol. Specifically, $\mathbf{s}[n,k]$ is the m_{t}-dimensional signal vector transmitted from the m_{t} transmit antennas, $\mathbf{y}[n,k]$ and $\mathbf{w}[n,k]$ are the n_{r}-dimensional signal and noise vectors recorded at the n_{r} receive antennas, while $\mathbf{H}[n,k]$ is the $(n_{\mathrm{r}} \times m_{\mathrm{t}})$-dimensional matrix, which characterizes the MIMO-CTFs encountered. Let us assume a relatively simple MIMO scenario of having $m_{\mathrm{t}} = n_{\mathrm{r}} = 4$ transmit and receive antennas. The corresponding MIMO-CTF matrix is constituted by $4 \times 4 = 16$ uncorrelated coefficients, which have to be calculated using four recorded samples comprising the received signal $\mathbf{y}[n,k]$, as well as four pilots or decision based symbols estimating the transmitted signal $\mathbf{s}[n,k]$. Notice that even in the presence of the *a priori* known pilot-based transmitted signal $\mathbf{s}[n,k]$, the MIMO-CTF matrix $\boldsymbol{H}[n,k]$ may not be estimated reliably using a linear solution reminiscent of that derived in Section 2.4.2. Consequently, the estimation of the $(n_{\mathrm{r}} \times m_{\mathrm{t}})$-dimensional MIMO-CTF matrix $\mathbf{H}[n,k]$ requires a sufficiently sophisticated exploitation of both the time- and the frequency-domain correlation properties of the MIMO-CTF coefficients.

In this treatise we propose a MIMO channel estimation scheme, which follows the decision-directed channel estimation philosophy of Figure 2.1, as employed in Section 2.3 for SISO multicarrier systems.

Similarly to the SISO case of Section 2.3, our MIMO channel estimation scheme comprises an array of K per-subcarrier MIMO-CTF estimators, followed by a $(n_{\mathrm{r}} \times m_{\mathrm{t}})$-dimensional array of parametric CIR estimators and a corresponding array of $(n_{\mathrm{r}} \times m_{\mathrm{t}} \times L)$ CIR tap predictors, where L is the number of tracked CIR taps per link for the MIMO channel. The structure of both the parametric PASTD -aided MIMO-CIR tap estimators and that of the RLS MIMO-CIR tap predictors is to a large extent identical to those devised in Sections 2.6.2 and 2.7.4, respectively, in the context of our SISO channel estimation scheme advocated in Section 2.8. On the other hand, our MIMO-CTF estimators exhibit a substantially different structure, which reflects the rank-deficient nature of the MIMO channel estimation problem.

In order to exploit the time-domain correlation properties of the MIMO-CTF coefficients matrix $\mathbf{H}[n,k]$ we employ an iterative tracking approach instead of the MMSE estimation method of Section 2.4.2.

Algorithm 5 *A Posteriori* LMS MIMO-CTF Tracking

$$\hat{\mathbf{s}}[n,k] = \mathtt{Detect}\left\{\mathbf{y}[n,k], \check{\mathbf{H}}[n,k]\right\} \tag{2.91a}$$

$$\mathbf{e}[n,k] = \mathbf{y}[n,k] - \tilde{\mathbf{H}}[n,k]\hat{\mathbf{s}}[n,k] \tag{2.91b}$$

$$\tilde{\mathbf{H}}[n,k] = \tilde{\mathbf{H}}[n-1,k] + (1-\zeta)\mathbf{e}[n,k]\hat{\mathbf{s}}^{\mathrm{H}}[n,k] \tag{2.91c}$$

2.9.1 Soft Recursive MIMO-CTF Estimation

Analogous to the SISO channel estimator architechture outlined in Section 2.8, at the first stage of our MIMO channel estimation scheme we employ an array of K per-subcarrier MIMO-CTF estimators, which function independently of each other. Consequently, for the sake of notational simplicity we omit the subcarrier related index k in the following section.

2.9.1.1 LMS MIMO-CTF Estimator

The Least Mean Square (LMS) estimation method, which constitutes a simple approximation of the stochastic gradient algorithm [64], was invoked for the iterative tracking of the channel parameters in the context of turbo equalization [40]. More specifically, following the LMS approach, we are seeking to minimize the mean square error-based cost function J_{LMS}, which may be expressed as follows

$$J_{\mathrm{LMS}} = \sum_{m=1}^{n} \mathbf{e}^{\mathrm{H}}[m]\mathbf{e}[m], \tag{2.88}$$

where $\mathbf{e}[m]$ denotes the error signal, which is given by

$$\mathbf{e}[m] = \mathbf{y}[m] - \tilde{\mathbf{H}}[m]\hat{\mathbf{s}}[m], \tag{2.89}$$

where $\mathbf{y}[m]$ is the signal vector recorded at the n_{r} transmit antennas, while $\hat{\mathbf{s}}$ is the corresponding estimate of the m_{t}-dimensional transmitted signal.

Hence, analogously to the solution derived in [40], the LMS estimate of the $(n_{\mathrm{r}} \times m_{\mathrm{t}})$-dimensional MIMO-CTF coefficient matrix associated with the kth subcarrier of the nth OFDM symbol may be obtained as follows

$$\tilde{\mathbf{H}}[n] = \tilde{\mathbf{H}}[n-1] + (1-\zeta)\mathbf{e}[n]\hat{\mathbf{s}}^{\mathrm{H}}[n], \tag{2.90}$$

where we define the forgetting factor ζ. The resultant LMS MIMO-CTF tracking method is summarized in Algorithm 5.

Algorithm 6 *A Posteriori* RLS MIMO-CTF Tracking

$$\hat{\mathbf{s}}[n,k] = \texttt{Detect}\left\{\mathbf{y}[n,k], \check{\mathbf{H}}[n,k]\right\} \tag{2.97a}$$

$$\mathbf{\Phi}[n,k] = \zeta\mathbf{\Phi}[n-1,k] + \hat{\mathbf{s}}[n,k]\hat{\mathbf{s}}^{\mathrm{H}}[n,k] \tag{2.97b}$$

$$\boldsymbol{\theta}[n,k] = \zeta\boldsymbol{\theta}[n-1,k] + \hat{\mathbf{s}}[n,k]\mathbf{y}^{\mathrm{H}}[n,k] \tag{2.97c}$$

$$\tilde{\mathbf{H}}[n,k] = (\mathbf{\Phi}^{-1}[n,k]\boldsymbol{\theta}[n,k])^{\mathrm{H}} \tag{2.97d}$$

2.9.1.2 RLS MIMO-CTF Estimator

The Recursive Least Squares (RLS) algorithm [101] constitutes a rapidly-converging least squares algorithm. The RLS method was considered in the context of recursive channel parameter estimation and tracking by multiple authors [40, 46, 50, 81]. As opposed to the LMS approach outlined in Section 2.9.1.1, the RLS method attempts to minimize the cost function created from the exponentially-weighted and windowed sum of the squared error. Namely, we have

$$J_{\mathrm{RLS}}[n] = \sum_{m=1}^{n} \zeta^{n-m}\mathbf{e}^{\mathrm{H}}[m,n]\mathbf{e}[m,n], \tag{2.92}$$

where, analogously to the LMS method of Section 2.9.1.1, the corresponding error signal is given by

$$\mathbf{e}[m,n] = \mathbf{y}[m] - \tilde{\mathbf{H}}[n]\mathbf{s}[m], \tag{2.93}$$

while ζ denotes the forgetting factor. The corresponding RLS estimate of the $(n_{\mathrm{r}} \times m_{\mathrm{t}})$-dimensional MIMO-CTF coefficient matrix associated with the kth subcarrier of the nth OFDM symbol may be calculated as follows [40]

$$\tilde{\mathbf{H}}[n] = \left(\mathbf{\Phi}^{-1}[n]\boldsymbol{\theta}[n]\right)^{\mathrm{H}}, \tag{2.94}$$

where we define the MIMO-CTF estimator's input autocorrelation function $\mathbf{\Phi}[n]$, which may be calculated recursively as follows

$$\mathbf{\Phi}[n] = \sum_{m=1}^{n} \zeta^{n-m}\mathbf{s}[m]\mathbf{s}^{\mathrm{H}}[m] = \zeta\mathbf{\Phi}[n-1] + \mathbf{s}[n]\mathbf{s}^{\mathrm{H}}[n], \tag{2.95}$$

while the MIMO-CTF estimator's input-output crosscorrelation matrices $\boldsymbol{\theta}[n]$ as follows

$$\boldsymbol{\theta}[n] = \sum_{m=1}^{n} \zeta^{n-m}\mathbf{s}[m]\mathbf{y}^{\mathrm{H}}[m] = \zeta\boldsymbol{\theta}[n-1] + \mathbf{s}[n]\mathbf{y}^{\mathrm{H}}[n]. \tag{2.96}$$

The resultant RLS MIMO-CTF tracking method is summarized in Algorithm 6.

2.9.1.3 Soft-Feedback Aided RLS MIMO-CTF Estimator

As suggested by the *decision-directed* philosophy of the channel estimation scheme outlined in Section 2.9, the transmitted signal vector $\mathbf{s}[n]$ may not always be readily available at the receiver. More specifically, the transmitted signal vector $\mathbf{s}[n]$ may be assumed to be known *a priori* if and only if $\mathbf{s}$ constitutes a *pilot symbol*, which occupies a small portion of the transmitted data-stream. Alternatively, whenever an information-carrying data-symbol is transmitted, the decision-based estimates $\hat{\mathbf{s}}[n]$ become available instead. Unfortunately, however, the decision-based estimates $\hat{\mathbf{s}}$ are prone to decision errors, which may potentially result in *error propagation* and thus in a substantial performance degradation.

Consequently, as pointed out in [40, 46, 49], it is highly beneficial to exploit the probability-related soft information available at the output of the MIMO-OFDM system's detector. More specifically, in addition to the *hard*-decision based values of the transmitted signal estimates $\hat{\mathbf{s}}[n]$ we may utilize the associated *soft*-information-related quantities, such as the expectations and the variances of the elements of the estimated transmitted signal vector $\hat{\mathbf{s}} = [\hat{s}_1, \cdots, \hat{s}_{m_t}]^T$. Specifically, the expectation of the ith transmitted symbol may be expressed as follows

$$\tilde{s}_i = \mathtt{E}\left\{\hat{s}_i\right\} = \sum_{c\in\mathcal{M}} c\, p\{s_i = c\}, \tag{2.98}$$

while the corresponding variance is given by

$$v_i = \mathtt{Var}\left\{\hat{s}_i\right\} = \left(\sum_{c\in\mathcal{M}} cc^*\, p\{s_i = c\}\right) - \tilde{s}_i\tilde{s}_i^*. \tag{2.99}$$

Subsequently, we may define the following alternative error signals

$$\hat{\mathbf{e}}[m,n] = \mathbf{y}[m] - \tilde{\mathbf{H}}[n]\hat{\mathbf{s}}[m], \tag{2.100}$$

$$\tilde{\mathbf{e}}[m,n] = \mathbf{y}[m] - \tilde{\mathbf{H}}[n]\tilde{\mathbf{s}}[m]. \tag{2.101}$$

The error signals of Equations (2.100) and (2.101) may be substituted into the LMS and RLS algorithms of Sections 2.9.1.1 and 2.9.1.2 in order to yield the hard and soft decision-based LMS and RLS CTF tracking algorithms, respectively.

2.9.1.4 Modified-RLS MIMO-CTF Estimator

A further improved version of the soft decision-based RLS tracking algorithm, namely the so-called modified RLS algorithm was proposed by Otnes [40]. More specifically, in the modified RLS method the cost function of Equation (2.92) associated with the classic RLS method of Algorithm 6 is substituted by a cost function, which takes into account the ambiguity inherent in the decision-based estimates $\hat{\mathbf{s}}[n]$. Firstly, for the sake of notational convenience the following covariance matrices were defined in [40]

$$\mathbf{D}[n] = \mathtt{Cov}\left\{\tilde{\mathbf{s}}[n], \tilde{\mathbf{s}}[n]\right\} = \mathtt{E}\left\{\tilde{\mathbf{s}}[n]\tilde{\mathbf{s}}^{\mathtt{H}}[n]\right\} = \operatorname{diag}\left(\mathbf{v}[n]\right) \tag{2.102}$$

and

$$\boldsymbol{U}[n] = \mathtt{E}\left\{\mathbf{s}[n]\mathbf{s}^{\mathtt{H}}[n]\right\} = \tilde{\mathbf{s}}[n]\tilde{\mathbf{s}}^{\mathtt{H}}[n] + \mathbf{D}[n], \tag{2.103}$$

Algorithm 7 MIMO-CTF *A Posteriori* Modified-RLS Tracking

$$\{\hat{\mathbf{s}}[n,k],\tilde{\mathbf{s}}[n,k]\} = \texttt{Detect}\left\{\mathbf{y}[n,k],\check{\mathbf{H}}[n,k]\right\} \tag{2.108a}$$

$$\boldsymbol{U}[n,k] = \operatorname{diag}\left(|\hat{\mathbf{s}}[n,k]|^2 - |\tilde{\mathbf{s}}[n,k]|^2\right) + \tilde{\mathbf{s}}[n,k]\tilde{\mathbf{s}}[n,k]^{\mathtt{H}} \tag{2.108b}$$

$$\mathbf{d}[n,k] = \mathbf{y}[n,k] - \check{\mathbf{H}}[n,k]\tilde{\mathbf{s}}[n,k] \tag{2.108c}$$

$$\mathbf{\Phi}[n,k] = \zeta\mathbf{\Phi}[n,k] + \mathbf{U}[n,k] \tag{2.108d}$$

$$\boldsymbol{\theta}[n,k] = \zeta\boldsymbol{\theta}[n,k] + \mathbf{U}[n,k]\check{\mathbf{H}}[n,k] + \tilde{\mathbf{s}}[n,k]\mathbf{d}^{\mathtt{H}}[n,k] \tag{2.108e}$$

$$\hat{\mathbf{H}}[n,k] = (\mathbf{\Phi}^{-1}[n,k]\boldsymbol{\theta}[n,k])^{\mathtt{H}} \tag{2.108f}$$

where the elements of the variance vector $\mathbf{v}[n]$ are given by Equation (2.99). The corresponding modified RLS cost function may be expressed as follows [40]

$$J_{\text{modRLS}}[n] = \sum_{m=1}^{n} \zeta^{n-m}\mathtt{E}\left\{\tilde{\mathbf{e}}^{\mathtt{H}}[m,n]\tilde{\mathbf{e}}[m,n] \mid \mathbf{y}[m],\tilde{\mathbf{s}}[m],\mathbf{D}[m],\tilde{\mathbf{H}}[n]\right\}, \tag{2.104}$$

where as previously, ζ denoted the forgetting factor. Observe, that as opposed to the RLS cost function of Equation 2.92, the modified RLS cost function of Equation 2.104 takes into account the ambiguity associated with both the estimated CTF matrix $\tilde{\mathbf{H}}[n]$ as well as the estimated transmitted signal vector $\hat{\mathbf{s}}[n]$.

Finally, following the approach proposed in [40], the modified-RLS MIMO-CTF estimate $\hat{\mathbf{H}}[n]$ may be calculated using Equation (2.94), which is repeated here for convenience. Specifically, we have

$$\hat{\mathbf{H}}[n] = \left(\mathbf{\Phi}^{-1}[n]\boldsymbol{\theta}[n]\right)^{\mathtt{H}}, \tag{2.105}$$

where the corresponding covariance matrices $\mathbf{\Phi}[n]$ and $\boldsymbol{\theta}[n]$ may be reformulated using the quantities $\mathbf{D}[n]$ and $\boldsymbol{U}[n]$ of Equations 2.102 and 2.103, respectively. Namely, we have

$$\mathbf{\Phi}[n] = \sum_{m=1}^{n} \zeta^{n-m}\mathbf{U}[m] = \zeta\mathbf{\Phi}[n-1] + \mathbf{U}[n] \tag{2.106}$$

and

$$\begin{aligned}\boldsymbol{\theta}[n] &= \sum_{m=1}^{n} \zeta^{n-m}\left(\tilde{\mathbf{s}}[n]\mathbf{y}^{\mathtt{H}}[n] + \mathbf{D}[m]\hat{\mathbf{H}}^{\mathtt{H}}[m]\right)\\ &= \zeta\boldsymbol{\theta}[n-1] + \mathbf{U}[n]\hat{\mathbf{H}}^{\mathtt{H}}[n-1] + \tilde{\mathbf{s}}[n]\tilde{\mathbf{e}}^{\mathtt{H}}[n].\end{aligned} \tag{2.107}$$

The resultant soft decision-based MIMO-CTF modified-RLS method is summarized in Algorithm 7.

2.9.1.5 MIMO-CTF Estimator Performance Analysis

The snapshots of the CTF estimation MSE exhibited by both hard- and soft-feedback aided LMS and RLS MIMO-CTF tracking methods of Sections 2.9.1.1 and 2.9.1.2, respectively, as well as that of the modified RLS method of Section 2.9.1.4, are depicted in Figure 2.22. We considered the 4x4 MIMO-OFDM system characterized in Table 1.4. We assumed transmitting a sequence of signal bursts comprising 24 OFDM-symbols each. Furthermore, each signal burst was constituted by an 8-OFDM-symbols pilot frame, followed by a 16-OFDM-symbol data frame. Additionally, we assumed encountering an OFDM-symbol-normalized Doppler frequency of $f_D = 0.003$ and SNRs of 6.0 and 10.0 dB.

In Figure 2.22(a) we may observe that at low SNRs, where the system suffers from frequent decision errors, the hard-feedback aided LMS and RLS methods of Algorithms 5 and 6 exhibit a substantially worse performance than their soft-feedback aided counterparts. On the other hand, Figure 2.22(b), which corresponds to the higher SNR value of 10 dB, where we have a relatively low probability of decision-errors demonstrates that the hard-feedback aided RLS MIMO-CTF tracking method outperforms its soft-feedback assisted counterpart. Nevertheless, the slightly lower performance of the soft-feedback aided methods recorded at higher SNRs is a price worth paying for their significantly better robustness against error-propagation at lower SNRs. Additionally, we can see in both Figures 2.22(a) and 2.22(b) that the modified RLS method of Algorithm 7 exhibits the best MSE performance among the soft-feedback aided tracking methods considered.

Consequently, from the results of Figure 2.22 we may draw the conclusion that the soft-feedback aided modified RLS MIMO-CTF tracking method of Algorithm 7 exhibits the best combination of attractive MSE performance and a high robustness against error propagation.

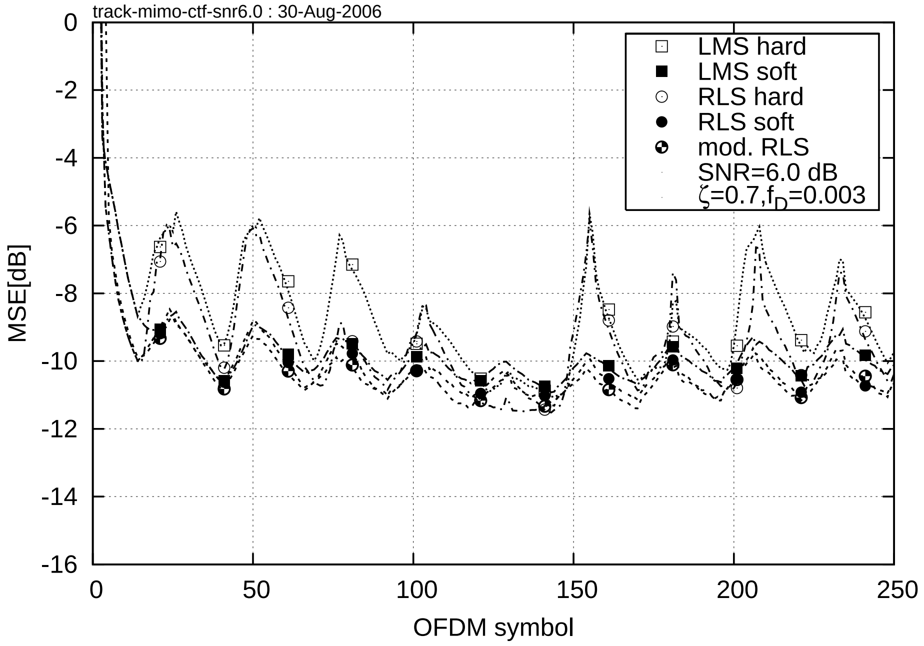

(a)

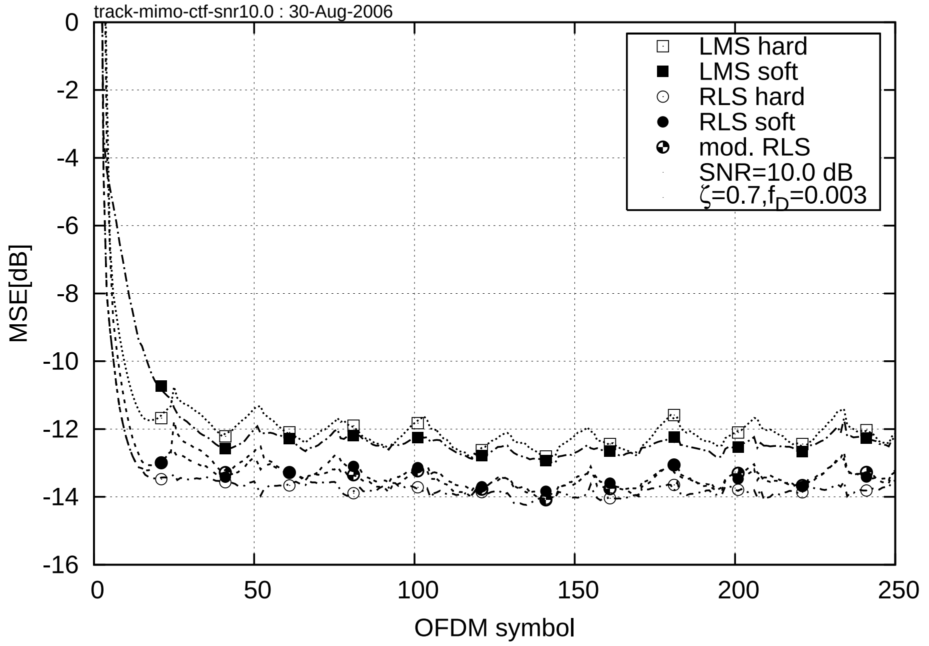

(b)

Figure 2.22: Snapshots of the **Mean Square Error** exhibited by both the hard- and soft-feedback aided recursive MIMO-CTF tracking methods of Sections 2.9.1.1, 2.9.1.2 and 2.9.1.4. We considered a 4x4 MIMO-OFDM system and a scenario of encountering an OFDM-symbol-normalized Doppler frequency of $f_D = 0.003$ as well as SNRs of (a) 6.0 dB and (b) 10.0 dB. The abscissa represents the index n of the received OFDM symbol.

2.9.2 PASTD -Aided DDCE for MIMO-OFDM

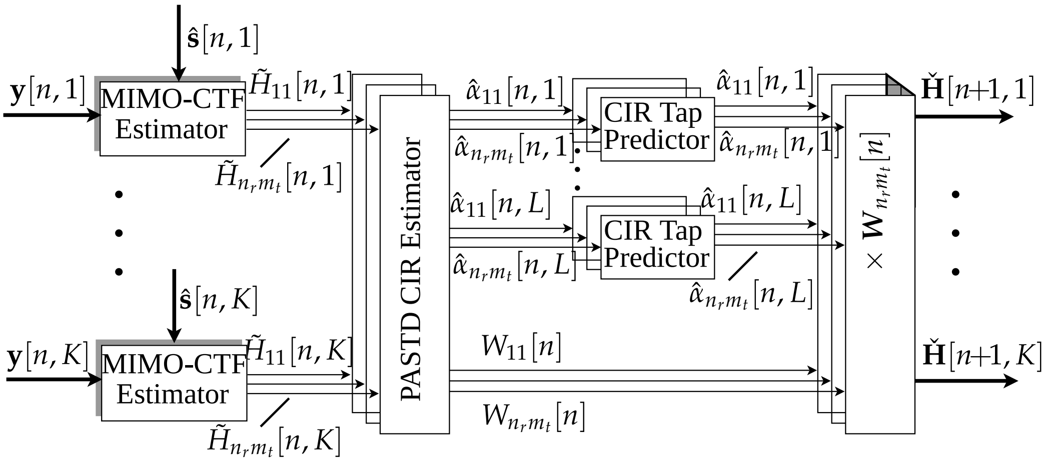

Figure 2.23: Detailed structure of the MIMO channel estimator corresponding to the DDCE module of Figure 2.1 in the context of the MIMO-OFDM system. The channel estimator comprises an array of PASTD modules, which performs recursive tracking of the MIMO-CIR. The resultant MIMO-CIR related taps $\hat{\alpha}_{ij;l}[n]$ are filtered by an array of adaptive RLS prediction filters resulting in the *a priori* estimates of the MIMO-CIR-related taps $\check{\alpha}_{ij;l}[n+1]$. Finally, the *a priori* estimates of the subcarrier-related coefficients $\check{\mathbf{H}}[n+1,k]$ are obtained by applying the array of transform matrices $\boldsymbol{W}_{ij}[n]$ provided by the PASTD modules.

As outlined in Section 2.9, we propose a MIMO channel estimation scheme, which follows the decision-directed channel estimation philosophy of Figure 2.1. The detailed structure of our MIMO-DDCE channel estimator is illustrated in Figure 2.23. More specifically, our MIMO channel estimation scheme comprises an array of K per-subcarrier MIMO-CTF estimators, followed by a $(n_{\mathrm{r}} \times m_{\mathrm{t}})$-dimensional array of parametric CIR estimators and a corresponding array of $(n_{\mathrm{r}} \times m_{\mathrm{t}} \times L)$ CIR tap predictors, where L is the number of tracked CIR taps per link for the MIMO channel. The structure of both the parametric PASTD -aided MIMO-CIR tap estimators and that of the RLS MIMO-CIR tap predictors is to a large extent identical to those devised in Sections 2.6.2 and 2.7.4 in the context of our SISO channel estimation scheme advocated in Section 2.8. On the other hand, our MIMO-CTF estimators may employ one of the recursive MIMO-CTF tracking methods outlined in Sections 2.9.1.1, 2.9.1.2, or 2.9.1.4.

The resultant MIMO-DDCE scheme illustrated in Figure 2.23 and employing the modified RLS MIMO-CTF estimator of Algorithm 7, the PASTD aided CIR estimator of Algorithm 2 as well as the RLS CIR tap predictor of Algorithm 3 is summarized in Algorithm 8.

Algorithm 8 PASTD -aided MIMO-DDCE

MIMO-CTF Tracking:

```
for  $k = 1, \ldots, K$  do
  $\boldsymbol{U}[n,k] = \mathrm{diag}\left(|\hat{\mathbf{s}}[n,k]|^2 - |\tilde{\mathbf{s}}[n,k]|^2\right) + \tilde{\mathbf{s}}[n,k]\tilde{\mathbf{s}}[n,k]^{\mathrm{H}}$    (2.109a)
  $\mathbf{d}[n,k] = \mathbf{y}[n,k] - \tilde{\mathbf{H}}[n,k]\tilde{\mathbf{s}}[n,k]$    (2.109b)
  $\mathbf{\Phi}[n,k] = \zeta\mathbf{\Phi}[n,k] + \mathbf{U}[n,k]$    (2.109c)
  $\boldsymbol{\theta}[n,k] = \zeta\boldsymbol{\theta}[n,k] + \mathbf{U}[n,k]\check{\mathbf{H}}[n,k] + \tilde{\mathbf{s}}[n,k]\mathbf{d}^{\mathrm{H}}[n,k]$    (2.109d)
  $\tilde{\mathbf{H}}[n,k] = (\mathbf{\Phi}^{-1}[n,k]\boldsymbol{\theta}[n,k])^{\mathrm{H}}$    (2.109e)
end for $k$
```

CIR Tracking:

```
for  $i = 1, \ldots, n_{\mathrm{r}}$  do,  for  $j = 1, \ldots, m_{\mathrm{t}}$  do
  $\boldsymbol{H}_1[n] = \hat{\boldsymbol{H}}_{ij}[n]$    (2.109f)
  for  $l = 1, 2, \ldots, L$  do
    $\hat{\alpha}_{ij;l}[n] = \boldsymbol{w}^{\mathrm{H}}_{ij;l}[n-1]\boldsymbol{H}_l[n]$    (2.109g)
    $\lambda_{ij;l}[n] = \eta\lambda_{ij;l}[n-1] + |\hat{\alpha}_{ij;l}[n]|^2$    (2.109h)
    $\boldsymbol{e}_l[n] = \boldsymbol{H}_l[n] - \boldsymbol{w}_{ij;l}[n-1]\hat{\alpha}_{ij;l}[n]$    (2.109i)
    $\boldsymbol{w}_{ij;l}[n] = \boldsymbol{w}_{ij;l}[n-1] + \boldsymbol{e}_l[n](\alpha^*_{ij;l}[n]/\lambda_{ij;l}[n])$    (2.109j)
    $\boldsymbol{H}_{l+1}[n] = \boldsymbol{H}_l[n] - \boldsymbol{w}_{ij;l}[n]\hat{\alpha}_{ij;l}[n]$    (2.109k)
  end for $l$
end for $i$,  end for $j$
```

CIR Prediction:

```
for  $i = 1, \ldots, n_{\mathrm{r}}$  do,  for  $j = 1, \ldots, m_{\mathrm{t}}$  do
  for  $l = 1, 2, \ldots, L$  do
    $e[n] = \hat{\alpha}_l[n] - \check{\alpha}_l[n] = \hat{\alpha}_l[n] - \boldsymbol{q}^{\mathrm{H}}_l[n-1]\hat{\boldsymbol{\alpha}}_l[n-1]$    (2.109l)
    $\boldsymbol{q}_l[n] = \boldsymbol{q}_l[n-1] + \boldsymbol{k}_l[n-1]e^*[n]$    (2.109m)
    $\check{\alpha}_l[n+1] = \boldsymbol{q}^{\mathrm{H}}_l[n]\hat{\boldsymbol{\alpha}}_l[n]$    (2.109n)
    $\boldsymbol{g}[n] = \boldsymbol{P}_l[n-1]\hat{\boldsymbol{\alpha}}_l[n]$    (2.109o)
    $\boldsymbol{k}_l[n] = \dfrac{\boldsymbol{g}[n]}{\beta + \hat{\boldsymbol{\alpha}}^{\mathrm{H}}_l[n]\boldsymbol{g}[n]}$    (2.109p)
    $\boldsymbol{P}_l[n] = \dfrac{1}{\beta}(\boldsymbol{I} - \boldsymbol{k}_l[n]\hat{\boldsymbol{\alpha}}^{\mathrm{H}}_l[n])\boldsymbol{P}_l[n-1]$    (2.109q)
  end for $l$
end for $i$,  end for $j$
```

CTF Reconstruction:

```
for  $i = 1, \ldots, n_{\mathrm{r}}$  do,  for  $j = 1, \ldots, m_{\mathrm{t}}$  do
  $\check{\boldsymbol{H}}_{ij}[n+1] = \boldsymbol{W}_{ij}[n]\check{\boldsymbol{\alpha}}_{ij}[n+1]$    (2.109r)
end for $i$,  end for $j$
```

2.9.2.1 PASTD -Aided MIMO-DDCE Performance Analysis

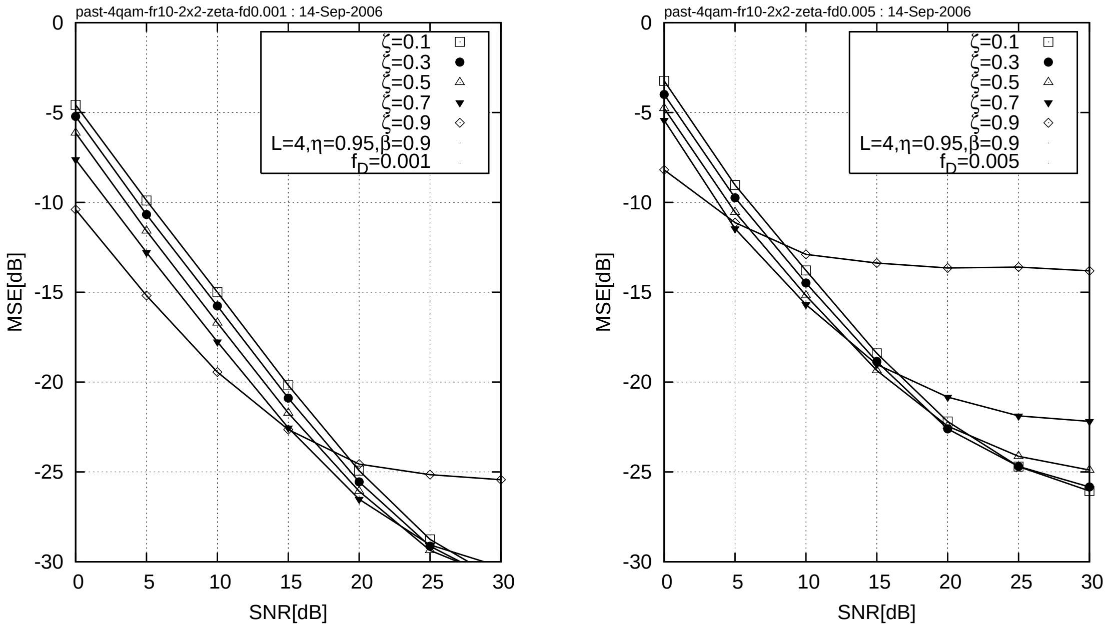

(a) (b)

Figure 2.24: The **Mean Square Error** exhibited by the **2x2 SDM-4QAM-OFDM** system employing the **SDM PASTD-aided DDCE** scheme of Algorithm 8. The PASTD-DDCE parameters are $\zeta = 0.1, 0.3, \cdots, 0.9$ as well as $\eta = 0.95$, $\beta = 0.9$. We considered the scenarios of encountering Doppler frequencies of (a) $f_D = 0.001$ and (b) $f_D = 0.005$. The abscissa represents the average SNR recorded at the receive antenna elements. We employ COST-207 BU channel model [119]. Additional system parameters are summarized in Table 1.4.

In this section we would like to characterize the achievable performance of the MIMO-DDCE scheme of Algorithm 8 in the context of the MIMO-OFDM system of Figure 1.13. More specifically, we consider a 2x2 MIMO-QPSK-OFDM system having $K = 128$ orthogonal QPSK-modulated subcarriers. The system parameters are outlined in Table 1.4. We employ an OFDM-frame-variant channel model having the time-variant 7-tap PDP characterized by the COST-207 BU channel model of [119], as detailed in Section 1.7.2. Additionally, each individual propagation path undergoes fast Rayleigh fading at an OFDM-symbol-normalized Doppler frequency of $f_D = 0.001$ and $f_D = 0.005$. The resultant channel can be characterised as a multi-path Rayleigh-fading channel with slowly-fluctuating PDP.

Firstly, Figure 2.24 characterizes the achievable MSE performance of the MIMO-DDCE method of Algorithm 8 for different values of the MIMO-CTF tracking scheme's forgetting factor ζ. Figures 2.24(a) and 2.24(b) correspond to encountering the Doppler frequencies of $f_D = 0.001$ and 0.005, respectively. As may be concluded from Figure 2.24, the optimum value of the forgetting factor ζ is largely dependent on the SNR as well as on the Doppler frequency encountered. Nevertheless, the compromise value of $\zeta = 0.7$ appears to constitute a relatively good choice in the practical range of SNR values and Doppler frequencies.

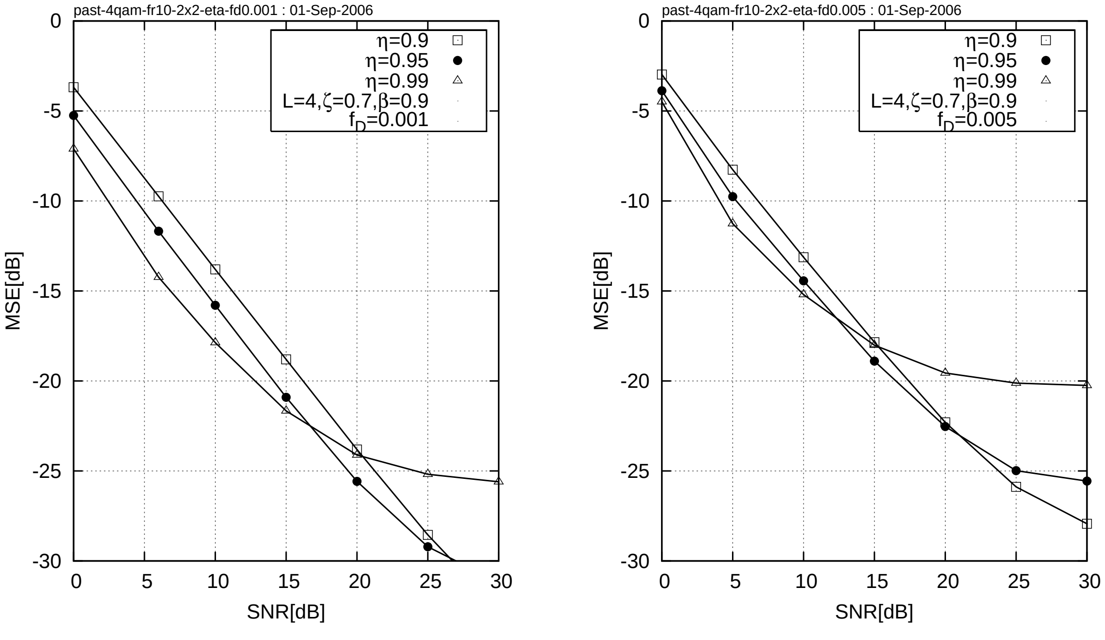

(a) (b)

Figure 2.25: The **Mean Square Error** exhibited by the 2×2 **SDM-4QAM-OFDM** system employing the **SDM PASTD-aided DDCE** scheme of Algorithm 8. The PASTD-DDCE parameters are $\eta = 0.9, 0.95$ and 0.99 as well as $\zeta = 0.7$, $\beta = 0.9$. We considered the scenarios of encountering the Doppler frequencies of (a) $f_D = 0.001$ and (b) $f_D = 0.005$. The abscissa represents the average SNR recorded at the receive antenna elements. We employ COST-207 BU channel model [119]. Additional system parameters are summarized in Table 1.4.

Secondly, Figure 2.25 characterizes the achievable MSE performance of the MIMO-DDCE method of Algorithm 8 for different values of the PASTD aided CIR tracking scheme's forgetting factor η. Figures 2.25(a) and 2.25(b) correspond to encountering the Doppler frequencies of $f_D = 0.001$ and 0.005, respectively. Similarly to the choice of the optimum MIMO-CTF tracking forgetting factor ζ, the optimum value of the PASTD aided CIR tracking forgetting factor η is largely dependent on the SNR as well as on the Doppler frequency encountered and the compromise value of $\eta = 0.95$ appears to constitute a good choice across the practical range of SNR values and Doppler frequencies.

Furthermore, Figure 2.26 characterizes the achievable MSE performance of the MIMO-DDCE method of Algorithm 8 for different ranks L of the PASTD aided CIR tracking-related estimated subspace, while assuming a constant value of the forgetting factors $\eta = 0.95$ and $\zeta = 0.7$. Figures 2.26(a) and 2.26(b) correspond to encountering the Doppler frequencies of $f_D = 0.001$ and 0.005, respectively. From Figure 2.26 we may conclude that a relatively high performance of the PASTD aided CIR estimator may be achieved when assuming that the rank of the estimated CTF signal subspace is $L = 4$, regardless of the actual number of paths constituting the multi-path CIR encountered.

In order to further characterize the performance of the resultant MIMO channel estimation scheme, we

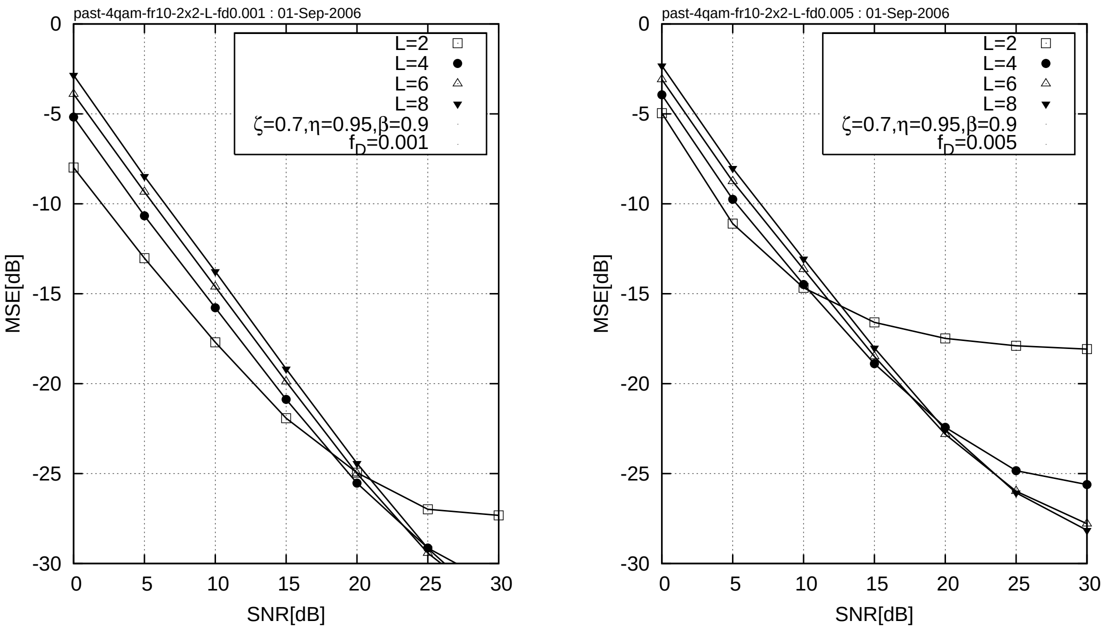

(a) (b)

Figure 2.26: The **Mean Square Error** exhibited by the **2x2 SDM-4QAM-OFDM** system employing the **SDM PASTD-aided DDCE** scheme of Algorithm 8 and tracking $L = 2, 4, 6$ and 8 CIR taps. The PASTD-DDCE parameters are $\zeta = 0.7, \eta = 0.95$ and $\beta = 0.9$. We considered the scenarios of encountering the Doppler frequencies of (a) $f_D = 0.001$ and (b) $f_D = 0.005$. The abscissa represents the average SNR recorded at the receive antenna elements. We employ COST-207 BU channel model [119]. Additional system parameters are summarized in Table 1.4.

would like to use the estimation efficiency criteria κ of Equation 2.85. In the case of a MIMO systems, the channel estimation efficiency factor κ may be redefined as follows

$$\kappa = \frac{1}{\sigma_e^2 \gamma} \frac{L m_{\rm t} n_{\rm r}}{K}, \tag{2.110}$$

where $L m_{\rm t} n_{\rm r}$ denotes the total number of the independent channel-related parameters estimated. The value of the channel estimation efficiency factor κ corresponding to the PAST-aided MIMO-DDCE scheme considered may be obtained empirically using the results depicted in Figure 2.26. Specifically we have $\kappa = -4dB$.

Finally, Figure 2.27 characterizes the achievable BER performance of the rate $\frac{1}{2}$ turbo-coded SDM-QPSK-OFDM system employing the MIMO-PASTD-DDCE method of Algorithm 8. The DDCE parameters are $\zeta = 0.7,\ L = 4,\ \eta = 0.95$ and $\beta = 0.9$. Furthermore, we assumed a pilot overhead of 10%. Figures 2.27(a) and 2.27(b) correspond to the 4x4 and 8x8 MIMO scenarios, respectively. We considered encountering the Doppler frequencies of $f_D = 0.001, 0.003$ and 0.005. Observe, that the system proposed attains a virtually error-free performance of a rate $1/2$ turbo-coded 8x8-QPSK-OFDM system, exhibiting a total bit rate of 8 bits/s/Hz and having a pilot overhead of only 10%, at SNR of 10dB and normalized Doppler frequency of 0.003, which corresponds to the mobile terminal speed of roughly 65 km/h[3].

---

[3] Additional system parameters are characterized in Table 1.4.

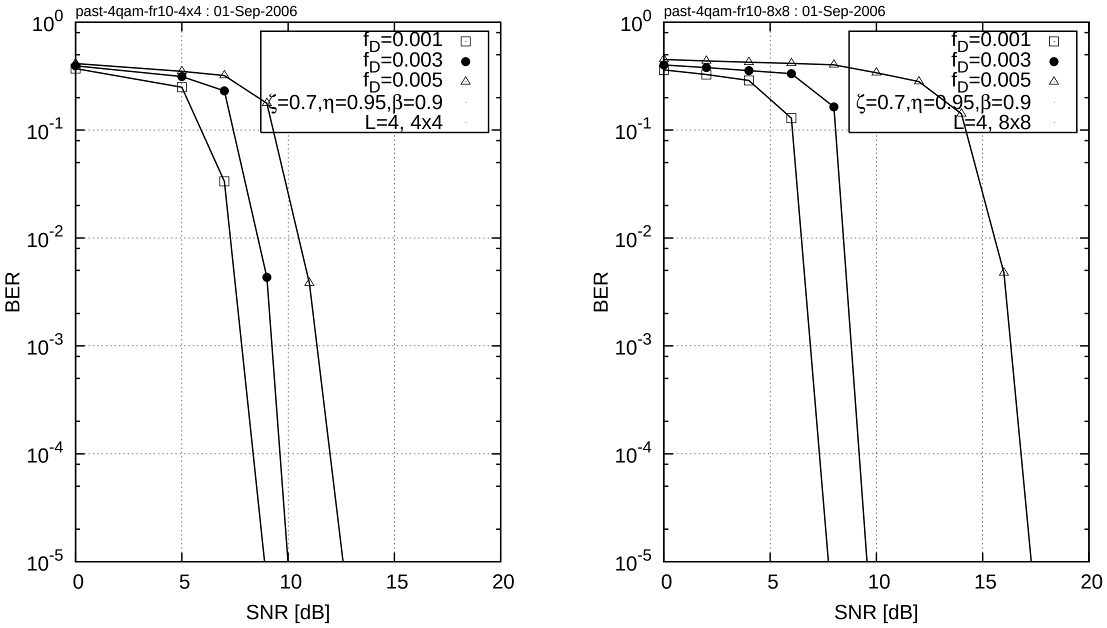

(a) (b)

Figure 2.27: **BER** versus **SNR** performance exhibited by the rate $\frac{1}{2}$ turbo-coded (a) 4x4 and (b) 8x8 **SDM-QPSK-OFDM** system employing the **MIMO-PASTD-DDCE** method of Algorithm 8. The abscissa represents the average SNR recorded at the receive antenna elements. We employ COST-207 BU channel model [119]. Additional system parameters are summarized in Table 1.4.

2.10 Conclusions

In this chapter we have developed a decision directed channel estimation scheme, which is suitable for employment in a wide range of multi-antenna multi-carrier communication systems. Our key findings may be summarized as follows:

- In Section 2.2 we have emphasised the significant advantages of the decision directed approach to channel estimation over its pilot-based counterpart.
- Correspondingly, in Section 2.3 we have derived a decision directed channel estimation scheme.
- In Section 2.4 we have discussed an MMSE CTF estimator and demonstrated its advantages in comparison to the LS-based CTF estimator.
- In Section 2.5 we discuss the benefits of employing the fractionally-spaced CIR-based channel estimation scheme in comparison to the conventional sample-spaced CIR-based approach.
- Furthermore, in order to facilitate a relatively low complexity FS-CIR estimation in Section 2.5 we employed a subspace tracking method, which is capable of recursive tracking the channel's delay profile.

- In Section 2.9 we have extended the scope of the proposed PASTD-aided DDCE scheme to the context of multi-antenna systems.

- Specifically, in Section 2.9.2.1 we demonstrated that an 8x8-QPSK-OFDM system, having a total bit rate of 8 bits/s/Hz and employing the soft-decision and PASTD aided MIMO-DDCE scheme of Algorithm 8, while having a pilot overhead of only 10% exhibits a virtually error-free performance at an SNR of 10dB.

- The optimum values of the relevant DDCE configuration parameters are summarized in Table 2.2.

Table 2.2: mRLS-PASTd-RLS MIMO-DDCE configuration parameters.

Parameter	Value
mRLS CTF estimator forgetting factor ζ	0.7
PASTd CIR estimator forgetting factor η	0.95
PASTd CIR estimator no. taps L	4
RLS CIR tap predictor forgetting factor β	0.9

Our future research is related to reducing the pilot-overhead required, potentially leading to semi-blind channel estimation schemes.

Chapter 3

Signal Detection for MIMO-OFDM Systems

3.1 Outline

In this chapter we would like to discuss and compare the performance of several SDM detection methods available in the literature. Specifically, in Section 3.3.1 we demonstrate that the linear increase in capacity, predicted by the information-theoretic analysis [29], may indeed be achieved by employing a relatively low-complexity linear SDM detection method, such as the MMSE SDM detection technique [101]. Secondly, in Section 3.4.1 we show that a substantially better performance can be achieved by employing a non-linear Maximum Likelihood (ML) SDM detector [83, 102, 103], which constitutes the optimal detection method from a probabilistic sequence-estimation point of view. To elaborate a little further, the ML SDM detector is capable of attaining transmit diversity in *fully-loaded* systems, where the number of transmit and receive antennas is equal. Moreover, as opposed to the linear detection schemes considered, the ML SDM detector is capable of operating in the *rank-deficient* system configuration, when the number of transmit antennas exceeds that of the receive antennas. Unfortunately, however, the excessive computational complexity associated with the exhaustive search employed by the ML detection method renders it inapplicable to practical implementation in systems having a large number of transmit antennas. Subsequently, in Sections 3.4.2 and 3.4.3 we explore a range of advanced non-linear SDM detection methods, namely the SIC and Genetic Algorithm-aided MMSE detection, respectively, where the latter may potentially constitute an attractive compromise between the low complexity of the linear SDM detection and the high performance of the ML SDM detection schemes. Indeed, we will demonstrate in Section 3.4.3 that the SDM detection method based on the SIC as well as on the GA-MMSE detector [100] are both capable of satisfying these requirements.

In Section 3.5 our discourse evolves further by proposing an enhancement of the SDMD schemes considered by employing both Space-Frequency Interleaving (SFI) and Space-Frequency Walsh-Hadamard Transform (SFWHT)-aided spreading. The performance benefits of employing SFI and SFWHT are quantified in

Section 3.5. Finally, our conclusions are summarized in Section 3.7.

3.2 SDM/V-BLAST OFDM Architecture

In a simple SDM/V-BLAST OFDM architecture [97] the incoming data-stream is demultiplexed into m_t parallel data-streams. Each of the resultant data-streams is independently channel encoded and OFDM-modulated. The resultant m_t OFDM-modulated signals are processed by a bank of m_t synchronised transmitters, which operate within the same frequency band. Each of the m_t transmitters comprises a conventional OFDM transmitter having K subcarriers and an OFDM-symbol period of T. In contrast to the D-BLAST scheme [84], the V-BLAST system configuration [97] imposes no special requirements on the particular structure of each of the multiple transmitters employed. Thus each of the transmitters can be thought of as a single-user transmitter employing a single transmit antenna. The SDM-OFDM architecture is illustrated in Figure 3.1. Observe that the structure of the SDM scheme depicted in Figure 3.1 is equally applicable to point-to-point SDM systems, as well as to systems supporting multiple users, each employing one or more transmit antennas. Consequently, the system configuration considered in this section is equivalent to the uplink multi-user SDMA-OFDM system discussed in [28].

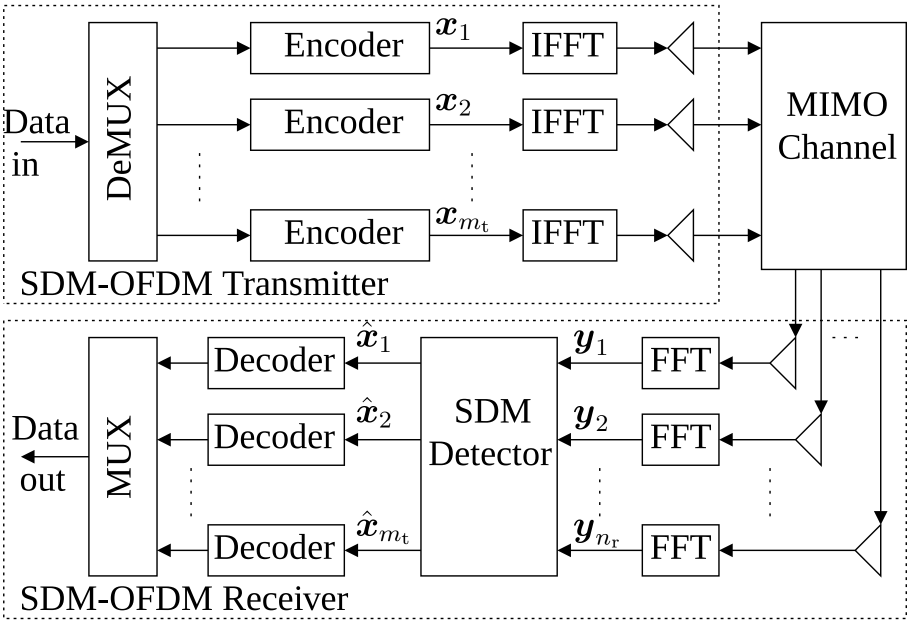

Figure 3.1: Schematic of an SDM-OFDM BLAST-type transceiver. In contrast to Figure 1.14, here the demultiplexed data substreams associated with different transmit antennas are channel encoded independently, which makes this system model equavalent to a multi-user SDMA system.

3.3 Linear Detection Methods

The simple phylosophy of the linear SDM detector is to recover the signal vector $\mathbf{x}[n,k] \in \mathbb{C}^{m_\mathrm{t}}$ transmitted from the m_t elements of the transmit antenna array at time instance n and OFDM-subcarrier k from the corresponding signal vector $\mathbf{y}[n,k] \in \mathbb{C}^{n_\mathrm{r}}$, which is described by the received signal vector of Equation (1.25) recorded at the n_r elements of the receiver antenna array at time instance n and OFDM-subcarrier k. More explicitly, we have

$$\hat{\mathbf{x}}[n,k] = \mathbf{W}^\mathrm{H}[n,k]\mathbf{y}[n,k], \tag{3.1}$$

where $\mathbf{W}[n,k] \in \mathbb{C}^{n_\mathrm{r}\times m_\mathrm{t}}$ is the corresponding linear SDM detector weight-matrix, which is designed to yield the optimal linear estimate of the transmitted signal vector $\mathbf{x}[n,k]$, as detailed henceforth.

By substituting Equation (1.25) into (3.1) we have

$$\begin{aligned}\hat{x}_i &= \mathbf{w}_i^\mathrm{H}\mathbf{y}\\ &= \mathbf{w}_i^\mathrm{H}(\mathbf{H}\mathbf{x}+\mathbf{v})\\ &= \underbrace{\mathbf{w}_i^\mathrm{H}(\mathbf{H})_i x_i}_{\hat{x}_{i;\mathrm{S}}} + \underbrace{\mathbf{w}_i^\mathrm{H}\sum_{j=1;j\neq i}^{m_\mathrm{t}}(\mathbf{H})_j x_j}_{\hat{x}_{i;\mathrm{I}}} + \underbrace{\mathbf{w}_i^\mathrm{H}\mathbf{v}}_{\hat{x}_{i;\mathrm{N}}} && (3.2)\\ &= H_{ii;\mathrm{eff}}x_i + v_{i;\mathrm{eff}}, && (3.3)\end{aligned}$$

where $(\mathbf{H})_i$ is the ith column of the channel matrix $\mathbf{H}$, while $\mathbf{w}_i$ denotes the ith column of the weight-matrix $\mathbf{W}$. We also define the corresponding additive components $\hat{x}_{i;\mathrm{S}}, \hat{x}_{i;\mathrm{I}}$ and $\hat{x}_{i;\mathrm{N}}$ of the estimated signal $\hat{x}_i$ as suggested by Equation (3.2), where the subscripts S, I and N denote the Signal, Interference and the AWGN-related Noise signal components, respectively. Furthermore, we define the corresponding quantities seen in Equation (3.3) as in [28], namely as

$$H_{ii;\mathrm{eff}} = \mathbf{w}_i^\mathrm{H}(\mathbf{H})_i \quad \text{and} \quad v_{i;\mathrm{eff}} = \hat{x}_{i;\mathrm{I}} + \hat{x}_{i;\mathrm{N}}, \tag{3.4}$$

which are the effective channel coefficient and the effective interference-plus-noise component, respectively.

The choice of the particular linear SDM detector weight-matrix $\mathbf{W}$ is dependent on the optimization criterion used. A number of examples of the relevant optimalisation criteria are discussed in [28] and include maximising the Signal-to-Interference Ratio (SIR) as in the Least Squares (LS) method, maximising the Signal-to-Interference-plus-Noise Ratio (SINR) as in Minimum Mean Square Error (MMSE) technique, as well as maximising the SIR, while ensuring a partial suppression of the AWGN as in the Minimum Variance (MV) method. When maximizing the SINR, which can be expressed as

$$SINR_i = \frac{\sigma_{i;S}^2}{\sigma_{i;I}^2 + \sigma_{i;N}^2}, \tag{3.5}$$

the associated MMSE method [28, Section 17.2.6.1] constitutes an optimal linear approach to the problem of the SDM detection. Thus, in this report we will limit our discussion of the linear SDM detection methods to the characterization of the MMSE SDM detector.

3.3.1 Minimum Mean Square Error Detection

As advocated in [28], the problem of maximizing the *SINR* of Equation (3.5) is equivalent to minimizing the mean square error at the output of the linear SDM detector of Equation (3.1). The MSE of the linear SDM detector of Equation (3.1) may be expressed as

$$\begin{aligned} MSE =& \mathrm{E}\left\{\Delta\mathbf{x}^{\mathrm{H}}\Delta\mathbf{x}\right\} \\ =& \mathrm{E}\left\{(\mathbf{x}-\mathbf{W}^{\mathrm{H}}\mathbf{y})^{\mathrm{H}}(\mathbf{x}-\mathbf{W}^{\mathrm{H}}\mathbf{y})\right\}. \end{aligned} \tag{3.6}$$

Differentiating the MSE of Equation (3.6) with respect to the elements of the liner SDM detector weight matrix **W** yields

$$\begin{aligned} \frac{\partial\, MSE}{\partial\mathbf{W}} =& \frac{\partial}{\partial\mathbf{W}}\sum_i \Delta x_i^*\Delta x_i \\ =& \mathrm{E}\left\{\sum_i\left(\frac{\partial}{\partial\mathbf{W}}\Delta x_i^*\ \Delta x_i + \Delta x_i^*\ \frac{\partial}{\partial\mathbf{W}}\Delta x_i\right)\right\} \\ =& -2\mathrm{E}\left\{\mathbf{y}(\mathbf{x}-\mathbf{W}^{\mathrm{H}}\mathbf{y})^{\mathrm{H}}\right\} \\ =& -2\mathrm{E}\left\{\mathbf{y}\Delta\mathbf{x}^{\mathrm{H}}\right\} = \mathbf{0} \qquad (3.7) \\ =& -2\mathrm{E}\left\{\mathbf{y}\mathbf{x}^{\mathrm{H}} - \mathbf{y}\mathbf{y}^{\mathrm{H}}\mathbf{W}\right\} \\ =& -2(\mathbf{R}_{yx} - \mathbf{R}_y\mathbf{W}) = \mathbf{0}, \qquad (3.8) \end{aligned}$$

where $\mathbf{0} \in \mathbb{C}^{n_{\mathrm{r}}\times m_{\mathrm{t}}}$ is a zero matrix, while the cross-correlation and auto-correlation matrices R_{yx} and R_y of the transmitted and received signals, respectively are given by

$$\begin{aligned} \mathbf{R}_{yx} =& \mathrm{E}\left\{(\mathbf{H}\mathbf{x}+\mathbf{v})\mathbf{x}^{\mathrm{H}}\right\} \\ =& \mathbf{H}\mathrm{E}\left\{\mathbf{x}\mathbf{x}^{\mathrm{H}}\right\} = \mathbf{H}\mathbf{R}_x \end{aligned} \tag{3.9}$$

and

$$\begin{aligned} \mathbf{R}_y =& \mathrm{E}\left\{(\mathbf{H}\mathbf{x}+\mathbf{v})(\mathbf{H}\mathbf{x}+\mathbf{v})^{\mathrm{H}}\right\} \\ =& \mathbf{H}\mathrm{E}\left\{\mathbf{x}\mathbf{x}^{\mathrm{H}}\right\}\mathbf{H}^{\mathrm{H}} + \mathrm{E}\left\{\mathbf{v}\mathbf{v}^{\mathrm{H}}\right\} \\ =& \mathbf{H}\mathbf{R}_x\mathbf{H}^{\mathrm{H}} + \mathbf{R}_v \\ =& \mathbf{H}\mathbf{R}_x\mathbf{H}^{\mathrm{H}} + \sigma_v^2\mathbf{I}. \end{aligned} \tag{3.10}$$

Observe that Equation (3.7) represents the so-called *orthogonality principle* [101]. More specifically, the extremum of the cost function defined by the MSE of Equation (3.6) occurs, when the estimation error signal $\Delta\mathbf{x}$ is orthogonal to the received signal $\mathbf{y}$. From Equation (3.8) we can deduce that

$$\mathbf{W}_{\mathrm{MMSE}} = (\mathbf{R}_y)^{-1}\mathbf{R}_{yx}. \tag{3.11}$$

Furthermore, substituting Equations (3.10) and (3.9) into (3.11) yields

$$\mathbf{W}_{MMSE} = (\mathbf{H}\mathbf{R}_x\mathbf{H}^{\mathrm{H}} + \sigma_v^2\mathbf{I})^{-1}\mathbf{H}\mathbf{R}_x. \tag{3.12}$$

Equation (3.12) may be further expanded as follows

$$\begin{aligned}\mathbf{W} =&(\mathbf{R}_x^{-1}\mathbf{H}^{-1}(\mathbf{H}\mathbf{R}_x\mathbf{H}^{\mathrm{H}} + \sigma_v^2\mathbf{I}))^{-1}\\ =&((\mathbf{H}^{\mathrm{H}}\mathbf{H}\frac{1}{\sigma_v^2}\mathbf{R}_x + \mathbf{I})\sigma_v^2\mathbf{R}_x^{-1}\mathbf{H}^{-1})^{-1}\\ =&\frac{1}{\sigma_v^2}\mathbf{H}\mathbf{R}_x(\mathbf{H}^{\mathrm{H}}\mathbf{H}\frac{1}{\sigma_v^2}\mathbf{R}_x + \mathbf{I})^{-1}.\end{aligned} \tag{3.13}$$

Finally, substituting the Hermitian transpose of the weight matrix $\mathbf{W}$ of Equation (3.13) into Equation (3.1) yields the MMSE SDM detector, which can be expressed as

$$\hat{\mathbf{x}} = (\mathbf{R}_{x;SNR}^{\mathrm{H}}\mathbf{H}^{\mathrm{H}}\mathbf{H} + \mathbf{I})^{-1}\mathbf{R}_{x;SNR}^{\mathrm{H}}\mathbf{H}^{\mathrm{H}}\mathbf{y}, \tag{3.14}$$

where we define the SNR-dependent auto-correlation matrix of the transmitted space-division signal vector $\mathbf{x}$ as $\mathbf{R}_{x;SNR} = \frac{1}{\sigma_v^2}\mathbf{R}_x$. In the typical case of mutually independent transmitted signal substreams $\mathbf{R}_{x;SNR}$ may be expressed as $\mathbf{R}_{x;SNR} = \mathrm{diag}\left(\sigma_i^2/\sigma_v^2\right)$, where σ_i^2 is the transmission power corresponding to the ith transmit antenna element. Furthermore, in the scenario, where all the transmit antenna elements transmit the same power $\sigma_i^2 = \sigma_x^2/m_{\mathrm{t}},\ i = 1, \cdots, m_{\mathrm{t}}$ we have

$$\mathbf{R}_{x;SNR} = \frac{\sigma_x^2}{m_{\mathrm{t}}\sigma_v^2}\mathbf{I} = \frac{\gamma}{m_{\mathrm{t}}}\mathbf{I}, \tag{3.15}$$

where as before, γ is the average SNR value recorded at the receive antenna elements. Hence, the expression in Equation (3.14) can be further simplified by substituting Equation (3.15) into (3.14), yielding

$$\hat{\mathbf{x}} = \left(\frac{\gamma}{m_{\mathrm{t}}}\mathbf{H}^{\mathrm{H}}\mathbf{H} + \mathbf{I}\right)^{-1}\frac{\gamma}{m_{\mathrm{t}}}\mathbf{H}^{\mathrm{H}}\mathbf{y}. \tag{3.16}$$

3.3.1.1 Generation of Soft-Bit Information for Turbo Decoding

The BER associated with the process of communicating over a fading noisy MIMO channel can be dramatically reduced by means of employing channel coding. A particularly effective channel coding scheme is constituted by the *soft-input soft-output* turbo coding method. Turbo coding however requires *soft* information concerning the bit decisions at the output of the SDM detector, in other words the *a posteriori* information regarding the confidence of the bit-decision is required.

The derivation of an expression for the low-complexity evaluation of the soft-bit information associated with the bit estimates of the linear SDM detector's output characterized by Equation (3.16) is given in [28]. Here, we present a brief summary of the results deduced in [28].

The soft-bit value associated with the mth bit of the QAM symbol transmitted from the ith transmit antenna element is determined by the log-likelihood function defined in [136]

$$L_{im} = \ln \frac{\mathrm{P}\left\{b_{im} = 1 | \hat{x}_i, H_{ii;\text{eff}}\right\}}{\mathrm{P}\left\{b_{im} = 0 | \hat{x}_i, H_{ii;\text{eff}}\right\}}, \tag{3.17}$$

which is the logarithm of the *a posteriori* probabilities' ratio associated with the logical values of 1 and 0 of the mth bit corresponding to the QAM symbol transmitted from the ith transmit antenna. The term $\hat{x}_i$ in Equation (3.17) denotes the estimate of the transmitted signal $\mathbf{x}$ obtained by applying the linear SDM detection method considered, while $H_{ii;\text{eff}}$ is the effective channel coefficient defined by Equation (3.2), which can be evaluated as the ith element on the main diagonal of the effective channel matrix given by $\mathbf{H}_{\text{eff}} = \mathbf{W}^{\text{H}}\mathbf{H}$, where $\mathbf{W}$ is the linear SDM detector's weight matrix associated with the particular linear SDM detection method employed. More explicitly, in the case of the MMSE SDM detector of Equation (3.16) we have

$$\mathbf{H}_{\text{eff}} = \left(\frac{\gamma}{m_{\text{t}}} \mathbf{H}^{\text{H}}\mathbf{H} + \mathbf{I} \right)^{-1} \frac{\gamma}{m_{\text{t}}} \mathbf{H}^{\text{H}}\mathbf{H}. \tag{3.18}$$

The PDF of Equation (3.17) can be expressed as [28, Section 17.2.5]

$$\mathrm{P}\left\{b_{im} = b \mid \hat{x}_i, H_{ii;\text{eff}}\right\} = \sum_{\check{x} \in \mathcal{M}_m^b} \mathrm{P}\left\{\check{x}_i | \hat{x}_i, H_{ii;\text{eff}}\right\}, \tag{3.19}$$

where $\mathcal{M}_m^b$ denotes the specific subset of the total set $\mathcal{M}$ of constellation points associated with the modulation scheme employed, which have a logical value b at their mth bit position, namely we have

$$\mathcal{M}_m^b = \{\, \check{x} \,|\check{x} \in \mathcal{M}, b_m = b\}, \quad b \in \{0, 1\} \tag{3.20}$$

and b_m denotes the mth bit associated with the constellation point $\check{x}$. Furthermore, it is demonstrated in [28, Section 17.2.5] that

$$\mathrm{P}\left\{\check{x}_i | \hat{x}_i, H_{ii;\text{eff}}\right\} = \frac{1}{(\pi \sigma^2_{v_{i;\text{eff}}})} \exp\left(-\frac{1}{\sigma^2_{v_i;\text{eff}}} |\hat{x}_i - H_{ii;\text{eff}}\check{x}_i|^2 \right). \tag{3.21}$$

Consequently, substituting Equation (3.19) and (3.21) into (3.17) yields

$$L_{im} = \ln \frac{\sum_{\check{\mathbf{x}} \in \mathcal{M}^1} \exp\left(-\frac{1}{\sigma^2_{v_{i;\text{eff}}}} |\hat{x}_i - H_{ii;\text{eff}}\check{x}_i^0|^2 \right)}{\sum_{\check{\mathbf{x}} \in \mathcal{M}^0} \exp\left(-\frac{1}{\sigma^2_{v_{i;\text{eff}}}} |\hat{x}_i - H_{ii;\text{eff}}\check{x}_i^1|^2 \right)}. \tag{3.22}$$

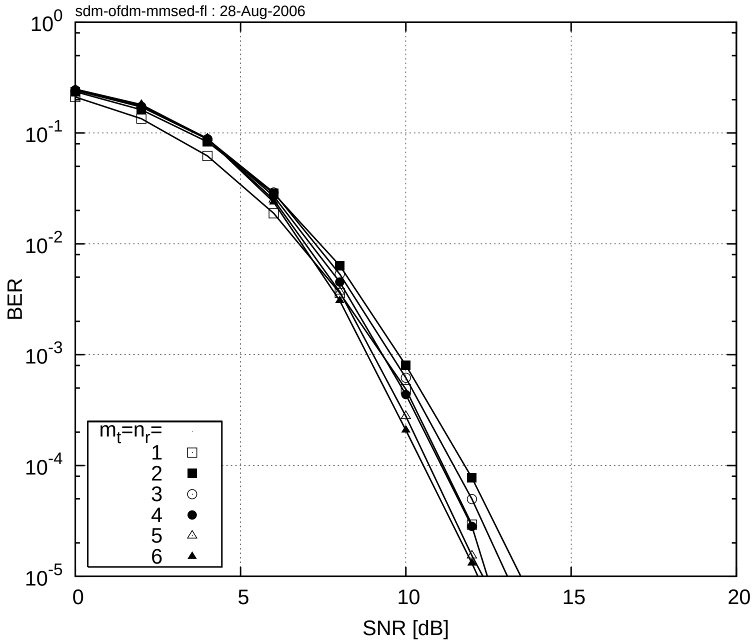

Figure 3.2: Bit Error Rate exhibited by the QPSK-modulated **SDM-OFDM** system employing an **MMSE** SDM detector of Equation (3.14) and $m_\mathrm{t} = n_\mathrm{r} = 1, \cdots, 6$ transmit and receive antennas. The abscissa represents the average SNR recorded at the receive antenna elements. The system parameters are summarized in Table 2.1.

3.3.1.2 Performance Analysis of the Linear SDM Detector

In this section, we present our simulation results for the SDM-OFDM system employing the MMSE SDM detection schemes described in Section 3.3.1.

Our simulations were performed in the base-band frequency domain and the system configuration characterised in Table 2.1 is to a large extent similar to that used in [38]. We assume having a total bandwidth of 800kHz. The OFDM system utilises 128 QPSK-modulated orthogonal subcarriers. For Forward Error Correction (FEC) we use $\frac{1}{2}$-rate turbo coding [26] employing two constraint-length $K = 3$ Recursive Systematic Convolutional (RSC) component codes and the standard 124-bit WCDMA UMTS turbo code interleaver of [131]. The octally represented RCS generator polynomials of (7,5) were used. Finally, throughout this report we stipulate the assumption of perfect channel knowledge, where the knowledge of the frequency-domain subcarrier-related coefficients $H[n,k]$ is deemed to available in the receiver.

Figure 3.2 demonstrates the ability of the SDM-OFDM system employing the **MMSE** SDM detector of Equation (3.16) to exploit the available MIMO channel capacity gain in the **fully loaded** system configuration, namely when the number of the transmit antenna elements m_t is equal to that of the receiver antenna elements n_r. Figure 3.2 depicts the achievable **BER** performance of the SDM-OFDM system considered as a function of the average SNR recorded at each of the receiver antenna elements. More explicitly, the results depicted in Figure 3.2 illustrate that the SDM-OFDM system employing $m_\mathrm{t} = n_\mathrm{r} = 6$ transmit and

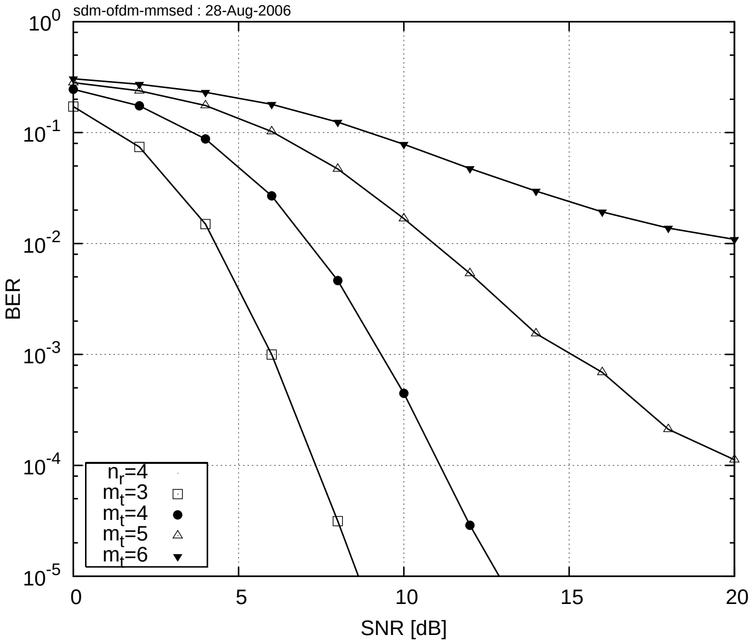

Figure 3.3: Bit Error Rate performance exhibited by the **SDM-QPSK-OFDM** system employing an **MMSE** SDM detector of Equation (3.14) and $m_t = 3, 4, 5$ and 6 transmit antennas, as well as $n_r = 4$ receive antennas. The abscissa represents the average SNR recorded at the receive antenna elements. The system parameters are summarized in Table 2.1.

receive antennas, as well as the **MMSE** SDM detector of Equation (3.16) is capable of achieving an SNR gain of about 1dB at the target BER of 10^{-3}, when compared to the same system employing a single antenna element at both the transmitter and receiver.

Figure 3.3 demonstrates the SDM-OFDM system's capability to detect the spatially multiplexed signals arriving from various number of transmit antennas, when employing the MMSE SDM detection method of Equation (3.16) and having a constant number of $n_r = 4$ receive antenna elements. Specifically, we aim for exploring the performance of the MMSE SDM detector in the **over-loaded** system scenario, where the number of transmit antenna elements exceeds that of the receiver elements. Figure 3.3 demonstrates the achievable BER performance of the MMSE SDM detector considered as a function of the average SNR recorded at each of the receiver antenna elements. We can see that the MMSE SDM detector exhibits a relatively good performance, whenever the number of transmit antenna elements is lower than or equal to the number of the receiver antenna elements. As seen in Figure 3.3, the system exhibits a diversity gain of about 2dB recorded in terms of the SNR at the target BER of 10^{-3}, when comparing the scenarios of $m_t = 3$ and $m_t = 4$ receiver antenna elements. On the other hand, however, the MMSE SDM detector of Equation (3.16) exhibits a severe performance degradation in the **over-loaded** scenario, namely when we have $m_t > n_r$, which is confirmed by the curves corresponding to the scenarios of $m_t = 5$ and 6 characterised in Figure 3.3.

3.4 Non-Linear SDM Detection Methods

In Section 3.3 we discussed the linear approach to the problem of SDM detection. The major advantage of the linear detection strategy is its conceptual simplicity and corresponding low computational complexity. Unfortunately however, as it is evident from our discussions in Section 3.3, the output of the linear SDM detector contains a substantial amount of residual interference.

In this section we explore a family of **non-linear** SDM detection methods. We would like to commence our discourse with the derivation of the Maximum Likelihood (ML) SDM detection method, which constitutes an optimal solution of the SDM detection problem from the maximum likelihood sequence detection point of view. Unfortunately however, the brute-force ML detection method does not provide a feasible solution to the generic SDM detection problem as a result of its excessive computational complexity. Nevertheless, it provides an important benchmark for the overall achievable performance of a generic SDM detector.

We will then continue our discussions by considering two additional non-linear SDM detection methods, which achieve a sub-optimal performance at a realistic computational complexity. More explicitly, in Section 3.4.2 we will consider the SIC-aided SDM detection method. Furthermore, in Section 3.4.3 we will invoke the Genetic Algorithm-aided MMSE SDM detector.

3.4.1 Maximum Likelihood Detection

The ML method [28, 71, 137] constitutes an optimal SDM detection method in the sense of an *a posteriori* probability. The simple philosophy of the ML detection is based on an exhaustive search through **all possible** values of the transmitted signal vector $\mathbf{x}$ with the aim of determining the value, which is most likely to have been transmitted. Clearly, the major drawback of this strategy is its excessive computational complexity. Specifically, the number of potential candidate values of the signal vector $\mathbf{x}[n,k]$ of the m_{t} transmit antennas associated with the kth OFDM subcarrier of the nth OFDM symbol is given by $M^{m_{\mathrm{t}}} = 2^{rm_{\mathrm{t}}}$, where M is the number of phasor-constellation points comprising the M-QAM/M-PSK constellation employed, while r is the corresponding number of bits per M-QAM/M-PSK modulated symbol. More explicitly, this relationship suggests that the number of the potential signal vector candidates to be examined by the ML detector increases exponentially with the number of transmitter antennas, as well as with the number of bits per modulated symbol. The resultant computational complexity may become excessive for systems employing a high number of transmit antennas and/or high-level modulation schemes, which renders it unsuitable for practical applications. As noted above, however, the performance of the ML SDM detector constitutes an important benchmarker for the performance evaluation of other, more practical SDM detection schemes.

Let us recall that our channel model described by Equation (1.25) was given by

$$\mathbf{y} = \mathbf{H}\mathbf{x} + \mathbf{w}, \tag{3.23}$$

where, as before, we omit the OFDM subcarrier and symbol indices k and n, respectively. As outlined above, the output of the ML SDM detector considered comprises a signal vector candidate $\hat{\mathbf{x}}$, which maximises the *a posteriori* probability function

$$\hat{\mathbf{x}} = \arg \max_{\check{\mathbf{x}} \in \mathcal{M}^{m_\mathrm{t}}} \mathrm{P}\left\{\check{\mathbf{x}} | \mathbf{y}, \mathbf{H}\right\}, \tag{3.24}$$

where $\mathcal{M}^{m_\mathrm{t}}$ is the set of **all possible** candidate symbol values of the transmitted signal vector $\mathbf{x}$, namely we have

$$\mathcal{M}^{m_\mathrm{t}} = \left\{\check{\mathbf{x}} = (\check{x}_1, \cdots, \check{x}_{m_\mathrm{t}})^\mathrm{T};\ \check{x}_i \in \mathcal{M}\right\} \tag{3.25}$$

and $\mathcal{M}$ denotes the entire set of M complex constellation points associated with the particular M-QAM/M-PSK modulation scheme employed.

It follows from the Bayes' theorem [136] that the conditional probability of Equation (3.24) can be expressed as

$$\mathrm{P}\left\{\check{\mathbf{x}} | \mathbf{y}, \mathbf{H}\right\} = \mathrm{P}\left\{\mathbf{y} | \check{\mathbf{x}}, \mathbf{H}\right\} \frac{\mathrm{P}\left\{\check{\mathbf{x}}\right\}}{\mathrm{P}\left\{\mathbf{y}\right\}}, \tag{3.26}$$

where all possible values of the transmitted signal vector $\check{\mathbf{x}}$ are assumed to be equally probable and therefore we have $\mathrm{P}\left\{\check{\mathbf{x}}\right\} = 1/M^{m_\mathrm{t}} = const$. Moreover, we have

$$\mathrm{P}\left\{\mathbf{y}\right\} = \sum_{\check{\mathbf{x}} \in \mathcal{M}^{m_\mathrm{t}}} \mathrm{P}\left\{\mathbf{y} | \check{\mathbf{x}}, \mathbf{H}\right\} \mathrm{P}\left\{\check{\mathbf{x}}\right\} = const., \tag{3.27}$$

which follows from the probability function normalisation property of

$$\sum_{\check{\mathbf{x}} \in \mathcal{M}^{m_\mathrm{t}}} \mathrm{P}\left\{\check{\mathbf{x}} | \mathbf{y}, \mathbf{H}\right\} \equiv 1. \tag{3.28}$$

We can therefore infer that

$$\hat{\mathbf{x}} = \arg \max_{\check{\mathbf{x}} \in \mathcal{M}^{m_\mathrm{t}}} \mathrm{P}\left\{\check{\mathbf{x}} | \mathbf{y}, \mathbf{H}\right\} \quad \Leftrightarrow \quad \hat{\mathbf{x}} = \arg \max_{\check{\mathbf{x}} \in \mathcal{M}^{m_\mathrm{t}}} \mathrm{P}\left\{\mathbf{y} | \check{\mathbf{x}}, \mathbf{H}\right\}. \tag{3.29}$$

As it was pointed out in [28], the signal vector $\mathbf{y}$ recorded at the n_r receive antenna elements can be represented as a sample of multi-variate complex Gaussian distributed random variables with the mean $\mathbf{H}\mathbf{x}$ and the covariance matrix given by Equation (3.10), which may be summarised as $\mathbf{y} \sim \mathcal{CN}(\mathbf{H}\mathbf{x}, \mathbf{R}_y)$, where we denote the complex-values normal distribution having a mean given by the vector $\boldsymbol{\mu}$ and the covariance matrix $\mathbf{C}$ as $\mathcal{CN}(\boldsymbol{\mu}, \mathbf{C})$. The corresponding Probability Density Function (PDF) can be thus expressed as in [101]

$$\mathrm{P}\left\{\mathbf{y} | \mathbf{x}, \mathbf{H}\right\} = \frac{1}{(\pi\sigma_w^2)^{n_\mathrm{r}}} \exp\left(-\frac{1}{\sigma_w^2}\|\mathbf{y} - \mathbf{H}\mathbf{x}\|_2^2\right). \tag{3.30}$$

The PDF in Equation (3.30) has a form of $\mathtt{P}\{J\} = \alpha e^{-\beta J}$, where α and β are constants and we define $J(\check{\mathbf{x}}) = \|\mathbf{y} - \mathbf{H}\check{\mathbf{x}}\|_2^2$. Clearly, $\mathtt{P}\{J\}$ is a monotonically decreasing function of its argument J. Consequently, the maximum of the *a posteriori* probability function of Equation (3.24) can be substituted by the minimum of the corresponding argument $J(\check{\mathbf{x}})$, such that we have

$$\hat{\mathbf{x}} = \arg \min_{\check{\mathbf{x}} \in \mathcal{M}^{m_\mathrm{t}}} J(\check{\mathbf{x}}), \tag{3.31}$$

where again, $J(\check{\mathbf{x}})$ is defined as an Euclidean distance-based cost-function, which may be expressed as

$$J(\check{\mathbf{x}}) = \|\mathbf{y} - \mathbf{H}\check{\mathbf{x}}\|_2^2 = \sum_{i=1}^{m_\mathrm{t}} \left| y_i - \sum_{j=1}^{n_\mathrm{r}} H_{ij}\check{x}_j \right|^2 . \tag{3.32}$$

3.4.1.1 Generation of Soft-Bit Information

Based on our arguments in Section 3.3.1.1, the soft-bit value associated with the mth bit of the QAM symbol transmitted from the ith transmit antenna element is determined by the log-likelihood function defined in [136]

$$L_{mi} = \ln \frac{\sum_{\check{\mathbf{x}} \in \mathcal{M}_{mi}^{1;m_\mathrm{t}}} \mathtt{P}\{\mathbf{y}|\check{\mathbf{x}}, \mathbf{H}\}}{\sum_{\check{\mathbf{x}} \in \mathcal{M}_{mi}^{0;m_\mathrm{t}}} \mathtt{P}\{\mathbf{y}|\check{\mathbf{x}}, \mathbf{H}\}}; \tag{3.33}$$

where we define

$$\mathcal{M}_{mi}^{b;m_\mathrm{t}} = \left\{ \check{\mathbf{x}} = (\check{x}_1, \cdots, \check{x}_{m_\mathrm{t}})^\mathrm{T};\ \check{x}_j \in \mathcal{M} \text{ for } j \neq i,\ \check{x}_i \in \mathcal{M}_m^b \right\} \tag{3.34}$$

and $\mathcal{M}_m^b$ denotes the specific subset of the entire set $\mathcal{M}$ of constellation points of the modulation scheme employed, which comprises the bit value $b = \{0, 1\}$ at the mth bit position.

Substituting Equation (3.30) into (3.33) yields

$$L_{mi} = \ln \frac{\sum_{\check{\mathbf{x}} \in \mathcal{M}_{mi}^{1;m_\mathrm{t}}} \exp\left(-\frac{1}{\sigma_w^2}\|\mathbf{y} - \mathbf{H}\check{\mathbf{x}}\|^2\right)}{\sum_{\check{\mathbf{x}} \in \mathcal{M}_{mi}^{0;m_\mathrm{t}}} \exp\left(-\frac{1}{\sigma_w^2}\|\mathbf{y} - \mathbf{H}\check{\mathbf{x}}\|^2\right)}. \tag{3.35}$$

Note that Equation (3.35) involves summation over $2^{rm_\mathrm{t}-1}$ exponential functions. This operation may potentially impose an excessive computational complexity for large values of m_t and/or r. As demonstrated in [28] however, the expression in (3.35) may be closely approximated by a substantially simpler expression, namely by

$$L_{mi} \approx \frac{1}{\sigma_w^2} \left[\|\mathbf{y} - \mathbf{H}\check{\mathbf{x}}_m^0\|^2 - \|\mathbf{y} - \mathbf{H}\check{\mathbf{x}}_m^1\|^2 \right], \tag{3.36}$$

where we have

$$\check{\mathbf{x}}_m^b = \arg \min_{\check{\mathbf{x}} \in \mathcal{M}_{mi}^{b;m_\mathrm{t}}} \|\mathbf{y} - \mathbf{H}\check{\mathbf{x}}\|^2, \quad b = 0, 1. \tag{3.37}$$

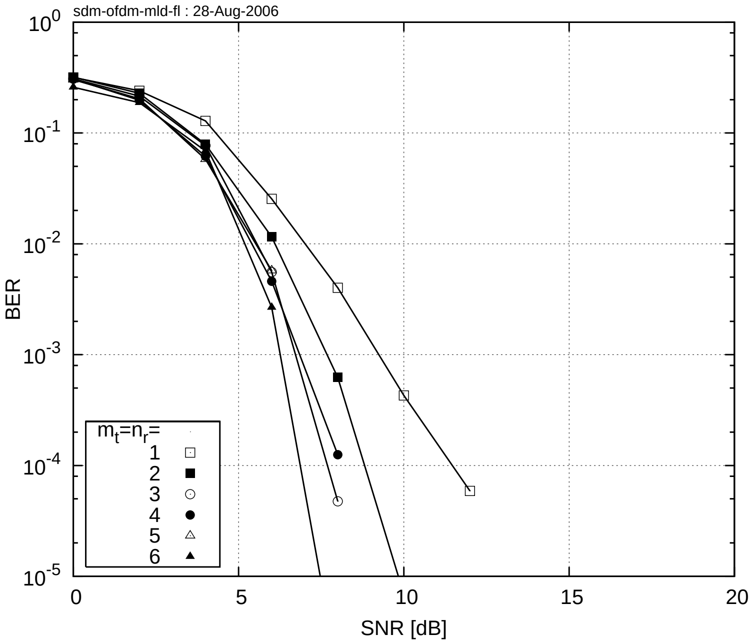

Figure 3.4: Bit Error Rate exhibited by the QPSK-modulated **SDM-OFDM** system employing an **ML** SDM detector of Equation (3.24) and $m_t = n_r = 1, \cdots, 6$ transmit and receive antennas. The abscissa represents the average SNR recorded at the receive antenna elements. The system parameters are summarized in Table 2.1.

3.4.1.2 Performance Analysis of the ML SDM Detector

In this section, we present our simulation results characterizing the SDM-OFDM system employing the ML SDM detection schemes described in Section 3.4.1. Our simulation setup is identical to that described in Section 3.3.1.2 and the corresponding simulation parameters are summarised in Table 2.1.

Figure 3.4 demonstrates that the SDM-OFDM system employing the **ML** SDM detector of Equation (3.31) is capable of exploiting the available MIMO channel's **multiplexing gain** in the **fully loaded** system scenario, when the number of the transmit antenna elements m_t is equal to that of the receiver antenna elements n_r. More specifically, Figure 3.4 depicts the achievable **BER** performance of the SDM-OFDM ML detector considered as a function of the average SNR recorded at the receiver antenna elements.

The results depicted in Figure 3.4 illustrate that the SDM-OFDM ML detector having $m_t = n_r = 6$ transmit and receive antennas exhibits an SNR gain of 3dB at the target BER of 10^{-3}, when compared to the same system employing a single antenna element at both the transmitter and receiver, as well as a factor six higher throughput.

Additionally, Figure 3.5 characterizes the capability of the SDM-OFDM system employing the **ML** SDM detector of Equation (3.31) and having a constant number of $n_r = 4$ receive antenna elements, to detect the multiplexed signals arriving from various numbers of transmit antenna elements. Specifically,

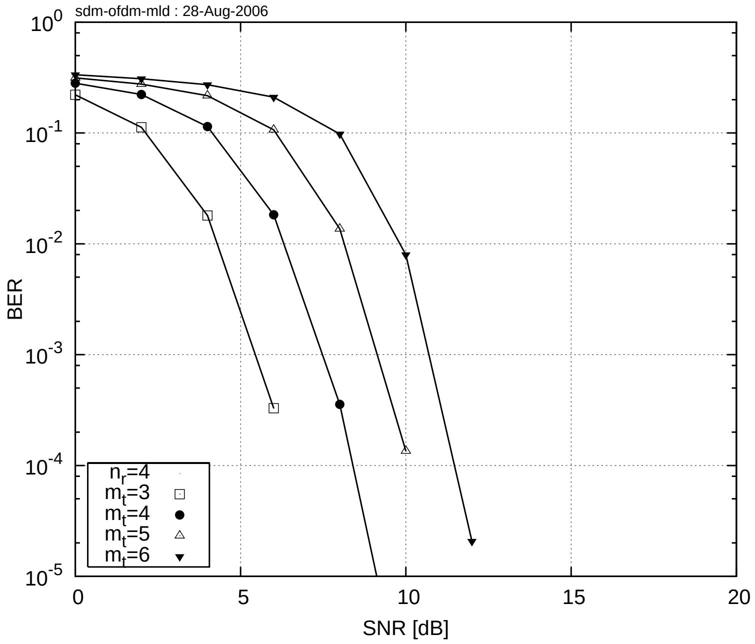

Figure 3.5: Bit Error Rate performance exhibited by the **SDM-QPSK-OFDM** system employing an **ML** SDM detector of Equation (3.24) and $m_{\rm t} = 3, 4, 5$ and 6 transmit antennas, as well as $n_{\rm r} = 4$ receive antennas. The abscissa represents the average SNR recorded at the receive antenna elements. The system parameters are summarized in Table 2.1.

we aim for exploring the performance of the **ML** SDM detector in the **overloaded** system scenario, where the number of transmit antenna elements exceeds that of the receiver elements and thus we have $m_{\rm t} > n_{\rm r}$. Figure 3.5 demonstrates the achievable BER performance of the SDM-OFDM system employing the **ML** SDM detector as a function of the average SNR recorded at the receive antenna elements. We can see that as opposed to the MMSE SDM detector discussed in Section 3.4.1, the **ML** SDM detector exhibits a good performance both when we have $m_{\rm t} \leq n_{\rm r}$, as well as in the overloaded system scenario, when the number of transmit antenna elements exceeds the number of the receive antenna elements, *i. e.* when we have $m_{\rm t} > n_{\rm r}$.

3.4.2 SIC Detection

The SIC-assisted SDM detector was proposed by Foschini *et al.* in [84] and it was discussed in further detail in [97, 98, 138–140].

In order to commence our discourse, let us recall the philosophy of the linear SDM detector discussed in Section 3.3, where the detection of the transmitted signal vector $\mathbf{x}[n,k]$ was performed using a linear transformation described by Equation (3.1), namely by

$$\hat{\mathbf{x}}[n,k] = \mathbf{W}^{\rm H}[n,k]\mathbf{y}[n,k], \tag{3.38}$$

where $\mathbf{W}[n,k] \in \mathbb{C}^{n_{\rm r} \times m_{\rm t}}$ is the corresponding linear SDM detector weight-matrix.

As it was further inferred in Section 3.3, the corresponding SINR at the output of the linear SDM detector may vary considerably across different elements of the transmitted signal vector $\mathbf{x}[n,k]$, as substantiated by Equation (3.5). Consequently, as suggested in [28], the overall MSE at the output of the linear SDM detector employed is dominated by the SINR associated with the transmitted signal component having the lowest signal power [28] determined by $\sum_j |H_{ij}|^2$. This observation suggests that a considerably higher performance can be achieved by employing successive interference cancellation.

Following the SIC paradigm, the detection of the transmitted signal vector $\mathbf{x}[n,k]$ associated with the kth OFDM subcarrier of the nth OFDM symbol is performed in a successive manner, where at each detection iteration i we detect a single vector component $x_i[n,k]$ using the linear MMSE SDM detection method discussed in Section 3.3.1. We then modify the received signal vector $\mathbf{y}[n,k]$ by removing the remodulated interfering signal components and repeat the aforementioned linear detection process in order to estimate the next transmitted signal component $x_{j_{i+1}}$. The iterative process described above is then repeated until the transmitted signal components associated with all transmitter antenna elements are detected. In this section we will demonstrate that the successive structure of the detection process results in a substantially improved SIR for the weaker signal components. Note that in our forthcoming derivation we, once again, omit the OFDM symbol and subcarrier indices n and k, which does not restrict the generality of the results obtained, since the space-devision detection process described is performed independently for each pair of time and frequency domain indices $[n,k]$.

More specifically, we commence our SIC detection process with a linear detection of the transmitted signal component x_{j_1}, as suggested by Equation (3.1), where we have

$$\hat{x}_{j_1} = \mathbf{w}_1^{\mathrm{H}} \mathbf{y}_1, \tag{3.39}$$

and $\mathbf{w}_1 = (\mathbf{W})_{j_1}$ is the j_1th column of the SDM MMSE detector's weight matrix described by Equation (3.13), while $\mathbf{y}_1$ is assumed to be identical to the original received signal vector $\mathbf{y}$.

In the next step, the interference imposed by the just detected and remodulated signal component x_{j_1} is subtracted from the received signal $\mathbf{y}_1$, yielding

$$\mathbf{y}_2 = \mathbf{y}_1 - (\mathbf{H})_{j_1} Q(\hat{x}_{j_1}), \tag{3.40}$$

where $(\mathbf{H})_{j_1}$ is the j_1th column of the channel matrix $\mathbf{H}$, while $Q(x)$ represents the slicing or hard-decision operation performed in the receiver in order to estimate the transmitted information-carrying QAM/PSK symbol. The resultant partially-decontaminated signal $\mathbf{y}_2$ comprises the contributions of a reduced number of interferers. In order to detect our next desired transmitted signal component x_{j_2} we now have to calculate the updated linear SDM detector weight matrix $\mathbf{W}_2$, which may be readily achieved by substituting the effective channel matrix $\mathbf{H}_{\overline{j_1}}$, obtained by zeroing column j_1 of the original channel matrix $\mathbf{H}$, into Equation

(3.13) yielding

$$\mathbf{W}_2 = \mathbf{H}_{\overline{j_1}}(\mathbf{H}^{\mathrm{H}}_{\overline{j_1}}\mathbf{H}_{\overline{j_1}} + m_{\mathrm{t}}\sigma_w^2\mathbf{I})^{-1}, \tag{3.41}$$

where we follow the notation employed in [138] and correspondingly $\mathbf{H}_{\overline{j_i}}$ denotes the matrix obtained by zeroing columns $j_1, \cdots, j_i$ of the original matrix $\mathbf{H}$. By substituting the terms $\hat{x}_{j_1}$, $\mathbf{w}_1$ and $\mathbf{y}_1$ of Equation (3.39) by the corresponding terms $\hat{x}_{j_2}$, $\mathbf{y}_2$ of Equation (3.40) and $\mathbf{w}_2 = (\mathbf{W})_2$ of Equation (3.41), we arrive at the desired estimate of next transmitted signal component. Finally, the iterative detection process described above is repeated, until all desired transmitted signal components are successfully detected.

As it was argued in [138], the order in which the detection of the transmitted signal components $x_j[n], j = 1, \cdots, m_{\mathrm{t}}$ is performed is important for the overall performance of the detection process. Moreover, as it was demonstrated in [138], the optimal ordering arises if the "best first" successive detection strategy is applied, where the best possible performance is achieved, when at each iteration i of the SIC detection process the desired signal component is selected according to the selection criterion of

$$j_{i+1} = \underset{j}{\operatorname{argmax}} \, \|(\mathbf{H}_{\overline{j_i}})_j\|^2, \tag{3.42}$$

implying that the least attenuated , *i.e.* the highest-power antenna's signal is detected first.

The SDM SIC detection process employing the MMSE detection method of Section 3.3.1 is summarised in Algorithm 9.

3.4.2.1 Performance Analysis of the SIC SDM Detector

In this section we present our performance results for the SDM-OFDM system employing the SIC SDM detection scheme described in Section 3.4.2. The simulation setup is identical to that described in Section 3.3.1.2 and the corresponding simulation parameters are summarised in Table 2.1.

Figure 3.6 characterizes the ability of the SDM-OFDM system employing the **SIC** SDM detector of Algorithm 9 to exploit the available MIMO **multiplexing** gain in the **fully loaded** system configuration, when the number of the transmit antenna elements m_{t} is equal to that of the receiver antenna elements n_{r}. More explicitly, Figure 3.6 depicts the achievable **BER** performance of the SDM-OFDM SIC system considered as a function of (a) the average SNR recorded at the receiver antenna elements, as well as (b) versus the corresponding E_b/N_0 value for various numbers of $m_{\mathrm{t}} = n_{\mathrm{r}} = 1, \cdots, 6$ transmit and receive antenna elements.

More specifically, the results portrayed in Figure 3.6 illustrate on the SNR scale that the SDM-OFDM SIC system having $m_{\mathrm{t}} = n_{\mathrm{r}} = 6$ transmit and receive antennas exhibits an SNR gain of about 2dB at the target BER of 10^{-3}, when compared to the same system employing a single antenna element at both the transmitter and receiver.

Algorithm 9 MMSE-aided V-BLAST SIC SDM Detector

```
$\mathbf{y}_1 = \mathbf{y}[n]$
$\mathbf{W}_1 = \mathbf{H}(\mathbf{H}^{\mathrm{H}}\mathbf{H} + m_{\mathrm{t}}\sigma_w^2\mathbf{I})^{-1}$
$j_1 = \arg\max_{j} \|(\mathbf{H})_j\|^2$    (3.43a)
for  $i = 1, 2, \ldots, m_{\mathrm{t}}$  do
    $\mathbf{w}_{j_i} = (\mathbf{W}_i)_{j_i}$    (3.43b)
    $\hat{x}_{j_i}[n] = \mathbf{w}_{j_i}^{\mathrm{H}}\mathbf{y}_i$    (3.43c)
    $\mathbf{y}_{i+1} = \mathbf{y}_i - (\mathbf{H}[n])_{j_i} Q(\hat{x}_{j_i})$    (3.43d)
    $\mathbf{W}_{i+1} = \mathbf{H}_{\bar{j}_i}(\mathbf{H}_{\bar{j}_i}^{\mathrm{H}}\mathbf{H}_{\bar{j}_i} + m_{\mathrm{t}}\sigma_w^2\mathbf{I})^{-1}$    (3.43e)
    $j_{i+1} = \operatorname{argmax}_{j} \|(\mathbf{H}_{\bar{j}_i})_j\|^2$    (3.43f)
end  for
```

Furthermore, Figure 3.7 illustrates the capability of the SDM-OFDM system employing the **SIC** SDM detector of Algorithm 9 and having a constant number of $n_{\mathrm{r}} = 4$ receive antenna elements to detect the multiplexed signal arriving from various numbers of transmit antenna elements. Specifically, we aim for exploring the attainable performance of the **SIC** SDM detector in the **overloaded** system scenario, where the number of transmit antenna elements exceeds that of the receiver antenna elements and thus we have $m_{\mathrm{t}} > n_{\mathrm{r}}$. Figure 3.7 demonstrates the achievable BER performance of the SDM-OFDM system employing the **SIC** SDM detector as a function of the average SNR recorded at the receive antenna elements. In can be seen by comparing Figures 3.7 and 3.3 that in an overloaded scenario the **SIC** SDM detector considered performs better than the MMSE SDM detector of Section 3.3.1. Nevertheless, observe from the comparison of Figures 3.7 and 3.5 that a substantial performance degradation may still be observed in comparison to the ML SDM detector of Section 3.4.1. A more detailed comparison of the achievable performance corresponding to the various SDM detection methods considered will be carrier out in Section 3.6.

3.4.3 Genetic Algorithm-Aided MMSE Detection

Genetic Algorithms (GA) [99, 141] constitute a family of optimization algorithms often utilized for finding approximate solutions to optimization problems having irregular error surfaces associated with local minima, such as in interference, rather than noise-limited propagation environments [142]. Genetic Algorithms

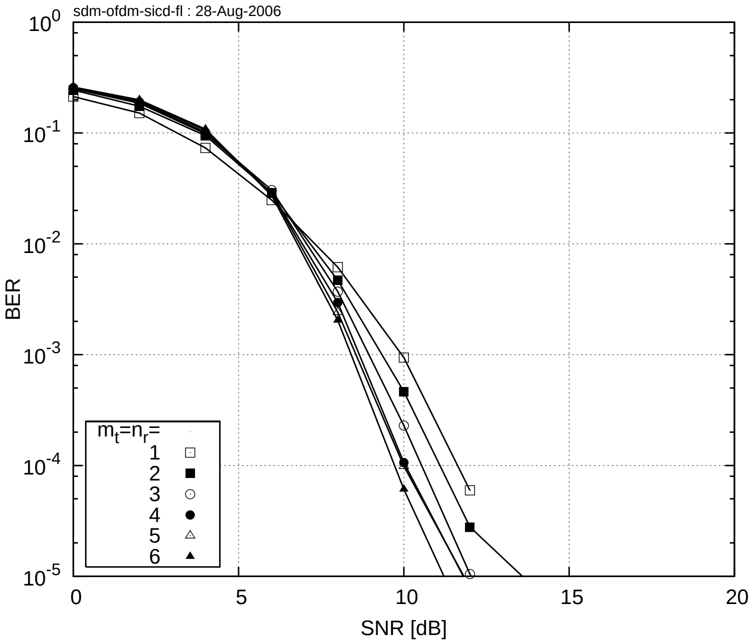

Figure 3.6: Bit Error Rate exhibited by the QPSK-modulated **SDM-OFDM** system employing an **SIC** SDM detector of Equation (3.38) and $m_\mathrm{t} = n_\mathrm{r} = 1, \cdots, 6$ transmit and receive antennas. The abscissa represents the average SNR recorded at the receive antenna elements. The system parameters are summarized in Table 2.1.

use biologically-inspired search and optimization methods, such as inheritance, mutation, natural selection and recombination (or crossover) of genes, each representing for example a bit string, describing a potential candidate of the transmitted multiplexed signal vector. Again, the GA's individuals are represented as strings of discrete symbols, such as for instance, 0s and 1s, but using different encoding schemes is also possible. In each generation, pairs of parent individuals are selected from the current population based on their *fitness* properties. They are modified (mutated or recombined) to form a new population, which becomes the current population in the next iteration of the algorithm.

Genetic algorithms were found to be highly efficient in numerous global search and optimisation problems, especially when their solution using conventional methods is not feasible, or otherwise would impose an excessive computational complexity. GAs were first applied to the problem of multi-user detection by Juntti *et al.* in [100] and Wang *et al.* in [143]. They were then documented in great detail in [142].

In our case, we explore the achievable performance of the GA-aided SDM detection method in the the context of the SDM-OFDM system of Section 1.8.3. We employ an SDM-MMSE detector described in Section 3.3.1 as our solution in the initial population at the input of the GA-aided SDM detector. The detailed description of GA-aided detection and the particular configuration of the GA employed is beyond the scope of this report. The configuration of the GA employed here is identical to that described in much detail in [144]. The interested readers may also refer to [142] for further insight.

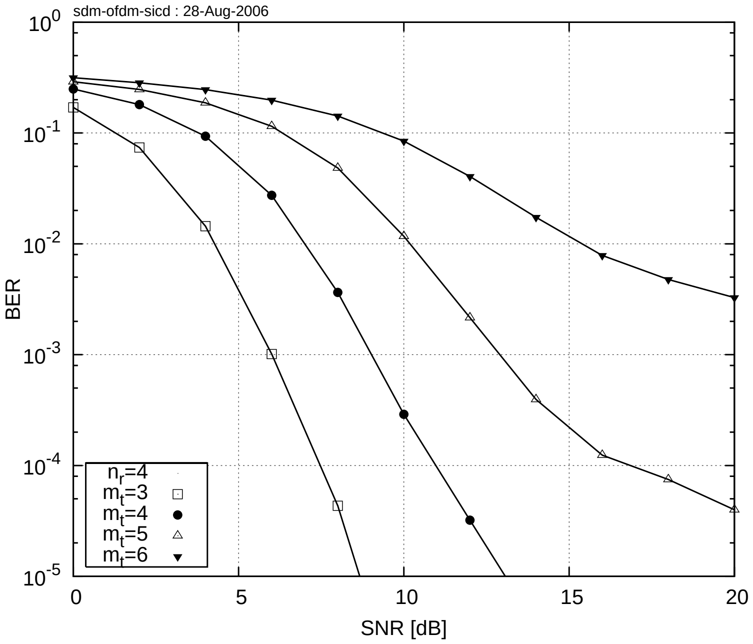

Figure 3.7: Bit Error Rate performance exhibited by the **SDM-QPSK-OFDM** system employing an **SIC** SDM detector of Equation (3.38) and $m_t = 3, 4, 5$ and 6 transmit antennas, as well as $n_r = 4$ receive antennas. The abscissa represents the average SNR recorded at the receive antenna elements. The system parameters are summarized in Table 2.1.

In the next section, we explore the achievable performance of the GA-aided SDM detector in the context of the SDM-OFDM system of Figure 3.1. The simulation setup of the SDM-OFDM system is identical to that described in Section 3.3.1.2, as summarized in Table 2.1, while details concerning the configuration of the GA-MMSE SDM detector employed can be found in Table 3.1.

3.4.3.1 Performance Analysis of the GA-MMSE SDM Detecor

The achievable BER performance of the SDM-OFDM system of Figure 3.1 employing the **GA-MMSE** SDM detection method described in [144] is depicted in Figure 3.8. More explicitly, Figure 3.8 demonstrates the ability of the SDM-OFDM system employing the **GA-MMSE** SDM detector [144] to exploit the available MIMO capacity gain in the **fully loaded** system configuration, when the number of transmit antenna elements m_t is equal to that of the receiver antenna elements n_r. To elaborate a little further, Figure 3.8 depicts the achievable **BER** performance of the SDM-OFDM system considered as a function of the average SNR recorded at each of the receiver antenna elements. As can be seen in Figure 3.8, the SDM-OFDM system employing the **GA-MMSE** SDM detector and $m_t = n_r = 6$ transmit and receive antennas exhibits an SNR gain of above 2dB at the target BER of 10^{-3}, when compared to the same system of Table 2.1 employing a single antenna element at both the transmitter and receiver.

Population initialization method	Output of the MMSE MUD
Mating Pool Creation Strategy	Pareto-Optimality
Selection method	Fitness-Proportionate
Cross-over operation	Uniform cross-over
Mutation operation	M-ary mutation
Elitism	Enabled
Incest prevention	Enabled
Population size X	Varied
Number of generations Y	Varied
Mutation probability p_m	0.1

Table 3.1: The configuration parameters of the GA-aided SDM detector [144].

3.5 Performance Enhancement Using Space-Frequency Interleaving

Employing frequency-domain interleaving is common practice in OFDM transceivers [28], since it enables the exploitation of the available Frequency Domain (FD) diversity provided by a frequency-selective wireless fading channel. In this section we explore the further benefits of employing space-frequency interleaving in the context of the SDM-OFDM system architecture investigated.

3.5.1 Space-Frequency-Interleaved OFDM

The structure of the Space-Frequency Interleaved (SFI) SDM-OFDM system considered is illustrated in Figure 3.9. Observe, that in contrast to the system architecture portrayed in Figure 3.1 the set of OFDM-subcarrier related data substreams at the outputs of the bank of channel encoders seen in Figure 3.9 are jointly interleaved, resulting in the space-frequency interleaved signal vectors $\mathbf{x}_i$, where $i = 1, \cdots, m_\mathrm{t}$ is the index corresponding to the different transmit antenna elements. Correspondingly, at the SDM-SFI-OFDM receiver of Figure 3.9 the set of detected OFDM-subcarrier related signal vectors $\hat{\mathbf{x}}_i$ are space-frequency deinterleaved, before they are processed by the bank of channel decoders portrayed in Figure 3.9. As a result, the impact of the channel impairments, such as fading and interference, is uniformly spread across the data substreams associated with the different transmit antenna elements. In other words, the SDM-SFI-OFDM system considered is capable of more efficiently exploiting both the space and frequency diversity benefits of the wireless MIMO channel. Consequently, we may expect that the SDM-SFI-OFDM system advocated will outperform the SDM-OFDM system of Section 3.2 in terms of the achievable BER performance.

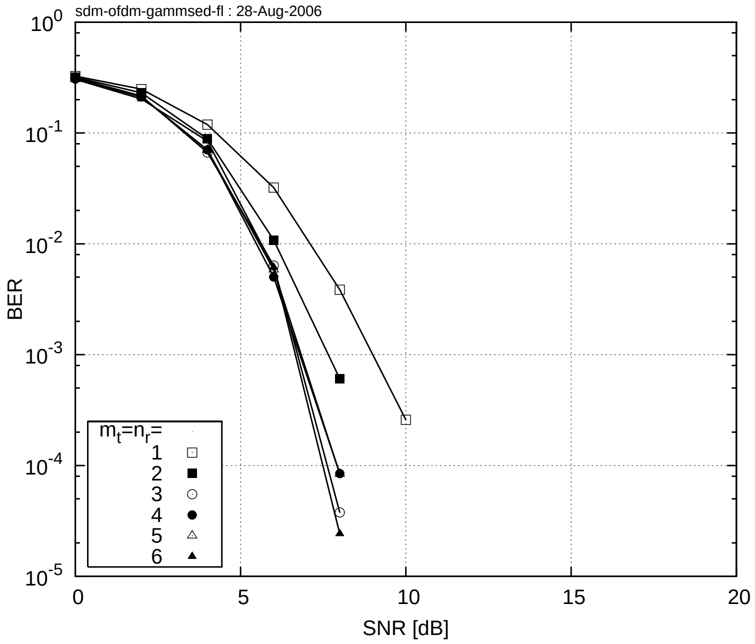

Figure 3.8: Bit Error Rate exhibited by the QPSK-modulated **SDM-OFDM** system employing an **SIC** SDM detector described in [144] and $m_\mathrm{t} = n_\mathrm{r} = 1, \cdots, 6$ transmit and receive antennas. The abscissa represents the average SNR recorded at the receive antenna elements. The system parameters are summarized in Table 2.1.

3.5.1.1 Performance Analysis of the SFI-SDM-OFDM

As a test-case for exploring the achievable performance of the SDM-SFI-OFDM scheme advocated, we employ the GA-MMSE SDM detector characterized in Section 3.4.3. Figure 3.10 demonstrates the ability of the SDM-SFI-OFDM system employing the **GA-MMSE** SDM detector of Section 3.4.3 to exploit the available MIMO channel capacity gain in the **fully loaded** system configuration, namely when the number of the transmit antenna elements m_t is equal to that of the receiver antenna elements n_r. Specifically, Figure 3.10 depicts the achievable **BER** performance of the SDM-OFDM system considered as a function of the average SNR recorded at each of the receiver antenna elements. Furthermore, the results depicted in Figure 3.10 illustrate that the SDM-OFDM system employing $m_\mathrm{t} = n_\mathrm{r} = 6$ transmit and receive antennas, as well as the **GA-MMSE** SDM detector is capable of achieving an SNR gain of 3dB at the target BER of 10^{-3}, when compared to the same system employing a single antenna element at both the transmitter and receiver.

3.6 Performance Comparison and Discussion

In this section we compare the achievable performance of the SDM detection methods considered in Sections 3.3 and 3.4 in the context of both the SDM-OFDM and SDM-SFI-OFDM systems of Sections 3.2 and 3.5.1, respectively. More specifically, Figure 3.11 portrays the achievable BER performance of the SDM-

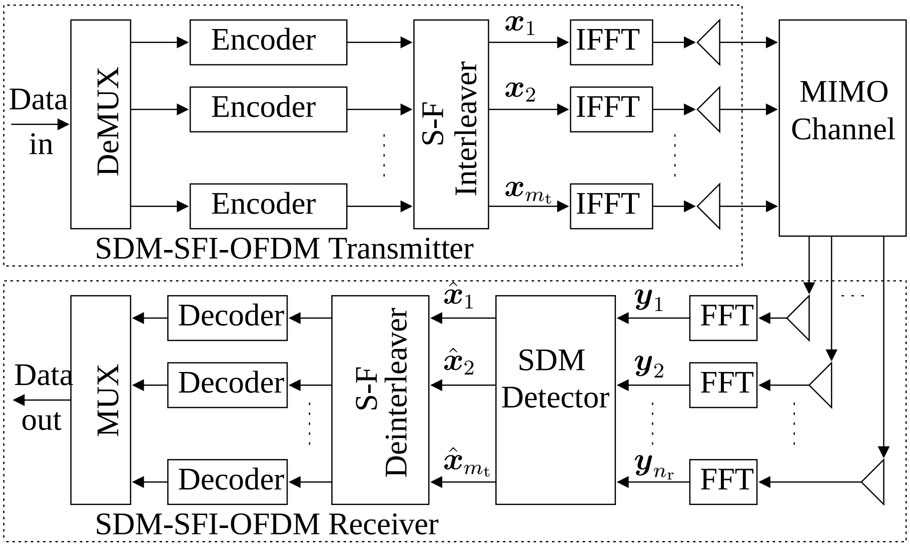

Figure 3.9: Schematic of a SDM-SFI-OFDM transceiver. In contrast to the SDM-OFDM scheme characterized in Figure 3.1, here the OFDM-subcarrier related data substreams associated with different transmit antenna elements are space-frequency interleaved at the output of the channel encoder.

MMSE detector of Section 3.3.1, as well as that of the ML, SIC and GA-MMSE SDM detectors described in Sections 3.4.1, 3.4.2 and 3.4.3, respectively. Figures 3.11 (a) and (b) correspond to the scenarios of $m_{\rm t} = n_{\rm r} = 2$ and 6 transmit and receive antenna elements, respectively. Furthermore, the hollow markers in Figures 3.11 (a) and (b) correspond to the SDM-OFDM scheme characterized in Figure 3.1, while the bold markers correspond to the SDM-SFI-OFDM arrangement portrayed in Figure 3.9.

It can be seen in Figures 3.11 (a) and (b) that the SNR performance of the non-linear SDM detection methods, namely that of the ML, SIC and GA-MMSE detectors of Sections 3.4.1, 3.4.2 and 3.4.3, respectively, is significantly higher than the corresponding performance of the linear MMSE SDM detector characterized in Section 3.3.1. This conclusion holds for the scenarios of both the SDM-OFDM and SDM-SFI-OFDM systems. Furthermore, the SNR performance of the GA-MMSE detector is within 1dB margin of the SNR performance exhibited by the ML SDM detector in both the SDM-OFDM and SDM-SFI-OFDM scenarios.

By comparing Figures 3.11 (a) and (b) we may conclude that the SNR performance of all the SDM detection methods considered improves upon increasing the number of the transmit and receive antenna elements. Additionally, Figure 3.11(b) suggests that for a high number of transmit and receive antennas the achievable performance of the turbo-coded SDM-SFI-OFDM system employing the ML SDM detector of Section 3.4.1 and communicating over the dispersive fading channel categorized by the Bug's chanel model [118] approaches the performance attained over an AWGN channel. Specifically, in the scenario of $m_{\rm t} = n_{\rm r} = 6$ characterized in Figure 3.11(b) the SNR performance of the turbo-coded SDM-SFI-OFDM system communicating over the dispersive fading channel categorized by the Bug's chanel model [118] is

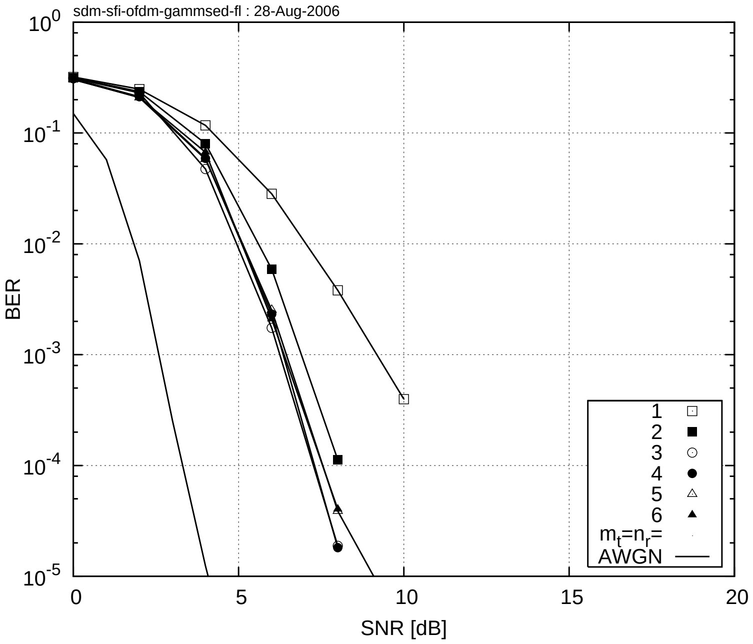

Figure 3.10: Bit Error Rate exhibited by the rate $\frac{1}{2}$ turbo-coded QPSK-modulated **SDM-SFI-OFDM** system employing the **GA-MMSE** SDM detector described in [144] and $m_{\rm t} = n_{\rm r} = 1, \cdots, 6$ transmit and receive antennas. The abscissa represents the average SNR recorded at the receive antenna elements. The achievable performance of the SDM-OFDM system employing the GA-MMSE detector was characterized in Figure 3.8. The OFDM system parameters are summarized in Table 2.1 and the corresponding GA configuration parameters are outlined in Table 3.1.

within a 2dB margin of the corresponding performance in AWGN channel.

Finally, it can be seen in Figures 3.11 (a) and (b) that the SDM-SFI-OFDM system employing the SDM detectors considered outperforms its SDM-OFDM counterpart. Quantitatively, in the scenario of $m_{\rm t} = n_{\rm r} = 6$, the SDM-SFI-OFDM system employing the ML, SIC or GA-MMSE SDM detector exhibits an SNR gain of about 1dB, when compared to its SDM-OFDM counterpart. In the case of employing the linear MMSE detector, the corresponding SNR difference between the SDM-SFI-OFDM and SDM-OFDM systems is about 2dB at the target BER of 10^{-3}. It should be noted that the performance gains portrayed here are dependent on the particular channel model considered. The diversity gain associated with employing the SFI method becomes higher if the channel considered is less dispersive, *i.e.* the corresponding power delay profile characterizing the channel considered comprises less non-zero taps.

3.7 Conclusions

In this chapter we investigated the attainable performance benefits of employing multiple-antenna-aided SDM-OFDM architectures invoked in wireless communication systems in the context of a *point-to-point*

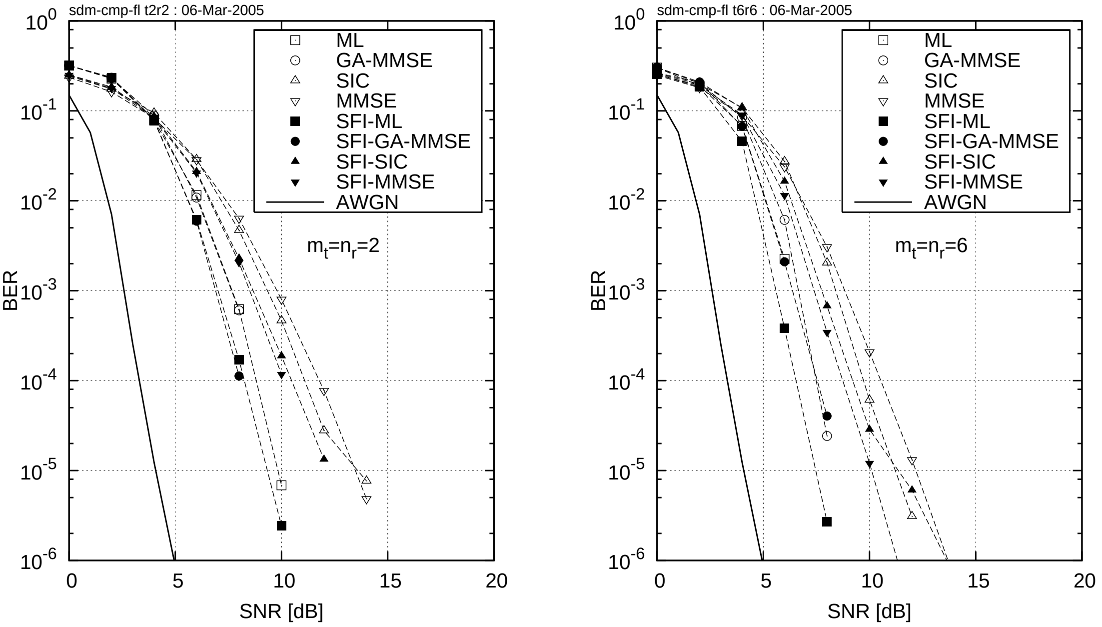

(a) (b)

Figure 3.11: Bit Error Rate exhibited by the rate $\frac{1}{2}$ turbo-coded QPSK-modulated **SDM-OFDM** system of Section 3.2, as well as by the **SDM-SFI-OFDM** system employing the SDM detection methods of Sections 3.3 and 3.4. The abscissa represents the average SNR recorded at the receive antenna elements and the results conrrespond to the cases of (a) $n_{\rm r} = m_{\rm t} = 2$ and (b) $n_{\rm r} = m_{\rm t} = 6$. The OFDM system parameters are summarized in Table 2.1, while the corresponding GA configuration parameters are outlined in Table 3.1.

system scenario, where two *peer* terminals employing multiple antennas communicate over a time-varying frequency-selective fading channel. We have demonstrated that the linear capacity increase, predicted by the relevant information-theoretic analysis [82] can indeed be achieved by employing a relatively low-complexity linear detection technique, such as the MMSE detector. We also showed that the ML detector is capable of attaining significant transmit diversity gains in *fully-loaded* systems, where the number of transmit and receive antennas is identical. Furthermore, the ML detector is capable of adequately performing in a *over-loaded* system configuration, where the number of transmit antennas exceeds that of the receive antennas. Subsequently, we explored the potential of a range of additional advanced non-linear SDM detection methods, which may potentially constitute an attractive compromise between the low complexity of the MMSE linear detector and the high performance of the ML detector. More explicitly, we demonstrated that the family of detection methods based on SIC as well as GA-aided MMSE detection are capable of satisfying these challenging requirements. Finally, we proposed a novel technique termed here as SFI, which may be employed in the SDM system architecture advocated and may be beneficially combined with all the aforementioned detection techniques, resulting in a further SNR performance improvement of up to 2dB. The SNR values required by different SDM detection schemes considered in order to achieve the target BER

Table 3.2: SDM detection SNR [dB] required for a target BER of 10^{-4}.

Detection method	2x2	2x2 SFI	6x6	6x6 SFI
ML	8.8	8.1	7.7	5.9
GA-MMSE	8.8	8.1	7.8	7.6
SIC	12.0	10.2	9.8	8.3
MMSE	11.5	10.1	10.7	8.1

of 10^{-4} are summarized in Table 3.2.

Chapter 4

Approximate Log-MAP SDM Detection

4.1 Outline

As it was pointed out in [28] , the "brute-force" ML detection method does not provide a feasible solution to the generic SDM detection problem owing to its excessive computational complexity. Nevertheless, since typical wireless communication systems operate at moderate-to-high SNRs, Reduced Search Algorithms (RSA) may be employed, which are capable of approaching the ML solution at a complexity, which is considerably lower than that imposed by the ML detector of [28] . The most potent among the RSA methods found in the literature is constituted by the Sphere Decoder (SD) [104]. The SD was first proposed for employment in the context of space-time processing in [105], where it was utilized for computing the ML estimates of the modulated symbols transmitted simultaneously from multiple transmit antennas. The *complex*-valued version of the sphere decoder, which is capable of approaching the channel capacity was proposed by Hochwald and ten Brink in [106]. The subject was further investigated by Damen *et al.* in [107]. Subsequently, an improved version of the Complex Sphere Decoder (CSD) was advocated by Pham *et al.* in [108]. The issue of achieving near-capacity performance, while reducing the associated complexity was revisited by Wang and Giannakis in [114, 145]. Further results on reduced complexity CSD were published by Zhao and Giannakis in [113]. Finally, CSD-aided detection was considered by Tellambura *et al.* in a joint channel estimation and data detection scheme explored in [57], while a revised version of the CSD method, namely the so-called Multistage Sphere Decoding (MSD) was introduced in [109, 111].

In this chapter we would like to introduce a novel Optimized Hierarchy RSA (OHRSA)-aided SDM detection method, which may be regarded as an advanced extension of the CSD method portrayed in [108]. The algorithm proposed extends the potential range of applications of the CSD methods of [106] and [108], as well as reduces the associated computational complexity, rendering the algorithm attractive for employment in practical systems.

The method proposed, which we refer to as the Soft-output OPtimized HIErarchy (SOPHIE) algorithm exhibits the following attractive properties:

1. It can be employed in the so-called rank-deficient scenario, where the number of transmit antenna elements exceeds that of the receive antenna elements. A particularly interesting potential application is found in a Multiple Input Single Output scenario, where the system employs multiple transmit antennas and a single receive antenna. Moreover, the associated computational complexity is only moderately increased even in heavily overloaded scenarios and it is almost independent of the number of receive antennas.
2. As opposed to the conventional CSD schemes, the calculation of the sphere radius is not required and therefore the method proposed is robust to the particular choice of the initial parameters both in terms of the achievable performance and the associated computational complexity.
3. The method proposed allows for a selected subset of the transmitted information-carrying symbols to be detected, while the interference imposed by the undetected signals is suppressed.
4. The overall computational complexity required is only slightly higher than that imposed by the linear MMSE multiuser detector designed for detecting a similar number of users.
5. Finally, the associated computational complexity is fairly independent of the channel conditions quantified in terms of the Signal-to-Noise Ratio encountered.

The rest of this chapter is constructed as follows. In Section 4.2.1 we derive the OHRSA-aided ML SDM detector, which benefits from the optimal performance of the ML SDM detector [28], while exhibiting a relatively low computational complexity, which is only slightly higher than that required by the low-complexity MMSE SDM detector [28]. To elaborate a little further, in Section 4.2.2 we derive a bit-wise OHRSA-aided ML SDM detector, which allows us to apply the OHRSA method of Section 4.2 in high-throughput systems, which employ multi-level modulation schemes, such as M-QAM [28].

In Section 4.2.3 our discourse evolves further by deducing the OHRSA-aided Max-Log-MAP SDM detector, which allows for an efficient evaluation of the soft-bit information and therefore results in highly efficient turbo decoding. Unfortunately however, in comparison to the OHRSA-aided ML SDM detector of Section 4.2.2 the OHRSA-aided Max-Log-MAP SDM detector of Section 4.2.3 exhibits a substantially higher complexity. Consequently, in Section 4.2.5 we derive an approximate Max-Log-MAP method, which we refer to as Soft-output OPtimized HIErarchy (SOPHIE) SDM detector. The SOPHIE SDM detector combines the advantages of both the OHRSA-aided ML and OHRSA-aided Max-Log-MAP SDM detectors of Sections 4.2.2 and 4.2.3, respectively. Specifically, it exhibits a similar performance to that of the optimal Max-Log-MAP detector, while imposing a modest complexity, which is only slightly higher than that required by the low-complexity MMSE SDM detector [28]. The computational complexity as well as the achievable performance of the SOPHIE SDM detector of Section 4.2.5 are analysed and quantified in Sections 4.2.5.1 and 4.2.5.2, respectively.

Our conclusions are summarized in Section 4.3. Specifically, we report achieving a BER of 10^{-4} at SNRs of $\gamma = 4.2,\ 9.2$ and 14.5 dB in high-throughput 8x8 rate-$\frac{1}{2}$ turbo-coded $M = 4, 16$ and 64-QAM systems communicating over dispersive Rayleigh fading channel. Additionally, we report achieving a BER of 10^{-4} at SNRs of $\gamma = 9.5,\ 16.3$ and 22.8 dB in high-throughput rank-deficient 4x4, 6x4 and 8x4 rate-$\frac{1}{2}$ turbo-coded 16-QAM systems, respectively.

4.2 OHRSA-Aided SDM Detection

4.2.1 OHRSA-Aided ML SDM Detection

We commence our discourse by deriving an OHRSA-aided ML SDM detection method for a constant-modulus modulation scheme, such as M-PSK, where the transmitted symbols s satisfy the condition of $|s|^2 = 1,\ \forall s \in \mathcal{M}$, and $\mathcal{M}$ denotes the set of M complex-valued constellation points. In the next section, we will then demonstrate that the method derived is equally applicable for high-throughput multi-level modulation schemes, such as M-QAM.

Let us recall that our system model described in detail in Section 1.8 is given by

$$\mathbf{y} = \mathbf{H}\mathbf{s} + \mathbf{w}, \tag{4.1}$$

where we omit the OFDM subcarrier and symbol indices k and n, respectively. As outlined in [28] , the ML SDM detector provides an m_{t}-antenna-based estimated signal vector candidate $\hat{\mathbf{s}}$, which maximizes the objective function defined as the conditional *a posteriori* probability function $\mathrm{P}\left\{\check{\mathbf{s}}|\mathbf{y},\mathbf{H}\right\}$ over the set $\mathcal{M}^{m_{\mathrm{t}}}$ of legitimate solutions. More explicitly, we have

$$\hat{\mathbf{s}} = \arg \max_{\check{\mathbf{s}} \in \mathcal{M}^{m_{\mathrm{t}}}} \mathrm{P}\left\{\check{\mathbf{s}}|\mathbf{y},\mathbf{H}\right\}, \tag{4.2}$$

where $\mathcal{M}^{m_{\mathrm{t}}}$ is the set of **all possible** m_{t}-dimensional candidate symbol vectors of the m_{t}-antenna-based transmitted signal vector $\mathbf{s}$. More specifically, we have

$$\mathcal{M}^{m_{\mathrm{t}}} = \left\{\check{\mathbf{s}} = (\check{s}_1, \cdots, \check{s}_{m_{\mathrm{t}}})^{\mathrm{T}};\ \check{s}_i \in \mathcal{M}\right\}. \tag{4.3}$$

Furthermore, it was shown in [28] that we have

$$\mathrm{P}\left\{\check{\mathbf{s}}|\mathbf{y},\mathbf{H}\right\} = A \exp\left[-\frac{1}{\sigma_w^2}\|\mathbf{y} - \mathbf{H}\check{\mathbf{s}}\|^2\right], \tag{4.4}$$

where A is a constant, which is independent of any of the values $\{\check{s}_i\}_{i=1,\cdots,m_\mathrm{t}}$. Thus, it may be shown [28] that the probability maximization problem of Equation (4.2) is equivalent to the corresponding Euclidean distance minimization problem. Specifically, we have

$$\hat{\mathbf{s}} = \arg \min_{\check{\mathbf{s}} \in \mathcal{M}^{m_\mathrm{t}}} \|\mathbf{y} - \mathbf{H}\check{\mathbf{s}}\|^2, \tag{4.5}$$

where the probability-based objective function of Equation (4.2) is substituted by the objective function determined by the Euclidean distance between the received signal vector $\mathbf{y}$ and the corresponding product of the channel matrix $\mathbf{H}$ with the *a priori* candidate of the transmitted signal vector $\check{\mathbf{s}} \in \mathcal{M}^{m_\mathrm{t}}$.

Consequently, our detection method relies on the observation, which may be summarized in the following lemma.

Lemma 1. The ML solution of Equation (4.2) of a noisy linear problem described by Equation (4.1) is given by

$$\hat{\mathbf{s}} = \arg \min_{\check{\mathbf{s}} \in \mathcal{M}^{m_\mathrm{t}}} \left\{ \|\mathbf{U}(\check{\mathbf{s}} - \hat{\mathbf{x}})\|^2 \right\}, \tag{4.6}$$

where $\mathbf{U}$ is an upper-triangular matrix having positive real-valued elements on the main diagonal and satisfying

$$\mathbf{U}^\mathrm{H}\mathbf{U} = (\mathbf{H}^\mathrm{H}\mathbf{H} + \sigma_w^2\mathbf{I}), \tag{4.7}$$

while

$$\hat{\mathbf{x}} = (\mathbf{H}^\mathrm{H}\mathbf{H} + \sigma_w^2\mathbf{I})^{-1}\mathbf{H}^\mathrm{H}\mathbf{y} \tag{4.8}$$

is the unconstrained MMSE estimate of the transmitted signal vector $\mathbf{s}$, which was derived in [28] .

Note 1: Observe that Lemma 1 imposes no constraints on the dimensions, or rank of the matrix $\mathbf{H}$ of the linear system described by Equation (4.1). This property is particularly important, since it enables us to apply our proposed detection technique to the scenario of *over-loaded* systems, where the number of transmit antenna elements exceeds that of the receive antenna elements.

Note 2: As substantiated by Equation (4.5), it is sufficient to prove that the following minimization problems are equivalent

$$\hat{\mathbf{s}} = \arg \min_{\check{\mathbf{s}} \in \mathcal{M}^{m_\mathrm{t}}} \|\mathbf{y} - \mathbf{H}\check{\mathbf{s}}\|^2 \tag{4.9}$$

$$\Leftrightarrow \quad \hat{\mathbf{s}} = \arg \min_{\check{\mathbf{s}} \in \mathcal{M}^{m_\mathrm{t}}} \|\mathbf{U}(\check{\mathbf{s}} - \hat{\mathbf{x}})\|^2. \tag{4.10}$$

Proof of Lemma 1: It is evident that in contrast to the matrix $\mathbf{H}^{\mathrm{H}}\mathbf{H}$, the matrix $(\mathbf{H}^{\mathrm{H}}\mathbf{H} + \sigma_w^2\mathbf{I})$ of Equation (4.6) is always Hermitian and positively definite, regardless of the rank of the channel matrix $\mathbf{H}$ associated with the particular MIMO channel realization encountered. Consequently, it may be represented as the product of an upper-triangular matrix $\mathbf{U}$ and its Hermitian adjoint matrix $\mathbf{U}^{\mathrm{H}}$ using for example the Cholesky factorization method [146].

Let $\mathbf{U}$ be the matrix generated by the Cholesky decomposition of the Hermitian positive definite matrix $(\mathbf{H}^{\mathrm{H}}\mathbf{H} + \sigma_w^2\mathbf{I})$ of Equation (4.7). More specifically, we have

$$\mathbf{U}^{\mathrm{H}}\mathbf{U} = (\mathbf{H}^{\mathrm{H}}\mathbf{H} + \sigma_w^2\mathbf{I}), \tag{4.11}$$

where $\mathbf{U}$ is an upper-triangular matrix having positive real-valued elements on its main diagonal.

Upon expanding the objective function of Equation (4.6) and subsequently invoking Equation (4.7) we obtain

$$\begin{aligned} J(\check{\mathbf{s}}) &= \|\mathbf{U}(\check{\mathbf{s}} - \hat{\mathbf{x}})\|^2 \\ &= (\check{\mathbf{s}} - \hat{\mathbf{x}})^{\mathrm{H}}\mathbf{U}^{\mathrm{H}}\mathbf{U}(\check{\mathbf{s}} - \hat{\mathbf{x}}) \\ &= (\check{\mathbf{s}} - \hat{\mathbf{x}})^{\mathrm{H}}(\mathbf{H}^{\mathrm{H}}\mathbf{H} + \sigma_w^2\mathbf{I})(\check{\mathbf{s}} - \hat{\mathbf{x}}) \\ &= \check{\mathbf{s}}^{\mathrm{H}}(\mathbf{H}^{\mathrm{H}}\mathbf{H} + \sigma_w^2\mathbf{I})\check{\mathbf{s}} - \hat{\mathbf{x}}^{\mathrm{H}}(\mathbf{H}^{\mathrm{H}}\mathbf{H} + \sigma_w^2\mathbf{I})\check{\mathbf{s}} \\ &\quad - \check{\mathbf{s}}^{\mathrm{H}}(\mathbf{H}^{\mathrm{H}}\mathbf{H} + \sigma_w^2\mathbf{I})\hat{\mathbf{x}} + \hat{\mathbf{x}}^{\mathrm{H}}(\mathbf{H}^{\mathrm{H}}\mathbf{H} + \sigma_w^2\mathbf{I})\hat{\mathbf{x}}. \end{aligned} \tag{4.12}$$

Furthermore, substituting Equation (4.8) into (4.12) yields

$$\begin{aligned} J(\check{\mathbf{s}}) &= \check{\mathbf{s}}^{\mathrm{H}}\mathbf{H}^{\mathrm{H}}\mathbf{H}\check{\mathbf{s}} - \mathbf{y}^{\mathrm{H}}\mathbf{H}\check{\mathbf{s}} - \check{\mathbf{s}}^{\mathrm{H}}\mathbf{H}^{\mathrm{H}}\mathbf{y} \\ &\quad + \sigma_w^2\check{\mathbf{s}}^{\mathrm{H}}\check{\mathbf{s}} + \mathbf{y}^{\mathrm{H}}\mathbf{H}(\mathbf{H}^{\mathrm{H}}\mathbf{H} + \sigma_w^2\mathbf{I})^{-1}\mathbf{H}^{\mathrm{H}}\mathbf{y} \\ &= \|\mathbf{y} - \mathbf{H}\check{\mathbf{s}}\|^2 + \underbrace{\sigma_w^2\check{\mathbf{s}}^{\mathrm{H}}\check{\mathbf{s}} + \mathbf{y}^{\mathrm{H}}(\mathbf{H}(\mathbf{H}^{\mathrm{H}}\mathbf{H} + \sigma_w^2\mathbf{I})^{-1}\mathbf{H}^{\mathrm{H}} - \mathbf{I})\mathbf{y}}_{\psi}. \end{aligned} \tag{4.13}$$

Observe that in the case of a system employing a constant-modulus modulation scheme, such as M-PSK, where we have $\check{\mathbf{s}}^{\mathrm{H}}\check{\mathbf{s}} = 1$, ψ of Equation (4.13) constitutes a real-valued scalar and its value does not depend on the argument $\check{\mathbf{s}}$ of the minimization problem formulated in Equation (4.6). Consequently, the minimization of the objective function $J(\check{\mathbf{s}})$ of Equation (4.13) can be reduced to the minimization of the term $\|\mathbf{y} - \mathbf{H}\check{\mathbf{s}}\|^2$, which renders it equivalent to the minimization problem of Equation (4.9). This completes the proof.

Using Lemma 1, in particular the fact that the matrix $\mathbf{U}$ is an upper-triangular matrix, the objective function $J(\check{\mathbf{s}})$ of Equation (4.13) may be reformulated as follows

$$\begin{aligned} J(\check{\mathbf{s}}) &= \|\mathbf{U}(\check{\mathbf{s}} - \hat{\mathbf{x}})\|^2 \\ &= (\check{\mathbf{s}} - \hat{\mathbf{x}})^{\mathrm{H}}\mathbf{U}^{\mathrm{H}}\mathbf{U}(\check{\mathbf{s}} - \hat{\mathbf{x}}) \\ &= \sum_{i=1}^{m_{\mathrm{t}}} \Big| \sum_{j=i}^{m_{\mathrm{t}}} u_{ij}(\check{s}_j - \hat{x}_j) \Big|^2 = \sum_{i=1}^{m_{\mathrm{t}}} \phi_i(\check{\mathbf{s}}_i), \end{aligned} \tag{4.14}$$

where $J(\check{\mathbf{s}})$ and $\phi_i(\check{\mathbf{s}}_i)$ are positive real-valued cost and sub-cost functions, respectively. Elaborating a little further we have

$$\begin{aligned} \phi_i(\check{\mathbf{s}}_i) &= \Big| \sum_{j=i}^{m_{\mathrm{t}}} u_{ij}(\check{s}_j - \hat{x}_j) \Big|^2 \\ &= \Big| u_{ii}(\check{s}_i - \hat{x}_i) + \underbrace{\sum_{j=i+1}^{m_{\mathrm{t}}} u_{ij}(\check{s}_j - \hat{x}_j)}_{a_i} \Big|^2. \end{aligned} \tag{4.15}$$

Note that the term a_i is a complex-valued scalar, which is independent of the specific symbol value $\check{s}_i$ of the ith element of the *a priori* candidate signal vector $\check{\mathbf{s}}$.

Furthermore, let $J_i(\check{\mathbf{s}}_i)$ be a Cumulative Sub-Cost (CSC) function recursively defined as

$$J_{m_{\mathrm{t}}}(\check{s}_{m_{\mathrm{t}}}) = \phi_{m_{\mathrm{t}}}(\check{s}_{m_{\mathrm{t}}}) = |u_{m_{\mathrm{t}}m_{\mathrm{t}}}(\check{s}_{m_{\mathrm{t}}} - \hat{x}_{m_{\mathrm{t}}})|^2 \tag{4.16a}$$

$$J_i(\check{\mathbf{s}}_i) = J_{i+1}(\check{\mathbf{s}}_{i+1}) + \phi_i(\check{\mathbf{s}}_i), \quad i = m_{\mathrm{t}}–1, \cdots, 1, \tag{4.16b}$$

where we define the candidate subvector as $\check{\mathbf{s}}_i = [\check{s}_i, \cdots, \check{s}_{m_{\mathrm{t}}}]$. Clearly, $J_i(\check{\mathbf{s}}_i)$ exhibits the following properties

$$J(\check{\mathbf{s}}) = J_1(\check{\mathbf{s}}_1) > J_2(\check{\mathbf{s}}_2) > \cdots > J_{m_{\mathrm{t}}}(\check{s}_{m_{\mathrm{t}}}) > 0 \tag{4.17a}$$

$$J_i(\check{\mathbf{s}}_i) = J_i(\{\check{s}_j\}, \ j = i, \cdots, m_{\mathrm{t}}) \tag{4.17b}$$

for all possible realizations of $\hat{\mathbf{x}} \in \mathbb{C}^{m_{\mathrm{t}}}$ and $\check{\mathbf{s}} \in \mathcal{M}^{m_{\mathrm{t}}}$, where the space $\mathbb{C}^{m_{\mathrm{t}}}$ contains all possible unconstrained MMSE estimates $\hat{\mathbf{x}}$ of the transmitted signal vector $\mathbf{s}$.

Equations (4.17a) and (4.17b) enable us to employ a highly efficient reduced search algorithm, which decreases the number of objective function evaluations of the minimization problem outlined in Equation (4.6) to a small fraction of the set $\mathcal{M}^{m_{\mathrm{t}}}$. This reduced-complexity search algorithm is outlined in the next section.

4.2.1.1 Search Strategy

Example 1. OHRSA-ML 3x3 BPSK

Consider a BPSK system having $n_{\mathrm{r}} = m_{\mathrm{t}} = 3$ transmit and receive antennas, which is described by Equation (4.1). The transmitted signal $\mathbf{s}$, the received signal $\mathbf{y}$ as well as the channel matrix $\mathbf{H}$ of Equation (4.1) are exemplified by the following values

$$\mathbf{s} = \begin{bmatrix} 1 \\ -1 \\ 1 \end{bmatrix}, \quad \mathbf{y} = \begin{bmatrix} 0.2 \\ 0.8 \\ -1.2 \end{bmatrix}, \quad \mathbf{H} = \begin{bmatrix} 0.5 & 0.4 & -0.2 \\ 0.4 & -0.3 & 0.2 \\ 0.9 & 1.8 & -0.1 \end{bmatrix}. \tag{4.18}$$

Our task is to obtain the ML estimate of the transmitted signal vector $\mathbf{s}$. Firstly, we evaluate the triangular matrix $\mathbf{U}$ of Equation (4.7) as well as the unconstrained MMSE estimate $\hat{\mathbf{x}}$ of Equation (4.8). The resultant quantities are given by

$$\mathbf{U} = \begin{bmatrix} 1.15 & 1.48 & -0.10 \\ 0 & 1.18 & -0.15 \\ 0 & 0 & 0.40 \end{bmatrix}, \quad \hat{\mathbf{x}} = \begin{bmatrix} 0.85 \\ -1.05 \\ -0.01 \end{bmatrix}. \tag{4.19}$$

Observe that the direct slicing of the MMSE estimate $\hat{\mathbf{x}}$ will result in an erroneously decided signal $\hat{\mathbf{s}} = \begin{bmatrix} 1 & -1 & -1 \end{bmatrix}^{\mathrm{T}}$. Subsequently, following the philosophy outlined in Section 4.2.1, for each legitimate candidate $\check{\mathbf{s}} \in \mathcal{M}^{m_{\mathrm{t}}}$ of the m_{t}-antenna-based composite transmitted signal vector $\mathbf{s}$ we calculate the corresponding value of the cost function $J(\check{\mathbf{s}})$ of Equation (4.14) using the recursive method described by Equation (4.16). The search process performed is illustrated in Figure 4.1(a). Each evaluation step, namely each evaluation of the CSC function $J_i(\check{\mathbf{s}}_i)$ of Equation (4.16b) is indicated by an elliptic node in Figure 4.1(a). The label inside each node indicates the order of evaluation as well as the corresponding value $J_i(\check{\mathbf{s}}_i)$ of the CSC function inside the brackets. Furthermore, the branches corresponding to the two legitimate values of $\check{s}_i = -1$ and 1 are indicated using the dashed and solid edges and nodes, respectively.

More specifically, commencing from the top of Figure 4.1(a), at recursive step $i = 3$ we calculate the CSC function of Equation (4.16a) associated with all legitimate values of the last element of the signal vector $\mathbf{s}$, where we have

$$J_3(\check{s}_3 = -1) = |u_{33}(\check{s}_3 - \hat{x}_3)|^2 = (0.40(-1 - (-0.01)))^2 = 0.15 \tag{4.20}$$

and

$$J_3(\check{s}_3 = 1) = (0.40(1 - (-0.01)))^2 = 0.16. \tag{4.21}$$

The corresponding values of $J_3(\check{s}_3 = -1) = 0.15$ and $J_3(\check{s}_3 = 1) = 0.16$ are indicated by the nodes 1 and 8 in Figure 4.1(a). Observe that the *recursive* nature of the search process considered suggests that the latter value of $J_3(\check{s}_3 = 1)$ is not considered until the entire search branch originating from the more promising node 1 associated with the lower CSC value of 0.15 is complited. Consequently, the value $J_3(\check{s}_3 = 1)$ is the 8th value of the CSC function to be evaluated, which is indicated by the corresponding node's index 8.

Furthermore, at recursive step $i = 2$ for each hypothesised value $\check{s}_3$ we calculate both the quantity a_2 of Equation (4.15) as well as the sub-cost function of Equation (4.15) and the corresponding CSC function of Equation (4.16b) associated with all legitimate values of the last-but-one element of the signal vector $\mathbf{s}$. Explicitly, for $\check{s}_3 = -1$ we have

$$a_2 = u_{23}(\check{s}_3 - \hat{x}_3) = -0.15(-1 - (-0.01)) = 0.15 \tag{4.22}$$

and

$$\begin{aligned} J_2(\check{s}_2 = -1, \check{s}_3 = -1) &= J_3(\check{s}_3 = -1) + \phi_2(\check{s}_2 = -1, \check{s}_3 = -1) \\ &= J_3(\check{s}_3 = -1) + |u_{22}(\check{s}_2 - \hat{x}_2)) + a_2|^2 \\ &= 0.15 + (1.18(-1 - (-1.05)) + 0.15) = 0.20 \\ J_2(\check{s}_2 = 1, \check{s}_3 = -1) &= J_3(\check{s}_3 = -1) + \phi_2(\check{s}_2 = 1, \check{s}_3 = -1) \\ &= 0.15 + (1.18(1 - (-1.05)) + 0.15) = 6.79. \end{aligned} \tag{4.23}$$

The corresponding values of $J_2(\check{\mathbf{s}}_2 = [-1, -1]) = 0.20$ and $J_2(\check{\mathbf{s}}_2 = [1, -1]) = 6.79$ are indicated by the nodes 2 and 5 in Figure 4.1(a).

Finally, at recursive index $i = 1$ for each hypothesised subvector $\check{\mathbf{s}}_2$ we calculate the quantity $a_1(\check{\mathbf{s}}_2)$ and the sub-cost function $\phi_1(\check{\mathbf{s}}_1)$ of Equation (4.15) as well as the corresponding *total* cost function $J(\check{s}_1 = -1, \check{\mathbf{s}}_2)$ and $J(\check{s}_1 = 1, \check{\mathbf{s}}_2)$ of Equation (4.14) associated with all legitimate values of the first element of the signal vector $\mathbf{s}$. Specifically, for the left-most search branch of Figure 4.1(a) corresponding to the *a priori* candidate $\check{\mathbf{s}}_2 = [-1, -1]$ we have

$$\begin{aligned} a_1 &= u_{12}(\check{s}_2 - \hat{x}_2) + u_{13}(\check{s}_3 - \hat{x}_3) \\ &= 1.48(-1 - -1.05) + -0.10(-1 - -0.01) = 0.17 \end{aligned} \tag{4.24}$$

and

$$\begin{aligned}
&J_1(\check{s}_1 = -1, \check{s}_2 = -1, \check{s}_3 = -1) \\
&\quad = J_2(\check{s}_2 = -1, \check{s}_3 = -1) + \phi_1(\check{s}_1 = -1, \check{s}_2 = -1, \check{s}_3 = -1) \\
&\quad = J_2(\check{s}_2 = -1, \check{s}_3 = -1) + |u_{11}(\check{s}_1 - \hat{x}_1)) + a_1|^2 \\
&\quad = 0.20 + (1.15(-1 - 0.85) + 0.17) = 4.03, \\
&J_1(\check{s}_1 = 1, \check{s}_2 = -1, \check{s}_3 = 1) \\
&\quad = J_2(\check{s}_2 = -1, \check{s}_3 = -1) + \phi_2(\check{s}_1 = 1, \check{s}_2 = -1, \check{s}_3 = -1) \\
&\quad = 0.20 + (1.15(1 - 0.85) + 0.17) = 0.31.
\end{aligned} \tag{4.25}$$

Upon completing the entire search process outlined above we arrive at eight values of the total cost function $J(\check{\mathbf{s}})$ associated with eight legitimate 3-bit solutions of the detection problem considered. The eight different candidate solutions are indicated by the eight bottom-most elliptic nodes in Figure 4.1(a). Clearly, the ML solution is constituted by the search branch terminating at node 11 of Figure 4.1(a) and having the minimum value $J(\check{\mathbf{s}}) = 0.19$ of the total cost function.

Observe that the difference between the values of $J_3(\check{s}_3 = -1)$ and $J_3(\check{s}_3 = 1)$ associated with nodes 1 and 8 in Figure 4.1(a) is quite small and thus the potential of finding the ML solution along either of the search branches commencing at nodes 1 and 8 in Figure 4.1(a) may not be recognised with a high degree of confidence. On the other hand, the difference between the values of the CSC function along two complementary search branches commencing at nodes 1 and 8 becomes substantially more evident, if we apply the *best-first* detection strategy suggested in [147]. More specifically, we sort the columns of the channel matrix **H** in the increasing order of their Euclidean or square norm. The resultant reordered channel matrix $\mathbf{H}'$ as well as the corresponding triangular matrix **U** and the unconstrained MMSE estimate $\hat{\mathbf{x}}'$ may be expressed as

$$\mathbf{H}' = \begin{bmatrix} -0.2 & 0.5 & 0.4 \\ 0.2 & 0.4 & -0.3 \\ -0.1 & 0.9 & 1.8 \end{bmatrix}, \mathbf{U}' = \begin{bmatrix} 0.44 & -0.25 & -0.73 \\ 0 & 1.12 & 1.35 \\ 0 & 0 & 1.11 \end{bmatrix}, \hat{\mathbf{x}}' = \begin{bmatrix} -0.01 \\ 0.85 \\ -1.05 \end{bmatrix}. \tag{4.26}$$

The search tree generated by applying the aforementioned search process and using the modified quantities $\mathbf{H}', \mathbf{U}'$ and $\hat{\mathbf{x}}'$ is depicted in Figure 4.1(b). Note the substantial difference between the values of the CSC function $J_3(\check{s}_3 = -1)$ and $J_3(\check{s}_3 = 1)$ associated with the nodes 1 and 8. Moreover, by comparing the value of the CSC function $J_3(\check{s}_3)$ of node 8 with that of the total cost function $J(\check{\mathbf{s}})$ of node 7 we can conclude that the search along the branch commencing at node 8 is in fact redundant.

In order to further optimize our search process, at recursive steps of $i = 3$ and 2 we first calculate the sub-cost functions $\phi_3(\check{s}_3 = \{-1, 1\})$ and $\phi_2(\check{s}_3, \check{s}_2 = \{-1, 1\})$ of Equation (4.15). We then compare the values obtained and continue with the processing of the specific search branch corresponding to the smaller value of the sub-cost function $\phi_i(\check{\mathbf{s}}_i)$ first. The resultant search tree is depicted in Figure 4.1(c). Observe that in Figure 4.1(c) the minimum value of the total cost function $J(\check{\mathbf{s}}) = 0.19$ is obtained faster, namely in 3 evaluation steps in comparison to 7 steps required by the search tree of Figure 4.1(b).

Finally, we discard all the search branches commencing at nodes having an associated value of the CSC function, which is in excess of the minimum total cost function value obtained. Specifically, we discontinue the search branches commencing at nodes 5 and 8 having the CSC function values in excess of 0.19, namely 4.03 and 5.15, respectively. The resultant reduced search tree is depicted in Figure 4.1(d). Note that the ML solution is obtained in 6 evaluation steps in comparison to the 14 steps required in the case of the exhaustive search of Figure 4.1(a). In conclusion, upon performing the approprite reordering of the obtained ML estimate, we arrive at the correct value of the transmitted signal vector $\hat{\mathbf{s}} = \begin{bmatrix} 1 & -1 & 1 \end{bmatrix}^{\mathrm{T}}$.

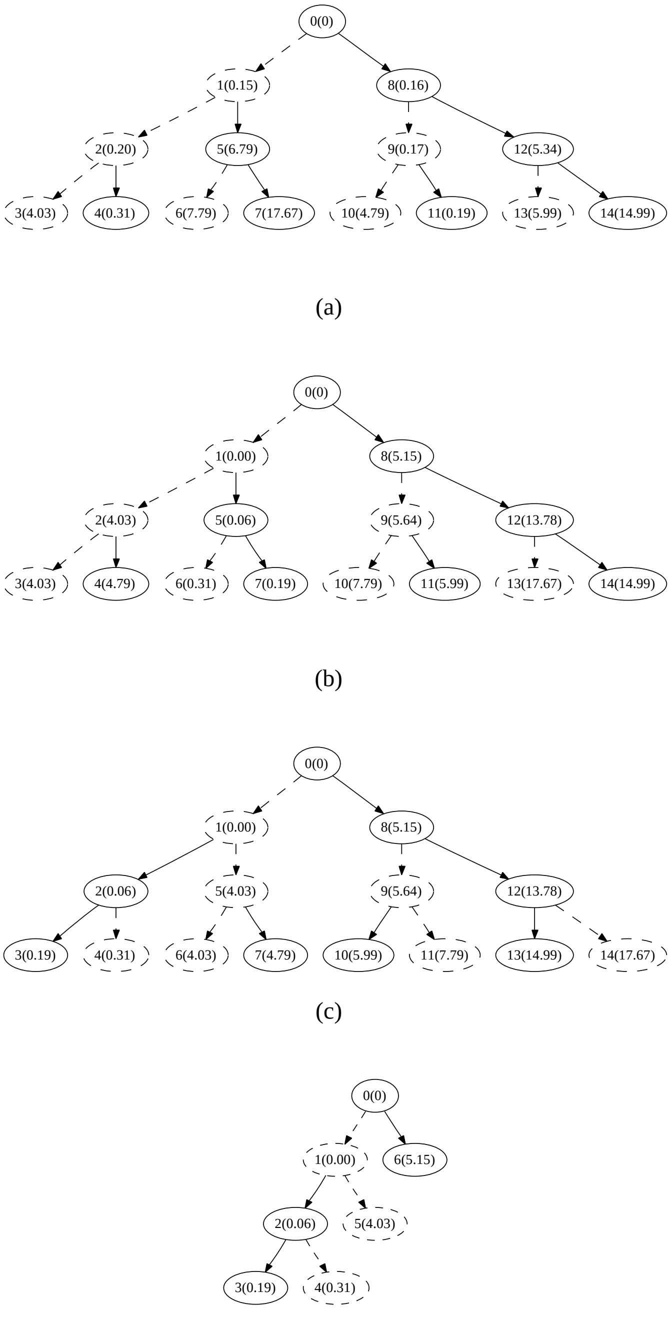

(a)

(b)

(c)

(d)

Figure 4.1: Examples of a search tree formed by the OHRSA-ML SDM detector in the scenario of a system employing BPSK modulation, $m_\mathrm{t} = n_\mathrm{r} = 3$ transmit and receive antennas and encountering average SNRs of 10dB. The labels indicate the order of evaluation, as well as the corresponding value $J_i(\check{\mathbf{s}}_i)$ of the CSC function of Equation (4.16), as seen in the brackets. The dashed and solid arrows indicate the values of $\check{s}_i = -1$ and 1, respectively.

4.2.1.2 Generalization of the OHRSA-ML SDM Detector

Let us now generalize and substantiate further the detection paradigm derived in Example 1. Firstly, we commence the recursive search process with the evaluation of the CSC function value $J_{m_\mathrm{t}}(\check{s}_{m_\mathrm{t}})$ of Equation (4.16a). Secondly, at each recursive step i of the search algorithm proposed we stipulate a series of hypotheses concerning the value of the M-ary transmitted symbol s_i associated with the ith transmit antenna element and subsequently calculate the conditioned sub-cost function $J_i(\check{\mathbf{s}}_i)$ of Equation (4.16b), where $\check{\mathbf{s}}_i = (\check{s}_i, \cdots, \check{s}_{m_\mathrm{t}})^\mathrm{T}$ denotes the subvector of the m_t-antenna-based candidate vector $\check{\mathbf{s}}$ comprising only the indices higher than or equal to i. Furthermore, for each tentatively assumed value of $\check{s}_i$ we execute a successive recursive search step $i-1$, which is conditioned on the hypotheses made in all preceding recursive steps $j = i, \cdots, m_\mathrm{t}$. As substantiated by Equations (4.15) and (4.16b), the value of the CSC function $J_i(\check{\mathbf{s}}_i)$ is dependent only on the values of the elements $\{\check{s}_j\}_{j=i,\cdots,m_\mathrm{t}}$ of the *a priori* candidate signal vector $\check{\mathbf{s}}$, which are hypothesized from step $j = m_\mathrm{t}$ up to the present step i of our recursive process. At each arrival at the step $i = 1$ of the recursive process, a complete candidate vector $\check{\mathbf{s}}$ is hypothesized and the corresponding value of the cost function $J(\check{\mathbf{s}})$ formulated in Equation (4.14) is evaluated.

Observe that the recursive hierarchical search procedure described above may be employed to perform an exhaustive search through all possible values of the transmitted signal vector $\check{\mathbf{s}}$ and the resultant search process is guaranteed to arrive at the ML solution $\check{\mathbf{s}}_\mathrm{ML}$, which minimizes the value of the cost function $J(\check{\mathbf{s}})$ of Equation (4.14). Fortunately however, as opposed to other ML search schemes, the search process described above can be readily optimized, resulting in a dramatic reduction of the associated computational complexity. Specifically, the potential optimization complexity gain originates from the fact that most of the hierarchical search branches can be discarded at an early stage of the recursive search process. The corresponding optimization rules proposed may be outlined as follows.

Rule 1. We reorder the system model of Equation (4.1) as suggested in [147]. Specifically, we apply the *best-first* detection strategy outlined in [28, pp.754-756] , which implies that the transmitted signal vector components are detected in the decreasing order of the associated channel quality. As it was advocated in [28, pp.754-756] , the quality of the channel associated with the ith element of the transmitted signal vector $\mathbf{s}$ is determined by the norm of the ith column of the channel matrix $\mathbf{H}$. Consequently, for the sake of applying the *best-first* detection strategy, the columns of the channel matrix $\mathbf{H}$ are sorted in the increasing order of their norm. Thus, the resultant, column-reordered channel matrix $\mathbf{H}$ complies with the following criterion

$$\|(\mathbf{H})_1\|^2 \leq \|(\mathbf{H})_2\|^2 \leq \cdots \leq \|(\mathbf{H})_{m_\mathrm{t}}\|^2, \tag{4.27}$$

where $(\mathbf{H})_i$ denotes the ith column of the channel matrix $\mathbf{H}$. Note that the elements of the transmitted signal vector $\mathbf{s}$ are reordered correspondingly, but their original order has to be reinstated in the final stage of the detection process.

Rule 2. At each recursive detection index $i = m_{\mathrm{t}}, \cdots, 1$, the potential candidate values $\{c_m\}_{m=1,\cdots,M} \in \mathcal{M}$ of the transmitted signal component s_i are considered in the increasing order of the corresponding value of the sub-cost function $\phi_i(\check{\mathbf{s}}_i) = \phi_i(c_m, \check{\mathbf{s}}_{i+1})$ of Equation (4.15), where we have

$$\phi_i(c_1, \check{\mathbf{s}}_{i+1}) < \cdots < \phi_i(c_m, \check{\mathbf{s}}_{i+1}) < \cdots < \phi_i(c_M, \check{\mathbf{s}}_{i+1}),$$

and according to Equation (4.15)

$$\begin{aligned}\phi_i(c_m, \check{\mathbf{s}}_{i+1}) &= |u_{ii}(c_m - \hat{x}_i) + a_i|^2 \\ &= u_{ii}|c_m - \hat{x}_i + \frac{a_i}{u_{ii}^2}|^2. \end{aligned} \tag{4.28}$$

Consequently, the more likely candidates c_m of the ith element of the transmitted signal vector $\mathbf{s}$ are examined first. Observe that the sorting criterion of Equation (4.28) may also be interpreted as a biased Euclidean distance of the candidate constellation point c_m from the unconstrained MMSE estimate $\hat{x}_i$ of the transmitted signal component s_i.

Rule 3. We define a *cut-off* value of the cost fuction $J_{\min} = \min\{J(\check{\mathbf{s}})\}$ as the minimum value of the total cost function obtained up to the present point of the search process. Consequently, at each arrival at step $i = 1$ of the recursive search process, the *cut-off* value of the cost function is updated as follows

$$J_{\min} = \min\{J_{\min}, J(\check{\mathbf{s}})\}. \tag{4.29}$$

Rule 4. Finally, at each recursive detection step i, only the high probability search branches corresponding to the highly likely symbol candidates c_m resulting in low values of the CSC function obeying $J_i(c_m) < J_{\min}$ are pursued. Furthermore, as follows from the sorting criterion of the optimization Rule 2, as soon as the inequality $J_i(c_m) > J_{\min}$ is encountered, the search loop at the ith detection step is discontinued.

An example of the search tree generated by the algorithm invoking the Rules 1-4 described above is depicted in Figure 4.2. The search trees shown correspond to the scenario of using QPSK modulation and employing $m_{\mathrm{t}} = n_{\mathrm{r}} = 8$ antenna elements at both the transmitter and the receiver. The cases of encountering the average SNRs of (a) 10 and (b) 20 dB were considered. Each step of the search procedure is depicted as an ellipsoidal-shaped node. The label associated with each node indicates the order of visitation, as well as the corresponding value of the CSC function $J_i(\check{\mathbf{s}}_i)$ formulated in Equation (4.16), as seen in the brackets. As suggested by the fact that QPSK modulation is considered, at each recursive step i, **four** ligitimate search branches are possible. However, as can be seen in Figure 4.2(a), only a small fraction of the potential search branches are actually pursued. Observe that the rate of convergence of the algorithm proposed is particularly rapid at high values of SNR. In the case of encountering low SNR values, the convergence rate decreases. Nevertheless, the associated computational complexity is dramatically lower than that associated with an exhaustive ML search.

The pseudo-code summarizing the recursive implementation of the OHRSA-based ML SDM detector proposed is depicted in Algorithm 10.

Given the cost-functions of Equation (4.14) and the appropriately ordered matrix $\mathbf{H}$ of Equation (4.1), the proposed algorithm may be viewed as a specific manifestation of a tree search algorithm [148]. Another example of a tree search algorithm commonly employed in the design of communication systems constitutes the well-known Viterbi algorithm [26, 149]. More specifically, the sub-cost function values of Equation (4.15) may be regarded as being analogous to the branch metrics, while the CSC values of Equations (4.16) as accumulated path metrics. It should be noted however, that the OHRSA-ML algorithm described here and the classic tree-search-based Viterbi algorithm exhibit substantial differences. Specifically, the Viterbi algorithm assumes that the branch metric is a function of the system states constituting one particular state transition, which is equivalent to the assumption of having a diagonal matrix $\mathbf{U}$ in Equation (4.7). Evidently, this requirement cannot be satisfied by our generic MIMO system. Consequently, the tree-search-based Viterbi algorithm cannot be applied to the search problem described above.

The operation of the OHRSA-ML SDM detector of Algorithm 10 is further exemplified in Figure 4.2 where we illustrate the search process corresponding to 8x8-QPSK signal detection in a MIMO fading channel characterized by the SNR values of (a) 10 and (b) 20 dB. The labels corresponding to each elliptic node in Figure 4.2 indicate the order of visitation, as well as the corresponding value $J_i(\check{\mathbf{s}}_i)$ of the CSC function of Equation (4.16), as seen in the brackets, corresponding to the signal subvector $\check{\mathbf{s}}_i$ associated with that node. Observe that at each level of the search tree of Figure 4.2, we first explore the branch corresponding to the lower value of the objective function. The actual ML solution in Figure 4.2(a) is attained in node 25 with the corresponding value $J_i(\check{\mathbf{s}}_0) = 4.03$ and is formed by the search branch comprising nodes 0-1-19-20-21-22-23-24-25. Observe that the nodes forming the ML solution do not necessarily correspond to the lowest value of the objective function $J_i(\check{\mathbf{s}}_i)$ at each level of the search tree. The ML solution is attained in (a) 41 and (b) 16 evaluation steps in comparison to the $4^8 = 65536$ evaluation steps required in the case of the exhaustive ML search.

Algorithm 10 OHRSA-aided ML SDM Detector

```
Sort$\{\mathbf{H}\}$, such that $\|(\mathbf{H})_1\|^2 \leq \cdots \leq \|(\mathbf{H})_{m_t}\|^2$    (4.30a)
$\mathbf{G} = (\mathbf{H}^{\mathrm{H}}\mathbf{H} + \sigma_w^2\mathbf{I})$    (4.30b)
$\mathbf{U} =$ CholeskyDecomposition$(\mathbf{G})$    (4.30c)
$\hat{\mathbf{x}} = \mathbf{G}^{-1}\mathbf{H}^{\mathrm{H}}\mathbf{y}$    (4.30d)
Calculate $J_{m_t}$    (4.30e)
Unsort$\{\hat{\mathbf{s}}\}$    (4.30f)

function Calculate $J_i(\check{\mathbf{s}}_i)$    (4.30g)
  $a_i = \sum_{j=i+1}^{m_t} u_{ij}(\check{s}_j - \hat{x}_j)$    (4.30h)
  Sort$\{c_m\}$, such that $\phi_i(c_1) < \cdots < \phi_i(c_M)$,    (4.30i)
  where $\phi_i(c_m) = |u_{ii}(c_m - \hat{x}_i) + a_i|^2$    (4.30j)
  for $m = 1, 2, \ldots, M$ do
    $\check{s}_i = c_m$    (4.30k)
    $J_i(\check{\mathbf{s}}_i) = J_{i+1}(\check{\mathbf{s}}_{i+1}) + \phi_i(\check{s}_i)$    (4.30l)
    if $J_i(\check{\mathbf{s}}_i) < J_{\min}$ then    (4.30m)
      if $i > 0$ then Calculate $J_{i-1}$    (4.30n)
      else
        $J_{\min} = J(\check{\mathbf{s}})$    (4.30o)
        $\hat{\mathbf{s}} = \check{\mathbf{s}}$    (4.30p)
      end if
    end if
  end for
end function
```

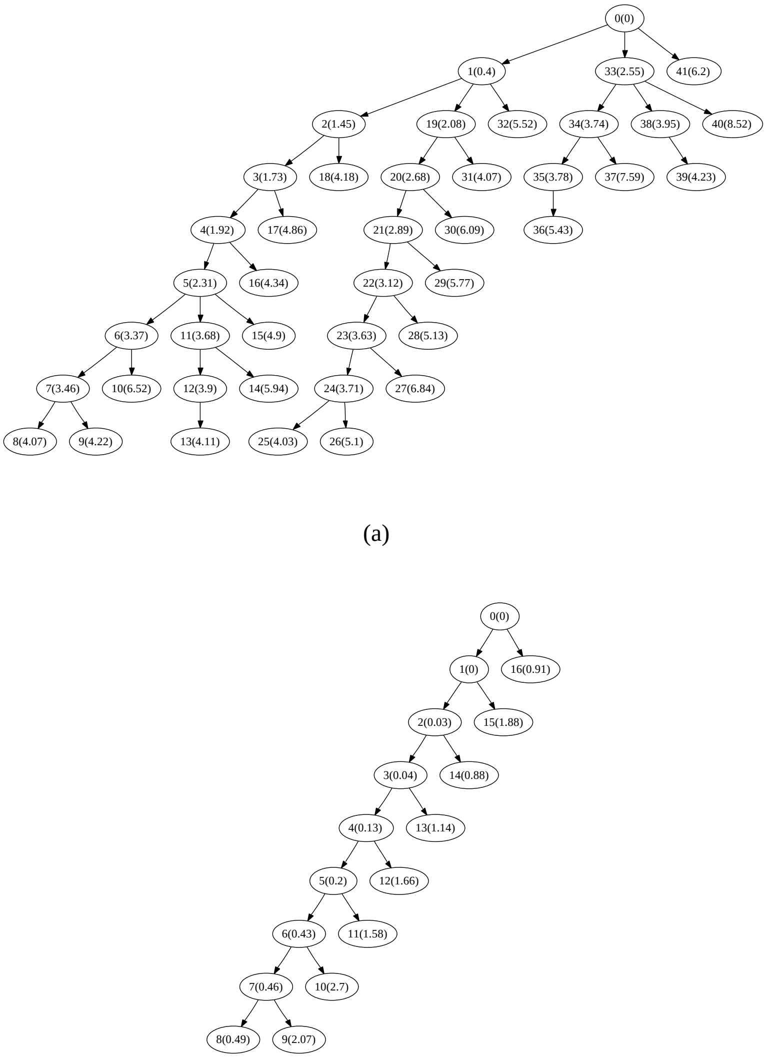

(a)

(b)

Figure 4.2: Examples of a search tree formed by the OHRSA-ML SDM detector in the scenario of a system employing QPSK modulation, $m_{\mathrm{t}} = n_{\mathrm{r}} = 8$ transmit and receive antennas and encountering average SNRs of (a) 10dB and (b) 20dB. The labels indicate the order of visitation, as well as the corresponding value $J_i(\check{\mathbf{s}}_i)$ of the CSC function of Equation (4.16), as seen in the brackets. The ML solution is attained in (a) 41 and (b) 16 evaluation steps in comparison to the $4^8 = 65536$ evaluation steps required in the case of the exhaustive ML search.

4.2.2 Bitwise OHRSA ML SDM Detection

Example 2. OHRSA-ML QPSK 2x2

Let us now consider a QPSK system having $n_\mathrm{r} = m_\mathrm{t} = 3$ transmit and receive antennas, which is described by Equation (4.1). The transmitted signal **s**, the received signal **y** as well as the *best-first* reordered channel matrix **H** of Equation (4.1) are exemplified by the following values

$$\mathbf{s} = \begin{bmatrix} 1 - 1\jmath \\ -1 - 1\jmath \end{bmatrix}, \quad \mathbf{y} = \begin{bmatrix} 0.2 + 1.1\jmath \\ 1.4 + 1.7\jmath \end{bmatrix},$$

$$\mathbf{H} = \begin{bmatrix} 0.1 - 0.2\jmath & -0.7 - 0.6\jmath \\ 0.3 + 0.4\jmath & -1.3 - 0.5\jmath \end{bmatrix}. \tag{4.31}$$

As before, our task is to obtain the ML estimate of the transmitted signal vector **s**. Firstly, we apply the OHRSA-ML method of Algorithm 10.

As suggested by Algorithm 10, we commence the detection process by evaluating the quantities **U** and $\hat{\mathbf{x}}$ of Equations (4.30c) and (4.30d) respectively, which yields

$$\mathbf{U} = \begin{bmatrix} 0.63 & -0.85 + 0.27\jmath \\ 0 & 1.45 \end{bmatrix}, \quad \hat{\mathbf{x}} = \begin{bmatrix} 0.43 - 0.34\jmath \\ -1.10 - 0.79\jmath \end{bmatrix}. \tag{4.32}$$

Furthermore, we proceed by calculating *four* values of the CSC function $J_2(\check{s}_2 = c_m),\ m = 1, \cdots, 4$ of Equation (4.30l) associated with the *four* different points c_m of the QPSK constellation. For instance, we have

$$\begin{aligned} J_2(\check{s}_2 = -1 - 1\jmath) &= \phi_2(\check{s}_2 = -1 - 1\jmath) = |u_{22}(\check{s}_2 - \hat{x}_2)|^2 \\ &= |1.45(-1 - 1\jmath - (-1.10 - 0.79\jmath))|^2 = 0.12. \end{aligned} \tag{4.33}$$

Subsequently, four QPSK symbol candidates c_m are sorted in the order of increasing sub-cost function $\phi_2(c_m)$, as described by Equation (4.30i) of Algorithm 10. For each hypothesized symbol value $\check{s}_2 = c_m$ we can now obtain *four* values of the total cost function $J(\check{\mathbf{s}}) = J_1(\check{s}_1, \check{s}_2)$ of Equation (4.30l) associated with *four* legitimate values of $\check{s}_1 = c_m$. For instance, we have

$$\begin{aligned} &J(\check{s}_1 = 1 - 1\jmath, \check{s}_2 = -1 - 1\jmath) \\ &\quad = J_2(\check{s}_2 = -1 - 1\jmath) + \phi_1(\check{s}_1 = 1 - 1\jmath, \check{s}_2 = -1 - 1\jmath) \\ &\quad = J_2(\check{s}_2 = -1 - 1\jmath) + |u_{11}(\check{s}_1 - \hat{x}_1)) + a_1|^2 \\ &\quad = 0.12 + |0.63[1 - 1\jmath - (0.43 - 0.34\jmath)] + (-0.03 + 0.21\jmath)|^2 = 0.27, \end{aligned} \tag{4.34}$$

where the quantity a_1 is given by Equation (4.30h) of Algorithm 10 as follows

$$\begin{aligned} &a_1(\check{s}_2 = -1 - 1\jmath) = u_{12}(\check{s}_2 - \hat{x}_2) \\ &\quad = (-0.85 + 0.27\jmath)[-1 - 1\jmath - (-1.10 - 0.79\jmath)] = -0.03 + 0.21\jmath. \end{aligned} \tag{4.35}$$

As further detailed in Algorithm 10, we calculate the values of the total cost function $J(\check{s}_1, \check{s}_2)$ only for the specific hypothesis $\check{s}_2$, for which the value of the CSC function $J_2(\check{s}_2)$ is lower than the minimum value $J_{\min}$ obtained.

The resultant search tree is depicted in Figure 4.3(a), where as before, each evaluation step, namely each evaluation of the CSC function $J_i(\check{\mathbf{s}}_i)$ of Equation (4.30l) is indicated by an elliptic node. Moreover, the label inside each node indicates the order of evaluation as well as the corresponding value $J_i(\check{\mathbf{s}}_i)$ of the CSC function inside the brackets. The branches corresponding to *four* legitimate values of the QPSK symbol are indicated by the specific type of the edges and nodes. Specifically, the *gray* and *black* lines indicate the value of the real part of the QPSK symbol $\mathcal{R}\{\check{s}_i\} = -1$ and 1, while the *dashed* and *solid* lines indicate the value of the imaginary part $\mathcal{I}\{\check{s}_i\} = -1$ and 1.

Example 3. Bitwise OHRSA-ML QPSK 2x2

Let us consider a QPSK system identical to that described in Example 2 and attempt to derive an alternative way of finding the ML estimate of the transmitted signal vector **s** using the bit-based representation of the QPSK symbols. In order to describe this bit-based multiuser phasor constellation, let us develop a matrix and vector-based mathematical model. Firstly, observe that each point of the QPSK constellation $c_m \in \mathcal{M}$ may be represented as the inner product $c_m = \boldsymbol{q}^{\mathrm{T}}\boldsymbol{d}_m$ of a unique bit-based vector $\boldsymbol{d}_m = [d_{m1}, d_{m2}]^{\mathrm{T}}$, $d_{ml} = \{-1, 1\}$ and the vector $\boldsymbol{q} = [1, 1\jmath]^{\mathrm{T}}$. For instance we have

$$c_1 = -1 - 1\jmath = \boldsymbol{q}^{\mathrm{T}}\boldsymbol{d}_1 = \begin{bmatrix} 1 & 1\jmath \end{bmatrix} \cdot \begin{bmatrix} -1 \\ -1 \end{bmatrix}. \tag{4.36}$$

Furthermore, let us define a (4×2)-dimensional matrix

$$\mathbf{Q} = \mathbf{I} \otimes \boldsymbol{q} = \begin{bmatrix} 1 & 1\jmath & 0 & 0 \\ 0 & 0 & 1 & 1\jmath \end{bmatrix}, \tag{4.37}$$

where **I** is (2×2)-dimensional identity matrix, while $\otimes$ denotes the *matrix direct product* [150]. Consequently, the QPSK-modulated signal vector **s** may be represented as

$$\mathbf{s} = \begin{bmatrix} 1 - 1\jmath \\ -1 - 1\jmath \end{bmatrix} = \mathbf{Qt} = \begin{bmatrix} 1 & 1\jmath & 0 & 0 \\ 0 & 0 & 1 & 1\jmath \end{bmatrix} \begin{bmatrix} 1 \\ -1 \\ -1 \\ -1 \end{bmatrix}, \tag{4.38}$$

where $\mathbf{t} = [\boldsymbol{t}_1^{\mathrm{T}}, \boldsymbol{t}_2^{\mathrm{T}}]^{\mathrm{T}}$ is a column supervector comprising the two bit-based vectors $\boldsymbol{t}_1$ and $\boldsymbol{t}_2$ associated with the QPSK-modulated symbols s_1 and s_2, respectively.

Substituting Equation (4.38) into the system model of Equation (4.1) yields

$$\mathbf{y} = \mathbf{HQt} + \mathbf{w}, \tag{4.39}$$

Moreover, since $\mathbf{t}$ is a real-valued vector, we can elaborate a bit further and deduce a real-valued system model as follows

$$\begin{bmatrix} \mathcal{R}\{\mathbf{y}\} \\ \mathcal{I}\{\mathbf{y}\} \end{bmatrix} = \begin{bmatrix} \mathcal{R}\{\mathbf{HQ}\} \\ \mathcal{I}\{\mathbf{HQ}\} \end{bmatrix} \mathbf{t} + \begin{bmatrix} \mathcal{R}\{\mathbf{w}\} \\ \mathcal{I}\{\mathbf{w}\} \end{bmatrix} = \tilde{\mathbf{H}}\mathbf{t} + \tilde{\mathbf{w}}, \tag{4.40}$$

where $\tilde{\mathbf{H}}$ is a real-valued (4×4)-dimensional bitwise channel matrix, which may be expressed as

$$\tilde{\mathbf{H}} = \begin{bmatrix} \mathcal{R}\{\mathbf{HQ}\} \\ \mathcal{I}\{\mathbf{HQ}\} \end{bmatrix} = \begin{bmatrix} 0.1 & 0.2 & -0.7 & 0.6 \\ 0.3 & -0.4 & -1.3 & 0.5 \\ -0.2 & 0.1 & -0.6 & -0.7 \\ 0.4 & 0.3 & -0.5 & -1.3 \end{bmatrix}. \tag{4.41}$$

Thus, we arrive at the new system model of Equation (4.40), which may be interpreted as a (4×4)-dimensional BPSK-modulated SDM sytem. By applying the OHRSA-ML method of Algorithm 10 we have

$$\mathbf{U} = \begin{bmatrix} 0.63 & 0 & -0.85 & -0.27 \\ 0 & 0.63 & 0.27 & -0.85 \\ 0 & 0 & 1.45 & 0 \\ 0 & 0 & 0 & 1.45 \end{bmatrix}, \quad \hat{\mathbf{x}} = \begin{bmatrix} 0.43 \\ -0.34 \\ -1.10 \\ -0.79 \end{bmatrix}. \tag{4.42}$$

Furthermore, the first two steps of the recursive search process of Algorithm 10 are given by

$$\begin{aligned} J_4(\check{t}_4 = -1) &= |u_{44}(\check{t}_4 - \hat{x}_4)|^2 \\ &= |1.45(-1-(-0.79))|^2 = 0.10 \end{aligned} \tag{4.43}$$

and

$$\begin{aligned} a_3(\check{t}_4 = -1) &= u_{34}(\check{t}_4 - \hat{x}_4) \\ &= 0(-1-(-0.79)) = 0, \\ J_3(\check{t}_3 = -1, \check{t}_4 = -1) &= |u_{33}(\check{t}_3 - \hat{x}_3) + a_3|^2 \\ &= |1.45(-1-(-1.10)) + (0)|^2 = 0.12. \end{aligned} \tag{4.44}$$

Upon completing the recursive search process of Algorithm 10 we arrive at the search tree depicted in Figure 4.3(b). As before, each evaluation step, namely each evaluation of the CSC function $J_i(\check{\mathbf{t}}_i)$ of Equation (4.30l) is indicated by an elliptic node. Moreover, the label inside each node indicates the order of evaluation as well as the corresponding value $J_i(\check{\mathbf{t}}_i)$ of the CSC function inside the brackets. The branches corresponding to two legitimate values $\check{t}_i = -1$ and 1 are indicated using the *dashed* and *solid* edges and nodes, respectively.

Observe that the ML estimates $\hat{\mathbf{s}}$ and $\hat{\mathbf{t}}$ of Figures 4.3 (a) and (b) are obtained within the same number of evaluation steps. Nevertheless, the latter search procedure is constituted by lower-complexity real-valued operations. Furthermore, in contrast to the detection method considered in Example 2, the search method outlined in this QPSK-based example can be readily generalized for the scenario of M-QAM SDM systems, as demonstrated in the forthcoming section.

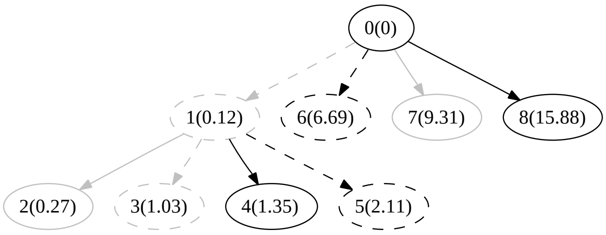

(a)

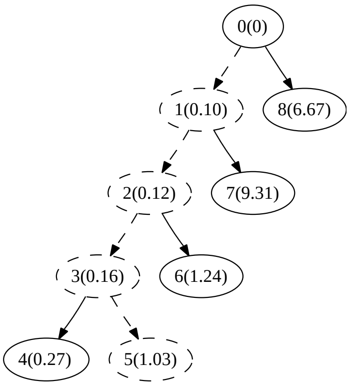

(b)

Figure 4.3: Examples of a search tree formed by the (a) OHRSA-ML and (b) BW-OHRSA-ML SDM detectors in the scenario of a system employing QPSK modulation, $m_\mathrm{t} = n_\mathrm{r} = 3$ transmit and receive antennas and encountering average SNRs of 10dB. The labels indicate the order of execution, as well as the corresponding value $J_i(\check{\mathbf{s}}_i)$ of the CSC function of Equation (4.16), as seen in the brackets.

4.2.2.1 Generalization of the BW-OHRSA-ML SDM Detector

In this section we generalize the result obtained in Section 4.2.1 to the case of systems employing hyper-rectangular modulation schemes, namely M-QAM, where each modulated symbol belongs to a discrete phasor constellation $\mathcal{M} = \{c_m\}_{m=1,\cdots,M}$. It is evident that each phasor point c_m of an M-QAM constellation map may be represented as the inner product of a unique bit-based vector $\boldsymbol{d}_m = \{d_{ml} = -1, 1\}_{l=1,\cdots,b}$ and the corresponding *quantisation vector* $\boldsymbol{q}$. Specifically, we have

$$c_m = \boldsymbol{q}^{\mathrm{T}} \boldsymbol{d}_m. \tag{4.45}$$

Some examples of the quantization vectors corresponding to the modulation schemes of BPSK, QPSK, 16-QAM as well as 64-QAM are portrayed in Table 4.1.

Table 4.1: Examples of quantization vectors.

Modulation scheme	$\boldsymbol{q}^{\mathrm{T}}$
BPSK	[1]
QPSK	$\frac{1}{\sqrt{2}}[1,\ \jmath]$
16QAM	$\frac{1}{\sqrt{10}}[1,\ 1\jmath,\ 2,\ 2\jmath]$
64QAM	$\frac{1}{\sqrt{42}}[1,\ 1\jmath,\ 2,\ 2\jmath,\ 4,\ 4\jmath]$

Furthermore, we define a $(bm_{\mathrm{t}} \times m_{\mathrm{t}})$-dimensional *quantization matrix* $\mathbf{Q} = \mathbf{I} \otimes \boldsymbol{q}$, where $\mathbf{I}$ is an $(m_{\mathrm{t}} \times m_{\mathrm{t}})$-dimensional identity matrix and $\boldsymbol{q}$ is the aforementioned *quantization vector*, while $\otimes$ denotes the *matrix direct product* [150]. Consequently the M-QAM-modulated signal vector $\mathbf{s}$ may be represented as

$$\mathbf{s} = \mathbf{Q}\mathbf{t}, \tag{4.46}$$

where $\mathbf{t} = [\boldsymbol{t}_1^{\mathrm{T}}, \cdots, \boldsymbol{t}_{m_{\mathrm{t}}}^{\mathrm{T}}]^{\mathrm{T}}$ is a column supervector comprising the bit-based vectors $\boldsymbol{t}_i$ associated with each transmitted signal vector component s_i. Substituting Equation (4.46) into the system model of Equation (4.1) yields

$$\mathbf{y} = \mathbf{H}\mathbf{Q}\mathbf{t} + \mathbf{w}. \tag{4.47}$$

Moreover, since $\mathbf{t}$ is a real-valued vector, we can elaborate a bit further and deduce a real-valued system model as follows

$$\tilde{\mathbf{y}} = \begin{bmatrix} \mathcal{R}\{\mathbf{y}\} \\ \mathcal{I}\{\mathbf{y}\} \end{bmatrix} = \begin{bmatrix} \mathcal{R}\{\mathbf{HQ}\} \\ \mathcal{I}\{\mathbf{HQ}\} \end{bmatrix} \mathbf{t} + \begin{bmatrix} \mathcal{R}\{\mathbf{w}\} \\ \mathcal{I}\{\mathbf{w}\} \end{bmatrix} = \tilde{\mathbf{H}}\mathbf{t} + \tilde{\mathbf{w}}, \tag{4.48}$$

where $\tilde{\mathbf{H}}$ is a real-valued $(2n_{\mathrm{r}} \times bm_{\mathrm{t}})$-dimensional bitwise channel matrix. Observe in Equation (4.47) that the requirement of having constant-modulus symbols is satisfied by the modified system model of Equation

Algorithm 11 Bit-Wise OHRSA-aided ML SDM Detector

```
$\tilde{\mathbf{H}} = \begin{bmatrix} \mathcal{R}\{\mathbf{HQ}\} \\ \mathcal{I}\{\mathbf{HQ}\} \end{bmatrix}$    (4.49a)
Sort$\{\tilde{\mathbf{H}}\}$, such that $\|(\tilde{\mathbf{H}})_1\|^2 \leq \cdots \leq \|(\tilde{\mathbf{H}})_r\|^2$    (4.49b)
$\mathbf{G} = (\tilde{\mathbf{H}}^{\mathrm{H}}\tilde{\mathbf{H}} + \sigma_w^2\mathbf{I})$    (4.49c)
$\mathbf{U} =$ CholeskyDecomposition$(\mathbf{G})$    (4.49d)
$\hat{\mathbf{x}} = \mathbf{G}^{-1}\tilde{\mathbf{H}}^{\mathrm{H}}\tilde{\mathbf{y}}$    (4.49e)
Calculate  $J_r$    (4.49f)
Unsort$\{\hat{\mathbf{t}}\}$    (4.49g)

function  Calculate  $J_i$    (4.49h)
  $a_i = \sum_{j=i+1}^{m_{\mathrm{t}}} u_{ij}(\check{t}_j - \hat{x}_j)$    (4.49i)
  Sort$\{\boldsymbol{d}\}$, such that $\phi_i(d_1) < \phi_i(d_2)$,    (4.49j)
  where  $\phi_i(d) = |u_{ii}(d - \hat{x}_i) + a_i|^2$    (4.49k)
  for  $m = 1,2$  do    (4.49l)
    $\check{t}_i = d_m$    (4.49m)
    $J_i = J_{i+1} + \phi_i(\check{t}_i)$    (4.49n)
    if  $J_i < J_{\min}$  then    (4.49o)
      if  $i > 0$  then  Calculate  $J_{i-1}$    (4.49p)
      else
        $J_{\min} = J_0$    (4.49q)
        $\hat{\mathbf{t}} = \check{\mathbf{t}}$    (4.49r)
      end  if
    end  if
  end  for
end  function
```

(4.47), since we have $|t_i|^2 = 1$ and thus the method described in Section 4.2.1 and summarized in Algorithm 10 is applicable for the evaluation of the bitwise ML estimate $\hat{\mathbf{t}}$ of Equation (4.47). Consequently, we apply the following changes to Algorithm 10:

1. Include the evaluation of the bitwise channel matrix $\tilde{\mathbf{H}}$ in (4.49a) and
2. Adjust the number of candidate bit values of t_i to $d_m = \{-1, 1\}$ in (4.49l).

Hence we arrive at a new detection technique, namely the Bitwise OHRSA-aided ML SDM detector, which is summarized in Algorithm 11.

In order to further explore the operation of Algorithm 11 let us consider the search tree diagram depicted in Figure 4.4. The search-tree diagram depicted in Figure 4.4 corresponds to the scenario of a system, which employs QPSK modulation and $m_{\mathrm{t}}{=}n_{\mathrm{r}}{=}8$ transmit and receive antennas, while operating at the average

SNR of 6 dB. Each circular node in the diagram represents a bit candidate $\check{t}_i$. The bold and hollow nodes denote the binary values of the bit $\check{t}_i = \{-1, 1\}$ assumed in the current step of the recursive search process. The corresponding signal vector candidates $\check{\mathbf{t}}_i = \{\check{t}_j\}_{j=i,\cdots,r}$ of the transmitted bit-based signal vector **t** are represented by the complete search branches starting at top node 0 and ending at the bottom, namely at level 16 of the search tree. Furthermore, the values of the CSC function $J_i(\check{\mathbf{t}}_i)$ associated with each branch $\check{\mathbf{t}}_i$ of the search tree of Figure 4.4 are indicated by both the colour and thickness of the transitions connecting each *child* or *descendent* node $\check{\mathbf{t}}_i$ with the corresponding *parent* node $\check{\mathbf{t}}_{i+1}$. The reference scale of the objective function values ranging from $J = 0$ at the top tree level 0 to a value of $J = 2.6$ at the bottom tree level 16 is depicted on the left of Figure 4.4. For instance, the first attained signal candidate associated with the left-most search branch of Figure 4.4 may be associated with the 16-bit binary vector $\check{\mathbf{t}}_1 = [0111101000110111]$. As suggested by the bottom node of the left-most search branch in Figure 4.4, the corresponding value of the objective function is $J_1 = J(\check{\mathbf{t}}_1) \approx 2.6$. Subsequently, only the specific branches of the search tree having their objective function values $J_i(\check{\mathbf{t}}_i)$ below J_1 are pursued. The second candidate solution attained by the search tree of Figure 4.4 is constituted by a binary vector $\check{\mathbf{t}}_2 = [0111101000100101]$, which differs from the first candidate $\check{\mathbf{t}}_1$ in its last five bits and has the associated objective function value of $J_2 = J(\check{\mathbf{t}}_2) \approx 2.1$. Finally, the ML solution is constituted by the last search branch, reaching the bottom level 16 of the search tree in Figure 4.4, namely the binary vector $\check{\mathbf{t}}_{\mathrm{ML}} = [1111001110100101]$ associated with the corresponding objective function value of $J_{\mathrm{ML}} = J(\check{\mathbf{t}}_{\mathrm{ML}}) \approx 1.7$. Observe that the ML solution is attained in 139 evaluation steps in comparison to the $2^{16} = 65536$ evaluation steps required by the exhaustive ML search.

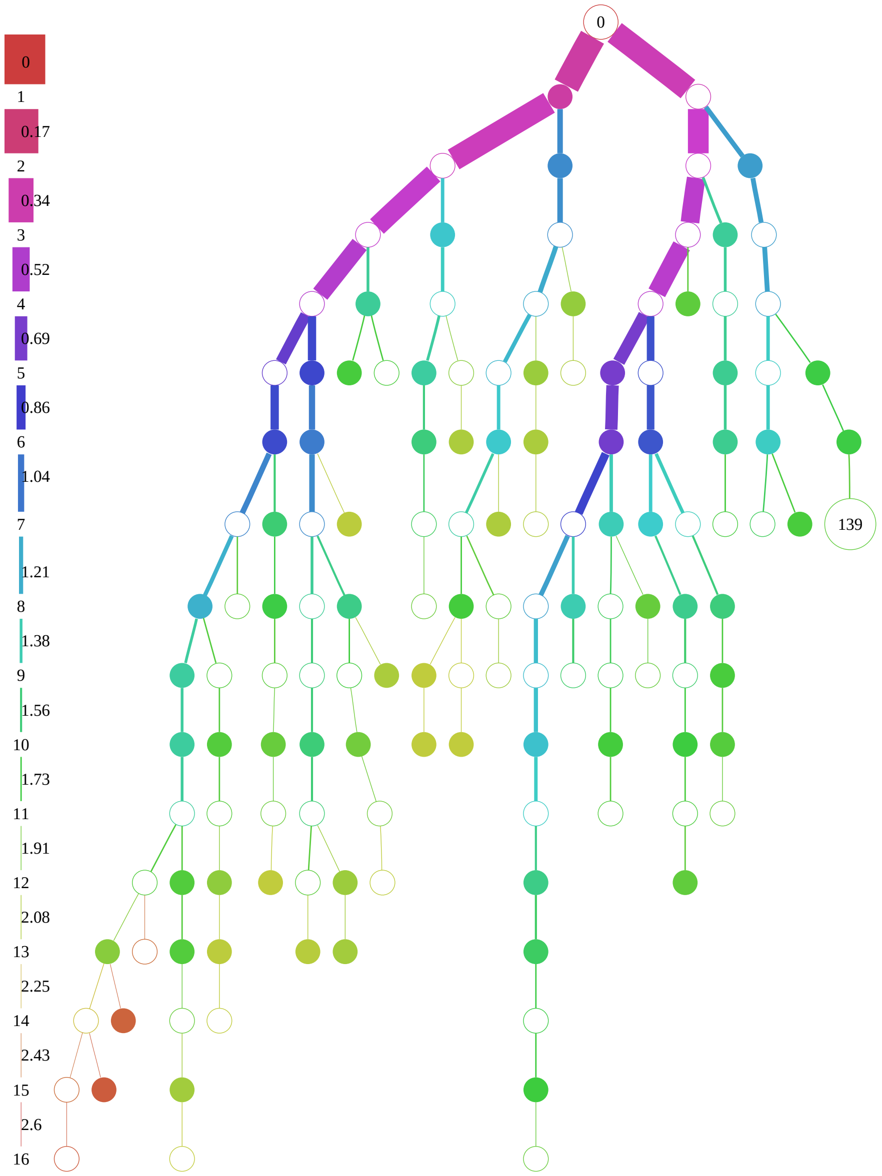

Figure 4.4: Example of a search tree formed by the BW-OHRSA method of Algorithm 11 in the scenario of QPSK, m_{t}=n_{r}=8 and an average SNR of 6 dB. Each circular node in the diagram represents a subvector candidate $\check{\mathbf{t}}_i = \{\check{t}_j\}_{j=i,\cdots,r}$ of the transmitted bit-based signal vector $\mathbf{t}$. The bold and hollow nodes denote the duo-binary values of the bit $\check{t}_i = \{-1, 1\}$ assumed. The corresponding value of the CSC function $J_i(\check{\mathbf{t}}_i)$ quatified in Equation (4.17b) is indicated by both the color and the thickness of the transitions connecting each child node $\check{\mathbf{t}}_i$ with the corresponding parent node $\check{\mathbf{t}}_{i+1}$. The ML solution is attained in 139 evaluation steps in comparison to the $2^{16} = 65536$ evaluation steps required by the exhaustive ML search.

4.2.3 OHRSA-aided Log-MAP SDM Detection

It is evident [28] that the BER associated with the process of communicating over a noisy fading MIMO channel can be dramatically reduced by means of employing channel coding. A particularly effective channel coding scheme is constituted by the *soft-input soft-output* turbo coding method [26]. Turbo coding, however, requires *soft* information concerning the bit decisions at the output of the SDM detector, in other words the *a posteriori* soft information regarding the confidence of the bit-decision is required.

The derivation of an expression for the low-complexity evaluation of the soft-bit information associated with the bit estimates of the SDM detector's output characterized by Equation (4.5) is given in [28]. Here, we present a brief summary of the results deduced in [28].

The probability of the mth bit of the QAM symbol transmitted from the ith transmit antenna element is determined by the *likelihood* function, which may be expressed as follows [136]

$$\mathcal{P}(b_{im}) = \sum_{\check{\mathbf{s}} \in \mathcal{M}_{im}^{1;m_\mathrm{t}}} P(\check{\mathbf{s}}) p(\mathbf{y}|\check{\mathbf{s}}, \mathbf{H}), \tag{4.50}$$

where we define

$$\mathcal{M}_{im}^{b;m_\mathrm{t}} = \left\{ \check{\mathbf{s}} = (\check{s}_1, \cdots, \check{s}_{m_\mathrm{t}})^\mathrm{T};\ \check{s}_j \in \mathcal{M} \text{ for } j \neq i,\ \check{s}_i \in \mathcal{M}_m^b \right\} \tag{4.51}$$

and $\mathcal{M}_m^b$ denotes the specific subset of the entire set $\mathcal{M}$ of modulation constellation phasors, which comprises the bit value $b = \{0, 1\}$ at the mth bit position.

Correspondingly, the soft-bit value associated with the mth bit of the QAM symbol transmitted from the ith transmit antenna element is determined by the log-likelihood ratio (LLR) values defined in [136] as

$$\mathcal{L}_{im} = \log \frac{\mathcal{P}(b_{im} = 1)}{\mathcal{P}(b_{im} = 0)} = \log \frac{\sum_{\check{\mathbf{s}} \in \mathcal{M}_{im}^{1;m_\mathrm{t}}} P(\check{\mathbf{s}}) p(\mathbf{y}|\check{\mathbf{s}}, \mathbf{H})}{\sum_{\check{\mathbf{s}} \in \mathcal{M}_{im}^{0;m_\mathrm{t}}} P(\check{\mathbf{s}}) p(\mathbf{y}|\check{\mathbf{s}}, \mathbf{H})}. \tag{4.52}$$

However, the direct calculation of the accumulate *a posteriori* conditional probabilities in the nominator and denominator of Equation (4.52) may have an excessive complexity in practice. Fortunately, as advocated in [28], the LLR values characterized in Equation (4.52) may be closely approximated as follows

$$\mathcal{L}_{im} \approx \log \left(\frac{\max_{\check{\mathbf{s}} \in \mathcal{M}_{im}^{0;m_\mathrm{t}}} P(\check{\mathbf{s}}) p(\check{\mathbf{s}}|\mathbf{y}, \hat{\mathbf{H}})}{\max_{\check{\mathbf{s}} \in \mathcal{M}_{im}^{0;m_\mathrm{t}}} P(\check{\mathbf{s}}) p(\check{\mathbf{s}}|\mathbf{y}, \hat{\mathbf{H}})} \right), \tag{4.53}$$

where we assume equiprobable transmitted phasors $\check{\mathbf{s}}$ and hence may elaborate a little further. Namely, we have

$$\mathcal{L}_{im} \approx \log \frac{p(\mathbf{y}|\check{\mathbf{s}}_{im}^1, \mathbf{H})}{p(\mathbf{y}|\check{\mathbf{s}}_{im}^0, \mathbf{H})}, \tag{4.54}$$

where we define

$$\check{\mathbf{s}}_{im}^b = \arg \max_{\check{\mathbf{s}} \in \mathcal{M}_{im}^{b;m_\mathrm{t}}} p(\mathbf{y}|\check{\mathbf{s}}, \mathbf{H}), \quad b = 0, 1. \tag{4.55}$$

As suggested by the nature of Equation (4.54), the detection process employing the objective function determined by Equations (4.54) and (4.55) is usually referred to as the Logarithmic Maximum *A Posteriori* (Log-MAP) probability detector.

A practical version of the Log-MAP detector may be derived as follows. Substituting Equation (4.4) into Equations (4.52) and (4.50) yields

$$\mathcal{P}(b_{im}) = \sum_{\check{\mathbf{s}}\in\mathcal{M}_{im}^{b;m_\mathrm{t}}} \exp\left(-\frac{1}{n_\mathrm{r}\sigma_w^2}\|\mathbf{y}-\mathbf{H}\check{\mathbf{s}}\|^2\right) \tag{4.56}$$

and

$$\mathcal{L}_{im} = \log\frac{\sum_{\check{\mathbf{s}}\in\mathcal{M}_{im}^{1;m_\mathrm{t}}} \exp\left(-\frac{1}{n_\mathrm{r}\sigma_w^2}\|\mathbf{y}-\mathbf{H}\check{\mathbf{s}}\|^2\right)}{\sum_{\check{\mathbf{s}}\in\mathcal{M}_{im}^{0;m_\mathrm{t}}} \exp\left(-\frac{1}{n_\mathrm{r}\sigma_w^2}\|\mathbf{y}-\mathbf{H}\check{\mathbf{s}}\|^2\right)}, \tag{4.57}$$

respectively. Note that Equation (4.57) involves two summations over $2^{rm_\mathrm{t}-1}$ exponential functions. This operation may potentially impose an excessive computational complexity for large values of m_t and/or r. However, as demonstrated in [28], the expression in (4.57) may be closely approximated by a substantially simpler expression, namely by

$$\mathcal{L}_{im} \approx \frac{1}{n_\mathrm{r}\sigma_w^2}\left[\|\mathbf{y}-\mathbf{H}\check{\mathbf{s}}_{im}^0\|^2 - \|\mathbf{y}-\mathbf{H}\check{\mathbf{s}}_{im}^1\|^2\right], \tag{4.58}$$

where we have

$$\check{\mathbf{s}}_{im}^b = \arg\min_{\check{\mathbf{s}}\in\mathcal{M}_{im}^{b;m_\mathrm{t}}} \|\mathbf{y}-\mathbf{H}\check{\mathbf{s}}\|^2, \quad b=0,1, \tag{4.59}$$

and again, $\mathcal{M}_{im}^{b;m_\mathrm{t}}$ denotes the specific subset of the entire set $\mathcal{M}^{m_\mathrm{t}}$ of signal vector candidates associated with the modulation scheme employed, which comprises the bit value $b=\{0,1\}$ at the mth bit position of the ith signal vector component.

The Log-MAP detector defined by Equations (4.58) and (4.59) may be applied for obtaining the soft-bit information associated with the bitwise OHRSA ML SDM detector derived in Section 4.2.2. Consequently, substituting the bitwise system model of Equation (4.47) into (4.58) and (4.59) yields

$$\mathcal{L}_i \approx \frac{1}{n_\mathrm{r}\sigma_w^2}\left[\|\mathbf{y}-\tilde{\mathbf{H}}\check{\mathbf{t}}_{i;\mathrm{min}}^0\|^2 - \|\mathbf{y}-\tilde{\mathbf{H}}\check{\mathbf{t}}_{i;min}^1\|^2\right], \tag{4.60}$$

where we have

$$\check{\mathbf{t}}_{i;\mathrm{min}}^b = \arg\min_{\check{\mathbf{t}}\in\mathcal{D}_i^{m;r}} \|\mathbf{y}-\tilde{\mathbf{H}}\check{\mathbf{t}}\|^2, \quad b=0,1 \tag{4.61}$$

and $\mathcal{D}_i^{b;r}$ denotes the subset of the entire set $\mathcal{D}^r$ of $(r=m_\mathrm{t}\log_2 M)$-dimensional bitwise vectors, which comprise the binary value $\check{t}_i = d_b = \{-1,1\}$ at the ith bit position.

Furthermore, substituting the bitwise objective function of Equation (4.58) into (4.60) yields

$$\begin{aligned}\mathcal{L}_i \approx & \frac{1}{n_{\mathrm{r}}\sigma_w^2}\left[J(\check{\mathbf{t}}^0_{i;\min}) + \phi - J(\check{\mathbf{t}}^1_{i;\min}) - \phi\right] \\ = & \frac{1}{n_{\mathrm{r}}\sigma_w^2}\left[J(\check{\mathbf{t}}^0_{i;\min}) - J(\check{\mathbf{t}}^1_{i;\min})\right], \end{aligned} \tag{4.62}$$

where $\check{\mathbf{t}}^m_{i;\min}$ and the corresponding cost function value $J(\check{\mathbf{t}}^m_{i;\min})$ may be obtained by applying the constrained OHRSA-aided ML detection method derived in Section 4.2.2.

Consequently, the evaluation of the bitwise Max-Log-MAP estimates of the transmitted bitwise signal vector **t** involves repetitive evaluation of $2r$ constrained ML estimates $\check{\mathbf{t}}^m_{i;\min}$ along with the associated $2r$ values of the objective function $J(\check{\mathbf{t}}^m_{i;\min})$.

Example 4. OHRSA-Log-MAP BPSK 3x3

Consider a BPSK system having $n_{\mathrm{r}} = m_{\mathrm{t}} = 3$ transmit and receive antennas, which is described by Equation (4.1). The transmitted signal **s**, received signal **y** as well as the channel matrix **H** of Equation (4.1) are exemplified by the following values

$$\mathbf{s} = \begin{bmatrix} -1 \\ 1 \\ 1 \end{bmatrix}, \quad \mathbf{y} = \begin{bmatrix} 0.2 \\ 0.3 \\ -0.5 \end{bmatrix}, \quad \mathbf{H} = \begin{bmatrix} 0.1 & -1 & 1.1 \\ -0.2 & 0.7 & -0.7 \\ 0.4 & 0.5 & -0.5 \end{bmatrix}. \tag{4.63}$$

Observe that the channel matrix **H** of Equation (4.63) happens to be *best-first* ordered and does not require any further reordering. Furthermore, in our scenario of BPSK modulation the channel matrix **H** of Equation (4.63) is equivalent to the bitwise channel matrix $\tilde{\mathbf{H}}$ of Algorithm 12.

Subsequently, our task is to obtain the Log-MAP estimate of the transmitted signal vector $\mathbf{t} = \mathbf{s}$. We apply the OHRSA-Log-MAP method of Algorithm 12. Firstly, we evaluate the triangular matrix **U** of Equation (4.82d) as well as the unconstrained MMSE estimate $\hat{\mathbf{x}}$ of Equation (4.82e). The resultant quantities are given by

$$\mathbf{U} = \begin{bmatrix} 0.56 & -0.07 & 0.09 \\ 0 & 1.35 & -1.35 \\ 0 & 0 & 0.46 \end{bmatrix}, \quad \hat{\mathbf{x}} = \begin{bmatrix} -0.80 \\ -0.01 \\ 0.13 \end{bmatrix}. \tag{4.64}$$

Secondly, as further suggested by Algorithm 12, for each transmitted bitwise symbol t_i we calculate the quantities $J(\check{\mathbf{t}}^{-1}_{i;\min})$ and $J(\check{\mathbf{t}}^1_{i;\min})$ corresponding to the values of the cost function $J(\check{\mathbf{t}})$ of Equation (4.82o) associated with the constrained ML estimates of the transmitted bitwise vector **t** with the ith bit-component assuming values of -1 and 1, respectively.

For instance, the cost function value $J(\check{\mathbf{t}}^{-1}_{1;\min})$ associated with the ML estimate of the bitwise signal vector **t** constrained by bit-component value $\check{t}_1 = -1$ may be calculated as follows

$$\begin{aligned} J_3(\check{t}_3 = 1) &= |u_{33}(\check{t}_3 - \hat{x}_3)|^2 = (0.46(1 - (0.13)))^2 = 0.16, \\ a_2(\check{t}_3 = 1) &= u_{23}(\check{t}_3 - \hat{x}_3) = -1.35(1 - (0.13)) = -1.17, \\ J_2(\check{t}_2 = 1, \check{t}_3 = 1) &= J_3(\check{t}_3 = 1) + |u_{22}(\check{t}_2 - \hat{x}_2) + a_2|^2 \\ &= 0.16 + |1.35(1 - (-0.01)) + (-1.17)|^2 = 0.20. \end{aligned} \tag{4.65}$$

Furthermore, we have

$$\begin{aligned} a_1(\check{t}_2 = 1, \check{t}_3 = 1) &= u_{12}(\check{t}_2 - \hat{x}_2) + u_{13}(\check{t}_3 - \hat{x}_3) \\ &= -0.07(1 - (-0.01)) + 0.09(1 - (0.13)) = 0.00, \\ J(\check{\mathbf{t}}^{-1}_{1;\min}) &= J_1(\check{t}_1 = -1, \check{t}_2 = 1, \check{t}_3 = 1) \\ &= J_2(\check{t}_2 = 1, \check{t}_3 = 1) + |u_{11}(\check{t}_1 - \hat{x}_1) + a_1|^2 \\ &= 0.20 + |0.56(-1 - (-0.80)) + (0.00)|^2 = 0.21. \end{aligned} \tag{4.66}$$

Observe that for the sake of brevity we omit the calculation of the CSC values outside the major search branch of Algorithm 12, *i. e.* outside the search branch leading to the constrained ML estimate. The corresponding search tree formed by the evaluation of the value of $J(\check{\mathbf{s}}^{-1}_{1;\min})$ using Algorithm 12 is depicted in Figure 4.5(a). Furthermore, Figures 4.5 (b)-(f) illustrate the search trees formed by the search sub-processes of Algorithm 12 corresponding to the remaining *five* values $\left\{J(\check{\mathbf{s}}^{b}_{i;\min})\right\}^{b=-1,1}_{i=1,\cdots,3}$.

Finally, upon completing the calculation of all *six* values $\left\{J(\check{\mathbf{s}}^{b}_{i;\min})\right\}^{b=-1,1}_{i=1,\cdots,3}$ we arrive at the following matrix

$$\hat{\mathbf{J}} = \left\{J(\check{\mathbf{s}}^{b}_{i;\min})\right\}^{b=-1,1}_{i=1,\cdots,3} = \begin{bmatrix} 0.21 & 1.21 \\ 0.33 & 0.21 \\ 0.33 & 0.21 \end{bmatrix}, \tag{4.67}$$

where the elements of the matrix $\hat{\mathbf{J}}$, which we refer to as Minimum Cost Function (MCF) matrix, are defined as $\hat{J}_{ij} = J(\check{\mathbf{s}}^{b_j}_{i;\min})$. Consequently, the *soft-bit* vector representing the Log-MAP estimate of the transmitted bitwise signal vector **t** may be expressed as

$$\mathbf{L} = \frac{1}{\sigma_w^2}\left[(\hat{\mathbf{J}})_1 - (\hat{\mathbf{J}})_2\right] = \begin{bmatrix} -9 \\ 1.2 \\ 1.2 \end{bmatrix}, \tag{4.68}$$

where $(\hat{\mathbf{J}})_j$ denotes the jth column of the MCF matrix $\hat{\mathbf{J}}$ defined in Equation (4.67).

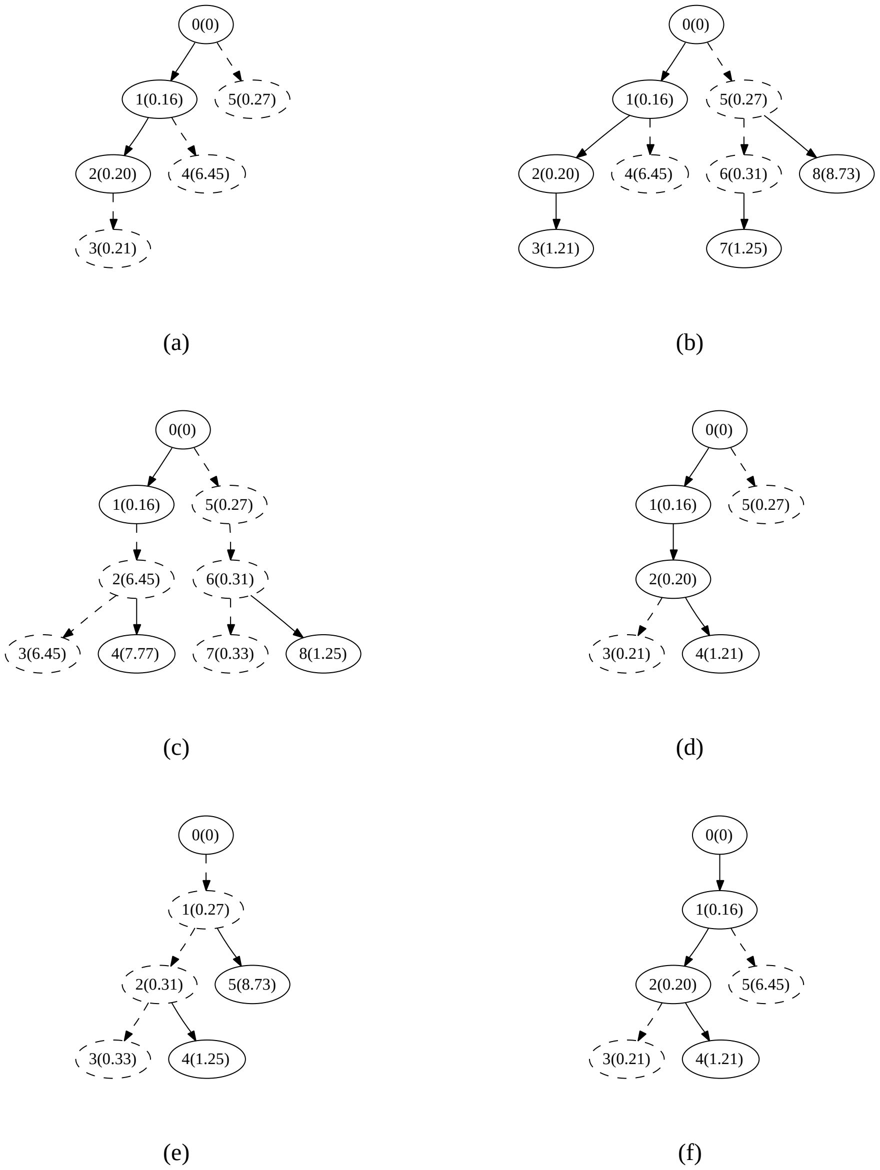

Figure 4.5: Example of search trees formed by the OHRSA-Log-MAP SDM detector of Algorithm 12 in the scenario of a system employing BPSK modulation, $m_{\mathrm{t}} = n_{\mathrm{r}} = 3$ transmit and receive antennas and encountering average SNRs of 10dB. The labels indicate the order of visitation, as well as the corresponding value $J_i(\check{\mathbf{t}}_i)$ of the CSC function of Equation (4.82o), as seen in the brackets.

Example 5. OHRSA Approximate Log-MAP BPSK 3x3

Again, consider a BPSK system identical to that described in Example 4. Specifically, we have a (3×3)-dimensional real-valued linear system described by Equation (4.1) with the corresponding transmitted signal **s**, the received signal **y** and the channel matrix **H** described in Equation (4.63). In this example we would like to demonstrate an alternative search paradigm, which avoids the repetitive process characterized by Algorithm 12 and examplified in Figure 4.5 of Example 4, while obtaining a similar result.

Firstly, we apply the OHRSA-ML method of Algorithm 11. The triangular matrix **U** of Equation (4.49d) as well as the unconstrained MMSE estimate $\hat{\mathbf{x}}$ of Equation (4.49e) are similar to those evaluated in Example 4 and are characterized by Equation (4.64). The resultant search process is characterized by the search tree diagram portrayed in Figure 4.6(a).

Additionally, however, we define a (3×2)-dimensional Minimum Cost Function (MCF) matrix $\hat{\mathbf{J}}$, which will be used for evaluation of the soft-bit information, and assign to it an initial value of $\hat{\mathbf{J}} = J_0\, \mathbf{1}$, where $\mathbf{1}$ is a (3×2)-dimensional matrix of ones and $J_0 \gg \gamma$ is some large constant, which should be greater than the average SNR of $\gamma = 10$ encountered. For instance let us assume $J_0 = 100$. Subsequently, the cost-function-related matrix $\hat{\mathbf{J}}$ is updated according to a procedure to be outlined below each time when the search branch forming the search tree portrayed in Figure 4.6(a) is terminated, regardless whether its termination occured due to reaching the final recursive index value of $i = 1$, or owing to exceeding the minimum value of the cost function $J_{\min}$. More specifically, we update the elements of the matrix $\hat{\mathbf{J}}$ corresponding to the bitwise symbols $\check{t}_j,\ j = i, \cdots, 3$ constituting the bitwise subvector candidate $\check{\mathbf{t}}_i$ associated with the particular search branch, as outlined below

$$\hat{J}_{jb_j} = \min\left\{\hat{J}_{jb_j}, J_i(\check{\mathbf{t}}_i)\right\}, \quad j = i, \cdots, 3, \quad \check{t}_j = \{-1, 1\}_{b_j}. \tag{4.69}$$

For instance, upon completing the first, left-most search branch depicted in Figure 4.6(a) and associated with the transmitted signal candidate $\check{\mathbf{t}} = \begin{bmatrix} -1 & 1 & 1 \end{bmatrix}^{\mathrm{T}}$, namely upon reaching the node number 3 of the search tree, the following update of the MCF matrix $\hat{\mathbf{J}}$ is performed

$$\begin{aligned} \hat{J}_{11} &= \min\left\{\hat{J}_{11}, J(\check{\mathbf{t}})\right\} = \min\{100, 0.21\} = 0.21 \\ \hat{J}_{22} &= \hat{J}_{32} = \min\{100, 0.21\} = 0.21. \end{aligned} \tag{4.70}$$

Consequently, the matrix $\hat{\mathbf{J}}$ becomes

$$\hat{\mathbf{J}}(3) = \begin{bmatrix} 0.21 & 100 \\ 100 & 0.21 \\ 100 & 0.21 \end{bmatrix} \tag{4.71}$$

Furthermore, the states of the MCF matrix corresponding to the search steps 4, 5 and 6 of Figure 4.6(a) are

$$\hat{\mathbf{J}}(4) = \begin{bmatrix} 0.21 & 1.21 \\ 100 & 0.21 \\ 100 & 0.21 \end{bmatrix}, \quad \hat{\mathbf{J}}(5) = \begin{bmatrix} 0.21 & 1.21 \\ 6.45 & 0.21 \\ 100 & 0.21 \end{bmatrix}, \quad \hat{\mathbf{J}}(6) = \begin{bmatrix} 0.21 & 1.21 \\ 6.45 & 0.21 \\ 0.27 & 0.21 \end{bmatrix}. \tag{4.72}$$

Finally, by substituting the resultant value of the MCF matrix $\hat{\mathbf{J}}(6)$ into Equation (4.68) we obtain the following soft-bit estimate of the transmitted bitwise signal vector **t**

$$\mathcal{L}_a = \begin{bmatrix} -9 \\ 62.39 \\ 0.60 \end{bmatrix}. \tag{4.73}$$

Observe that the soft-bit estimate $\mathcal{L}_a$ of Equation (4.73) appears to be considerably more reliable than the MMSE estimate $\hat{\mathbf{x}}$ of Equation (4.64). Specifically, as opposed to the MMSE estimate $\hat{\mathbf{x}}$ in Equation (4.19) the direct slicing of the soft-bit estimate $\mathcal{L}_a$ results in the correct signal vector **s** of Equation (4.63). Moreover, the soft-bit estimate $\mathcal{L}_a$ provides further information concerning the reliability of each estimated bit, albeit the resultant soft-bit information of Equation (4.73) substantially deviates from the more reliable exact Log-MAP estimate **L** given by Equation (4.68).

Fortunately, however, the precision of the soft-bit estimate $\mathcal{L}_a$ may be readily improved. Specifically, we introduce an additional parameter ρ, which will allow us to control the rate of convergence in the search process of Algorithm 11 by increasing the threshold value of the CSC function, which controls the passage of the recursive search process through *low likelihood* search branches having CSC function values $J_i(\check{\mathbf{t}}_i)$ in excess of $\rho J_{\min}$, as opposed to $J_{\min}$ of Equation (4.49o) in Algorithm 11. Let us now execute the modified OHRSA-ML method of Algorithm 11, where the condition $J_i < J_{\min}$ of Equation (4.49o) is replaced by the corresponding condition of $J_i < \rho J_{\min}$.

The search trees formed by the execution of the modified Algorithm 11 in the scenarios of setting (b) $\rho = 1.3$ and (c) $\rho = 2.0$ are depicted in Figures 4.5 (b) and (c), respectively. Furthermore, the convergence of the MCF matrix $\hat{\mathbf{J}}$ as well as the resultant soft-bit estimate **L** in both scenarious may be characterized as follows

$$(b) \quad \hat{\mathbf{J}}(7) = \begin{bmatrix} 0.21 & 1.21 \\ 0.31 & 0.21 \\ 0.31 & 0.21 \end{bmatrix}, \hat{\mathbf{J}}(8) = \begin{bmatrix} 0.21 & 1.21 \\ 0.31 & 0.21 \\ 0.31 & 0.21 \end{bmatrix}, \mathcal{L}_b = \begin{bmatrix} -9 \\ 0.99 \\ 0.99 \end{bmatrix} \tag{4.74}$$

and

$$(c) \quad \hat{\mathbf{J}}(8) = \begin{bmatrix} 0.21 & 1.21 \\ 0.33 & 0.21 \\ 0.33 & 0.21 \end{bmatrix}, \hat{\mathbf{J}}(10) = \begin{bmatrix} 0.21 & 1.21 \\ 0.33 & 0.21 \\ 0.33 & 0.21 \end{bmatrix}, \mathcal{L}_c = \begin{bmatrix} -9 \\ 1.2 \\ 1.2 \end{bmatrix}, \tag{4.75}$$

where as before, $\hat{\mathbf{J}}(n)$ denotes the state of the MCF matrix at search step n corresponding to the nth node of the search tree in Figures 4.5 (b) and (c). Note that the search processes characterized by Figures 4.5 (b) and (c) merely expand the search process portrayed in Figure 4.5(a). Consequently, for the sake of brevity, the corresponding Equations (4.74) and (4.75) depict only the extra states of the MCF matrix introduced by the expanded search procedure. For instance, the states $\hat{\mathbf{J}}(10)$ and $\hat{\mathbf{J}}(8)$ of Equation (4.75) complement the state $\hat{\mathbf{J}}(7)$ of Equation (4.74), as well as the states $\hat{\mathbf{J}}(6), \hat{\mathbf{J}}(5), \hat{\mathbf{J}}(4)$ and $\hat{\mathbf{J}}(3)$ of Equations (4.71) and (4.72), respectively.

Finally, by comparing the resultant soft-bit estimates $\mathcal{L}_a, \mathcal{L}_b$ and $\mathcal{L}_c$ of Equations (4.73), (4.74) and (4.75) corresponding to the scaling values of $\rho = 1.0, 1.3$ and 2.0 to the corresponding Log-MAP estimate $\mathbf{L}$ of Equation (4.68), we may hypothesize that the value of the soft-bit estimate obtained by the modified OHRSA-ML method of Algorithm 11 rapidly converges to the Log-MAP estimate of the OHRSA-Log-MAP method of Algorithm 12 upon increasing the value of the parameter ρ. As expected, there is a tradeoff between the accuracy of the soft-bit information obtained and the corresponding computational complexity associated with the particular choice of ρ. In the next section we will generalize the results obtained in this example and substantiate the aforementioned convergence-related hypothesis, as well as deduce the optimal value of the associated scaling parameter ρ.

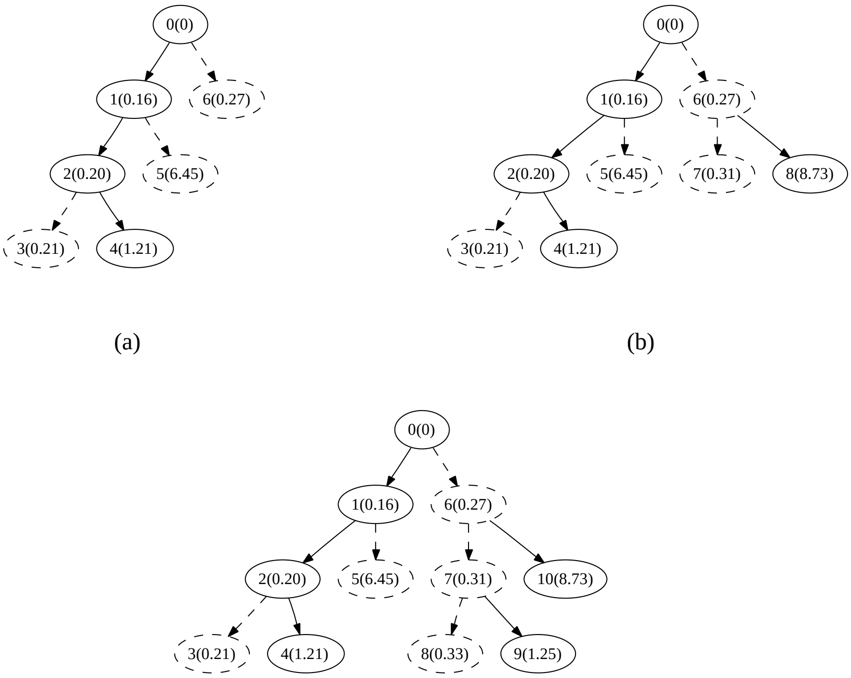

(a) (b)

(c)

Figure 4.6: Example of the search trees formed by the modified OHRSA-ML SDM detector of Algorithm 11 using different values of the parameter ρ, namely, (a) $\rho = 1.0$, (b) 1.3 and (c) 2.0. We consider a system employing BPSK modulation, $m_{\mathrm{t}} = n_{\mathrm{r}} = 3$ transmit and receive antennas and encountering an average SNR of 10dB. The labels indicate the order of evaluation, as well as the corresponding value $J_i(\check{\mathbf{s}}_i)$ of the CSC function of Equation (4.16), as seen in the brackets.

4.2.4 Soft-Input Soft-Output Max-Log-MAP SDM Detection

The OHRSA aided Max-Log-MAP SDM detection method outlined in Section 4.2.3 may be easily adopted for the sake of expoiting any *a priori* bit-related soft information available. More specifically, in Section 4.2.3 we assumed having equiprobable transmitted phasors $\check{\mathbf{s}}$. Correspondingly, in order to accommodate any available *a priori* probability information $P(\check{t}_i)$ associated with the estimated bit values $t_i,\ i = 1, \cdots, r$, Equations (4.60) and (4.61) may be modified as follows

$$\mathcal{L}_i \approx \frac{1}{\sigma_w^2}\left[\|\mathbf{y} - \tilde{\mathbf{H}}\check{\mathbf{t}}^0_{i;\mathrm{min}}\|^2 - \|\mathbf{y} - \tilde{\mathbf{H}}\check{\mathbf{t}}^1_{i;min}\|^2\right], \tag{4.76}$$

and

$$\check{\mathbf{t}}^b_{i;\mathrm{min}} = \arg\min_{\check{\mathbf{t}}\in\mathcal{D}_i^{m;r}}\left\{-log(P(\check{\mathbf{t}})) + \frac{\|\mathbf{y} - \tilde{\mathbf{H}}\check{\mathbf{t}}\|^2}{\sigma_w^2}\right\}, \quad b = 0, 1, \tag{4.77}$$

where, again, $\mathcal{D}_i^{b;r}$ denotes the subset of the entire set $\mathcal{D}^r$ of $(r{=}m_\mathrm{t}\log_2 M)$-dimensional bitwise vectors, which comprise the binary value $\check{t}_i = d_b = \{-1, 1\}$ at the ith bit position.

In practice, the probability-related soft information associated with the estimated bit-values t_i is conveyed using the LLR values $\mathcal{L}_i$. Correspondingly logorithm of the probability value $\log(P(\check{\mathbf{t}}))$ of Equation (4.61) may be calculated as follows [26]

$$\log(P(\check{\mathbf{t}})) = \sum_i P(\check{t}_i), \tag{4.78}$$

where we have

$$P(\check{t}_i = -1) = \mathtt{JacLog}(0, \mathcal{L}_i) \tag{4.79}$$

and

$$P(\check{t}_i = 1) = 1 - \mathtt{JacLog}(0, \mathcal{L}_i), \tag{4.80}$$

where $\mathtt{JacLog}(\cdot)$ denotes the Jacobian logarithm [151] defined as $\mathtt{JacLog}(a, b) = \log(e^a + e^b)$.

The resultant *a priori* probility values $P(\check{t}_i)$ may be incorporated the OHRSA SDM detector of Algorithm 11. Namely, cost function constituent ϕ_i of Equation (4.49k) is redefined for the sake of accomodating the *a priori* log-probabilistic information $P(\check{t}_i)$ as follows

$$\phi_i(d) = |u_{ii}(d - \hat{x}_i) + a_i|^2 - \sigma_w^2 P(\check{t}_i). \tag{4.81}$$

The pseudo-code describing the implementation of the bitwise soft-input-soft-output OHRSA Max-Log-MAP SDM detector is summarized in Algorithm 12.

Clearly, the repetitive nature of the search process entailing Equations (4.82f,i-r) in Algorithm 12 and exemplified by Example 4 imposes a substantial increase in the associated computational complexity. Hence,

---

Algorithm 12 Bitwise SISO-OHRSA-LogMAP SDM Detector

```
$\tilde{\mathbf{H}} = \begin{bmatrix} \mathcal{R}\{\mathbf{HQ}\} \\ \mathcal{I}\{\mathbf{HQ}\} \end{bmatrix}$    (4.82a)
Sort$\{\tilde{\mathbf{H}}\}$, such that $\|(\tilde{\mathbf{H}})_1\|^2 \leq \cdots \leq \|(\tilde{\mathbf{H}})_{m_\mathrm{t}}\|^2$    (4.82b)
$\mathbf{G} = (\tilde{\mathbf{H}}^\mathrm{H}\tilde{\mathbf{H}} + \sigma_w^2\mathbf{I})$    (4.82c)
$\mathbf{U} = $ CholeskyDecomposition$(\mathbf{G})$    (4.82d)
$\hat{\mathbf{x}} = \mathbf{G}^{-1}\tilde{\mathbf{H}}^\mathrm{H}\tilde{\mathbf{y}}$    (4.82e)
for  $i = 1, \cdots, r$
    $\mathcal{L}_{im} = \frac{1}{\sigma_w^2}\left[J^0_{i;\min} - J^1_{i;\min}\right]$    (4.82f)
end  for
Unsort$\{\mathcal{L}_i\}_{i=1,\cdots,r}$    (4.82g)

function  Calculate  $J^b_{k;i}$    (4.82h)
  $a_i = \sum_{j=i+1}^{m_\mathrm{t}} u_{ij}(\check{t}_j - \hat{x}_j)$    (4.82i)
  if  $i = k$  then
    $d_0 = \{-1, 1\}_b$    (4.82j)
  else
    Sort$\{d_m = -1, 1\}$,    (4.82k)
    such that $\phi_i(d_0) < \phi_i(d_1)$,    (4.82l)
    where  $\phi_i(d_m) = |u_{ii}(d_m - \hat{x}_i) + a_i|^2 - \sigma_w^2 P(\check{t}_i)$    (4.82m)
  end  if
  for  $m = 0, 1$  do
    $\check{t}_i = d_m$    (4.82n)
    $J_{k;i} = J_{k;i+1} + \phi_i(d_m)$    (4.82o)
    if  $J_i < J_\mathrm{min}$  then    (4.82p)
      if  $i > 0$  then  Calculate  $J^b_{k;i-1}$    (4.82q)
      else
        $J_\mathrm{min} = J^b_{k;\min} = J^b_{k;0}$    (4.82r)
      end  if
    end  if
  if  $i = k$  then break for loop
  end  for
end  function
```

in the next section we derive an OHRSA-aided approximate Log-MAP method, which is capable of approaching the optimum Log-MAP performance, while avoiding the repetitive evaluation of Equation (4.82f) in Algorithm 12 and therefore imposes considerably reduced complexity requirements.

4.2.5 Soft-Output Optimized Hierarchy-Aided Approximate Log-MAP SDM Detection

Let us define the $(r \times 2)$-dimensional Bitwise Minimum Cost (BMC) function matrix $\hat{\mathbf{J}}$ having elements as follows

$$\hat{J}_{ib} = J(\hat{\mathbf{t}}_i^b),\ i = 1, \cdots, r,\ b = -1, 1, \tag{4.83}$$

where $\hat{\mathbf{t}}_i^b$ is defined by Equation (4.59). Using the BMC matrix of Equation (4.83), Equation (4.62) may also be expressed in a vectorial form as

$$\mathbf{L} = \frac{1}{\sigma_w^2}\left[(\hat{\mathbf{J}})_1 - (\hat{\mathbf{J}})_2\right], \tag{4.84}$$

where, as before, $(\hat{\mathbf{J}})_b$ denotes the bth column of the matrix $\hat{\mathbf{J}}$ having elements defined by Equation (4.83).

Consequently, in order to evaluate the bit-related soft information we have to populate the BMC matrix $\hat{\mathbf{J}}$ of Equation (4.83) with the corresponding values of the cost function of Equation (4.83). Observe, that the evaluation of the ML estimate $\hat{\mathbf{t}}$ will situate half elements of the cost matrix $\hat{\mathbf{J}}$ with the corresponing minimum value of the cost function associated with the ML estimate, such that we have

$$J_{ib} = J(\hat{\mathbf{t}}),\ i = 1, \cdots, r,\ b = \hat{t}_i. \tag{4.85}$$

Subsequently, let us introduce the following adjustments to Algorithm 11. Firstly, we introduce an additional parameter ρ, which we refer to as the *search radius factor*. More specifically, the parameter ρ allows us to control the rate of convergence for the tree search process of Algorithm 11 and affects the cut-off value of a CSC function, which limits the passage of the recursive search process through *low-likelihood* search branches having the a CSC function value $J_i(\check{\mathbf{t}}_i)$ in excess of $\rho J_{\min}$, as opposed to $J_{\min}$. Thus, the following rule replaces Rule 4 of Section 4.2.1.1.

Rule 4a At each recursive detection level i, only the high-probability search branches corresponding to the highly likely symbol candidates c_m resulting in low values of the CSC function obeying $J_i(c_m) < \rho J_{\min}$ are pursued. Furthermore, as follows from the sorting criterion of the optimisation Rule 2, as soon as the inequality $J_i(c_m) > \rho J_{\min}$ is sutisfied, the search loop at the ith recursive detection level is discontinued.

Secondly, we introduce an additional rule, which facilitates the evaluation of the elements of the BMC matrix $\hat{\mathbf{J}}$ of Equation (4.83). Explicitly, we postulate Rule 5.

Rule 5 At each arrival at the bottom of the search tree, which corresponds to search level 1, the resultant value of the branch cost function $J(\check{\mathbf{t}})$ is utilized to populate the elements of the BMC matrix $\hat{\mathbf{J}}$, which correspond to the bitwise signal components $\check{t}_i$ comprising the obtained signal candidate $\check{\mathbf{t}}$. Namely, we have

$$\hat{J}_{ib} = \min\{\hat{J}_{ib}, J(\check{\mathbf{t}})\},\ i = 1, \cdots, r,\ b = \check{t}_i. \tag{4.86}$$

Subsequently, we suggest that the evaluation of the BMC matrix $\hat{\mathbf{J}}$, which is performed in the process of the ML search of Algorithm 11 extended by Rule 4a and using Rule 5 will allow us to provide reliable soft-bit information, while imposing a relatively low computational complexity. The main rationale of this assumption will be outlined in our quantitative complexity and performance analysis portrayed in Section 4.2.5.1.

As we will further demonstrate in Section 4.2.5.1, the resultant approximate Log-MAP SDM detector exhibits a particularly low complexity at high SNR values. On the other hand, at low SNR values the associated complexity substantially increases. Consequently, in order to control the computational complexity at low SNR values, we indroduce the additional complexity-control parameter γ. Our aim is to avoid the computationally demanding and yet inefficient detection of the specific signal components, which have their signal energy well below the noise floor. More specifically, we modify Equation (4.49p) of Algorithm 11 according to Rule 6.

Rule 6 The branching of the tree search described by Algorithm 11 is truncated, if the SNR associated with the corresponding signal component is lower than the value of the complexity-control parameter γ. In other words, the search along a given branch is truncated if we have $\frac{||\mathbf{H}_i||^2}{\sigma_w^2} < \gamma$.

Upon applying Rules 4, 5 and 6 in the context of the OHRSA-ML method of Algorithm 11, we arrive at an *approximate* OHRSA-Log-MAP SDM detector, which avoids the repetitive search required by the OHRSA-Log-MAP SDM detector of Section 4.2.3. The resultant OHRSA-aided approximate Log-MAP SDM detector, which we refer to as the Soft-output OPtimised HIErarchy (SOPHIE) SDM detector is summarised in Algorithm 13.

Algorithm 13 SOPHIE Approximate Log-MAP SDM Detector

```
$\tilde{\mathbf{H}} = \begin{bmatrix} \mathcal{R}\{\mathbf{HQ}\} \\ \mathcal{I}\{\mathbf{HQ}\} \end{bmatrix}$    (4.87a)
Sort$\{\tilde{\mathbf{H}}\}$, such that $\|(\tilde{\mathbf{H}})_1\|^2 \leq \cdots \leq \|(\tilde{\mathbf{H}})_r\|^2$    (4.87b)
$\mathbf{G} = (\tilde{\mathbf{H}}^{\mathrm{H}}\tilde{\mathbf{H}} + \sigma_w^2\mathbf{I})$    (4.87c)
$\mathbf{U} =$ CholeskyDecomposition$(\mathbf{G})$    (4.87d)
$\hat{\mathbf{x}} = \mathbf{G}^{-1}\tilde{\mathbf{H}}^{\mathrm{H}}\tilde{\mathbf{y}}$    (4.87e)
Calculate  $J_r$    (4.87f)
$\mathbf{L} = \frac{1}{\sigma_w^2}\left[(\hat{\mathbf{J}})_0 - (\hat{\mathbf{J}})_1\right]$    (4.87g)
Unsort$\{\mathcal{L}_i\}_{i=1,\cdots,r}$    (4.87h)

function  Calculate  $J_i$    (4.87i)
  $a_i = \sum_{j=i+1}^{m_{\mathrm{t}}} u_{ij}(\check{t}_j - \hat{x}_j)$    (4.87j)
  Sort$\{\boldsymbol{d}\}$, such that $\phi_i(d_1) < \phi_i(d_2)$,    (4.87k)
  where  $\phi_i(d) = |u_{ii}(d - \hat{x}_i) + a_i|^2 - \sigma_w^2 P(\check{t}_i)$    (4.87l)
  for  $m = 1, 2$  do    (4.87m)
    $\check{t}_i = d_m$    (4.87n)
    $J_i = J_{i+1} + \phi_i(\check{t}_i)$    (4.87o)
    if  $J_i < \rho J_{\min}$  then    (4.87p)
      if  $i > 0$ and $\frac{\|(\tilde{\mathbf{H}})_i\|^2}{\sigma_w^2} > \gamma$  then    (4.87q)
        Calculate  $J_{i-1}$    (4.87r)
      else
        $J_{\min} = \min(J_i, J_{\min})$    (4.87s)
        for  $j = 1, \cdots, r$    (4.87t)
          $\hat{J}_{j\check{t}_j} = \min\{\hat{J}_{j\check{t}_j}, J(\check{\mathbf{t}})\},\ j = 1, \cdots, r$    (4.87u)
        end  for    (4.87v)
      end  if
    end  if
  end  for
end  function
```

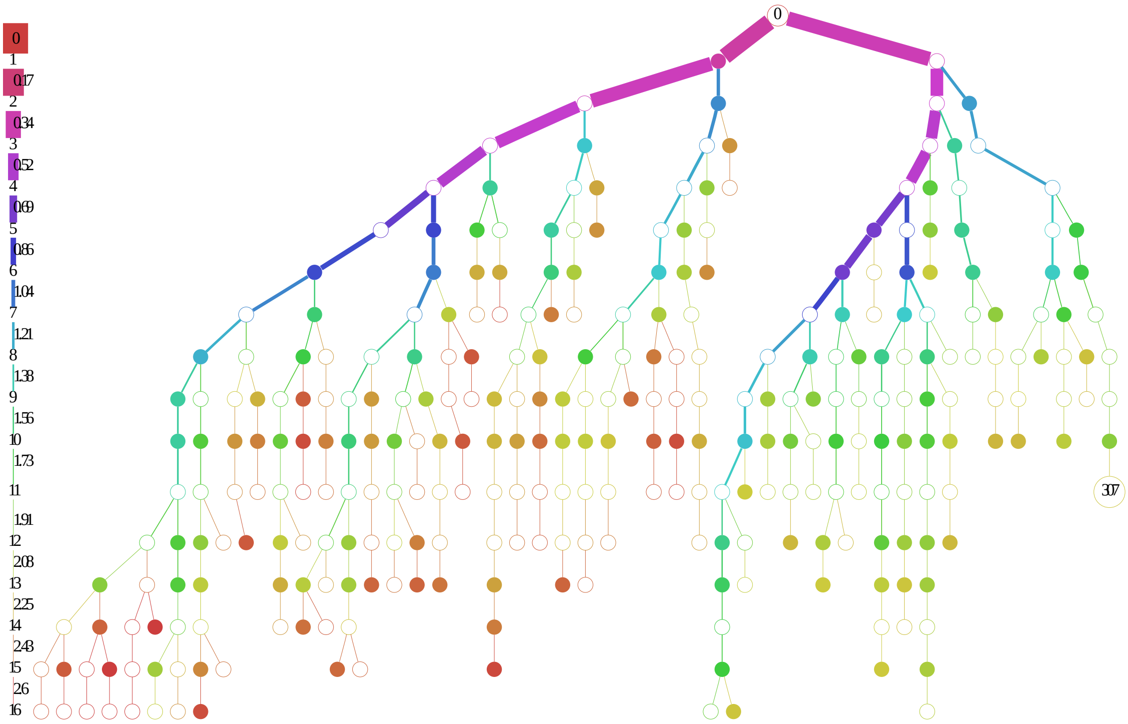

Figure 4.7: Example of a search tree formed by the SOPHIE SDM detector of Algorithm 11 in the scenario of QPSK, $m_t = n_r = 8$ and an average SNR of 6 dB. The approximate Log-MAP solution is attained in 307 evaluation steps in comparison to $32 \cdot 2^{15} = 1,048,576$ evaluation steps required by the exhaustive Log-MAP search. For more details on the notations employed in the diagram see the caption of Figure 4.4.

4.2.5.1 SOPHIE Algorithm Complexity Analysis.

As it was pointed out in [28] , "the brute-force" ML SDM detection method does not provide a feasible solution to the generic SDM detection problem, as a result of the excessive associated computational complexity. More explicitly, the ML SDM detector advocated in [28] has a computational complexity, which is of the order of

$$\mathcal{C}_{\mathrm{ML}} = O\{M^{m_{\mathrm{t}}} \cdot (3n_{\mathrm{r}} + 2n_{\mathrm{r}}m_{\mathrm{t}})\}, \tag{4.88}$$

where $3n_{\mathrm{r}} + 2n_{\mathrm{r}}m_{\mathrm{t}}$ is the complexity associated with a single search step, namely with the evaluation of the objective function value $||\mathbf{H}\check{\mathbf{s}} - \mathbf{y}||^2$, while $M^{m_{\mathrm{t}}}$ is the number of legitimate candidates of the transmitted signal vector $\mathbf{s}$. Clearly, the order of complexity imposed by Equation (4.88) becomes excessive for a large number of transmit antennas, *e.g.* in the case of employing 16QAM and $m_{\mathrm{t}} = n_{\mathrm{r}} = 8$ transmit and receive antennas, where the computational complexity associated with ML detection is of the order of 10^7 complex operations per channel use, or 10^9 complex operations per OFDM symbol formed by $K = 128$ subcarriers. Furthermore, the evaluation of the soft-bit information required by an efficient turbo-decoder implementation imposes a further substantial increase of the associated computational complexity. Specifically, the soft-output Log-MAP SDM detector advocated in [28] has a computational complexity, which is of the order of

$$\mathcal{C}_{\mathrm{LM}} = O\{m_{\mathrm{t}} \log_2 M \cdot 2^{m_{\mathrm{t}} \log_2 M - 1} \cdot (3n_{\mathrm{r}} + 2n_{\mathrm{r}}m_{\mathrm{t}})\}. \tag{4.89}$$

On the other hand, the MMSE SDM detector derived in [28] constitutes the low-complexity SDM detector. The complexity imposed by the MMSE SDM detector of [28] may be shown to be of the order of

$$\mathcal{C}_{\mathrm{MMSE}} = O\{m_{\mathrm{t}}^3 + m_{\mathrm{t}}n_{\mathrm{r}}^2 + m_{\mathrm{t}}^2 n_{\mathrm{r}} + m_{\mathrm{t}}n_{\mathrm{r}}\}. \tag{4.90}$$

Clearly, the MMSE SDM detector's complexity is substantially lower than that associated with the ML or Log-MAP SDM detectors. Specifically, *e.g.* only 1600 complex operations are required for detecting 16QAM signals transmitted and received by $m_{\mathrm{t}} = n_{\mathrm{r}} = 8$ transmit and receive antennas. Unfortunately, however, as it was demonstrated in [28] the achievable performance exhibited by the linear MMSE SDM detector is considerably lower than that attained by the optimal Log-MAP SDM detector advocated in [28] . Moreover, linear SDM detectors, such as the MMSE detector does not allow for the high-integrity detection of signals in the over-loaded scenario, where the number of the transmit antennas exceeds that of the receive antennas.

Consequently, in Sections 4.2.2, 4.2.3 and 4.2.5 we have derived a family of methods, which combine the advantageous properties of the ML and Log-MAP detection, while imposing a substantially lower complexity. In this section we demonstrate that the computational complexity associated with the SOPHIE-aided Log-MAP SDM detector of Algorithm 13 is in fact only slightly higher than that imposed by the low-complexity MMSE SDM detector advocated in [28] , while its performance is virtually identical to the performance of the Log-MAP SDM detector [28] .

The direct calculation of the complexity associated with the OHRSA methods of Algorithms 11, 12 and 13 is infeasible, since the complexity a random variable, which is a function of several parameters, such as the number m_t and n_r of transmit and receive antennas, the average SNR encountered as well as the value of the parameter ρ in Algorithm 13. Therefore, we perform the corresponding complexity analysis using computer simulations.

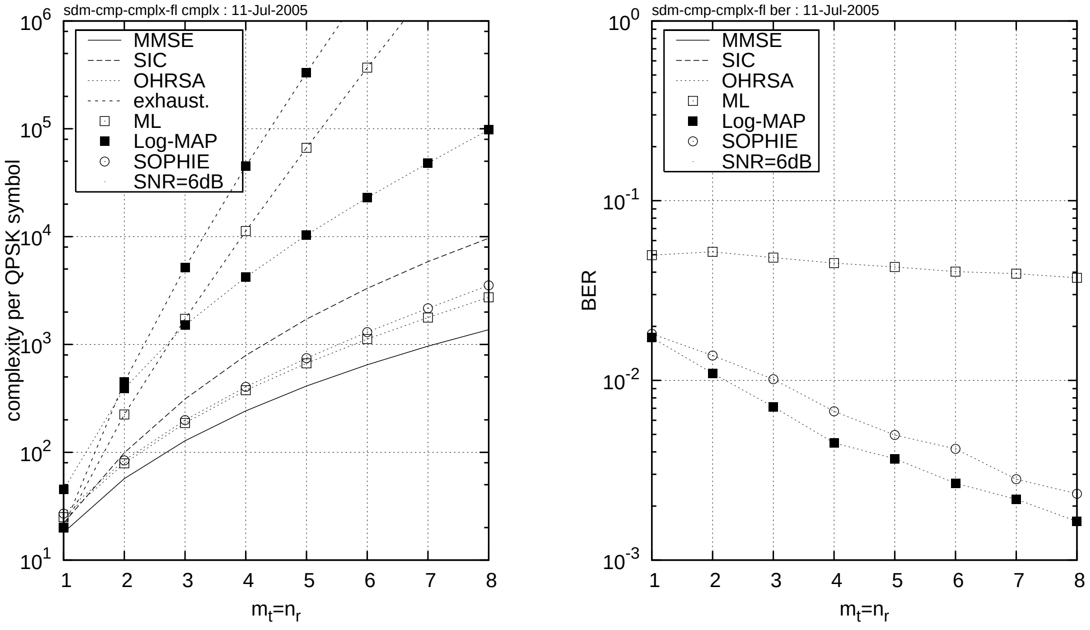

(a) (b)

Figure 4.8: (a) **Computational complexity** quantified in terms of the total number of real multiplications and additions per detected QPSK symbol and (b) the corresponding **BER** exhibited by the rate half turbo-coded **SDM-QPSK-OFDM** system employing the different SDM detection methods considered at SNR=6dB. The abscissa represents the number $m_\mathrm{t} = n_\mathrm{r} = 1, \cdots, 8$ of transmit and receive antenna elements. We employ COST-207 BU channel model [119]. We employ COST-207 BU channel model [119]. Additional system parameters are summarized in Table 1.4.

Figure 4.8(a) illustrates our comparison between the computational complexity required by different SDM detection methods, namely the linear MMSE detector advocated in [28] , the SIC detector of [28, pp.754-756] , the exhaustive search-based ML and Log-MAP detectors of [28] as well as the OHRSA-aided ML, Log-MAP and SOPHIE SDM detectors of Algorithms 11, 12 and 13, respectively. The results depicted in Figure 4.8(a) correspond to the *fully-loaded* scenario, where we have $m_\mathrm{t} = n_\mathrm{r}$ transmit and receive antennas. Observe that the complexity associated with both the OHRSA-ML and SOPHIE SDM detectors is only slightly higher than that imposed by the MMSE SDM detector and is in fact lower than the complexity imposed by the SIC SDM detector.

Furthermore, the achievable performance of the SDM-OFDM system employing the different SDM detection methods considered is depicted in Figure 4.8(b). Observe that both the OHRSA-Log-MAP and SOPHIE SDM detectors considerably outperform the linear MMSE detector. Moreover, the associated BER decreases upon increasing the number of transmit and receive antennas $m_t = n_r$, which suggests that as opposed to both the MMSE and the SIC SDM detectors, the OHRSA-Log-MAP SDM detector is capable of achieving spatial diversity even in the *fully-loaded* system. In other words, it is capable of simultaneously achieving both multiplexing and diversity gains, while maintaining a low computational complexity.

The relatively low performance of the OHRSA-ML SDM detector may be attributed to the fact that it produces no soft-bit information and therefore the efficiency of the turbo code employed is substantially degraded. Moreover, observe that while the SIC SDM detector outperforms its MMSE counterpart at high SNR values [28], the achievable performance of the two methods is fairly similar at low SNR values, such as 6dB.

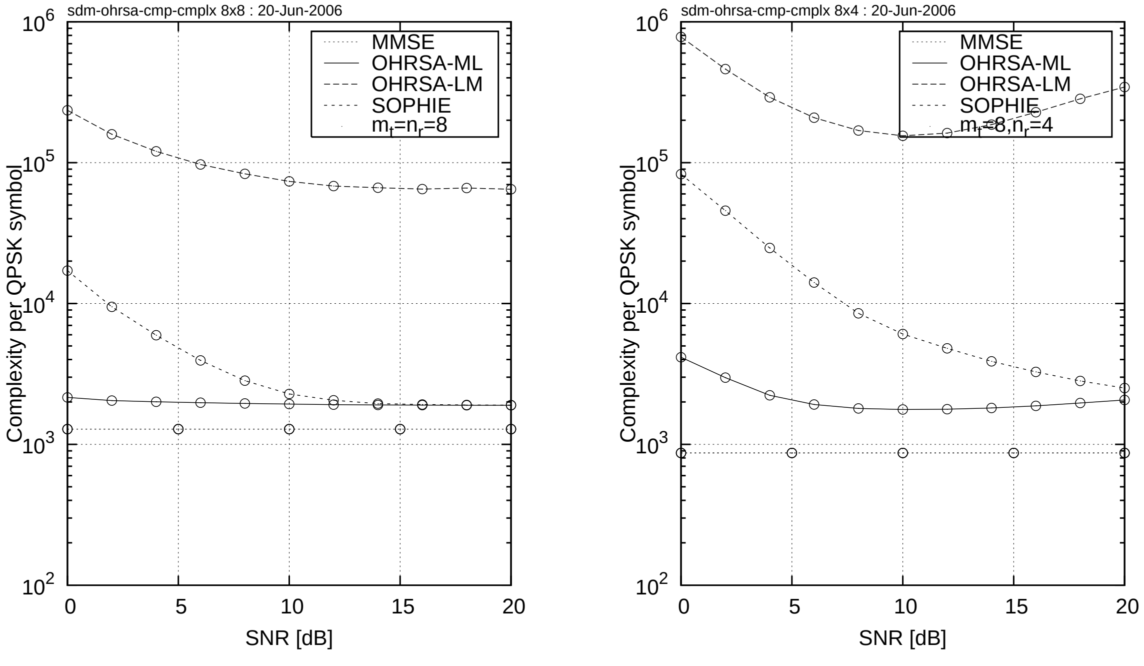

(a)

(b)

Figure 4.9: Computational complexity quantified in terms of the total number of real multiplications and additions per detected QPSK symbol. We consider the **OHRSA-ML, OHRSA-Log-MAP** and **SOPHIE** SDM detection methods of Algorithms 11, 12 and 13, respectively. Additionally, we show the corresponding computational complexity required by the low-complexity linear MMSE SDM detector as well as the optimum exhaustive Log-MAP detector. The abscissa represents the average SNR encountered.

Additionally, Figure 4.9 illustrates the complexity imposed by the OHRSA methods of Algorithms 11, 12 and 13 as a function of the average SNR encountered. Figures 4.9 (a) and (b) portray the average complexity encountered in the scenatios of $m_t = n_r = 8$ and $m_t = 8, n_r = 4$ transmit and receive antennas, respectively. Observe that the complexity associated with both the OHRSA-ML and SOPHIE methods of Algorithms 12 and 13 is mainly determined by the number m_t of transmit antennas employed. Furthermore, the complexity associated with the SOPHIE method closely matches that exhibited by the OHRSA-ML method at high SNR values and the complexity exhibited by both methods is only slightly higher than the complexity exhibited by the low-complexity MMSE SDM detector.

4.2.5.2 SOPHIE Algorithm Performance Analysis

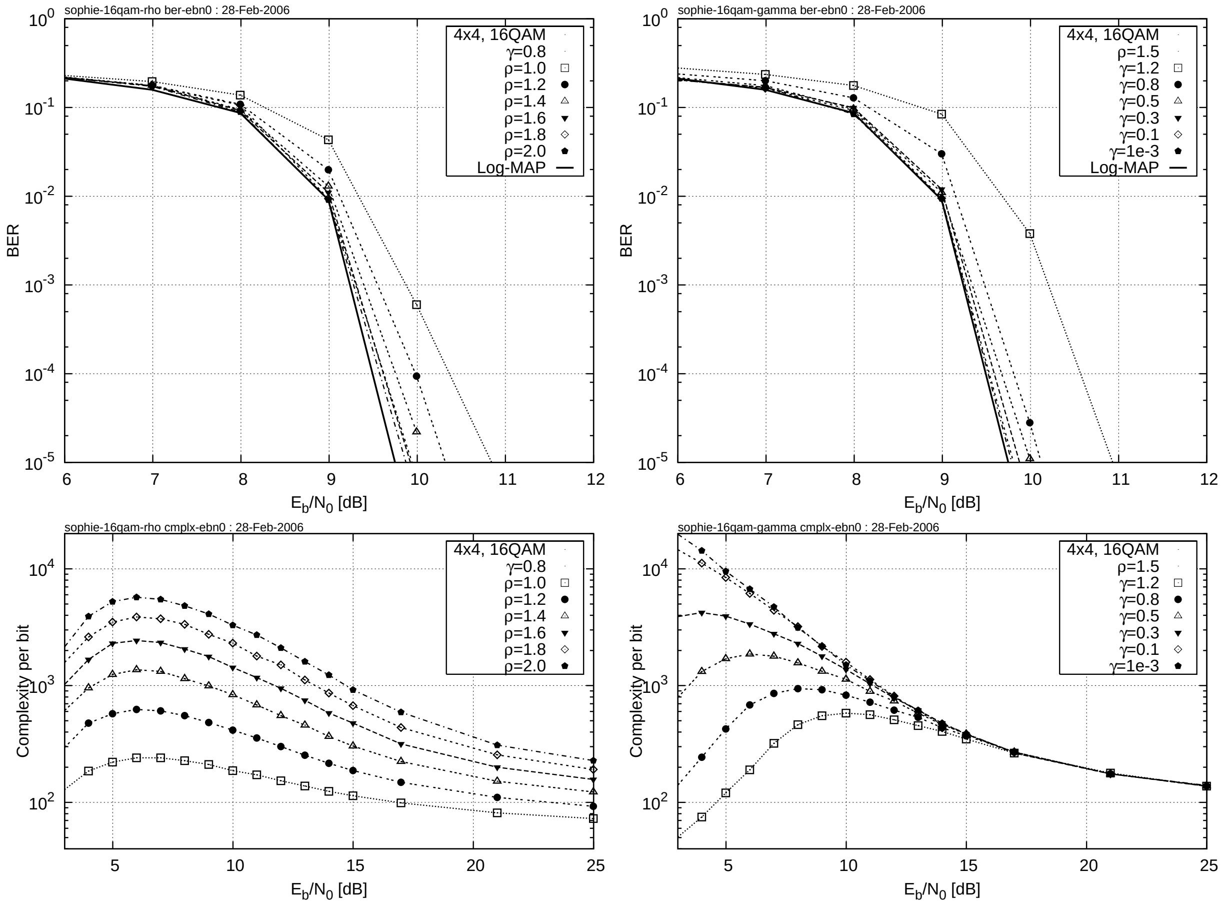

(a)

(b)

Figure 4.10: Bit Error Rate (top) and the associated **computational complexity per detected bit** (botom) exhibited by the 4 × 4 **16QAM-SDM-OFDM** system employing the **SOPHIE** SDM detector of Algorithm 13 and assuming different values of search radius and search resolution parameters (a) ρ and (b) γ. The abscissa represents the average E_b/N_0 recorded at the receive antenna elements. We employ COST-207 BU channel model [119]. Additional system parameters are summarized in Table 1.4.

In this section we present our simulation results characterizing the SDM-OFDM system employing the OHRSA-aided SDM detection schemes described in Section 4.2. Our simulations were performed in the base-band frequency domain and the system configuration characterised in Table 2.1 is to a large extent similar to that used in [38]. We assume having a total bandwidth of 800kHz. The OFDM system utilises 128 QPSK-modulated orthogonal subcarriers. For forward error correction (FEC) we use $\frac{1}{2}$-rate turbo coding [26] employing two constraint-length $K = 3$ Recursive Systematic Convolutional (RSC) component codes and the standard 124-bit WCDMA UMTS turbo code interleaver of [131]. The octally represented RCS generator polynomials of (7,5) were used. Furthermore, we employ the eight-path urban non-line-of-sight Bug Rayleigh-fading channel model characterised in [118]. Finally, throughout this report we stipulate the assumption of perfect channel knowledge, where the knowledge of the frequency-domain subcarrier-related coefficients $H[n,k]$ is deemed to be available in the receiver.

Figure 4.10 characterises the achievable performance as well as the associated computational complexity exhibited by the 4×4 16QAM-SDM-OFDM system employing the SOPHIE SDM detector of Algorithm 13. More specifically, we analyse the associated performance versus complexity trade-offs of using various values of the complexity-control parameters ρ and γ. In Figure 4.10(a) we can observe how the achievable BER performance (top) and the corresponding computational complexity depend on the value of the parameter γ. Using the results depicted in Figure 4.10(a) we may conclude that the optimum choice of the complexity-control parameter γ lies in the range $0.5 - 0.8$, where we have a minor BER performance degradation of less than 0.5 dB, while achieving up to two orders of magnitude complexity reduction at low SNR values, when compared to the full-complexity SOPHIE algorithm assuming $\gamma = 0$.

On the other hand, Figure 4.10(b) portrays both the achievable BER performance and the associated compexity of the 4×4 16QAM-SDM-OFDM system for different values of the complexity-control parameter ρ. We may conclude that the optimum trade-off between the attainable BER performance and the associated complexity is achieved, when the value of the complexity-control parameter ρ lies in the range of $1.3 - 1.5$, where the BER performance degradation imposed does not exceed 0.5 dB, while the associated computational complexity is reduced by more than an order of magnitude, when compared to large values of ρ, such as for instance $\rho = 2.0$.

Furthermore, Figure 4.11(a) demonstrates both the BER performance (top) and the associated computational complexity exhibited by the (8×8) 4, 16 and 64QAM SDM-OFDM systems employing the SOPHIE SDM detector of Algorithm 13. Figure 4.11(b) characterises the 16QAM-SDM-OFDM system employing the SOPHIE SDM detector of Algorithm 13 and having a constant number of $n_{\mathrm{r}} = 4$ receive antenna elements in terms of its ability to detect the multiplexed signals arriving from various numbers of transmit antenna elements. Specifically, we aim for exploring the performance of the SOPHIE SDM detector in the overloaded system scenario, where the number of transmit antenna elements exceeds that of the receiver elements and thus we have $m_{\mathrm{t}} > n_{\mathrm{r}}$. Indeed, the BER curves portrayed in Figure 4.11 (top) confirm the near-Log-MAP performance of the SOPHIE SDM detector of Algorithm 13 in both systems employing high-throughput modulation schemes as well as in the overloaded system scenario.

Figure 4.12 characterizes the computational complexity imposed by the SOPHIE SDM detector of Algorithm 13 as a function of the number $m_{\mathrm{t}} = n_{\mathrm{r}}$ of transmit and receive antennas. More specifically, we consider three ranges of SNR values: low SNRs, the critical SNR, which corresponds to the "waterfall" region of the BER versus SNR curve, as well as high SNRs, which corresponds to the error-free detection region. In Figure 4.12 we may observe that the computational complexity imposed by the SOPHIE detector increases according to a polynomial law as a function of the number of transmit antennas for both high and low SNRs.

Figure 4.13(a) demonstrates that the SDM-OFDM system employing the SOPHIE SDM detector of Algorithm 13 is capable of exploiting the available MIMO channel's multiplexing gain in the fully loaded system scenario, when the number of the transmit antenna elements m_{t} is equal to that of the receiver antenna elements n_{r}. More specifically, the results depicted in Figure 4.13(a) suggest that the SDM-OFDM SOPHIE SDM detector having $m_{\mathrm{t}} = n_{\mathrm{r}} = 8$ transmit and receive antennas exhibits an SNR-related diversity gain of 2dB at the target BER of 10^{-4}, as well as a factor four higher throughput, when compared to the same system employing two antennas at both the transmitter and receiver.

Additionally, Figure 4.13(b) characterises the SDM-OFDM system employing the SOPHIE SDM detector of Algorithm 13 and having a constant number of $n_{\mathrm{r}} = 4$ receive antenna elements in terms of its ability to detect the multiplexed signals arriving from various numbers of transmit antenna elements. Specifically, we aim for exploring the performance of the SOPHIE SDM detector in the over-loaded system scenario, where the number of transmit antenna elements exceeds that of the receiver elements and thus we have $m_{\mathrm{t}} > n_{\mathrm{r}}$. We can see that as opposed to the MMSE SDM detector [28] , the SOPHIE SDM detector exhibits a good performance both when we have $m_{\mathrm{t}} \leq n_{\mathrm{r}}$, as well as in the over-loaded system scenario, when the number of transmit antenna elements exceeds the number of the receive antenna elements, i.e. when we have $m_{\mathrm{t}} > n_{\mathrm{r}}$.

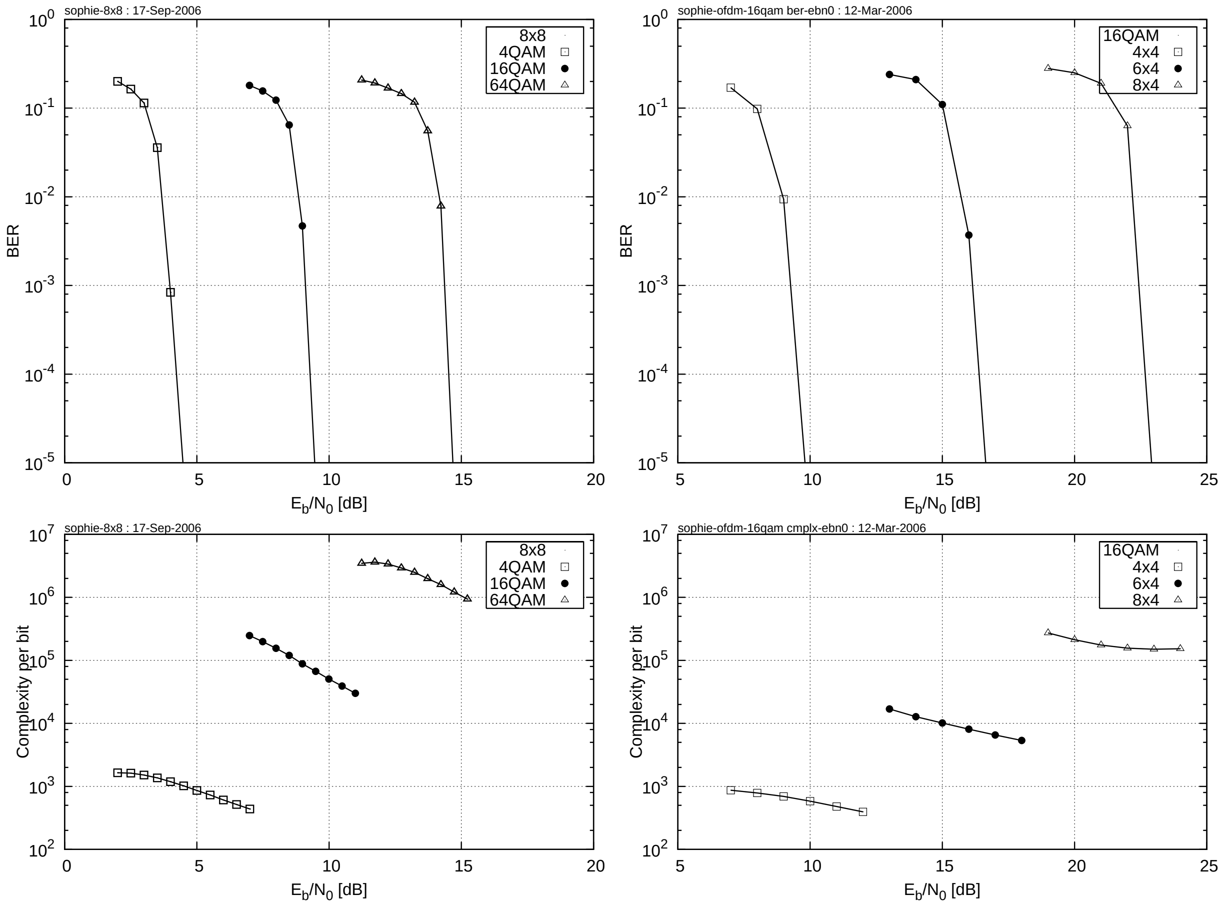

(a) (b)

Figure 4.11: Bit Error Rate (top) and the associated **computational complexity per detected bit** (bottom) exhibited by the **SDM-OFDM** system employing the **SOPHIE** SDM detector of Algorithm 13 and assuming $\rho = 1.3$, $\gamma = 0.8$. (a) 8×8 system employing 4, 16 and 64 QAM, and (b) 16QAM system employing a fixed number of 4 receive antennas, as well as 4, 6 and 8 transmit antennas. The abscissa represents the average E_b/N_0 recorded at the receive antenna elements. We employ COST-207 BU channel model [119]. Additional system parameters are summarized in Table 1.4.

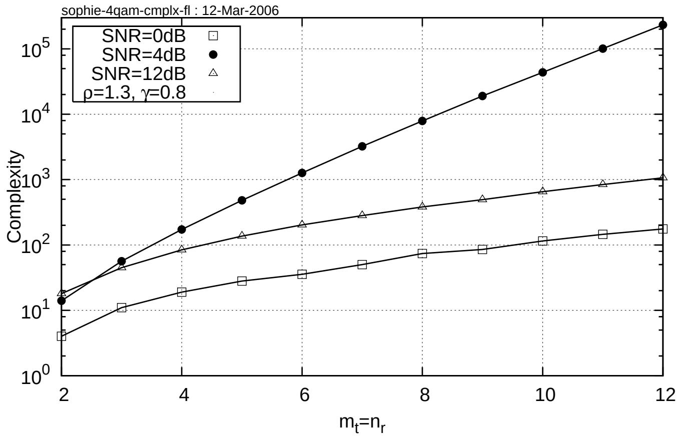

Figure 4.12: Computational complexity imposed by the MIMO-OFDM system employing the SOPHIE SDM detector of Algorithm 13 and assuming $\rho = 1.3$, $\gamma = 0.8$. The complexity is quantified in terms of total number of real additions and multiplications as a function of the number $m_t = n_r$ of transmit and receive antennas. We employ COST-207 BU channel model [119]. Additional system parameters are summarized in Table 1.4.

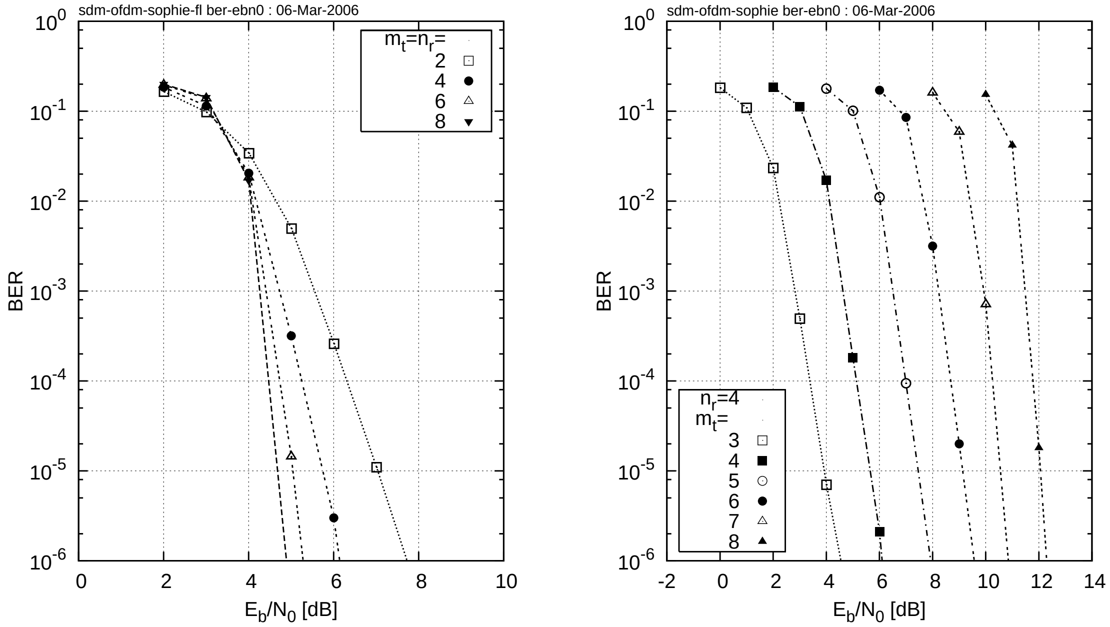

(a) (b)

Figure 4.13: Bit Error Rate exhibited by the **SDM-QPSK-OFDM** system employing **SOPHIE** SDM detector of Algorithm 13 in (a) fully-loaded scenario with $m_t = n_r = 2, 4, 6$ and 8 transmit and receive antennas, as well as (b) overloaded scenario with fixed number of $n_r = 4$ receive antennas and $m_t = 3, 4, \cdots, 8$ transmit antennas. The abscissa represents the average value of E_b/N_0 recorded at the receive antenna elements and. We employ COST-207 BU channel model [119]. Additional system parameters are summarized in Table 1.4.

4.3 Conclusions

In this chapter we proposed a novel OHRSA-aided SDM detection method, which may be regarded as an advanced extension of the CSD method. The algorithm proposed extends the potential range of applications of the CSD methods, as well as reduces the associated computational complexity, rendering them a feasible solution for implementation in practical systems.

Furthermore, we have shown that the OHRSA-aided SDM detector proposed combines the advantageous properties of both the optimum-performance Log-MAP SDM detector and the minimum-complexity linear MMSE SDM detector, which renders it an attractive alternative for implementation in practical systems. More specifically, we have shown that the OHRSA-aided SDM detector proposed exhibits the following advantageous properties 1–5 outlined in Section 4.2.

More specifically, the method can be employed in the over-loaded scenario, where the number of transmit antenna elements exceeds that of the receive antenna elements, while the associated computational complexity increases only moderately even in heavily overloaded scenarios and is almost independent of the number of receive antennas. Furthermore, as opposed to standard CSD schemes [106], no calculation of the sphere radius is required and therefore the method proposed is robust to the particular choice of the initial parameters both in terms of the achievable performance and the associated computational complexity. The overall computational complexity required is only slightly higher than that imposed by the linear MMSE multiuser detector designed for detecting a similar number of users. Specifically, the computational complexity per detected QAM symbol associated with both the MMSE and SOPHIE SDM detectors is of the order of $O\{m_{\mathrm{t}}^3\}$, where m_{t} is the number of transmit antennas. Finally, the associated computational complexity is fairly independent of the channel conditions quantified in terms of the SNR encountered.

Chapter 5

Iterative Channel Estimation and Detection for SDM-OFDM

5.1 Outline

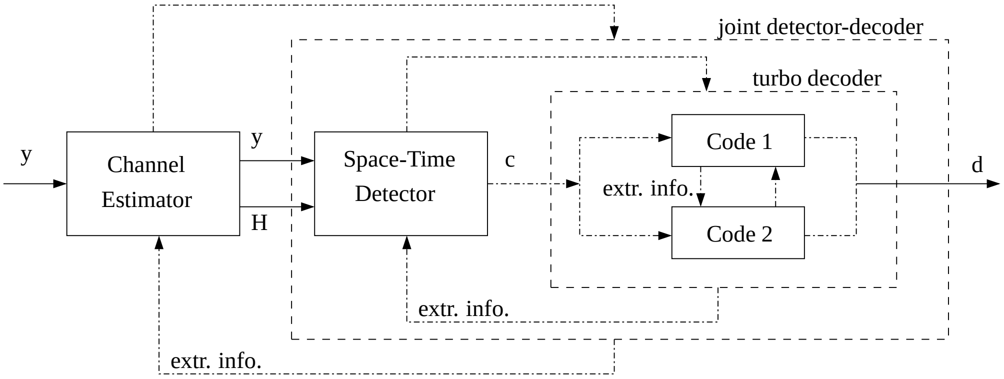

Figure 5.1: Schematic of an iterative turbo receiver employing an iterative decision-directed channel estimator as well as an iterative detection and decoding module.

Despite the immense interest of both the academic and the industrial research communities, the conception of a practical multiple-input multiple-output (MIMO) transceiver architecture, which is capable of approaching the MIMO channel's capacity in realistic channel conditions remains largely an open problem. An important overview encompassing most major aspects of broadband MIMO-OFDM wireless communications including both channel estimation and signal detection, as well as time- and frequency-domain synchronization was contributed by Stüber *et al.* [67]. Other important publications considering MIMO systems operating in realistic channel conditions include those by Münster and Hanzo [69], Li *et. al.* [66], Mai *et. al.* [81], Ronen *et. al.* [116] as well as Qiao *et. al.* [80]. Nevertheless, substantial contributions addressing all the major issues pertaining to the design of MIMO transceivers, namely error correction, space-time detection as well as channel estimation in realistic channel conditions remain scarce.

Against this background, in this chapter we would like to introduce an iterative, so called *turbo* multi-antenna-multi-carrier (MAMC) receiver architecture. Our turbo receiver is illustrated in Figure 5.1. Following the philosophy of turbo processing [26], our turbo SDM-OFDM receiver comprises a succession of detection modules, which iteratively exchange soft bit-related information and thus facilitate a substantial improvement of the overall system performance.

More specifically, our turbo SDM-OFDM receiver comprises three major components, namely the soft-feedback decision-directed channel estimator detailed in Section 2.9, followed by the soft-input-soft-output OHRSA Log-MAP SDM detector derived in Section 4.2.3 as well as a classic parallel-concatenated soft-input-soft-output turbo code [27]. Consequently, in this chapter we would like to analyze the achievable performance of each individual constituent of our turbo receiver, as well as the achievable performance of the entire iterative system. Our aim is to document the various design trade-offs, such as the achievable error-rate performance, the attainable data-rate as well as the associated computational complexity.

Against this background, in this chapter we derive an iterative, so called *turbo* multi-antenna-multi-carrier (MAMC) receiver architecture. Our turbo receiver is illustrated in Figure 5.1. Following the philosophy of turbo processing [26], our turbo SDM-OFDM receiver comprises a succession of detection modules, which iteratively exchange soft bit-related information and thus facilitate a substantial improvement of the overall system performance.

More specifically, our turbo SDM-OFDM receiver comprises three major components, namely, the soft-feedback decision-directed channel estimator, discussed in detail in Section 2.9, followed by the soft-input-soft-output OHRSA Log-MAP SDM detector derived in Section 4.2.3 as well as a soft-input-soft-output serially concatenated turbo code [27]. Consequently, in this chapter we would like to analyze the achievable performance of each individual constituent of our turbo receiver, as well as the achievable performance of the entire iterative system. Our aim is to identify the optimum system configuration, while considering various design trade-offs, such as achievable error-rate performance, achievable data-rate as well as associated computational complexity.

In Section 5.4.2.4 we demonstrate that our turbo SDM-OFDM system employing the MIMO-DDCE scheme of Section 2.9 as well as the OHRSA Log-MAP SDM detector of Section 4.2.3 remains effective in channel conditions associated with high terminal speeds of up to 130 km/h, which corresponds to the OFDM-symbol normalized Doppler frequency of 0.006. Additionally, we report a virtually error-free performance for a rate $1/2$ turbo-coded 8x8-QPSK-OFDM system, exhibiting an effective throughput of 8 MHz $\cdot$ 8 bits/s/Hz=64 Mbps and having a pilot overhead of only 10% at SNR of 7.5dB and a normalized Doppler frequency of 0.003, which corresponds to a mobile terminal speed of about 65 km/h.

5.2 Turbo Forward Error Correction Coding

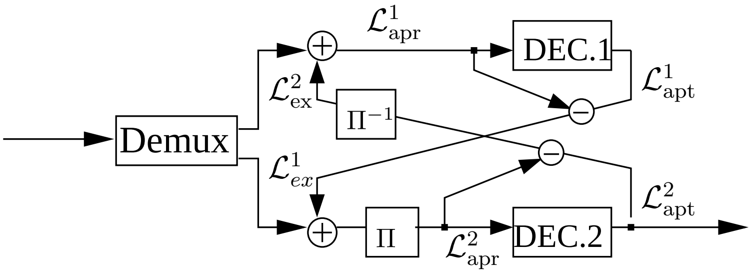

Figure 5.2: Scematic of an iterative turbo decoder employing two parallelly-concatenated RSC codes.

The family of the so-called *turbo* codes was first introduced by Berrou *et. al.* [27, 152, 153]. The properties of turbo codes have been extensively studied in the context of various system architectures by a multiplicity of authors, for instance Benedetto [154], Battail [155], Ömer *et. al.* [156] as well as Hanzo *et. al.* [26]. The plausible conclusion of these studies was that turbo codes are capable of approaching the capacity, while imposing a realistic computational complexity.

Consequently, at the first stage of our iterative turbo receiver architecture illustrated in Figure 5.1 we employ a turbo decoder. The detailed structure of the turbo decoder considered is depicted in Figure 5.2. More specifically, our turbo decoder is constituted by a pair of parallel-concatenated soft-input-soft-output (SISO) RSC decoders, which iteratively exchange information-bit-related extrinsic information in the form of LLR values $\mathcal{L}_{\text{ex}}$ for the sake of attaining the highest possible reliability of the decoded information-carrying bits. In this treatise we employed two rate-$\frac{1}{2}$ punctured RSC codes [156]. Observe that the parallel-concatenated codes share the same information bits, while the corresponding parity bits at the output of the encoder are punctured, which results in the overall concatenated code rate of $\frac{1}{2}$. The octally represented RCS generator polynomials of (7,5) having the constraint length of 3 were used for both RCS codes. Observe that in the introduction of this treatise, namely in Figure 1.3, we depict a serial-concatenated turbo decoder. In contrast, as seen in Figures 5.1 and 5.2, in this chapter we employed a parallel-concatenated code, reminiscent of that derived in [27]. Both the parallel and the serial versions of turbo codes are applicable in our system. Both methods were found to exhibit fairly similar performance, but in the rest of this chapter we will focus our attention on the former.

In this section we would like to quantify the achievable performance of the turbo code considered in the context of increasingly more sophisticated systems communicating under increasingly more realistic channel conditions. We commence our discourse by characterizing the achievable BER performance of the turbo code in the uncorrelated Rayleigh fading in Figure 5.3. Subsequently, in Figure 5.4 we consider the BER performance of the turbo code in the context of a 128-subcarrier OFDM system encountering both uncorrelated Rayleigh fading in the time-domain as well as correlated fading having a time-domain correlation determined by the OFDM-symbol-normalized Doppler frequency spanning the range of $f_D = 0.1$ to 0.003.

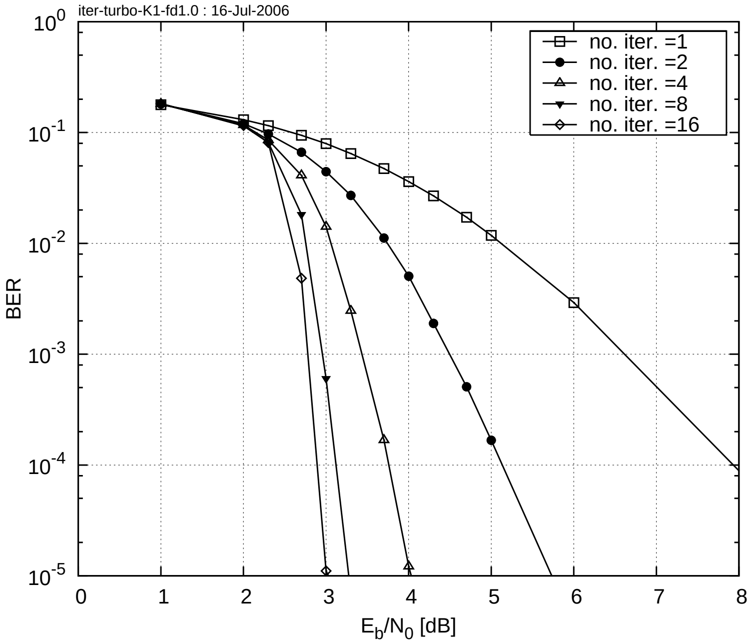

Figure 5.3: BER versus E_b/N_0 performance exhibited by the rate-$\frac{1}{2}$ parallel-concatenated turbo code in uncorrelated non-dispersive Rayleigh fading using single-antenna single-carrier QPSK transmissions. The CIR was the 7-path COST-207 BU model [119]. All our additional system parameters are summarized in Table 1.4.

For the sake of characterizing the achievable BER performance, in Figure 5.3 we portray the BER performance of the parallel-concatenated turbo decoder considered, when encountering uncorrelated Rayleigh fading. More specifically, we considered a narrowband single-carrier QPSK-modulated system, which employs a time-domain random block interleaver encompassing 1000 consecutive bits. Observe, that the BER performance exhibited by the turbo decoder improves rapidly upon increasing the number of decoding iterations performed. Furthermore, the decoder approaches its best possible performance after *eight* iterations. Consequently, in our further studies we consider performing $i_{\text{dec}} = 8$ iterations by the turbo decoder.

On a similar note, Figure 5.4 characterizes the achievable BER performance of the turbo decoder considered in the context of a QPSK-modulated OFDM system, while encountering a Rayleigh fading channel exhibiting various correlation properties. For benchmarking purposes, we contrast the performance of a narrow-band system encountering uncorrelated Rayleigh fading as well as that of a $K = 128$-subcarrier OFDM system encountering a dispersive channel having uncorrelated time-domain Rayleigh fading taps specified by the COST-207 Bad Urban (BU) 7-tap CIR [119]. In the frequency-domain this CIR results in a corresponding correlated frequency-selective CTF. Furthermore, we also consider the more realistic scenario of a $K = 128$-subcarrier OFDM system encountering correlated time-domain Rayleigh fading having the Doppler frequencies of $f_D = 0.1, 0.03$ and 0.003 as well as a dispersive CIR characterized by the

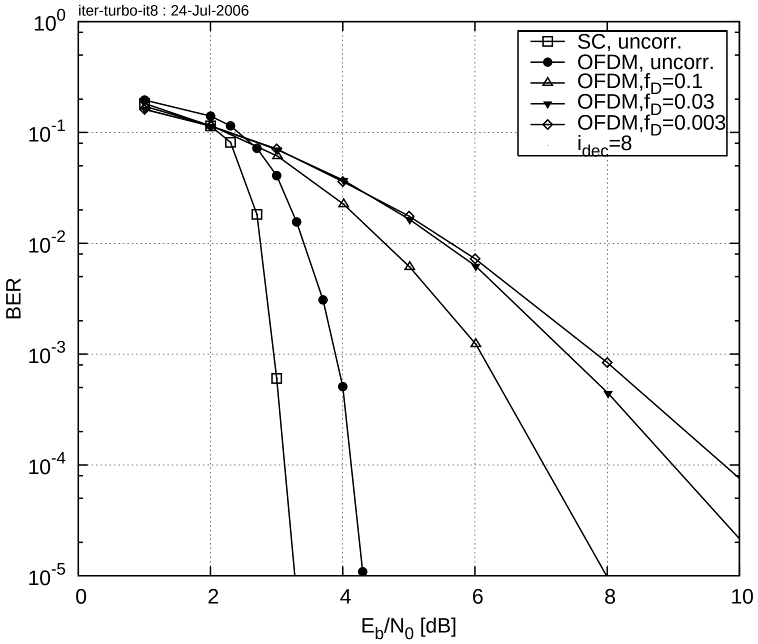

Figure 5.4: BER versus E_b/N_0 performance exhibited by the $K = 128$-subcarrier single-antenna QPSK-OFDM system employing a rate $\frac{1}{2}$ parallel-concatenated turbo code in correlated Rayleigh fading having the OFDM-symbol-normalized Doppler frequencies of $f_D = 0.1, 0.03$ and 0.003. The CIR was the 7-path COST-207 BU model [119]. All additional system parameters are summarized in Table 1.4.

COST-207 BU model [119].

From Figure 5.4 we conclude that as expected, while our turbo decoder exhibits a good BER performance [29] in uncorrelated Rayleigh fading, the corresponding BER performance recorded in correlated fading is substantially degraded owing to the relatively low-memory 1000-bit turbo-interleaver, which is unable to break up and randomize the long fading-induced error bursts.

5.3 Iterative Detection – Decoding

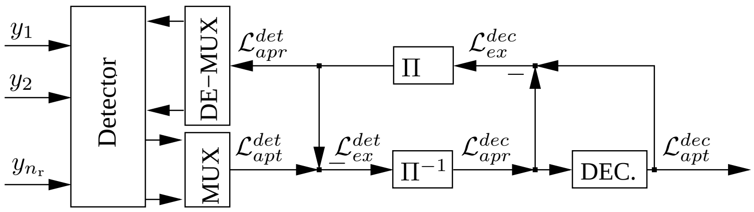

Figure 5.5: Schematic of a MIMO receiver employing iterative joint detection and decoding.

Figure 5.5 portrays the schematic of the iterative space-time detector and decoder considered. Following the philosophy of iterative turbo detection, the incoming subcarrier-related signal vector $\mathbf{y}[n,k]$ is processed by the soft-input-soft-output OHRSA Log-MAP detector of Algorithm 12, which delivers the bit-related *a posteriory* LLR values $\mathcal{L}_{\text{apt}}^{\text{det}}$. The resultant LLR values $\mathcal{L}_{\text{apt}}^{\text{det}}$ are then normalized and de-interleaved for the sake of generating the *a priori* bit-related LLR values $\mathcal{L}_{\rm apr}^{\rm dec}$, which may be utilized by the turbo decoder of Figure 5.5. Subsequently, the *a posteriori* LLR values $\mathcal{L}_{\rm apt}^{\rm dec}$ generated at the output of the decoder are normalized, interleaved and fed back to the SDM detector in the form of the *a priori* LLR values $\mathcal{L}_{\rm apr}^{\rm det}$. This iterative detection process is continued for $i_{\rm det}$ number of detection iterations.

As a next step, we would like to characterize the achievable performance of the iterative SDM detection and decoding scheme illustrated in Figure 5.5. Throughout this section we stipulate the idealistic assumption of having a perfect knowledge of the OFDM-subcarrier-related CTF.

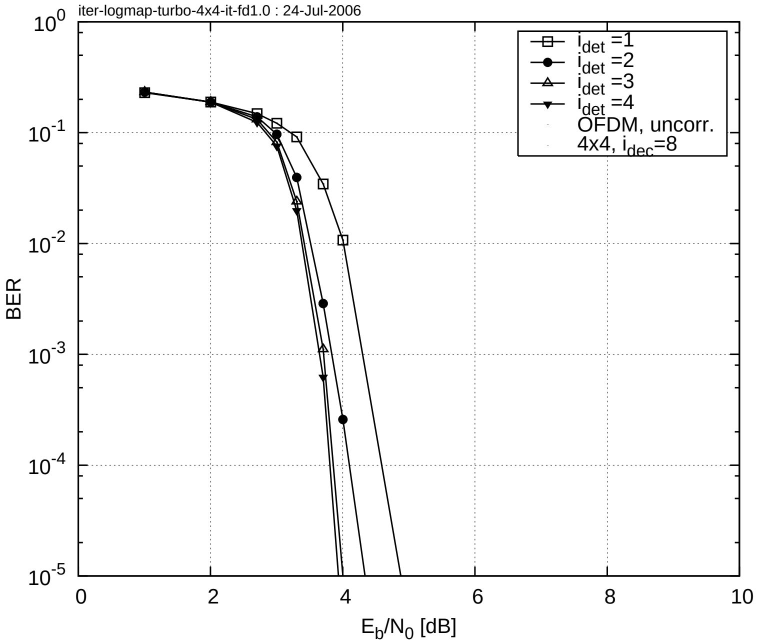

Figure 5.6: BER versus E_b/N_0 performance exhibited by the $K = 128$-subcarrier rate $\frac{1}{2}$ turbo-coded 4x4-SDM-QPSK-OFDM system employing the iterative SDM detection and decoding scheme of Figure 5.5 in uncorrelated time-domain Rayleigh fading channel characterized by the COST-207 BU model [119]. The effective throughput of the system was $4 \cdot 2 \cdot \frac{1}{2} = 4$ bits/sec/Hz. All additional system parameters are summarized in Table 1.4.

Firstly, for the sake of benchmarking, in Figure 5.6 we quantify the BER versus E_b/N_0 performance of the iterative SDM detection and decoding scheme of Figure 5.5 in the context of a rate-$\frac{1}{2}$ turbo-coded 4x4-SDM-QPSK-OFDM system communicating over the uncorrelated time-domain Rayleigh fading channel characterized by the COST-207 BU model [119]. We consider carrying out $i_{\rm det} = 1, 2, 3$ and 4 iterations for the SDM detector, while performing $i_{\rm dec} = 8$ iterations for the inner turbo decoder per each iteration of the SDM detector. From Figure 5.6 we may observe that an E_b/N_0 gain of about 1 dB is achieved by invoking $i_{\rm det} = 3$ iterations of the SDM detector and decoder in comparison to invoking a single detection iteration. By contrast, only a minor further E_b/N_0 improvement may be achieved by invoking $i_{\rm det} > 3$ number of iterations for the SDM detector and decoder complex of Figure 5.5.

Let us now consider the effects of realistic time-domain correlations encountered by our SDM-OFDM

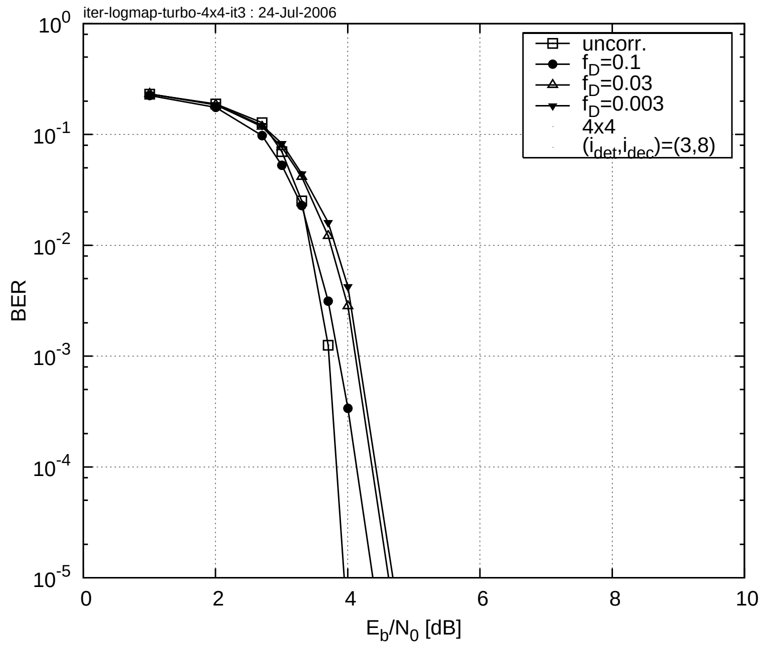

Figure 5.7: BER versus E_b/N_0 performance exhibited by the rate-$\frac{1}{2}$ turbo-coded 4x4-SDM-QPSK-OFDM system employing the iterative SDM detection and decoding scheme of Figure 5.5 in realistic correlated Rayleigh fading conditions when using the 7-path COST-207 BU CIR [119] and encountering the Doppler frequencies of $f_D = 0.1, 0.03$ and 0.003. The BER performance recorded in case of uncorrelated time-domain Rayleigh fading is also shown for the sake of benchmarking. We invoked an iteration pattern of $(i_{\text{det}}, i_{\text{dec}}) = (3, 8)$. The overall throughput was $4 \cdot 2 \cdot \frac{1}{2} = 4$ bits/sec/Hz. Additional system parameters are summarized in Table 1.4.

system employing the iterative SDM detection and decoding scheme of Figure 5.5. Figure 5.7 characterizes the achievable BER versus E_b/N_0 performance of the iterative SDM detection and decoding scheme, which assumes the iteration pattern of $(i_{\text{det}}, i_{\text{dec}}) = (3, 8)$, in the context of a rate-$\frac{1}{2}$ turbo-coded 4x4-SDM-QPSK-OFDM encountering the OFDM-normalized Doppler frequencies of $f_D = 0.1, 0.03$ and $f_D = 0.003$. The corresponding BER performance recorded in the uncorrelated time-domain Rayleigh fading conditions when using the 7-path COST-207 BU CIR is also shown for the sake of benchmarking. In contrast to the single antenna scenario characterized in Figure 5.4, we may observe from Figure 5.7 that the BER performance exhibited by the system encountering a realistic OFDM-symbol-normalized Doppler frequency of $f_D = 0.003$ lies within an E_b/N_0 range of 0.8 dB from the corresponding BER curve exhibited by the system encountering idealistic uncorrelated time-domain Rayleigh fading conditions, when using the 7-path COST-207 BU CIR. We may hence conclude that, as expected, our 4x4-SDM-QPSK-OFDM system efficiently exploits the spatial-diversity potential inherent in the MIMO channel.

This conclusion is further supported by the results depicted in Figure 5.8, where we plot the BER versus E_B/N_0 performance exhibited by the rate-$\frac{1}{2}$ turbo-coded SDM-QPSK-OFDM system employing the iterative SDM detection and decoding scheme of Figure 5.5 and having $m_{\text{t}} = n_{\text{r}} = 1, 2, 4$ and 8

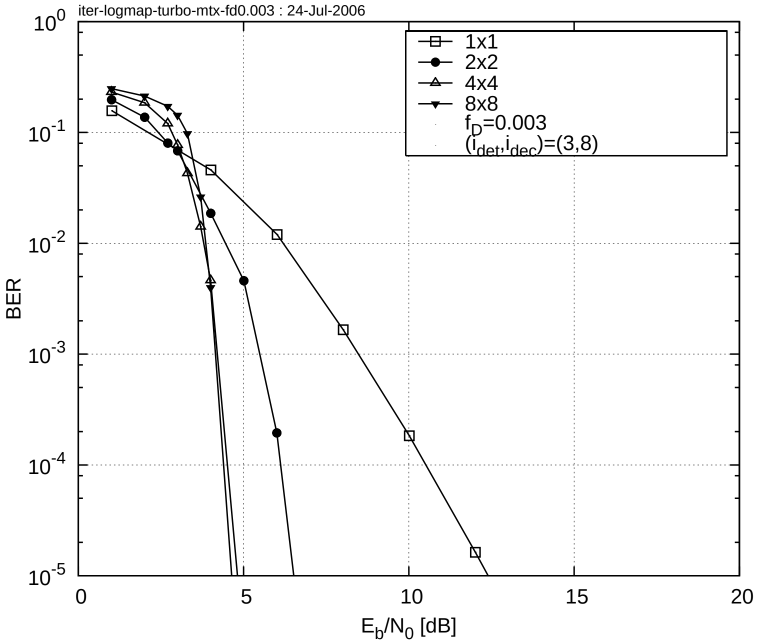

Figure 5.8: BER versus E_b/N_0 performance exhibited by the rate-$\frac{1}{2}$ turbo-coded SDM-QPSK-OFDM system employing the iterative SDM detection and decoding scheme of Figure 5.5 and having $m_\mathrm{t} = n_\mathrm{r} = 1, 2, 4$ and 8 transmit and receive antennas. We invoked an iteration pattern of $(i_\mathrm{det}, i_\mathrm{dec}) = (3, 8)$. The 7-path COST-207 BU channel model [119] was used and we assumed encountering the OFDM-symbol-normalized Doppler frequency of $f_D = 0.003$. The overall throughput was 1,2,4 and $8 \cdot 2 \cdot \frac{1}{2} = 8$ bits/sec/Hz, respectively. Additional system parameters are summarized in Table 1.4.

transmit and receive antennas. We assumed encountering an OFDM-symbol-normalized Doppler frequency of $f_D = 0.003$, while employing bit-interleaving across $N_d = 10$ OFDM symbols. Observe that having an interleaved block of bits spanning the duration of $N_d T_s = 10\ T_s$, which is substantially shorter than channel's coherence time of $1/f_D \approx 300\ T_s$ corresponds to having virtually no time-domain diversity gain. In other words, a relatively short interleaver is unable to break up and randomize the long fading-induced error bursts. Consequently, we may conclude from Figure 5.8 that the BER performance exhibited by the single-antenna OFDM system is limited by the probability of occurrence of a precipitated burst of errors in some of the OFDM symbols, which we may refer as an *outage* [29] inherent in single-antenna Rayleigh fading channels. On the other hand, SDM-OFDM systems operating in MIMO scenarios exhibit a BER performance, which improves upon increasing the number $m_\mathrm{t} = n_\mathrm{r}$ of transmit and receive antennas.

5.4 Iterative Channel Estimation – Detection – Decoding

In this section we consider the transmission of a sequence of consecutive SDM-OFDM transmission *bursts*, which are processed independently. In other words, each of the self-contained SDM-OFDM transmission bursts includes all the necessary data, such as for instance pilot signals, required for successful detection

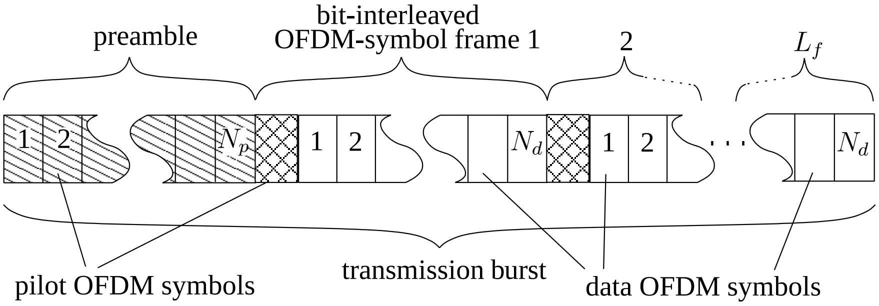

Figure 5.9: OFDM transmission burst structure comprising a preamble of N_p full-pilot OFDM symbols followed by a sequence of L_f data OFDM-symbol frames. Each data OFDM-symbol frame is preceded by a single full-pilot OFDM symbol followed by N_d information-carying OFDM symbols. Consequently, our OFDM transmission burst accommodates a total number of $N_p + L_f$ full-pilot OFDM symbols as well as a total number of $L_f N_d$ information-carrying OFDM symbols.

and decoding of the information accommodated by the OFDM transmission burst. Correspondingly, each SDM-OFDM transmission burst may be processed independently of the neighbouring bursts. This philosophy is reminiscent of the packet-based transmission scheme adopted, for example, in the IEEE 802.11 a/g WLAN standard [157]. The structure of a single SDM-OFDM transmission burst considered is depicted in Figure 5.9. More specifically, our OFDM transmission burst portrayed in Figure 5.9 commences with a channel-sounding preamble formed by N_p number of pure pilot SDM-OFDM symbols. Subsequently, our SDM-OFDM transmission burst accommodates a sequence of L_f number of so-called OFDM-symbol-frames. More explicitely, as seen in Figure 5.9, each OFDM-symbol-frame constitutes a single bit-interleaved turbo-encoded codeword and comprises a single full-pilot SDM-OFDM symbol followed by N_d number of information-carrying SDM-OFDM symbols.

For each SDM-OFDM transmission burst the detection process commences with the initialization of the channel estimator by utilizing the pilot SDM-OFDM symbols constituting the burst's preamble, as seen in Figure 5.9. Specifically, both the received signals $\mathbf{y}[n]$ as well as the corresponding transmitted signals $\mathbf{s}[n]$ associated with the N_p pilot SDM-OFDM symbols constituting the burst preamble of Figure 5.9 are sequentially fed into the channel estimator of Figure 2.1 for the sake of attaining an initial convergence for the three adaptive filters constituting the decision-directed channel estimator of Figure 2.1.

During the first iteration of the detection process, which is carried out for each subsequent N_d-OFDM-symbol data-frame of Figure 5.9 that commences with a full-pilot SDM-OFDM symbol associated with the SDM-OFDM-symbol index n, we perform a long-term prediction of the CIR-related taps using the CIR tap predictor of Figure 2.1. More specifically, we aim for predicting the CIR associated with the *last* OFDM symbol of the current OFDM-symbol-frame of Figure 5.9, namely the one associated with the SDM-OFDM-symbol index of $(n + N_d)$. The CIRs associated with the remaining $(N_d - 1)$ SDM-OFDM symbols hosted by the current OFDM-symbol-frame are then obtained using linear interpolation between those associated with the nth pilot SDM-OFDM symbol preceding the current OFDM-symbol-frame and the predicted CIR associated with the last $(n + N_d)$ data OFDM symbol.

The predicted and interpolated MIMO-CTF coefficients $\check{\mathbf{H}}[m],\ m = n+1,\ldots,n+N_d$ are utilized for the sake of performing an initial detection of the information-carrying data SDM-OFDM symbols $\mathbf{s}[n]$. Observe that in the possession of the CIRs and the corresponding CTFs associated with the entire SDM-OFDM-symbol frame, we are able to employ the iterative SDM detection and decoding scheme outlined in Section 5.3.

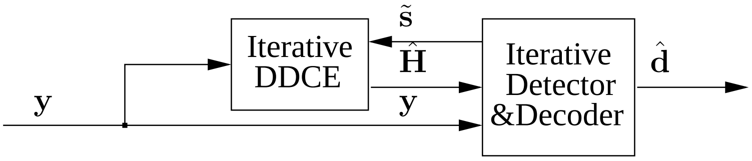

Figure 5.10: Schematic of an iterative turbo receiver employing the iterative decision-directed channel estimator of Figure 2.1 as well as the iterative detection and decoding module of Figure 5.5.

The resultant tentative estimates of the data-bits $\mathbf{d}$, as well as the associated soft-bit information, corresponding to the entire data SDM-OFDM-symbol frame of Figure 5.9 are remodulated in order to generate the soft reference signal $\tilde{\mathbf{s}}[m],\ m = n+1,\ldots,n+N_d$ of Equation (2.98). The reference signal $\tilde{\mathbf{s}}[m]$ is fed back to the soft-input channel estimator of Algorithm 8 for the sake of refining the estimates of the CTF coefficients $\mathbf{H}[m],\ m = n+1,\ldots,n+N_d$. The interaction between the iterative channel estimator of Algorithm 8 and the iterative SDM detection and decoding module of Section 5.3 is illustrated in Figure 5.10. The iterative channel estimation–detection–decoding process portrayed in Figure 5.10 is repeated, until a sufficiently reliable detected SDM-OFDM symbol $\hat{\mathbf{s}}$ is generated.

5.4.1 Mitigation of Error Propagation

As we noted in Section 2.3, the main difficulty associated with the decision-directed approach to channel estimation is constituted by the potential error propagation, where the erroneous data decisions result in erroneous channel estimation, which inflicts further precipitated data decision errors, *etc*. In other words, the reliability of the estimated CTF coefficients degrades rapidly in the presence of decision errors routinely occurring in the low SNR region. The resultant degradation of the channel state information accuracy results in further decision errors and ultimately in divergence of the iterative channel estimation – data detection process and in a subsequent avalanche of decision errors. As we pointed out in Section 2.9.1.4, the *soft feedback* assisted RLS CTF estimator of Algorithm 7 is capable of substantially mitigating the effects of error propagation. Nevertheless, ensuring the stability of an iterative channel estimation – data detection system in the presence of data decision errors remains a challenging issue. Consequently, for the sake of mitigating the system's vulnerability to error-propagation-related instability effects we propose the following method.

Firstly, after each channel estimation and SDM detection iteration, which is performed on the N_d-SDM-OFDM symbol data frame of Figure 5.9, we record the resultant MSE. The joint channel estimation and SDM detection MSE may be expressed as follows

$$e^i[n] = \sum_{m=n+1}^{n+N_d} \sum_{k=1}^{K} \|\mathbf{y}[m,k] - \hat{\mathbf{H}}^i[m,k]\hat{\mathbf{s}}^i[m,k]\|^2, \tag{5.1}$$

where, as before, $\mathbf{y}[m,k]$ denotes the SDM signal associated with the kth subcarrier of the mth SDM-OFDM symbol and recorded at the n_r receive antennas, while $\hat{\mathbf{H}}^i[m,k]$ and $\hat{\mathbf{s}}^i[m,k]$ are the corresponding estimates of the CTF coefficient matrix and the transmitted signal vector, which were obtained after the ith iteration of the channel estimation and detection process.

Subsequently, after carrying out i_ce number of channel estimation iterations we select the particular pair of CTF estimates $\hat{\mathbf{H}}^i[m,k]$ and data estimates $\hat{\mathbf{s}}^i[m,k]$, which correspond to the specific iteration resulting in the minimum MSE. More explicitely, the decision rule employed may be expressed as

$$\left\{\hat{\mathbf{H}}[m,k], \hat{\mathbf{s}}[m,k]\right\} = \arg\min_{i} e^i[n], \tag{5.2}$$

where we have $m = n+1, \cdots, n+N_d;\ k = 1, \cdots, K$ and $i = 1, \cdots, i_\mathrm{ce}$.

Let us now consider the scenario of encountering a large number of decision errors. Naturally, the decision errors in any of the iterations would result in a degraded channel estimation accuracy in the subsequent iteration and hence even more decision errors as well as an inevitable increase of the corresponding MSE $e^i[n]$. Consequently, invoking the final-decision rule of Equation 5.2 substantially mitigates the system's *avalanche*-like error propagation and hence improves the system's stability and robustness.

5.4.2 MIMO-PASTD-DDCE Aided SDM-OFDM Performance Analysis

5.4.2.1 Number of Channel Estimation – Detection Iterations

Firstly, we would like to characterize the BER performance gain attained by the iterative MIMO-PASTD - DDCE in comparison to single-iteration channel estimation. More specifically, Figure 5.11 portrayes the BER versus E_b/N_0 performance of the rate $1/2$ turbo-coded 4x4-SDM-QPSK-OFDM system employing the MIMO-PASTD -DDCE of Algorithm 8 and invoking $i_\mathrm{ce} = 1, 2, 3$ and 4 channel estimation iterations as well as $i_\mathrm{det} = 2$ SDM detector iterations and $i_\mathrm{dec} = 4$ iterations of the parallel-concatenated turbo decoder per each iteration of the channel estimator. We assumed employing the transmission burst structure depicted in Figure 5.9, where the corresponding parameters were given by $(L_f, N_p, N_d) = (8, 8, 10)$, which yields an overall pilot overhead of $\varepsilon = (N_p + L_f)/(L_f N_d) = 0.1$, or in other words 10%. The 7-path COST-207 BU channel model was used and we assumed encountering the Doppler frequency of $f_D = 0.003$. As may

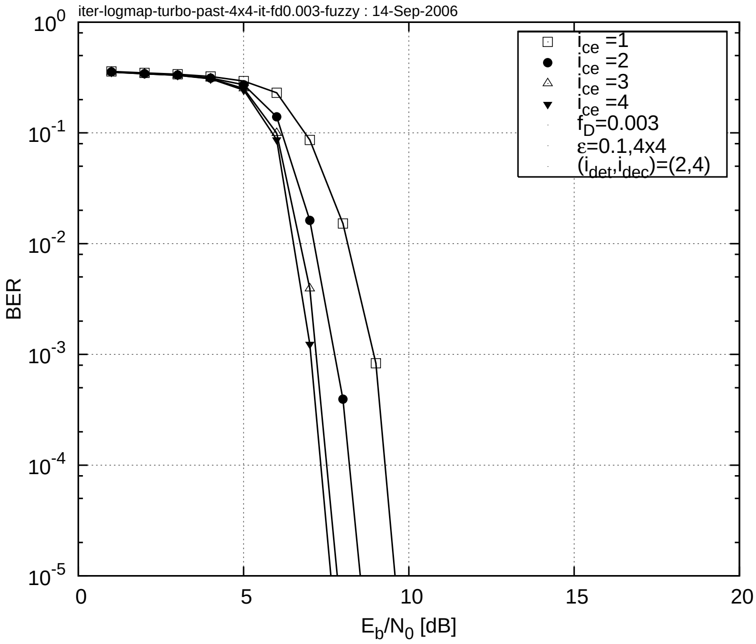

Figure 5.11: BER versus E_b/N_0 performance exhibited by the rate-$\frac{1}{2}$ turbo-coded 4x4-SDM-4QAM-OFDM iterative turbo receiver of Figure 5.10 employing the MIMO-PASTD-DDCE of Algorithm 8 and invoking $i_{\text{ce}} = 1, 2, 3$ and 4 channel estimation iterations as well as $(i_{\text{det}}, i_{\text{dec}}) = (2, 4)$ SDM detection and turbo decoding iterations, respectively. The 7-path COST-207 BU channel model [119] was used and we assumed encountering the OFDM-symbol-normalized Doppler frequency of $f_D = 0.003$. The overall throughput was $4 \cdot 2 \cdot \frac{1}{2} = 4$ bits/sec/Hz. All additional system parameters are summarized in Table 1.4.

be concluded from Figure 5.11, the SDM-OFDM system employing the iterative channel estimation scheme of Algorithm 8 exhibits an E_b/N_0 gain of about 2 dB, when comparing three iterations and a single iteration of the channel estimator. Moreover, only a modest further E_b/N_0 gain may be achieved upon invoking a higher number of channel estimation iterations.

5.4.2.2 Pilot Overhead

In order to provide further insights, Figure 5.12 characterizes the achievable BER versus E_b/N_0 performance of the MIMO-PASTD -DDCE of Algorithm 8 in the context of employing different m_{t} and n_{r} numbers of transmit as well as receive antennas. Specifically, we consider the SDM-QPSK-OFDM turbo receiver of Figure 5.10, which invokes $(i_{\text{ce}}, i_{\text{det}}, i_{\text{dec}}) = (3, 2, 4)$ channel estimation, detection and decoding iterations, respectively, while employing $m_{\text{t}} = n_{\text{r}} = 1, 2, 4, 6$ and 8 transmit and receive antennas. Observe, that the BER performance improves rapidly upon increasing the $m_{\text{t}} = n_{\text{r}}$ number of transmit and receive antennas, as long as it does not exceed $m_{\text{t}} = n_{\text{r}} = 4$. Furthermore, the BER performance degrades slowly upon further increasing the number of antennas according to $m_{\text{t}} = n_{\text{r}} > 4$. The simple explanation of this phenomenon is that as expected, the SDM-OFDM system benefits from the increased spatial diversity

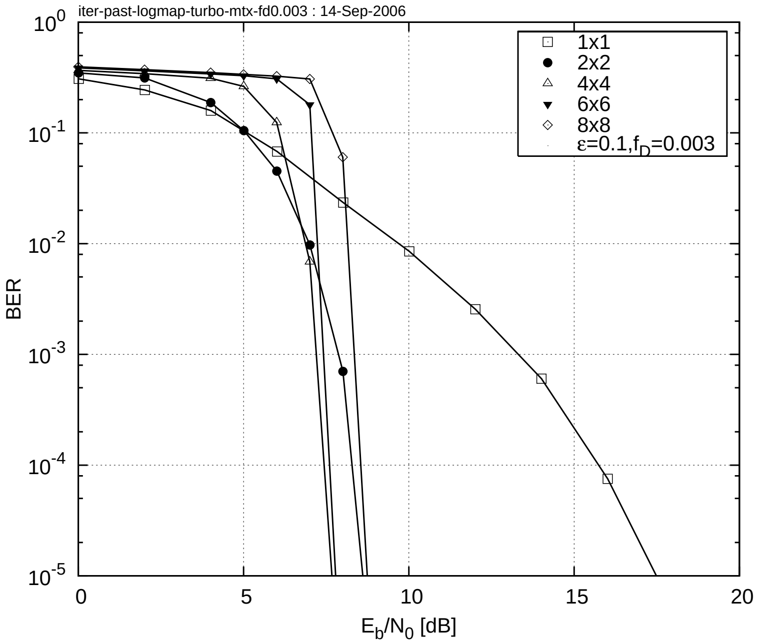

Figure 5.12: The BER versus E_b/N_0 performance exhibited by the rate-$\frac{1}{2}$ turbo-coded SDM-QPSK-OFDM turbo receiver of Figure 5.10 employing the iterative MIMO-PASTD-DDCE of Algorithm 8 and using $m_\mathrm{t} = n_\mathrm{r} = 1, 2, 4, 6$ and 8 transmit and receive antennas. The corresponding effective throughputs were $1, 2, 4, 6$ and $8 \cdot 2 \cdot \frac{1}{2} = 8$ bits/sec/Hz, respectively. The 7-path COST-207 BU channel model was used [119] and we assumed encountering the Doppler frequency of $f_D = 0.003$. The pilot overhead of 10% and the iteration pattern of $(i_\mathrm{ce}, i_\mathrm{det}, i_\mathrm{dec}) = (3, 2, 4)$ were used. All additional system parameters are summarized in Table 1.4.

associated with a higher number of antennas. On the other hand, as noted in Section 2.9, the channel estimation problem becomes increasingly more rank-deficient and hence the estimation accuracy of the CIR taps as well as the corresponding subcarrier-related CTF coefficients degrades upon increasing the number of independent spatial links constituting the MIMO channel. The overall system performance is determined by the associated trade-off between the beneficial diversity gain increase and the inevitable degradation of the estimated CTF accuracy. Ultimately, however, the deterioration of the estimated CTF accuracy does not appear to constitute a major impediment. Quantitatively, as evidenced by the results of Figure 5.12, the BER performance exhibited by the high-complexity system having $m_\mathrm{t} = n_\mathrm{r} = 8$ antennas lies within a 1 dB margin in comparison to the corresponding BER performance curve associated with the system having $m_\mathrm{t} = n_\mathrm{r} = 4$ transmit and receive antennas. Observe that the 4x4 system exhibits the best recorded performance and hence appears to represent an optimum tradeoff between the beneficial special diversity gain and the system-size-related channel estimation accuracy degradation.

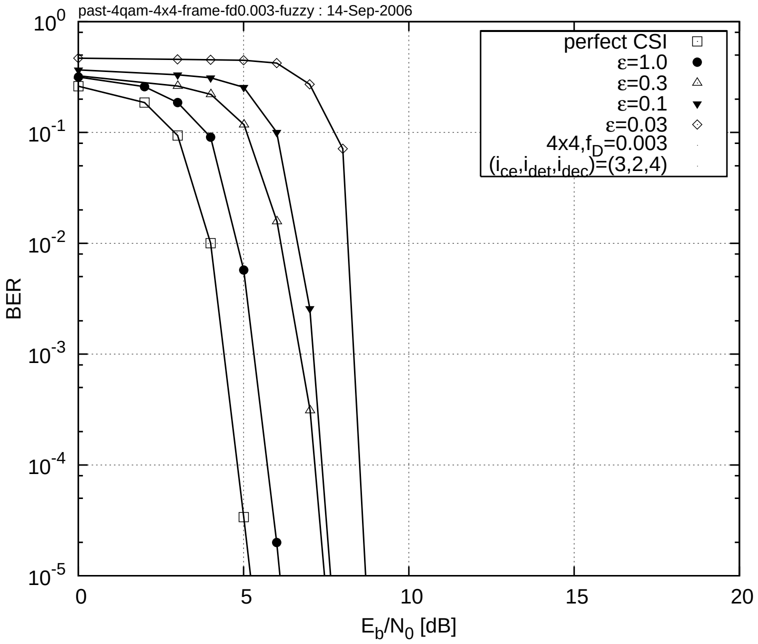

Figure 5.13: BER versus E_b/N_0 performance exhibited by the rate-$\frac{1}{2}$ turbo-coded 4x4-SDM-QPSK-OFDM turbo receiver of Figure 5.10 employing the MIMO-PASTD-DDCE scheme of Algorithm 8. The pilot overhead was either 3, 10, 30, or 100%, which corresponds to $\varepsilon = 0.03, 0.1, 0.3$ and 1.0, respectively, where we consider the idealistic scenario of having 100% pilots as well as the scenario of perfect channel state information for benchmarking purposes. The 7-path COST-207 BU channel model [119] was used and we assumed encountering the Doppler frequency of $f_D = 0.003$. The iteration pattern of $(i_{\text{ce}}, i_{\text{det}}, i_{\text{dec}}) = (3, 2, 4)$ was used. The effective throughput was $4 \cdot 2 \cdot \frac{1}{2} = 4$ bits/sec/Hz. All additional system parameters are summarized in Table 1.4.

5.4.2.3 Performance of a Symmetric MIMO System

Subsequently, we would like to characterize the achievable BER performance exhibited by the SDM-QPSK-OFDM turbo receiver of Figure 5.10 employing the MIMO-PASTD-DDCE scheme of Algorithm 8 and using various densities of the dedicated pilot SDM-OFDM symbols. More specifically, in Figure 5.13 we have plotted the rate $1/2$ turbo-coded QPSK-related BER exhibited by our SDM-OFDM system employing $m_{\text{t}} = n_{\text{r}}$ transmit and receive antennas. For benchmarking purposes we have included the BER versus E_b/N_0 performance of the SDM-OFDM system assuming perfect CIR knowledge, as well as assuming channel estimation based on the idealistic scenario of having 100% pilots. Furthermore, we present our results for the SDM-OFDM system using pilot overheads of 30, 10 and 3%, which corresponds to the pilot overhead ratio of $\varepsilon = 0.3, 0.1$ and 0.003, respectively. We observe from Figure 5.13 that the 100% pilot-based channel estimation results in an approximately 1 dB E_b/N_0 degradation in comparison to the perfect CIR estimation scenario. Furthermore, the more realistic assumption of employing up to 10% dedicated SDM-OFDM pilot symbols results in a further E_b/N_0 degradation of about 1.5 dB in comparison to the 100% pilot-based scenario. Additionally, a further reduction of the pilot overhead to as low as 3% of pilots results in an E_b/N_0 degradation of 2.5 dB in comparison to the 100% pilot-based scenario.

5.4.2.4 Performance of a Rank-Defficient MIMO System

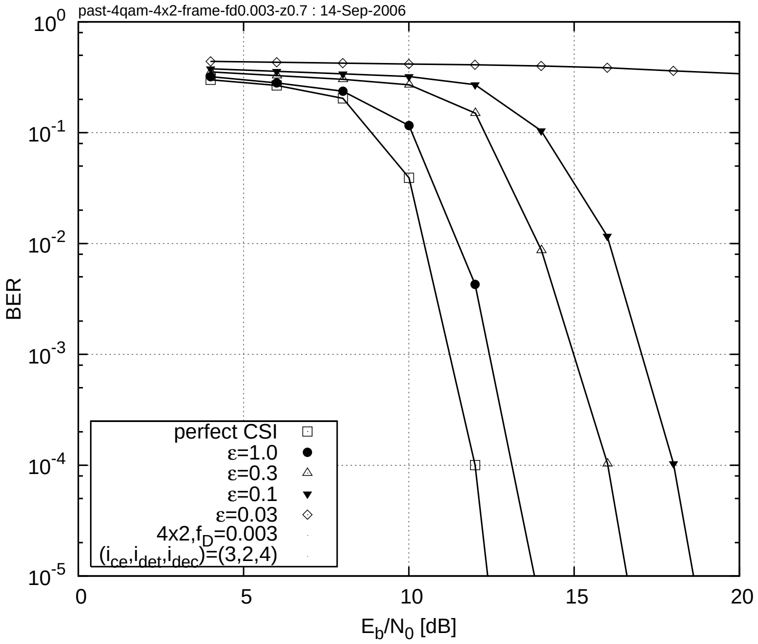

Figure 5.14: BER versus E_b/N_0 performance exhibited by the rank-deficient rate-$\frac{1}{2}$ turbo-coded 4x2-SDM-QPSK-OFDM turbo receiver of Figure 5.10 employing the MIMO-PASTD-DDCE scheme of Algorithm 8. The pilot overhead was either 3, 10, 30, or 100%, which corresponds to $\varepsilon = 0.03, 0.1, 0.3$ and 1.0, respectively, where we consider the idealistic scenario of having 100% pilots as well as the scenario of perfect channel state information for benchmarking purposes. The 7-path COST-207 BU channel model was used [119] and we assumed encountering the Doppler frequency of $f_D = 0.003$. The iteration pattern of $(i_{\text{ce}}, i_{\text{det}}, i_{\text{dec}}) = (3, 2, 4)$ was used. The effective throughput was $4 \cdot 2 \cdot \frac{1}{2} = 4$ bits/sec/Hz. All additional system parameters are summarized in Table 1.4.

Similar phenomena may be observed in Figure 5.14, which characterizes the achievable BER performance exhibited by a rank-deficient 4x2-SDM-QPSK-OFDM system. The 4x2 MIMO scenario constitutes a particularly interesting detection problem. More specifically, let us consider the kth subcarrier of the nth SDM-OFDM symbol. The computational challenge lies in the fact that we have to estimate as many as *four* transmitted M-QAM symbols $s_j[n,k],\ j = 1,\ldots,4$ as well as the corresponding *eight* CTF coefficients $H_{ij}[n,k], i = 1,2,\ j = 1,\ldots,4$, while utilising merely the *two* recorded signal samples of $y_i[n,k],\ i = 1,2$. Consequently, similarly to Figure 5.13 we have plotted the BER versus E_b/N_0 performance of the 4x2-SDM-QPSK-OFDM system assuming perfect CSI as well as assuming channel estimation based on the idealistic scenario of having 100% pilots. Furthermore, we have plotted the BER corresponding to the scenarios of using pilot overheads of 30, 10 and 3%. Similarly to the 4x4 scenario, assuming 100% pilot-based channel estimation results in an approximately 1 dB E_b/N_0 degradation in comparison to the perfect CIR knowledge scenario. On the other hand, in contrast to the 4x4 scenario characterized in Figure 5.13, in Figure 5.14 we may observe that the system employing 10% of dedicated SDM-OFDM pilot symbols results in nearly 6 dB E_b/N_0 degradation in comparison to the 100% pilot-based scenario. Furthermore, an additional reduction of the pilot overhead to 3% of pilots results in a system instability and hence no satisfactory BER performance may be achieved, regardless of the SNR encountered.

5.5 Conclusions

Table 5.1: MIMO-PAST-DDCE aided SDM-OFDM performance summary: the SNR [dB] required for attaining a target BER of 10^{-4}. The results were extracted from Figures 5.13 and 5.14.

Pilot to data ratio	Perfect CSI	$\varepsilon = 1.0$	$\varepsilon = 0.3$	$\varepsilon = 0.1$	$\varepsilon = 0.03$
4x4	4.8	5.7	7.2	7.4	8.6
4x2	12.1	12.8	15.8	17.6	–

In this chapter we have documented the performance trends exhibited by the proposed turbo SDM-OFDM receiver of Figure 5.1, which comprises three main components, namely the soft-feedback decision-directed MIMO channel estimator derived in Section 2.9, followed by the soft-input-soft-output OHRSA Log-MAP SDM detector of Section 4.2.3 as well as a soft-input-soft-output parallel-concatenated turbo code [27]. We analyzed the achievable performance of each individual constituent component of our turbo receiver, as well as the attainable performance of the entire iterative system.

In order to summarize the attained results, the achievable BER performance of the iterative MIMO-PAST-DDCE aided SDM-OFDM system considered in the context of both the symmetric MIMO configuration of Figure 5.13 as well as a rank-deficient MIMO configuration of Figure 5.14 are summarized in Table 5.1. Specifically, we have found that our turbo SDM-OFDM system employing the MIMO-DDCE scheme of Section 2.9 as well as the OHRSA Log-MAP SDM detector of Section 4.2.3 remains effective in channel conditions associated with high terminal speeds of up to 130 km/h, which corresponds to the OFDM-symbol normalized Doppler frequency of 0.006. Additionally, in Figure 5.12 we reported a virtually error-free performance for a rate $1/2$ turbo-coded 8x8-QPSK-OFDM system, exhibiting an effective throughput of 8 MHz $\cdot$ 8 bits/s/Hz=64 Mbps and having a pilot overhead of only 10% at an SNR of 7.5dB and a normalized Doppler frequency of 0.003, which corresponds to a mobile terminal speed of about 65 km/h[1].

---

[1] Additional system parameters are characterized in Table 1.4.

Chapter 6

Conclusions and Future Work

6.1 Achieved Results

In this treatise we characterized a suite of iterative turbo receivers suitable for employment in a wide range of multi-antenna aided multi-carrier systems operating in realistic rapidly-fluctuating channel conditions.

More specifically, we reported the following major findings:

- In Chapter 2 we derived an advanced decision directed channel estimation (DDCE) scheme, which is capable of recursive tracking and prediction of the rapidly-fluctuating channel parameters, characterized by time-variant statistics. More specifically, we employed the Projection Approximation Subspace Tracking (PAST) [117] technique for the sake of tracking the channel transfer function's low-rank signal subspace and thus facilitated the high-accuracy tracking of the channel's transfer function, while imposing a relatively low computational complexity.

- Additionally, in Chapter 2 we introduced an advanced MIMO channel estimation scheme for multi-antenna multi-carrier systems. Our advocated arrangement invokes the aforementioned PAST aided subspace technique in conjunction with an enhanced soft-decision aided RLS MIMO-CTF estimator, which utilizes the modified RLS tracking technique outlined in [40]. We demonstrated that our soft-decision aided MIMO-DDCE scheme is suitable for multi-carrier systems employing a high number of transmit and receive antennas for the sake of achieving a high throughput.

- In Chapter 4 we proposed a range of Optimized Hierarchy Reduced Search Algorithm (OHRSA)-aided space-time processing methods, which may be regarded as an advanced extension of the Complex Sphere Decoder (CSD), portrayed in [108]. The algorithm proposed extends the potential application range of the CSD methods of [106] and [108], as well as reduces the associated computational complexity. Moreover, the OHRSA-aided SDM detector proposed is capable of achieving the near-optimum performance of the Log-MAP SDM detector, while imposing a substantially lower computational complexity, which renders it an attractive design alternative for practical systems.

- Finally, in Chapter 5 we amalgamated both the soft decision feedback aided MIMO channel estimation scheme of Chapter 2 as well as the Log-MAP SDM detection method derived in Chapter 4 into an iterative receiver architecture. Additionally, we carried out an analysis of the associated design trade-offs.

In the following chapter we will summarize some of the major conclusions of this study and propose promising directions for future work.

6.1.1 Channel Estimation

The DDCE scheme proposed in Chapter 2 is suitable for employment in both OFDM and MC-CDMA systems. We analysed the achievable performance of the estimation scheme considered in conjunction with a realistic dispersive Rayleigh fading channel model having a realistic Fractionally-Spaced (FS) rather than an idealized Symbol-Spaced (SS) Power Delay Profile (PDP).

Specifically, in Section 2.5.1 we proposed the MMSE FD-CTF estimator, which is suitable for employment in both OFDM and MC-CDMA systems. In Section 2.5 we continued our discourse with the derivation of both sample-spaced as well as fractionally-spaced CIR estimators. In Section 2.5.5 we performed a comparison between the two methods considered and demonstrated the advantages of the fractionally-spaced scheme. Subsequently, in Section 2.6 we developed a parametric fractionally-spaced CIR tap tracking technique, which facilitates low-complexity channel estimation in realistic channel conditions characterized by time-variant fractionally-spaced power delay profiles. More specifically, we employ the deflation PAST method of Algorithm 2 for the sake of recursive tracking of the CTF's covariance matrix and for the subsequent tracking of the corresponding CIR taps. We demonstrated that the PAST-aided DDCE scheme proposed exhibits a good performance over the entire range of practical propagation conditions.

In Section 2.7 we discussed two major CIR tap prediction strategies, namely the robust predictor, which was capable of guaranteeing a certain level of performance under specified worst-case PDP conditions, as well as the adaptive RLS predictor. In Figures 2.18 and 2.19 of Section 2.7.5 we characterized and compared the achievable performance of both methods considered and drew conclusions concerning their relative merits. Specifically, we demonstrated that the RLS prediction technique outperforms its robust counterpart over the entire range of the relevant channel conditions.

Subsequently, in Section 2.9 we addressed the problem of channel estimation in multi-antenna aided multi-carrier systems. Specifically, we proposed a DDCE scheme, which is suitable for employment in a wide range of multi-antenna aided multi-carrier systems capable of operating over the entire range of practical channel conditions. In particular, we considered a generic MIMO-OFDM system employing K orthogonal frequency-domain subcarriers as well as having m_{t} and n_{r} transmit and receive antennas, respectively. The MIMO channel estimation scheme derived in Section 2.9 comprises an array of K per-subcarrier MIMO-CTF estimators, followed by a $(n_{\mathrm{r}} \times m_{\mathrm{t}})$-dimensional array of parametric CIR estimators and a corresponding array of $(n_{\mathrm{r}} \times m_{\mathrm{t}} \times L)$ CIR tap predictors, where L is the number of CIR taps tracked per each link of the MIMO channel.

In Section 2.9.1 we explored a family of recursive MIMO-CTF tracking methods, which were combined with the aforementioned PAST-aided CIR-tracking method of Section 2.6 as well as with the RLS CIR tap prediction method of Section 2.7.4 in order to create an efficient channel estimation scheme for MIMO-OFDM systems. More specifically, in Section 2.9.1 we considered both hard- and soft-feedback assisted LMS and RLS CIR tap tracking algorithms as well as the modified RLS algorithm, which is capable of improved exploitation of the soft information associated with the decision-based estimates.

Finally, in Figures 2.24–2.27 of Section 2.9.1.5 we documented the achievable performance of the resultant MIMO-DDCE scheme employing the recursive CTF tracking of Section 2.9.1 followed by the parametric CIR tap tracking and CIR tap prediction techniques of Sections 2.6 and 2.7, respectively. We demonstrated that the MIMO-DDCE scheme proposed exhibits a good performance over the entire range of practical conditions. More specifically, both the BER as well as the corresponding MSE performance of the channel estimation scheme considered was characterized in the context of a turbo-coded MIMO-OFDM system in Figures 2.24–2.27. We demonstrated that the MIMO-DDCE scheme proposed remains effective in channel conditions associated with high terminal speeds of up to 130 km/h, which corresponds to the OFDM-symbol normalized Doppler frequency of 0.006. Additionally, we reported a virtually error-free performance for a rate $1/2$ turbo-coded 8x8-QPSK-OFDM system, exhibiting a total bit rate of 8 bits/s/Hz and having a pilot overhead of only 10%, at an SNR of 10dB and normalized Doppler frequency of 0.003, which corresponds to a mobile terminal speed of about 65 km/h.

In conclusion, the performance of the PAST aided MIMO-DDCE scheme derived in Chapter 2 may be characterized based on the MSE performance results depicted in Figure 6.1. More specifically, the MSE σ_e^2 exhibited by the channel estimation scheme considered may be expressed as

$$\sigma_e^2 = \frac{1}{\kappa\gamma}\frac{L m_{\mathrm{t}} n_{\mathrm{r}}}{K}, \tag{6.1}$$

where L is the number of the estimated CIR taps, while m_{t} and n_{r} are the numbers of transmit and receive antennas, respectively. Correspondingly, $L m_{\mathrm{t}} n_{\mathrm{r}}$ denotes the total number of the independent channel-related parameters estimated, while γ is the average SNR encountered at the receiver. Furthermore, we employ the estimation efficiency factor κ of Equation 2.110. The value of the parameter κ was determined empirically using Equation 2.110, yielding $\kappa = 4$ dB.

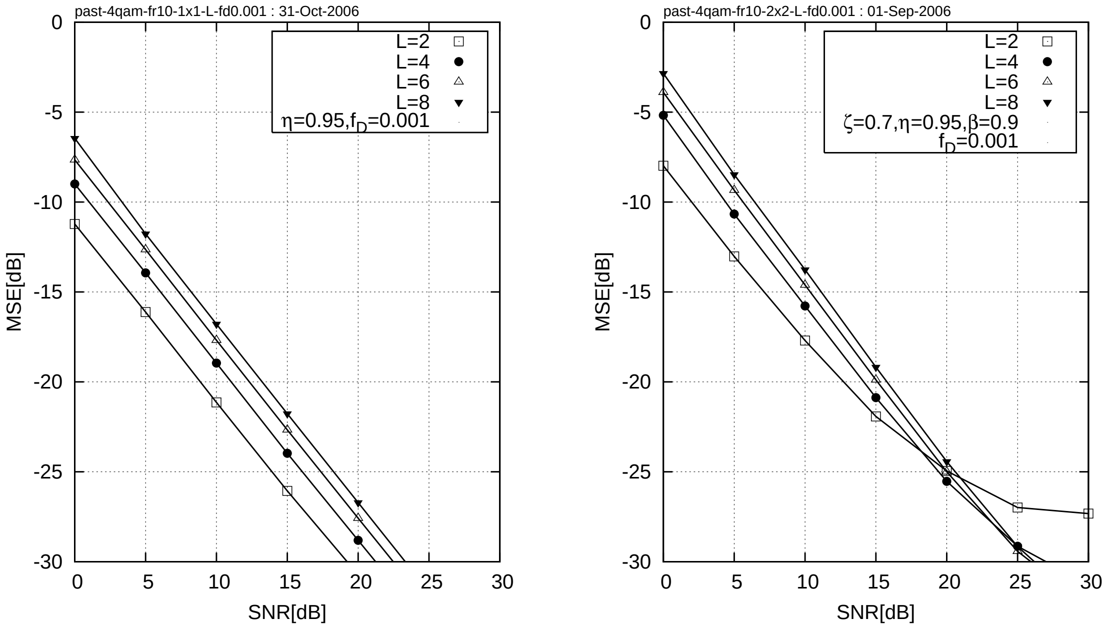

(a) (b)

Figure 6.1: The **Mean Square Error** exhibited by the (a) 1x1 and (b) 2x2 **4QAM-OFDM** system employing the **PASTD** CIR estimator of Algorithm 2 and tracking $L = 2, 4, 6$ and 8 CIR taps. The value of the PASTD forgetting factor was $\eta = 0.95$. The OFDM symbol normalized Doppler frequency was $f_D = 0.001$. The abscissa represents the average SNR recorded at the receive antenna elements.

6.1.2 Signal Detection in MIMO Systems

In Chapter 3, we have performed an overview study of several popular SDM detection methods available in the literature. Specifically, in Section 3.3.1 we demonstrated that the linear increase in capacity, which was predicted by the information-theoretic analysis of [29], may indeed be achieved by employing a relatively low-complexity linear SDM detection method, such as the MMSE SDM technique [101]. Secondly, in Section 3.4.1 we showed that a substantially better performance can be achieved by employing the higher-complexity non-linear Maximum Likelihood (ML) SDM detector [83, 102, 103], which constitutes the optimal detection method from a probabilistic sequence-estimation point of view. To elaborate a little further, the ML SDM detector is capable of attaining transmit diversity in *fully-loaded* systems, where the number of transmit and receive antennas is equal. Moreover, as opposed to the linear detection schemes considered, the ML SDM detector is capable of operating in the *rank-deficient* system configuration, when the number of transmit antennas exceeds that of the receive antennas. Unfortunately, however, the excessive computational complexity associated with the exhaustive search employed by the ML detection method renders it inapplicable to practical implementation in systems having a high number of transmit antennas. Subsequently, in Sections 3.4.2 and 3.4.3 we explored a range of advanced non-linear SDM detection methods, namely both a SIC and a Genetic Algorithm-aided MMSE detector, respectively, where the latter may constitute an attractive compromise between the low complexity of the linear SDM detector and the high performance of the ML SDM detection schemes. Indeed, we demonstrated in Section 3.4.3 that both the SDM detection method based on the SIC as well as the GA-MMSE detector [100] are capable of satisfying these requirements.

In Chapter 4 we have focused our attention on a family of potent Reduced Search Algorithm (RSA) aided space-time processing methods, the members of which exhibit a particularly advantageous trade-off between the achievable performance and the associated computational complexity, namely the family of the Sphere Decoding-aided SDM detection methods. Consequently, a set of novel OHRSA-aided SDM detection methods was outlined in Section 4.2. Specifically, in Section 4.2.1 we derived the OHRSA-aided ML SDM detector, which benefits from the optimal performance of the ML SDM detector [28], while exhibiting a relatively low computational complexity, which is only slightly higher than that required by the low-complexity MMSE SDM detector [28]. To elaborate a little further, in Section 4.2.2 we derived a bit-based OHRSA-aided ML SDM detector, which allows us to apply the OHRSA method of Section 4.2 in high-throughput systems, which employ multi-level modulation schemes, such as M-QAM [28].

In Section 4.2.3 we deduced the OHRSA-aided Max-Log-MAP SDM detector, which allows for an efficient evaluation of the soft-bit information and therefore results in highly efficient turbo decoding. Unfortunately however, in comparison to the OHRSA-aided ML SDM detector of Section 4.2.2 the OHRSA-aided Max-Log-MAP SDM detector of Section 4.2.3 still exhibits a substantially higher complexity. Consequently, in Section 4.2.5 we derive an approximate Max-Log-MAP method, namely the SOPHIE SDM detector. The SOPHIE SDM detector combines the advantages of both the OHRSA-aided ML and OHRSA-aided Log-MAP SDM detectors of Sections 4.2.2 and 4.2.3, respectively. Specifically, it exhibits a similar performance to that of the optimal Max-Log-MAP detector, while imposing a modest complexity, which is only slightly higher than that required by the low-complexity MMSE SDM detector [28]. The computational complexity as well as the achievable performance of the SOPHIE SDM detector of Section 4.2.5 were analysed and quantified in Sections 4.2.5.1 and 4.2.5.2, respectively.

Our related conclusions were summarized in Section 4.3. Specifically, based on Figure 4.11 and we reported achieving a BER of 10^{-4} at SNRs of $\gamma = 4.2, 9.2$ and 14.5 in high-throughput 8x8 rate-$\frac{1}{2}$ turbo-coded $M = 4, 16$ and 64-QAM systems communicating over a dispersive Rayleigh fading channel. Additionally, recall from Figure 4.10 that we reported achieving a BER of 10^{-4} at SNRs of $\gamma = 9.5, 16.3$ and 22.8 in high-throughput rank-deficient 4x4, 6x4 and 8x4 rate-$\frac{1}{2}$ turbo-coded 16-QAM systems, respectively.

6.1.3 Iterative Reciever Architecture

In Chapter 5 we derived an iterative, so-called *turbo* multi-antenna-multi-carrier (MAMC) receiver architecture. Following the philosophy of turbo processing [26], our turbo SDM-OFDM receiver of Figure 5.1

comprises a succession of detection modules, which iteratively exchange soft bit-related information and thus facilitate a substantial improvement of the overall system performance.

More specifically, our turbo SDM-OFDM receiver comprises three major components, namely, the soft-feedback decision-directed channel estimator discussed in detail in Section 2.9, followed by the soft-input-soft-output OHRSA Log-MAP SDM detector derived in Section 4.2.3 as well as a soft-input-soft-output serially concatenated turbo code [27]. Consequently, in Figures 5.3–5.14 of Chapter 5 we analyzed the achievable performance of each individual constituent component of our turbo receiver, as well as the achievable performance of the entire amalgamated iterative system. We aimed at identifying the optimum system configuration, while considering various design trade-offs, such as the achievable BER performance, the attainable data-rate as well as the associated computational complexity.

In Section 5.4.2.4 we demonstrated that our turbo SDM-OFDM system employing the MIMO-DDCE scheme of Section 2.9 as well as the OHRSA Max-Log-MAP SDM detector of Section 4.2.3 remains effective in channel conditions associated with high mobile speeds of up to 130 km/h, which corresponds to the OFDM-symbol normalized Doppler frequency of 0.006. Additionally, in Figure 5.13 we reported a virtually error-free performance for a rate $1/2$ turbo-coded 8x8-QPSK-OFDM system, exhibiting an effective throughput of 8 MHz · 8 bits/s/Hz=64 Mbps and having a pilot overhead of only 10% at an SNR of 7.5dB and a normalized Doppler frequency of 0.003, which corresponds to a mobile terminal speed of about 65 km/h.

In conclusion, we would like to offer the following important observations. The potential performance gain achievable by an iterative multi-antenna multi-carrier system may be dissected into several major regions, where we may identify the *diversity gain* region, the *detection gain* region as well as the *iterative gain* region. Consider the BER versus SNR performance curves depicted in Figure 6.2.

- Firstly, the diversity gain region may be associated with the interval spanning the SNR values of Figure 6.2, which lie between the performance curves 1 and 2 corresponding to the scenarios of low and high diversity ranks[1], respectively. Correspondingly, the achievable diversity gain may be realized by attaining a sufficient diversity rank contributed by the combination of the channel and waveform parameters. This phenomenon is exemplified, for instance, by Figure 5.8 of Section 5.3.
- The detection gain region may be identified as the region of the SNR values located between the performance curves 2 and 3 of Figure 6.2, which correspond to the systems employing for example a linear MMSE detector and a near-optimum Max-Log-MAP detector, respectively. The achievable detection gain may be realized by the means of employing an efficient MIMO detection method rem-

---

[1] Quantitatively speaking, the low diversity rank channel is a channel, where the distribution of the total channel energy is reminiscent to χ^2_{2D} distribution, with $D \approx 1$. Correspondingly, the high diversity channels are channels, where we have $D \gg 1$.

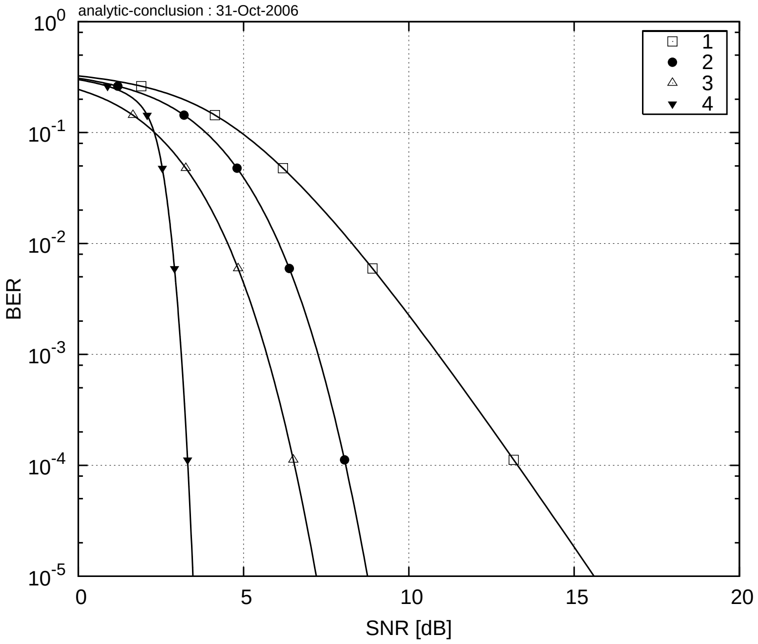

Figure 6.2: BER versus SNR performance of an iterative multi-antenna multicarrier system in dispersive Rayleigh fading channel. We consider the scenarios of 1. low diversity rank, 2. high diversity rank and suboptimum SDM detector, 3. high diversity rank and optimum SDM detector and 4. high diversity rank and iterative optimum SDM detector and decoder.

iniscent of the OHRSA method derived in Chapter 4. This phenomenon is exemplified, for instance, by Figure 3.11 of Section 3.6.

- Finally, the iterative gain region corresponds to the interval of the SNR values located between the performance curves 3 and 4 of Figure 6.2, which correspond to the systems employing a single as well as eight detection and decoding iterations. Correspondingly, the attainable iterative gain may be realized by employing iterative detection and decoding, which invokes iterative exchange of the soft bit-related information and thus facilitates the efficient exploitation of the diversity rank available. This phenomenon is exemplified, for instance, by Figures 5.3 and 5.6 of Sections 5.2 and 5.3, respectively.

6.2 Future work

6.2.1 Semi-Analytical Model

The family of state-of-the-art communication systems invokes a conglomerate of complex mathematical algorithms. The analytical expressions describing the behaviour of these algorithms are often hard to derive. Correspondingly, the performance of complex systems is typically evaluated using extensive software

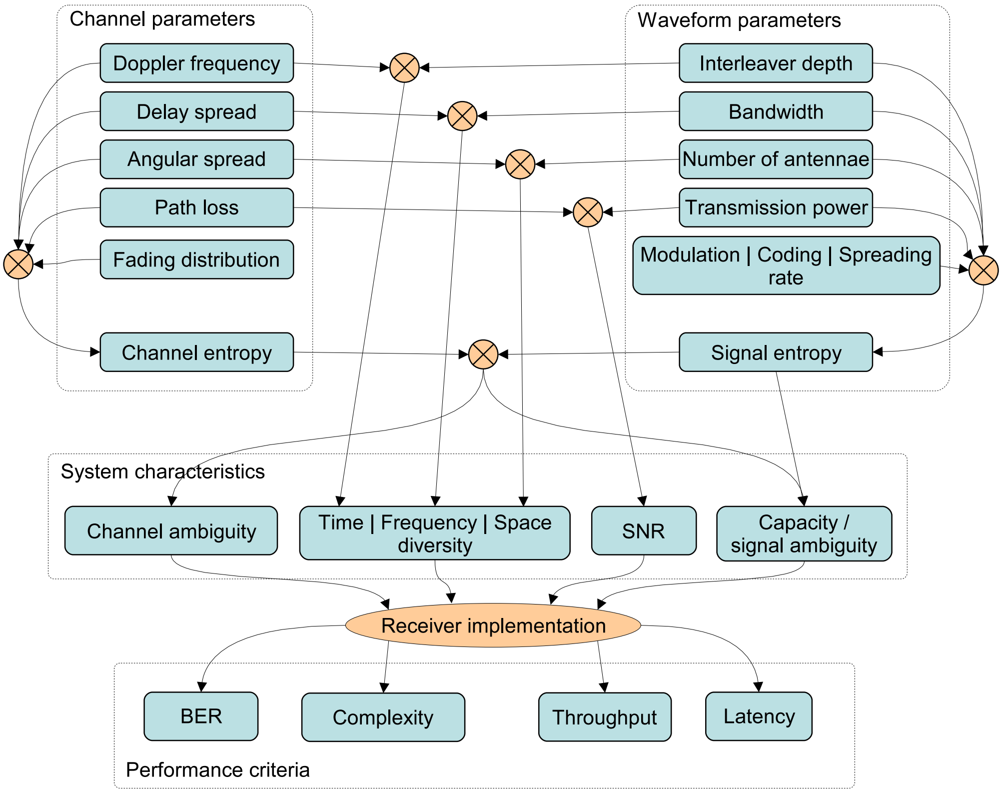

Figure 6.3: Mobile wireless communication system analysis methodology.

simulations. Unfortunately however, the multiplicity of effects imposed by the different phenomena in the complex systems considered tend to obscure the important trends and trade-offs, which have to be considered in the process of system design and optimization.

Consequently, we propose a semi-analytic methodology, which facilitates the prediction of the performance achievable by a system characterised by a specific ensemble of system and channel parameters.

The proposed semi-analytical technique attempts to dissect the complex problem of system performance analysis into a set of factors originating from different aspects of both the channel and the waveform characteristics, thus exposing the various trends and trade-offs inherent in the design of an efficient wireless mobile smart-antenna-aided multicarrier communication system.

Let us consider the system analysis methodology characterized in the stylised illustration of Figure 6.3, where we identify two sets of parameters, which characterize our system. Firstly, at the left of the figure we have a set of *channel parameters*, which comprizes the Doppler frequency f_D, the RMS delay spread τ_{rms}, the angular spread σ_a^2 as well as the AWGN variance σ_w^2. Additionally, we have to consider the statistical distribution of the CIR taps-related fading coefficients. Secondly, for each channel-related parameter, we have the corresponding *waveform parameter*, as seen at the right of Figure 6.3. Namely, we have the bit-interleaver depth T, the signal bandwidth B, the numbers m_{t} and n_{r} of transmit and receive antennas as

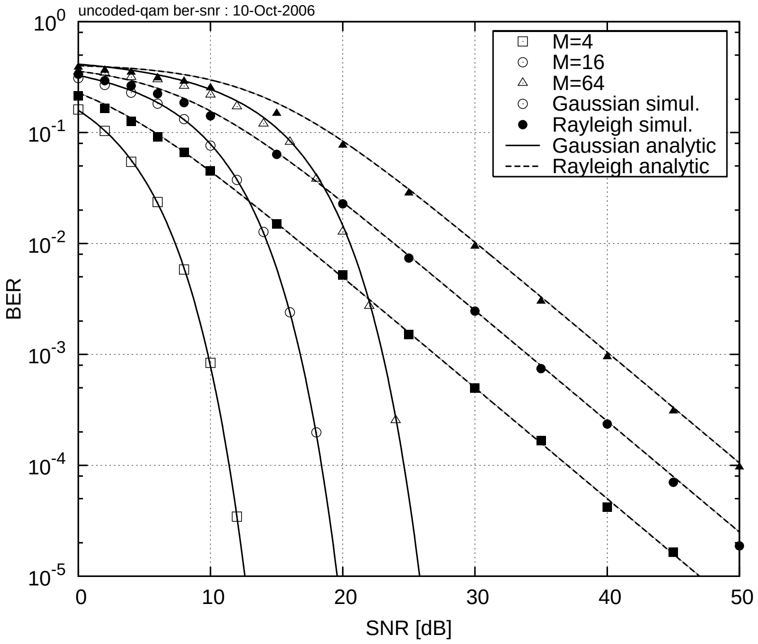

Figure 6.4: BER versus SNR performance of uncoded M-QAM in Gaussian and Rayleigh channels. The markers characterize the simulated results corresponding to $M = 4, 16$ and 64. The solid and dashed lines show the corresponding calculated BER versus SNR for Gaussian and Rayleigh channels, respectively, obtained using the semi-analytical model.

well as the signal to noise ratio γ. Additionally, we have the statistical distribution of the energy associated with the transmitted symbols, which is determined by the particular coding, spreading and modulation scheme. Some examples of the possible symbol-power distributions include the constant power in the case of a PSK modulation, the quantized multi-level uniform distribution in the case of M-QAM as well as the near-Rayleigh power distribution in the cases of CDMA and OFDM.

Consequently, our aim is to derive a set of semi-analytical expressions, which would describe the interdependencies between the aforementioned system parameters and a set of criteria characterizing the performance of the mobile wireless communication system considered. Specifically, we choose four major performance criteria, which form the performance metric depicted in Figure 6.3, namely we consider the *BER*, *Complexity*, *Throughput* as well as *Latency*.

We have completed a feasibility study and our preliminary results suggest that a semi-analytical model may be devised for characterizing the various phenomena, which is capable of accounting for the majority of the effects featuring in Figures 6.4–6.9, which determine the performance of a complex mobile wireless communication system. Some examples of these aspects, which may be taken into account in a corresponding model include

- Modulation scheme, *e.g.* 4,16,64 QAM (Figures 6.4 and 6.7).

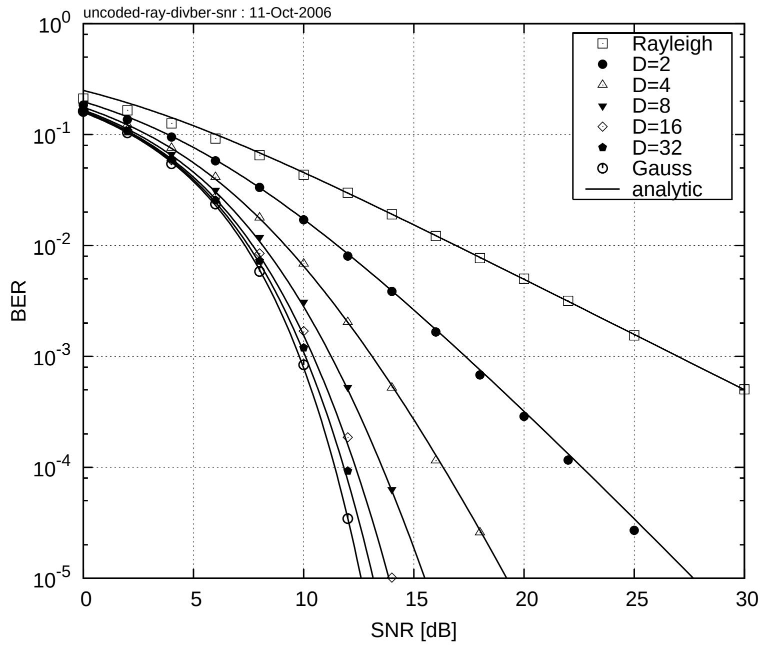

Figure 6.5: BER versus SNR performance of an uncoded QPSK system communicating over a χ^2_D-distributed flat-fading channel. The markers portray the simulated results associated with the diversity ranks $D = 1, 2, \cdots, 32$. The solid lines show the corresponding calculated BER versus SNR curves obtained using the semi-analytical model.

- Coding scheme, *e.g.* block, convolutional, turbo code with a given number of decoding iterations (Figure 6.6).
- MIMO system dimensions, *i.e.* number of transmit and receive antennas (Figure 6.7).
- Multi-user environment, *i.e.* number of coherent and non-coherent users (Figures 6.7 and 6.8).
- Channel correlation properties, *i.e.* Doppler frequency, delay spread (Figure 6.5).
- MIMO detection complexity (Figures 6.8 and 6.9).
- Imperfect channel estimation (Figure 6.10).

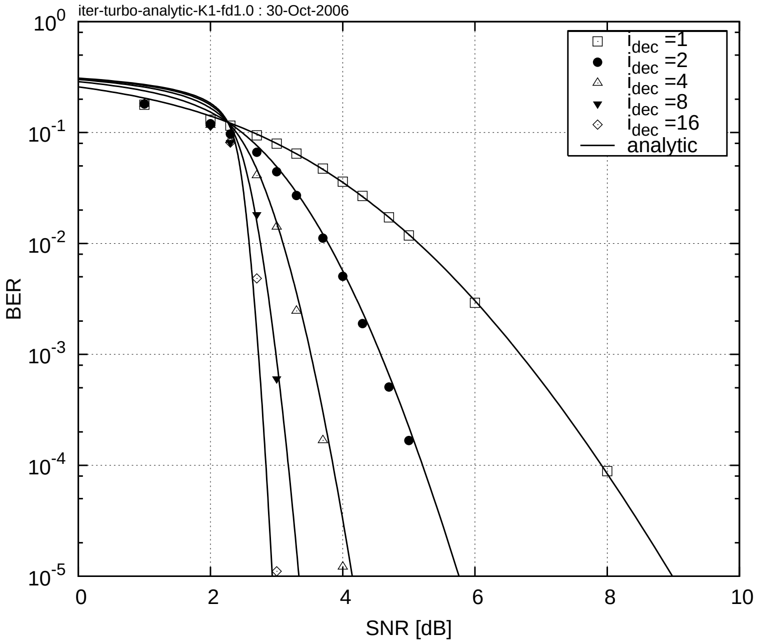

Figure 6.6: BER versus SNR performance of a turbo code in uncorrelated flat Rayleigh channel. The markers characterize the simulated results, while invoking 1 to 16 iterations of the turbo decoder. The lines show the corresponding calculated SNR versus BER obtained using the semi-analytical model.

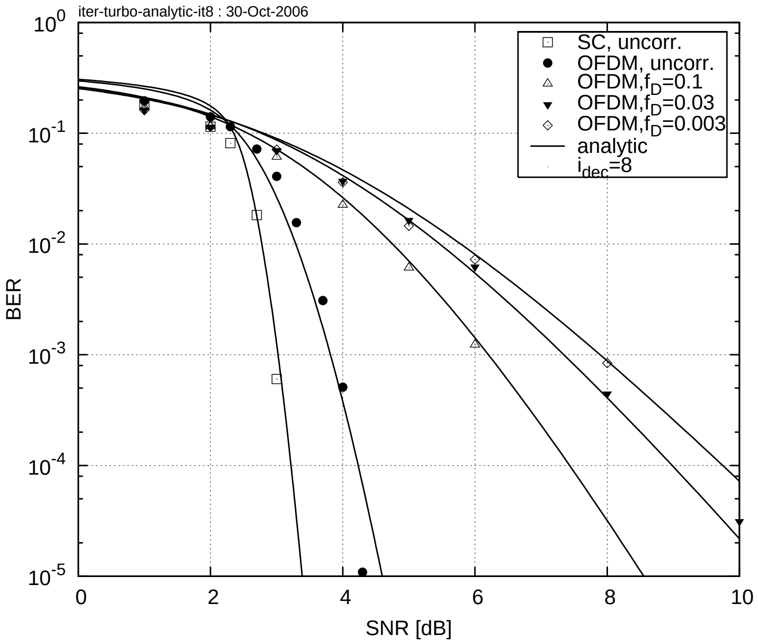

Figure 6.7: BER versus SNR performance exhibited by the $K = 128$-subcarrier single-antenna QPSK-OFDM system employing a rate $\frac{1}{2}$ parallel-concatenated turbo code in a correlated Rayleigh fading having the OFDM-symbol-normalized Doppler frequencies of $f_D = 0.1, 0.03$ and 0.003. The CIR was the 7-path COST-207 BU model [119]. All additional system parameters are summarized in Table 1.4. The markers characterize the simulated results, while invoking $i_{\text{dec}} = 8$ turbo decoder iterations. The solid lines show the corresponding calculated SNR versus BER obtained using the semi-analytical model.

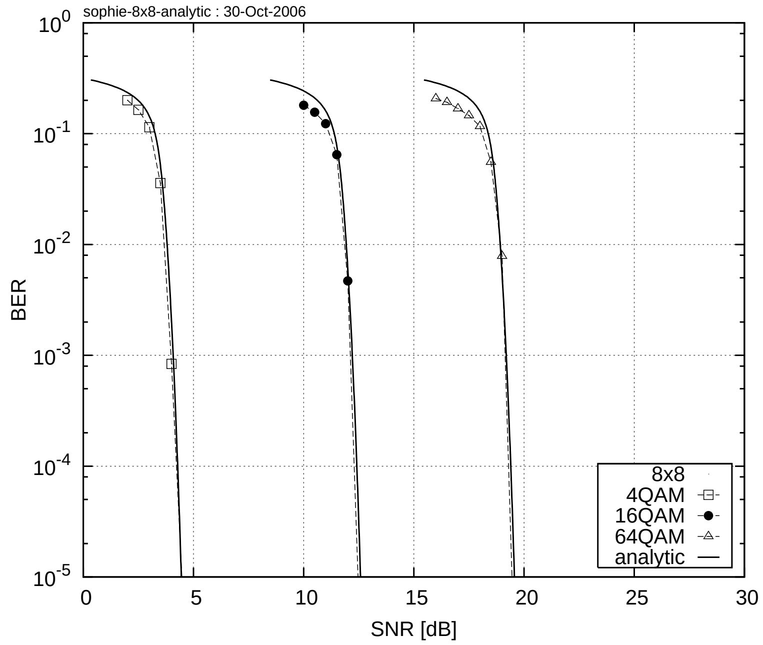

Figure 6.8: BER versus SNR performance exhibited by a rate-$\frac{1}{2}$ turbo coded 8x8 OFDM system employing 4,16 and 64-QAM and communicating over a dispersive Rayleigh fading channel. The markers portray the simulated results, while the solid lines show the corresponding results obtained using the semi-analytical model.

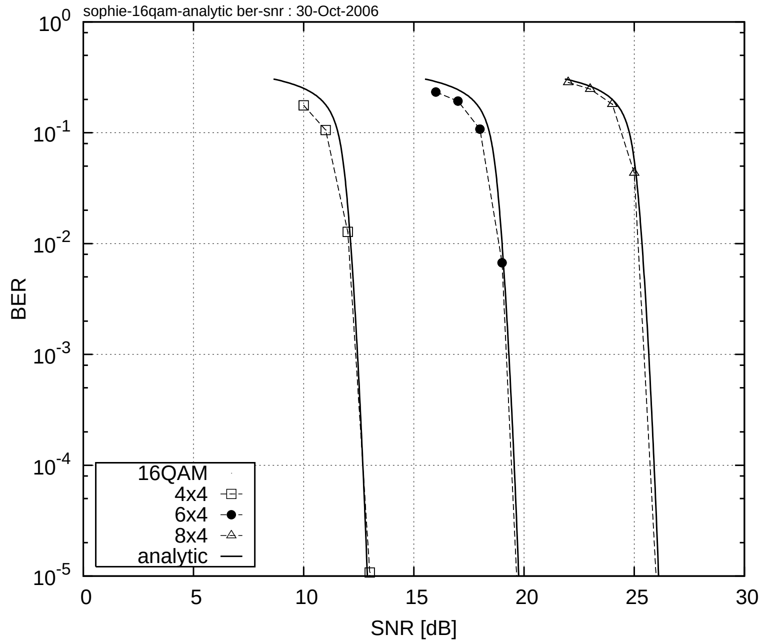

Figure 6.9: BER versus SNR performance exhibited by a turbo coded 16QAM-SDM-OFDM system using $m_{\mathrm{t}} = 4, 6$ and 8 transmit antennas as well as 4 receive antennas. The markers characterize the simulated results. The solid lines show the corresponding calculated SNR versus BER obtained using the semi-analytical model.

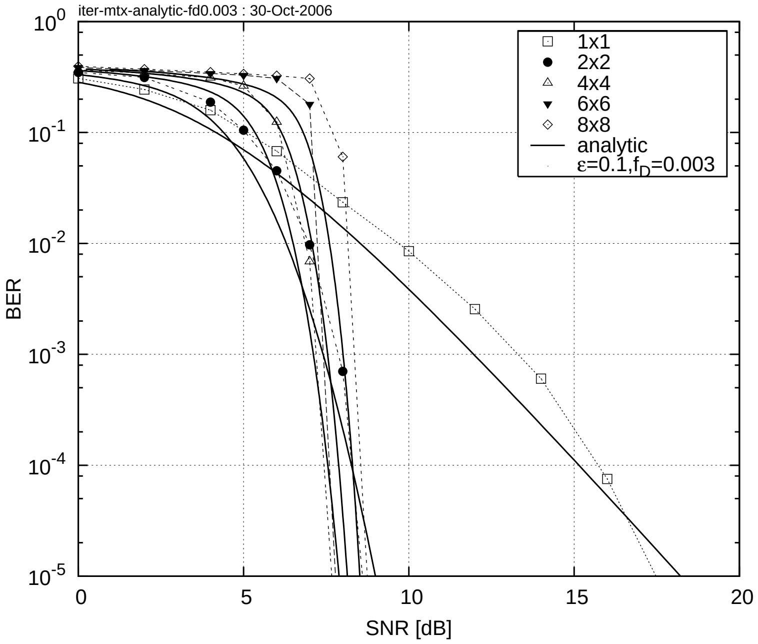

Figure 6.10: BER versus SNR performance exhibited by a rate-$\frac{1}{2}$ turbo coded QPSK-MIMO-OFDM system employing numbers $n_\mathrm{r} = m_\mathrm{t} = 1, 2, 4, 6$ and 8 of transmit and receive antennas and using the PAST-MIMO-DDCE scheme of Section 2.9, while communicating over dispersive Rayleigh fading channel. The markers portray the simulated results, while the solid lines show the corresponding results obtained using the semi-analytical model.

6.2.2 EXIT Chart Aided Optimization for Turbo Architecture

EXtrinsic Information Transfer (EXIT) chart aided analysis constitutes a powerful semi-analytic tool, which enables the visualisation and analysis of the convergence properties of iterative decoding algorithms. EXIT charts, originally developed by ten Brink [158] for the analysis of turbo codes, provide an insight into the interaction between different soft-input-soft-output component modules comprising a turbo system, such as for example the joint turbo receiver depicted in Figure 5.1, thus facilitating the design of a highly efficient system, which is capable of achieving a near-optimum performance. EXIT chart aided optimization of turbo equalisation was explored by Tüchler *et al.* [159] and was further developed by Otnes [160]. The application of EXIT charts in the context of iterative MIMO detection and decoding was first considered by ten Brink [161]. An example of a typical EXIT chart is depicted in Figure 6.11

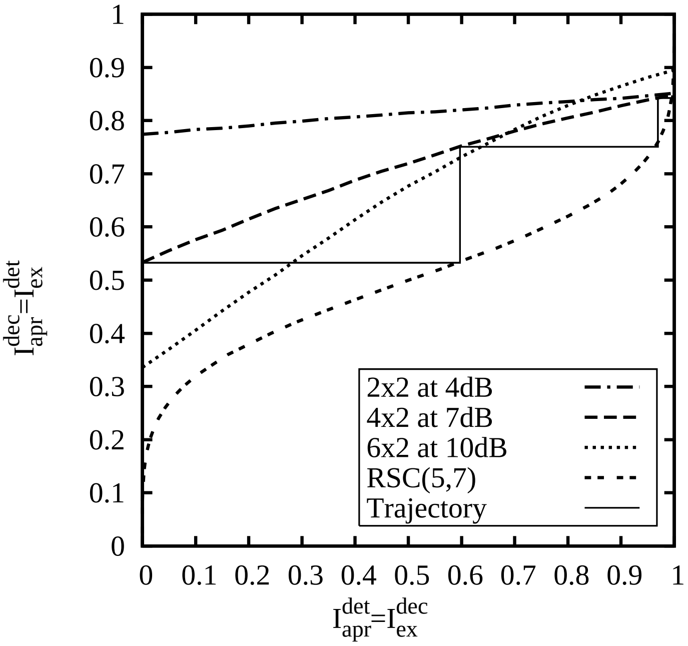

Figure 6.11: Typical EXIT chart for a MIMO system at different SNRs.

Glossary

BER	Bit Error Rate
BLAST	Bell Labs Layered Space-Time
CIR	Channel Impulse Response
CSC	Cumulative Sub-Cost
CSD	Complex Sphere Decoder
CSI	Channel State Information
CTF	Channel Transfer Function
D-BLAST	Diagonal BLAST
DDCE	Decision Directed Channel Estimation
DFT	Discrete Fourier Transform
FD-CTF	Frequency-Domain Channel Transfer Function
FEC	Forward Error Correction
FS	Fractionally-Spaced
FS-CIR	Fractionally-Spaced CIR
GA	Genetic Algorithms
GA-MMSE	Genetic Algorithm-aided MMSE
LLR	log-likelihood ratio
Log-MAP	Logarithmic Maximum *A Posteriori*
LS	Least Squares

MAMC	multi-antenna-multi-carrier
MC-CDMA	Multi-Carrier Code Division Multiple Access
MCF	Minimum Cost Function
MIMO	Multiple-Input Multiple-Output
ML	Maximum Likelihood
MMSE	Minimum Mean Square Error
MUD	Multi-User Detection
MV	Minimum Variance
NLOS	Non-Line-Of-Sight
NMSE	Normalized Mean Square Error
OFDM	Orthogonal Frequency Division Multiplexing
OHRSA	Optimized Hierarchy RSA
OHRSA	Optimized Hierarchy Reduced Search Algorithm
PAST	Projection Approximation Subspace Tracking
PDF	Probability Density Function
PDP	Power Delay Profile
PIC	Parallel Interference Cancellation
PSD	Power Spectral Density
RF	Radio Frequency
RMS	Root Mean Square
RSA	Reduced Search Algorithm
RSA	Reduced Search Algorithms
RSC	Recursive Systematic Convolutional
SD	Sphere Decoder
SDM	Space Devision Multiplexing
SDM	Space Division Multiplexing
SDMA	Space Devision Multiple Access
SDMD	SDM Detection
SIC	Successive Interference Cancellation

SINR	Signal-to-Interference-plus-Noise Ratio
SIR	Signal-to-Interference Ratio
SISO	Single Input Single Output
SOPHIE	Soft-output OPtimized HIErarchy
SS	Symbol-Spaced
STBC	Space-Time Block Codes
STC	Space-Time Codes
STTC	Space-Time Trellis Codes
V-BLAST	Vertical BLAST
WHT	Walsh-Hadamard Transform
WSS	Wide Sense Stationary

Bibliography[1]

[26] L. Hanzo, T. H. Liew, and B. L. Yeap, *Turbo Coding, Turbo Equalisation and Space-Time Coding*. Chichester, UK; Piscataway, NJ, USA: John Wiley and IEEE Press, 2002, 766 pages. (For detailed contents, please refer to http://www-mobile.ecs.soton.ac.uk.).

[27] C. Berrou, A. Glavieux, and P. Thitimajshima, “Near shannon limit error-correcting coding and decoding: Turbo codes,” in *Proceedings of IEEE International Conference on Communications*. Geneva, Switzerland: IEEE, May 1993, pp. 1064–1070.

[28] L. Hanzo, M. Münster, B. J. Choi, and T. Keller, *OFDM and MC-CDMA for Broadband Multi-User Communications, WLANs and Broadcasting*. John Wiley and IEEE Press, 2003, 992 pages.

[29] A. Goldsmith, S. A. Jafar, N. Jindal, and S. Vishwanath, “Capacity limits of MIMO channels,” *IEEE Journal on Selected Areas in Communications*, vol. 21, no. 5, pp. 684–702, June 2003.

[30] M. Münster, “Antenna diversity-assisted adaptive wireless multiuser OFDM systems,” Ph.D. dissertation, University of Southampton, UK, 2002.

[31] Y. Li, “Pilot-symbol-aided channel estimation for OFDM in wireless systems,” *IEEE Transactions on Vehicular Technology*, vol. 49, pp. 1207–1215, July 2000.

[32] M. Morelli and U. Mengali, “A Comparison of Pilot-Aided Channel Estimation Methods for OFDM Systems,” *IEEE Transactions on Signal Processing*, vol. 49, no. 12, pp. 3065–3073, December 2001.

[33] B. Yang, Z. Cao, and K. Letaief, “Analysis of low-complexity windowed DFT-based MMSE channel estimation for OFDM systems,” *IEEE Transactions on Communications*, vol. 49, pp. 1977–1987, November 2001.

[34] M.-X. Chang and Y. Su, “Model-based channel estimation for OFDM signals in Rayleigh fading,” *IEEE Transactions on Communications*, vol. 50, pp. 540–544, April 2002.

---

[1] for the List of Publications [1]–[25], please refer to pages vi–viii.

[35] P. Höher, S. Kaiser, and P. Robertson, “Pilot-symbol-aided channel estimation in time and frequency,” in *IEEE Global Telecommunications Conference: The Mini-Conference*, Phoenix, AZ, November 1997, pp. 90–96.

[36] ——, “Two-dimensional pilot-symbol-aided channel estimation by Wiener filtering,” in *IEEE International Conference on Acoustics, Speech and Signal Processing*, Munich, Germany, April 1997, pp. 1845–1848.

[37] O. Edfords, M. Sandell, J.-J. van de Beek, S. Wilson, and P. Börjesson, “OFDM channel estimation by singular value decomposition,” *IEEE Transactions on Communications*, vol. 46, pp. 931–939, July 1998.

[38] Y. Li, L. Cimini, and N. Sollenberger, “Robust channel estimation for OFDM systems with rapid dispersive fading channels,” *IEEE Transactions on Communications*, vol. 46, no. 7, pp. 902–915, April 1998.

[39] M. Münster and L. Hanzo, “RLS-adaptive parallel interference cancellation assisted decision-directed channel estimation for OFDM,” in *Processdings of IEEE Wireless Communications and Networking Conference*, vol. 1, New Orleans, Lousiana, USA, 16-20 March 2003, pp. 50–54.

[40] R. Otnes and M. Tüchler, “Iterative channel estimation for turbo equalization of time-varying frequency-selective channels,” *IEEE Transactions on Wireless Communications*, vol. 3, no. 6, pp. 1918–1923, 2004.

[41] J.-J. van de Beek, O. Edfors, M. Sandell, S. Wilson, and P. Börjesson, “On channel estimation in OFDM systems,” in *Proceedings of Vehicular Technology Conference*, vol. 2. Chicago, IL USA: IEEE, July 1995, pp. 815–819.

[42] V. Mignone and A. Morello, “A novel demodulation scheme for fixed and mobile receivers,” *IEEE Transactions on Communications*, vol. 44, pp. 1144–1151, September 1996.

[43] Y. Li and N. Sollenberg, “Clustered OFDM with channel estimation for high rate wireless data,” *IEEE Transactions on Communications*, vol. 49, pp. 2071–2076, December 2001.

[44] M. Münster and L. Hanzo, “Second-order channel parameter estimation assisted cancellation of channel variation-induced inter-subcarrier interference in OFDM systems,” in *Proceedings of International Conference on Trends in Communications*, vol. 1, Bratislava, Slovakia, 4-7 July 2001, pp. 1–5.

[45] ——, “MMSE channel prediction assisted symbol-by-symbol adaptive OFDM,” in *Proceedings of IEEE International Conference on Communications*, vol. 1, New York, USA, 28 April-2 May 2002, pp. 416–420.

[46] M. Sandell, C. Luschi, P. Strauch, and R. Yan, “Iterative channel estimation using soft decision feedback,” in *Proceedings of IEEE Global Telecommunications Conference*, vol. 6, Sydney, NSW, 1998, pp. 3728–3733.

[47] M. Valenti, “Iterative channel estimation for turbo codes over fading channels,” in *Proceedings of IEEE Wireless Communications and Networking Conference*, vol. 3, 23-28 September 2000, pp. 1019–1024.

[48] B.-L. Yeap, C. Wong, and L. Hanzo, “Reduced complexity in-phase/quadrature-phase M-QAM turbo equalization using iterative channel estimation,” *IEEE Transactions on Wireless Communications*, vol. 2, no. 1, pp. 2–10, 2003.

[49] S. Song, A. Singer, and K.-M. Sung, “Turbo equalization with an unknown channel,” in *Proceedings of IEEE International Conference on Ascoustics, Speech and Signal Processing*, vol. 3, Orlando, Florida, 13–17 May 2002, pp. 2805–2808.

[50] ——, “Soft input channel estimation for turbo equalization,” *IEEE Transactions on Signal Processing, [see also IEEE Transactions on Acoustics, Speech and Signal Processing]*, vol. 52, pp. 2885–2894, 2004.

[51] R. Otnes and M. Tüchler, “Soft iterative channel estimation for turbo equalization: comparison of channel estimation algorithms,” in *Proceeding of the 8th International Conference on Communication Systems*, vol. 1, Amsterdam, Netherlands, 21–24 April 2002, pp. 72–76. [Online]. Available: http://ieeexplore.ieee.org/iel5/8429/26550/01182440.pdf

[52] N. Seshadri, “Joint data and channel estimation using blind trellis search techniques,” *IEEE Transactions on Communications*, vol. 42, no. 2/3/4, pp. 1000–1011, February/March/April 1994.

[53] E. Baccarelli and R. Cusani, “Combined channel estimation and data detection using soft statistics for frequency-selective fast-fading digital links,” *IEEE Transactions on Communications*, vol. 46, no. 4, pp. 424–427, Apr. 1998.

[54] A. Knickenberg, B.-L. Yeap, J. Hàmorskỳ, M. Breiling, and L. Hanzo, “Non-iterative Joint Channel Equalisation and Channel Decoding,” *IEE Electronics Letters*, vol. 35, no. 19, pp. 1628–1630, 16 September 1999.

[55] C. Cozzo and B. Hughes, “Joint channel estimation and data detection in space-time communications,” *IEEE Transactions on Communications*, vol. 51, no. 8, pp. 1266–1270, Aug. 2003.

[56] T. Cui and C. Tellambura, “Joint channel estimation and data detection for OFDM systems via sphere decoding,” in *Proceedings of IEEE Global Telecommunications Conference*, vol. 6, Dallas, Texas, 29 Nov.-3 Dec. 2004, pp. 3656–3660.

[57] ——, “Joint data detection and channel estimation for OFDM systems,” *IEEE Transactions on Communications*, vol. 54, no. 4, pp. 670–679, 2006.

[58] C. Antón-Haro, J. Fonolossa, and J. Fonolossa, “Blind channel estimation and data detection using hidden Markov models,” *IEEE Transactions on Signal Processing*, vol. 45, no. 1, pp. 241–247, January 1997.

[59] D. Boss, K. Kammeyer, and T. Petermann, “Is blind channel estimation feasible in mobile communication systems?; a study based on GSM,” *IEEE Journal on Selected Areas in Communications*, vol. 16, no. 8, pp. 1479–1492, October 1998.

[60] T. Endres, S. Halford, C. Johnson, and G. Giannakis, “Blind adaptive channel equalization using fractionally-spaced receivers: A comparison study,” in *Proceedings of the Conference on Information Sciences and Systems*, Princeton, USA, 20–22 March 1996.

[61] G. Giannakis and S. Halford, “Asymptotically optimal blind fractionally spaced channel estimation and performance results,” *IEEE Transactions on Signal Processing*, vol. 45, no. 7, pp. 1815–1830, July 1997.

[62] S. Zhou and G. Giannakis, “Finite-alphabet based channel estimation for OFDM and related multicarrier systems,” *IEEE Transactions on Communications*, vol. 49, pp. 1402–1414, August 2001.

[63] M. Necker and G. Stüber, “Totally Blind Channel Estimation for OFDM over Fast Varying Mobile Channels,” in *Proceedings of International Conference on Communications*. New York, NY USA: IEEE, April 28 - May 2 2002.

[64] S. Haykin, *Adaptive Filter Theory*. Englewood Cliffs, NJ, USA: Prentice-Hall, 1996.

[65] D. Schafhuber and G. Matz, “MMSE and adaptive prediction of time-varying channels for OFDM systems,” *IEEE Transactions on Wireless Communications*, vol. 4, no. 2, pp. 593–602, March 2005.

[66] Y. Li, J. Winters, and N. Sollenberger, “MIMO-OFDM for wireless communications: signal detection with enhanced channel estimation,” *IEEE Transactions on Communications*, vol. 50, no. 9, pp. 1471–1477, 2002.

[67] G. Stüber, J. Barry, S. McLaughlin, Y. Li, M. Ingram, and T. Pratt, “Broadband MIMO-OFDM wireless communications,” *Proceedings of the IEEE*, vol. 92, no. 2, pp. 271–294, Feb 2004.

[68] X. Deng, A. Haimovich, and J. Garcia-Frias, "Decision directed iterative channel estimation for MIMO systems," in *Proceedings of IEEE International Conference on Communications*, vol. 4, Seattle, Washington, 11-15 May 2003, pp. 2326–2329.

[69] M. Münster and L. Hanzo, "Parallel-interference-cancellation-assisted decision-directed channel estimation for OFDM systems using multiple transmit antennas," *IEEE Transactions on Wireless Communications*, vol. 4, no. 5, pp. 2148–2162, Sept. 2005.

[70] S. Yatawatta and A. Petropulu, "Blind channel estimation in MIMO OFDM systems with multiuser interference," *IEEE Transactions on Signal Processing [see also IEEE Transactions on Acoustics, Speech, and Signal Processing]*, vol. 54, no. 3, pp. 1054–1068, March 2006.

[71] P. Vandenameele, L. van der Perre, M. Engels, B. Gyselinckx, and H. D. Man, "A combined OFDM/SDMA approach," *IEEE Journal on Selected Areas in Communications*, vol. 18, no. 11, pp. 2312–2321, Nov. 2000.

[72] V. Jungnickel, T. Haustein, E. Jorswieck, V. Pohl, and C. von Helmolt, "Performance of a MIMO system with overlay pilots," in *Global Telecommunications Conference, 2001. GLOBECOM '01. IEEE*, vol. 1, 25-29 Nov. 2001, pp. 594–598vol.1.

[73] H. Bolcskei, R. Heath, and A. Paulraj, "Blind channel identification and equalization in OFDM-based multiantenna systems," *Signal Processing, IEEE Transactions on [see also Acoustics, Speech, and Signal Processing, IEEE Transactions on]*, vol. 50, no. 1, pp. 96–109, Jan 2002.

[74] H. Zhu, B. Farhang-Boroujeny, and C. Schlegel, "Pilot embedding for joint channel estimation and data detection in MIMO communication systems," *Communications Letters, IEEE*, vol. 7, no. 1, pp. 30–32, Jan 2003.

[75] Y. Li, N. Seshardi, and S. Ariyavisitakul, "Channel estimation for OFDM systems with transmitt diversity in mobile wireless channels," *IEEE Journal on Selected Areas in Communications*, vol. 17, pp. 461–471, March 1999.

[76] Y. Li, "Simplified channel estimation for OFDM systems with multiple transmit antennas," *IEEE Transactions on Wireless Communications*, vol. 1, no. 1, pp. 67–75, January 2002.

[77] M. Münster and L. Hanzo, "Multi-user OFDM employing parallel interference cancellation assisted decision-directed channel estimation," in *Proceedings of IEEE Vehicular Technology Conference*, vol. 3, Vancouver, Canada, 24–28 Sept. 2002, pp. 1413–1417.

[78] A. Grant, “Joint decoding and channel estimation for linear MIMO channels,” in *Proceedings of IEEE Wireless Communications and Networking Conference*, vol. 3, Chicago, Illinois, 23-28 Sept. 2000, pp. 1009–1012.

[79] H. Mai, Y. Zakharov, and A. Burr, “Iterative B-spline channel estimation for space-time block coded systems in fast flat fading channels,” in *Proceeding of IEEE Vehicular Technology Conference, Spring*, vol. 1, Stockholm, Sweden, 30 May-1 June 2005, pp. 476–480.

[80] X. Qiao, Y. Cai, and Y. Xu, “Joint iterative decision feedback channel estimation for turbo coded V-BLAST MIMO-OFDM systems,” in *IEEE International Symposium on Communications and Information Technology*, vol. 2, Beijing, China, 12–14 October 2005, pp. 1384–1388.

[81] H. Mai, A. Burr, and S. Hirst, “Iterative channel estimation for turbo equalization,” in *Proceedings of IEEE International Symposium on Personal, Indoor and Mobile Radio Communications*, vol. 2, Barcelona, Spain, 5–8 September 2004, pp. 1327–1331.

[82] G. Foschini Jr. and M. Gans, “On limits of wireless communication in a fading environment when using multiple antennas,” *Wireless Personal Communications*, vol. 6, no. 3, pp. 311–335, March 1998.

[83] A. van Zelst, R. van Nee, and G. Awater, “Space Division Multiplexing (SDM) for OFDM systems,” in *Proceedings of Vehicular Technology Conference*, vol. 2. Tokyo, Japan: IEEE, May 15-18 2000, pp. 1070–1074.

[84] G. Foschini, “Layered Space-Time Architecture for Wireless Communication in a Fading Environment when using Multi-Element Antennas,” *Bell Labs Technical Journal*, vol. Autumn, pp. 41–59, 1996.

[85] J. Blogh and L. Hanzo, *Third-Generation Systems and Intelligent Networking*. John Wiley and IEEE Press, 2002, (For detailed contents, please refer to http://www-mobile.ecs.soton.ac.uk.).

[86] S. X. Ng, B. L. Yeap, and L. Hanzo, “Full-rate, full-diversity adaptive space time block coding for transmission over Rayleigh fading channels,” in *Proceedings of the IEEE VTC’05 Spring*, vol. 2, Stockholm, Sweden, 30 May-1 June 2005, pp. 1210–1214.

[87] S. Alamouti, “A Simple Transmit Diversity Technique for Wireless Communications,” *IEEE Journal on Selected Areas in Communications*, vol. 16, no. 8, pp. 1451–1458, October 1998.

[88] V. Tarokh, N. Seshadri, and A. Calderbank, “Space-Time Codes for High Data Rate Wireless Communication: Performance Criterion and Code Construction,” *IEEE Transactions on Information Theory*, vol. 44, no. 2, pp. 744–765, March 1998.

[89] V. Tarokh, A. Naguib, N. Seshadri, and A. Calderbank, “A Space-Time Coding Modem for High-Data-Rate Wireless Communications,” *IEEE Journal on Selected Areas in Communications*, vol. 16, no. 8, pp. 1459–1477, October 1998.

[90] ——, “Space-Time Codes for High Data Rate Wireless Communication: Performance Criteria in the Presence of Channel Estimation Errors, Mobility and Multiple Paths,” *IEEE Transactions on Communications*, vol. 47, no. 2, pp. 199–207, February 1999.

[91] V. Tarokh, H. Jafarkhani, and A. Calderbank, “Space-Time Block Coding for Wireless Communications: Performance Results,” *IEEE Transactions on Communications*, vol. 17, no. 3, pp. 451–460, March 1999.

[92] V. Tarokh, A. Naguib, N. Seshadri, and A. R. Calderbank, “Combined array processing and space-time coding,” *IEEE Transactions on Information Theory*, vol. 45, no. 4, pp. 1121–1128, May 1999.

[93] V. Tarokh, H. Jafarkhani, and A. Calderbank, “Space-Time Block Codes from Orthogonal Designs,” *IEEE Transactions on Information Theory*, vol. 45, no. 5, pp. 1456–1467, July 1999.

[94] V. Tarokh and H. Jafarkhani, “A Differential Detection Scheme for Transmit Diversity,” *IEEE Journal on Selected Areas in Communications*, vol. 18, no. 7, pp. 1169–1174, July 2000.

[95] S. Ariyavisitakul, J. Winters, and I. Lee, “Optimum space-time processors with dispersive interference: Unified analysis and required filter span,” *IEEE Transactions on Communications*, vol. 47, no. 7, pp. 1073–1083, July 1999.

[96] S. Ariyavisitakul, J. Winters, and N. Sollenberger, “Joint Equalization and Interference Suppression for High Data Rate Wireless Systems,” *IEEE Journal on Selected Areas in Communications*, vol. 18, no. 7, pp. 1214–1220, July 2000.

[97] G. Golden, G. Foschini, R. Valenzuela, and P. Wolniansky, “Detection Algorithms and Initial Laboratory Results using V-BLAST Space-Time Communication Architecture,” *IEE Electronics Letters*, vol. 35, no. 1, pp. 14–16, January 1999.

[98] C. Hassell-Sweatman, J. Thompson, B. Mulgrew, and P. Grant, “A Comparison of Detection Algorithms including BLAST for Wireless Communication using Multiple Antennas,” in *Proceedings of International Symposium on Personal, Indoor and Mobile Radio Communications*, vol. 1. Hilton London Metropole Hotel, London, UK: IEEE, September 18-21 2000, pp. 698–703.

[99] D. E. Goldberg, *Genetic Algorithms in Search, Optimization, and Machine Learning*. Reading, Massachusetts: Addison-Wesley, 1989.

[100] M. J. Juntti, T. Schlösser, and J. O. Lilleberg, "Genetic algorithms for multiuser detection in synchronous CDMA," in *IEEE International Symposium on Information Theory – ISIT'97*, Ulm, Germany, 1997, p. 492.

[101] S. M. Kay, *Fundamentals of Statistical Signal Processing*. Englewood Cliffs, NJ, USA: Prentice-Hall, 1998.

[102] R. van Nee, A. van Zelst, and G. Awater, "Maximum Likelihood Decoding in a Space-Division Multiplexing System," in *Proceedings of Vehicular Technology Conference*, vol. 1. Tokyo, Japan: IEEE, May 15-18 2000, pp. 6–10.

[103] G. Awater, A. van Zelst, and R. van Nee, "Reduced Complexity Space Division Multiplexing Receivers," in *Proceedings of Vehicular Technology Conference*, vol. 1. Tokyo, Japan: IEEE, May 15-18 2000, pp. 11–15.

[104] U. Fincke and M. Pohst, "Improved method for calculating vector of short length in a lattice, including a complexity analysis," *Math. Comput.*, vol. 44, pp. 463–471, April 1985.

[105] M. O. Damen, A. Chkeif, and J.-C. Belfiore, "Lattice code decoder for space-time codes," *IEEE Commun. Letters*, vol. 4, pp. 161–163, May 2000.

[106] B. Hochwald and S. ten Brink, "Achieving near-capacity on a multiple-antenna channel," *IEEE Transactions on Communications*, vol. 51, no. 3, pp. 389–399, 2003.

[107] M. O. Damen, H. E. Gamal, and G. Caier, "On maximum-likelihood detection and the search for closest lattice point," *IEEE Transactions on Information Theory*, vol. 49, no. 10, pp. 2389–2402, October 2003.

[108] D. Pham, K. R. Pattipati, P. K. Willet, and J. Luo, "An improved complex sphere decoder for V-BLAST Systems," *IEEE Signal Processing Letters*, vol. 11, no. 9, pp. 748–751, September 2004.

[109] T. Cui and C. Tellambura, "Approximate ML detection for MIMO systems using multistage sphere decoding," *IEEE Signal Processing Letters*, vol. 12, no. 3, pp. 222–225, March 2005.

[110] M. Damen, K. Abed-Meraim, and J.-C. Belfiore, "Generalised sphere decoder for asymmetrical space-time communication architecture," *Electronics Letters*, vol. 36, no. 2, pp. 166–167, 2000.

[111] T. Cui and C. Tellambura, "An efficient generalized sphere decoder for rank-deficient MIMO systems," *IEEE Communications Letters*, vol. 9, no. 5, pp. 423–425, 2005.

[112] Z. Yang, C. Liu, and J. He, "A new approach for fast generalized sphere decoding in mimo systems," *Signal Processing Letters, IEEE*, vol. 12, no. 1, pp. 41–44, Jan. 2005.

[113] W. Zhao and G. Giannakis, “Sphere decoding algorithms with improved radius search,” *IEEE Transactions on Communications*, vol. 53, no. 7, pp. 1104–1109, 2005.

[114] R. Wang and G. Giannakis, “Approaching MIMO channel capacity with soft detection based on hard sphere decoding,” *IEEE Transactions on Communications*, vol. 54, no. 4, pp. 587–590, April 2006.

[115] H. Vikalo, B. Hassibi, and T. Kailath, “Iterative decoding for mimo channels via modified sphere decoding,” *IEEE Transactions on Wireless Communications*, vol. 3, no. 6, pp. 2299–2311, Nov. 2004.

[116] S. Ronen, S. Bross, S. Shamai, and T. Duman, “Iterative channel estimation and decoding in turbo coded space time systems,” in *Proceedings of the 23rd IEEE Convention of Electrical and Electronics Engineers in Israel*, 6-7 Sept. 2004, pp. 80–83.

[117] B. Yang, “Projection approximation subspace tracking,” *IEEE Transactions on Signal Processing*, vol. 43, no. 1, pp. 95–107, January 1995.

[118] S. Bug, C. Wengerter, I. Gaspard, and R. Jakoby, “Channel model based on comprehensive measurements for DVB-T mobile applications,” in *IEEE Instrumentation and Measurements Technology Conference*, Budapest, Hungary, May 21-23 2001.

[119] M. Failli, “Digital land mobile radio communications COST 207,” European Commission, Tech. Rep., 1989.

[120] R. Steele and L. Hanzo, Eds., *Mobile Radio Communications*, 2nd ed. New York, USA: John Wiley and IEEE Press, 1999, 1090 pages.

[121] W. Jakes Jr., Ed., *Microwave Mobile Communications*. New York, USA: John Wiley & Sons, 1974.

[122] M. C. Jeruchim, P. Balaban, and K. S. Shanmugan, *Simulation of Communication Systems*. Kluwer Academic, 2000, 2nd edition.

[123] L. Hanzo, C. Wong, and M. Yee, *Adaptive Wireless Transceivers*. John Wiley and IEEE Press, 2002, (For detailed contents, please refer to http://www-mobile.ecs.soton.ac.uk.).

[124] M.-S. Alouini and A. J. Goldsmith, “Capacity of Rayleigh fading channels under different adaptive transmission and diversity-combining techniques,” *IEEE Transactions on Vehicular Technology*, vol. 49, no. 4, pp. 1165–1181, July 1999.

[125] L. Zheng and N. Tse, “Diversity and multiplexing: A fundamental tradeoff in multiple-antenna channels,” *IEEE Transactions on Information Theory*, vol. 49, no. 5, pp. 1073–1096, May 2003.

[126] C. E. Shannon, “A mathematical theory of communication,” *Bell System Technical Journal*, vol. 27, pp. 379–423 and 623–656, June and October 1948.

[127] R. Chang, “Synthesis of Band-Limited Orthogonal Signals for Multichannel Data Transmission,” *Bell System Technical Journal*, vol. 46, pp. 1775–1796, December 1966.

[128] L. Cimini, “Analysis and simulation of a digital mobile channel using orthogonal frequency division multiplexing,” *IEEE Transactions on Communications*, vol. 33, no. 7, pp. 665–675, July 1985.

[129] A. Papoulis, *Probability, Random Variables, and Stochastic Processes*, 2nd ed. New York, USA: McGraw-Hill, 1984.

[130] J. Lee and K. B. Bae, “Numerically stable fast sequential calculation for projection approximation subspace tracking,” in *Proceedings of the 1999 IEEE International Symposium on Circuits and Systems*, vol. 3, Orlando, Florida, 30 May–2 June 1999, pp. 484–487.

[131] H. Holma and A. Toskala, Eds., *WCDMA for UMTS : Radio Access for Third Generation Mobile Communications*. John Wiley and Sons, Ltd., 2000.

[132] B. Yang, K. Letaief, R. Cheng, and Z. Cao, “Channel estimation for OFDM transmission in multipath fading channels based on parametric channel modeling,” *IEEE Transactions on Communications*, vol. 49, pp. 467–479, March 2001.

[133] J. Yang and M. Kaveh, “Adaptive eigensubspace algorithm for direction or frequency estimation and tracking,” *IEEE Transactions on Acoustics, Speech and Signal Processing*, vol. 36, pp. 241–251, 1988.

[134] S. L. Marple, *Digital spectral analysis with applications*. Englewood Cliffs, NJ, USA: Prentice Hall, 1987.

[135] D. Schafhuber, G. Matz, and F. Hlawatsch, “Adaptive prediction of time-varying channels for coded OFDM systems,” in *Proceedings of the IEEE International Conference on Acoustics, Speech, and Signal Processing*, vol. 3, Orlando, Florida, 13–17 May 2002, pp. 2549–2552.

[136] T. Moon and W. Stirling, *Mathematical Methods and Algorithms for Signal Processing*. Prentice Hall, 2000.

[137] P. Vandenameele, L. van der Perre, and M. Engels, *Space division multiple access for wireless local area networks*. Kluwer, 2001.

[138] P. W. Wolniansky, G. J. Foschini, G. D. Golden, and R. A. Valenzuela, “V-BLAST: An architecture for realizing very high data rates over the rich scattering wireless channels,” in *Proceedings of the IEEE ISSSE-98*, Pisa, Italy, September 1998, invited Paper.

[139] M. Münster and L. Hanzo, “Co-Channel Interference Cancellation Techniques for Antenna Array Assisted Multiuser OFDM Systems,” in *Proceedings of IEE 3G Conference*, vol. 1, London, Great Britain, March 27-29 2000, pp. 256–260.

[140] A. Bhargave, R. Figueiredo, and T. Eltoft, “A Detection Algorithm for the V-BLAST System,” in *Proceedings of IEEE Global Telecommunications Conference*, vol. 1, San Antonio, Texas, USA, 25–29 November 2001, pp. 494–498.

[141] M. Mitchell, *An Introduction to Genetic Algorithms*. Cambridge, Massachusetts: MIT Press, 1996.

[142] L. Hanzo, L.-L. Yang, E.-L. Kuan, and K. Yen, *Single- and Multi-Carrier DS-CDMA*. John Wiley and IEEE Press, 2003, 430 pages.

[143] X. F. Wang, W. S. Lu, and A. Antoniou, “A genetic algorithm-based multiuser detector for multiple-access communications,” in *IEEE International Symposium on Circuits and System – ISCAS’98*, Monterey, California, USA, 1998, pp. 534–537.

[144] M. Jiang, S. Ng, and L. Hanzo, “Hybrid iterative multiuser detection for channel coded space division multiple access OFDM systems,” *IEEE Transactions on Vehicular Technology*, vol. 55, no. 1, pp. 115–127, Jan. 2006.

[145] R. Wang and G. Giannakis, “Approaching MIMO channel capacity with reduced-complexity soft sphere decoding,” in *Proceedings of IEEE Wireless Communications and Networking Conference*, vol. 3, Atlanta, Georgia, 21-25 March 2004, pp. 1620–1625.

[146] J. E. Gentle, *Numerical Linear Algebra for Applications in Statistics*. Berlin: Springer-Verlag, 1998.

[147] M. K. Varanasi, “Decision feedback multiuser detection: A systematic approach,” *IEEE Transactions on Information Theory*, vol. 45, pp. 219–240, January 1999.

[148] G. Valiente, *Algorithms on Trees and Graphs*. New York: Springer, 2002.

[149] A. Viterbi, *CDMA: Principles of Spread Spectrum Communication*. Reading MA, USA: Addison-Wesley, June 1995, iSBN 0201633744.

[150] R. D. Schafer, *An Introduction to Nonassociative Algebras*. New York: Dover, 1996.

[151] J. Hagenauer, E. Offer, and L. Papke, “Iterative decoding of binary block and convolutional codes,” *IEEE Transactions on Information Theory*, vol. 42, pp. 429–445, March 1996.

[152] C. Berrou and A. Glavieux, “Near optimum error-correcting coding and decoding: Turbo codes,” *IEEE Transactions on Communications*, vol. 44, no. 10, pp. 1261–1271, October 1996.

[153] C. Berrou, “Some Clinical Aspects of Turbo Codes,” in *Proceedings of the International Symposium on Turbo Codes & Related Topics*, Brest, France, 3-5 September 1997, pp. 26–31.

[154] S. Benedetto, R. Garello, and G. Montorsi, “A search for good convolutional codes to be used in the construction of turbo codes,” *IEEE Transactions on Communications*, vol. 46, no. 9, pp. 1101–1105, September 1998.

[155] G. Battail, “A conceptual framework for understanding turbo codes,” *IEEE Journal on Selected Areas in Communications*, vol. 16, no. 2, pp. 245–254, 1998.

[156] O. Açikel and W. Ryan, “Punctured turbo-codes for BPSK/QPSK channels,” *IEEE Transactions on Communications*, vol. 47, no. 9, pp. 1315–1323, September 1999.

[157] *Wireless LAN Medium Access Control (MAC) and Physical Layer (PHY) specifications*, IEEE 802.11g ed., IEEE LAN/MAN Standards Committee, 2003. [Online]. Available: http://standards.ieee.org/getieee802/802.11.html

[158] S. ten Brink, “Designing iterative decoding schemes with the extrinsic information transfer chart,” *AEU International Journal of Electronics and Communications*, vol. 54, no. 6, pp. 389–398, November 2000.

[159] M. Tüchler, R. Koetter, and A. Singer, “Turbo equalization: principles and new results,” *IEEE Transactions on Communications*, vol. 50, no. 5, pp. 754–767, 2002.

[160] R. Otnes and M. Tüchler, “Exit chart analysis applied to adaptive turbo equalization.” [Online]. Available: citeseer.ist.psu.edu/566748.html

[161] S. ten Brink, G. Kramer, and A. Ashikhmin, “Design of low-density parity-check codes for modulation and detection,” *IEEE Transactions on Communications*, vol. 52, no. 4, pp. 670–678, 2004.

Subject Index

Author Index